UNIVERSITÀ
DEGLI STUDI
DI PADOVA

Sede Amministrativa: Università degli Studi di Padova

Dipartimento di Ingegneria Industriale

CORSO DI DOTTORATO DI RICERCA IN: Ingegneria Industriale
CURRICOLUM: Energetica
CICLO XXXI

PRELIMINARY DESIGN OF ORGANIC FLUID TURBINES TO PREDICT THE EFFICIENCY

Tesi redatta con il contributo finanziario della Fondazione Cariparo

Coordinatore del corso di dottorato: Prof. Paolo Colombo
Coordinatore del curriculum: Prof.ssa Luisa Rossetto
Supervisore: Prof. Andrea Lazzaretto
Co-Supervisori: Dr. Giovanni Manente
Prof. Massimo Masi

Dottorando: Luca Da Lio

Alla mia famiglia

Abstract

Turbine efficiency plays a key role in the design optimization of ORCs (organic Rankine cycles) and should be properly evaluated for an accurate estimate of the real power production. Most of the literature focuses on cycle configuration, design parameters and working fluid that maximize different performance metrics, but often ignores the expander design features that are necessary to obtain them, by fixing in advance the expander efficiency. This approach is questionable for ORC systems where the high volumetric expansion ratios, variable sizes and working fluids may markedly affect turbine efficiency.

This work focuses on the preliminary design of radial inflow turbines and single stage axial flow turbines operating with different organic fluids. The aim is to build general efficiency maps in accordance with the similarity principles for the performance prediction of turbines having very different design specifications (i.e., mass flow rate and enthalpy drop) and handling different working fluids. The so-called "size parameter" (SP) and the volumetric expansion ratio (VR) are identified as the best efficiency predictors for ORC turbines. The former is proportional to the turbine size and accounts for the scale effect, i.e. the detrimental effect on the performance when the machine is scaled down below a certain size; the latter accounts for the compressibility influence and, compared to the pressure expansion ratio, limits the influence of the fluid properties.

Mean-line models are built for the preliminary design and performance estimation of radial and axial turbines in the Matlab ® environment implementing recent loss correlations to account for the flow irreversibilities and real fluid properties evaluated using the Refprop database. These models are used to simulate the turbine behavior and generate new design charts relating the efficiency to the design parameters (i.e., specific speed and velocity ratio for radial turbines; loading coefficient and flow coefficient for

axial turbines). Several simulations are then carried out to generate the optimum designs for a wide range of design specifications and working fluids, and the associated efficiency maps in the SP-VR plane. These maps show that neither the size effect (SP), nor the compressibility effect (VR) have a negligible influence on the turbine performance: the efficiency increases as SP increases and VR decreases. Despite the similar general efficiency trends in the SP-VR maps are similar, differences due to the fluid effect exist. So, the critical temperature of the working fluid is proposed as third efficiency predictor and a general correlation between turbine efficiency and size parameter, volumetric flow ratio, critical temperature is obtained. The resulting generalized efficiency map is conceptually valid for any fluid and can be easily integrated into a comprehensive thermodynamic cycle optimization procedure to account for the real turbine performance and overcome the limitations due to a separate design of turbine and system.

Sommario

Il rendimento della turbina ha un ruolo fondamentale nell'ottimizzazione del progetto di cicli Rankine a fluido organico (ORC) e dovrebbe essere attentamente valutato per avere una stima accurata della reale produzione di potenza. Larga parte della letteratura si concentra sulla configurazione di ciclo, sui parametri di progetto e sul fluido di lavoro che massimizzano indici di prestazione differenti, ma spesso non tiene conto delle caratteristiche progettuali della turbina necessarie al loro conseguimento, fissandone a priori l'efficienza. Tale approccio è discutibile per i sistemi ORC in cui gli alti rapporti di espansione volumetrici, le taglie variabili e i diversi fluidi di lavoro possono influenzare marcatamente l'efficienza della turbina.

Questo lavoro si occupa di progettazione preliminare di turbine radiali centripete e turbine monostadio assiali che utilizzano diversi fluidi organici. Lo scopo è costruire, in accordo con i principi della similitudine, mappe di efficienza generalizzate per la previsione del rendimento di turbine aventi specifiche di progetto molto diverse (portata di massa e salto entalpico) e operanti con fluidi diversi. Il cosiddetto "parametro di taglia" (SP) ed il rapporto di espansione volumetrica (VR) vengono identificati come le variabili migliori per la previsione dell'efficienza di turbine per ORC. Il primo è proporzionale alla taglia della turbina e tiene conto dell'effetto scala, ossia dell'effetto penalizzante sulle prestazioni quando la macchina è scalata al di sotto di una certa taglia; il secondo tiene conto dell'influenza della comprimibilità e limita, rispetto all'impiego del rapporto di pressioni, l'effetto sul rendimento delle proprietà del fluido.

Per la progettazione preliminare e per la stima delle prestazioni di turbine radiali ed assiali si sono costruiti in ambiente Matlab® modelli a linea media che includono recenti correlazioni di perdita e le proprietà reali dei fluidi valutate con il database Refprop. Tali modelli vengono impiegati per simulare il funzionamento della turbina e per costruire nuovi diagrammi

in cui l'efficienza è posta in relazione con i parametri di progetto (velocità specifica e rapporto di velocità per le turbine radiali; cifra di pressione e di flusso per le turbine assiali). E' stato effettuato un gran numero di simulazioni per generare progetti ottimi per un ampio intervallo di specifiche di progetto e fluidi di lavoro e le corrispondenti mappe di efficienza nel piano SP-VR. Queste mappe mostrano che nè l'effetto taglia, nè quello della comprimibilità (VR) hanno una influenza trascurabile sulle prestazioni della turbina: l'efficienza aumenta all'aumentare di SP e al calare di VR. Nonostante le mappe SP-VR presentino trend simili, vi sono tra esse delle differenze dovute all'effetto del fluido. La temperatura critica del fluido viene quindi proposta come ulteriore parametro a cui legare l'efficienza per ottenere una correlazione generale tra efficienza e parametro di taglia, rapporto di espansione volumetrica e temperatura critica. La mappa generalizzata che ne deriva è concettualmente valida per qualunque fluido e può essere facilmente integrata in una procedura di ottimizzazione globale del sistema ORC per tenere conto delle reali prestazioni della turbina e superare così le limitazioni dovute ad una progettazione separata della turbina e del sistema.

Radial turbine nomenclature

α	flow angle (°)
β	blade angle (°)
Δ	normalized mass defect thickness
δ_c	clearance gap (m)
Δ_w	wall boundary layer blockage
δ_w^*	displacement thickness (m)
Δ_z	axial length (m)
$\dot{m}$	mass flow rate (kg/s)
$\dot{Q}$	volumetric flow rate (m^3/s)
η_s	total-to-static efficiency
γ	blade angle (°)
κ_m	mean curvature of the meridional channel
ν_s	velocity ratio
ω	angular velocity (rad/s)
ϕ	flow coefficient
ψ	loading coefficient
ρ	density (kg/m^3)
Θ	normalized momentum defect thickness
θ	blade camberline angle (°)
A	passage area (m^2)
a	speed of sound (m/s)
b	blade height or passage width (m)
C	absolute velocity (m/s)
c	chord (m)
C_0	spouting velocity (m/s)
c_f	skin friction coefficient
D	diameter (m)
esse	blade pitch (m)
h	specific enthalpy (J/kg)
I	rothalpy (J/kg)
i	incidence angle (°)
k_b	blockage factor
k_{load}	blade loading
L	length (m)
N	blade number
n	rotational speed (rpm)
n_s	specific speed
o	throat width (m)
p	pressure (bar or kPa)
R	degree of reaction
r	radius (m)
s	specific entropy (J/(kgK))
SP	size parameter (m)
t	blade thickness (m)
U	peripheral speed (m/s)
VR	volumetric expansion ratio
W	relative velocity (m/s)
Y	total pressure loss coefficient

Superscripts

’	relative frame
*	sonic or ideal flow conditions

Subscripts

0	total state
1	Design volute inlet or performance component inlet station
2	Design nozzle inlet or performance component mid station
3	Design nozzle outlet or performance component outlet station
4	Design rotor inlet
5	Design rotor outlet
a	annulus
ave	average
b	blade
bl	blade loading
bp	blade pressure
bs	blade suction
cl	clearance
d	diffuser
df	disk friction
dis	discharge
evap	evaporating
ex	post-expansion
h	hub
hs	hub-to-shroud
in	inlet
inc	incidence
m	meridional or mean
max	maximum
min	minimum
n	nozzle
p	profile
R	relative
r	rotor
s	shroud or isentropic
t	tangential
TOT	total
v	volute
w	wall

Axial turbine nomenclature

α	flow angle (°)
β	blade angle (°)
δ	rotor radial clearance (m)
$\dot{m}$	mass flow rate (kg/s)
$\dot{V}$	volumetric flow rate (m^3/s)
η	efficiency
γ	specific heat ratio
γ	sweep angle (°)
λ	hub to tip radius ratio
ω	angular velocity (rad/s or rpm)
ϕ	flow coefficient
ψ	loading coefficient
ρ	density (kg/m^3)
A	area (m^2)
a	sound speed (m/s)
b	blade axial chord (m)
c	blade chord (m)
D_m	root mean square diameter (m)
d_s	specific diameter
e	blade surface roughness (m)
FL	flaring angle (°)
h	blade span (m)
h	specific enthalpy (J/kg)
Ma	Mach number
n_s	specific speed
o	blade throat (m)
p	pressure (Pa)
R	degree of reaction
Re	Reynolds number
s	blade pitch (m)
SP	size parameter (m)
T	temperature (K or °C)
t	trailing edge thickness (m)
U	peripheral velocity (m/s)
V	absolute velocity (m/s)
VR	volumetric expansion ratio
W	relative velocity (m/s)
Y	total pressure loss coefficient
Z	loading factor
z	blade number

Superscripts

’	relative frame

Subscripts

0	total state
1	stator inlet
2	stator exit and rotor inlet
3	rotor exit
cond	condensing
evap	evaporating
h	hub
m	meridional
N	stator
R	rotor
s	isentropic
t	tangential
t	tip
tt	total to total

Contents

Introduction

The growing awareness towards environmental sustainability, reduction of pollution caused by fossil fuels and energy saving makes the conversion into power of low-to-medium temperature heat from renewable energy sources or industrial processes particularly attractive. Organic Rankine Cycle (ORC) systems represent in this respect a viable technology that is rapidly growing in terms of installed power capacity due to the inherent suitability to a variety of heat sources and power plant sizes (from few kW to few tens of MW). ORC systems can be effectively used to recover heat from the exhaust gases of micro-gas turbines or internal combustion engines [1], to exploit the heat content of biomass combustion gases [2], concentrated solar radiation [3], geothermal sources or waste heat from industrial processes ([4], [5]).

The selection of thermodynamic cycle parameters, working fluid and components is not trivial due to the need of "tailoring" the plant to both the specific thermal availability and temperature levels [6]. In addition, a correct estimate of the net power output cannot disregard the influence on the cycle design parameters of the real performance characteristics of each plant component on the design parameters of the cycle, and in particular of the turbine, which is one of the most critical part of the system. Depending on heat and temperature availability, turbines or volumetric expanders are installed in existing ORC systems. Turbines are typically used in the 100 kW - several MW power capacity range in axial or radial inflow con-

figurations. The former are typically used in multistage arrangements (up to three) in medium (0.5-5 MW) to large ($\geq$ 5 MW) ORC systems where relatively high mass flow rates of working fluids are employed; the latter are generally better suited to the lower capacity ranges. Also innovative radial outflow architectures could be a promising solution in the small-to-medium power range as they permit to better accommodate the large volume variations typical of organic fluids [7]. However, a strict definition of the power intervals of application is not possible and the above ones are only indicative.

In the last decade, a very high number of studies on ORC systems appeared in the literature. Most of these studies focus on the thermodynamic optimization of the whole system for an assigned heat source ([8], [9], [10]), i.e., on the identification of working fluid, cycle configuration and temperature/pressure levels resulting in the maximum (or minimum) value of a specified function. Less efforts have been devoted to the modeling of the turbine behavior, the efficiency of which is often somehow arbitrarily chosen ([11]), with the risk of misleading predictions.

On the other side, researchers in the field of fluid dynamics and turbines have produced a significant amount of studies at different levels of analysis ranging from the development of fluid-dynamic simulation tools able to manage dense gas flows [12] to the preliminary and detailed aerodynamic turbine design.

As for radial inflow turbine (RIT) preliminary design, Ventura et al. [13] developed an automated process which explores a large spectrum of flow coefficients (ϕ), loading coefficients (ψ) and rotational speeds (n) in order to select the optimum values of these parameters. Fiaschi et al. [14] developed a mean-line model of a RIT for a 50 kW ORC system considering six working fluids, all sharing the same turbine inlet temperature of 147 °C. The predicted efficiencies varied in the range $54\% - 83\%$, depending on the working fluid. In a subsequent study [15], the same authors carried

out a parametric analysis to evaluate losses against the main design parameters, namely ϕ, ψ and the degree of reaction (R). The total-to-static efficiencies varied between 69.3% for cyclohexane and 78.0% for R1234yf. They showed that backswept bladed turbines can achieve efficiencies from 1.5 to 2.0 points higher than radial ones. Rahbar et al. [16] developed a methodology for the optimization of a 15 kW radial turbine for ORC applications considering eight working fluids and turbine inlet temperatures in the range 60-145 °C. The authors employed a genetic algorithm to maximize the total-to-static efficiency by varying ψ and ϕ in the range 0.6-1.4 and 0.2-0.5, respectively, and the rotational speed between 35000 and 65000 rpm. The optimization results showed that the optimum values of ψ are higher than unity (in the range 1.004-1.215) whereas the values of ϕ are in the range 0.22-0.26. The maximum efficiency was found to vary between 82.9% and 84.0% whereas the optimum values of specific speed (n_s) and velocity ratio (ν_s) are close to 0.42 and 0.62, respectively. More recently, several studies based on CFD simulations have appeared in the literature which either confirm or revise the turbine efficiency predictions obtained by the mean-line analyses. For instance, Fiaschi et al. [17] developed a design procedure for a micro radial ORC turbine (5 kW) based on a mean-line model for the preliminary sizing, further refined by a 3D approach to maximize the performance. The efficiency predicted by this model (70%) was confirmed by the results of the 3D analysis. Sauret and Gu [18] compared the efficiency predicted by a commercial preliminary design software, which basically embeds the design procedure described by Moustapha et al. [19] for traditional fluids, with the outcomes of a detailed CFD analysis, and they found significant differences (in the order of 10%) appeared.

Despite the fundamental role of the turbine in the net power production of the plant, and can significantly influence the final choice of the ORC pressure and temperature levels, the findings on turbines designs

are seldom embedded in the thermodynamic cycle optimization. Only in few recent works there is an attempt to simultaneously optimize not only the cycle variables, but also the main turbine design variables ([20],[21]). In particular, there is the need to integrate the thermodynamic analysis/optimization of the ORC system with a correct estimate of turbine efficiency to ensure that the real turbine is able to obtain the inlet and outlet thermodynamic states resulting from the cycle optimization procedure, being these states necessarily influenced by the turbine efficiency itself. However, a direct integration of the complete turbine design procedure into the procedure for the search of the optimum cycle parameters would be too time consuming, and therefore nonviable, since the turbine design should be repeated in each optimization step. On the other hand, the use of the traditional performance charts developed in the steam turbine practice (e.g., Smith chart [22], Balje diagram [23]) is impractical as the efficiency in these charts depends on variables not directly related to cycle parameters, and unfit when dealing with organic fluids anyhow. In fact, it is apparent that the specific thermodynamic properties of organic fluids reflect on turbine design and, consequently, on the achievable efficiencies. Specifically, for a fixed temperature drop, the enthalpy drop in the expansion of an organic vapor is comparatively lower than the steam enthalpy drop, so that the relatively smaller specific work allows for lower stage number arrangements. Conversely, the high expansion ratio per stage and the low speed of sound of organic fluids often result in transonic and supersonic flows accompanied by shock waves, which reduce turbine efficiency and make the compressibility effect not negligible. Moreover, since organic fluid turbines cover a wide range of power, the influence of the size on performance should be carefully taken into account in the evaluation of the efficiency.

The pioneering contributions to the development of efficiency charts for ORC turbines given by Macchi and Perdichizzi [24] and Perdichizzi and

Lozza [25] were precisely focused on these two latter aspects. These authors built mean line models for the design and efficiency prediction of optimized axial and radial turbines having very different expansion ratios and sizes. The calculated efficiencies were correlated against the volumetric flow ratio (VR) and the so-called size parameter (SP). In particular, VR allows not only to take into account the compressibility effects but also to reduce the efficiency dependency on the fluid nature. So, the resulting maps can be used to a first approximation for different fluids. Instead, SP is a dimensional parameter proportional to the rotor diameter, which accounts for the influence of the turbine size on the performance. However, these studies assume that the working fluid is ideal despite real gas effects might be significant when using organic fluids [26], and the Reynolds number is constant.

This work addresses the need of new specific tools to properly estimate the turbine efficiency. The aim is to build general efficiency maps to predict the performance of turbines having very different design specifications in ORC systems. To this end, the work is organized as follows:

- A rigorous study on turbomachinery similarity principles is performed to confirm that the size parameter (SP) and volumetric flow ratio (VR) are well suited to predict the efficiency of ORC turbines.

- A SP-VR efficiency map is built from real data of radial turbines operating with air to verify the efficiency trends when these predictors are used and to experimentally demonstrate the impact of compressibility and size effects in real applications.

- Mean-line models are implemented in Matlab® codes to generate a series of radial and axial turbine preliminary designs encompassing a wide set of design specifications, design parameters and working fluids. Recent loss correlations are used to estimate the irreversibilities

throughout the turbine and accurate databases (NIST Refprop) are considered to evaluate the real flow properties.

- The calculated efficiencies are collected into two groups of maps. In the first group the efficiencies are correlated, for fixed design specifications, to the traditional turbine design parameters to provide indications about the optimum values of these parameters. According to the author's knowledge no similar maps specifically developed for organic fluids exist in the literature. The second group of maps correlates the efficiencies corresponding to the optimum design parameters to the size parameter and volumetric flow ratio for several combinations of the design specifications. Performance maps with the same meaning of those suggested by Macchi and Perdichizzi in [24] are therefore obtained: a single fluid (R245fa) is considered for the radial turbine, whereas a variety of working fluids (hydrocarbons, hydrofluorocarbons and hydrofluoroolefines) are considered for the axial case.

- A general efficiency map as a function of size parameter, volumetric flow ratio and critical temperature is finally built by regression of all the efficiency data obtained for the axial turbines.

Chapter 1

Design guidelines for radial inflow turbines

This Chapter presents fundamentals and guidelines commonly adopted in the traditional design practice of radial inflow gas turbines. The discussion mainly follows the findings of Whitfield and Baines [27] as presented by Korpela [28] and Dixon [29]. Ideal gas is assumed.

Section 1.1 briefly presents the architecture of the machine and deals with basic concepts of energy transfer relating them to the achievement of high specific works.

Section 1.2 focuses on the rotor inlet design which is based on the selection of the rotor inlet flow angle in order to minimize the Mach number at rotor inlet for assigned power ratio and relative flow angle. Accordingly, typical values of the absolute flow angles for traditional applications fall in the range 65-70°.

Section 1.3 deals with the design of the rotor exit which starts from the choice of the outlet Mach number in order to minimize the Mach number at the rotor shroud. Subsequently, useful relationships to calculate the rotor outlet-to-rotor inlet radius and the blade height-to-rotor inlet radius as a function of design specifications are derived. Finally, optimum incidence

considerations and the resulting criterion for the choice of the relative inlet flow angle close the Chapter.

1.1 General concepts of energy transfer

The radial inflow turbines are traditionally employed in automotive turbocharges, but they are also used in natural gas processing, air liquefaction and geothermal power plants. Radial turbines cover a wide range of power, mass flow rate and rotational speed and achieve slightly lower efficiencies compared to axial flow turbines. However, the significant advantages of radial turbines compared to axial ones are the higher specific work per stage, the ease of manufacture and their superior ruggedness.

Figure 1.1 shows a side view of a radial inflow turbine and the corresponding nomenclature of its components. Hot gases enter through a volute and are accelerated throughout a vaned stator before they enter in the rotor. Blades at rotor inlet are typically radial to withstand the loads due to the centrifugal force field and pulsating gas flows at high temperature better than curved blades. Rotor vanes extend radially inward and turn the flow into the axial direction; their exit part is curved in order to remove the discharge swirl velocity component. The kinetic energy left in the exit stream may be recovered in an exit diffuser.

Velocity triangles at the rotor inlet and outlet are sketched in Fig. 1.2. In this Chapter, velocity components are accounted as positive if they have the same direction of the peripheral velocity; flow angles are accounted with their own sign from the meridional direction.

Inspection of the fundamental equation of the specific work $\mathcal{W}$

$$\mathcal{W} = \frac{C_2^2 - C_3^2}{2} + \frac{U_2^2 - U_3^3}{2} + \frac{W_3^2 - W_2^2}{2} \tag{1.1}$$

indicates that the maximization of the specific work $\mathcal{W}$ is obtained if the inlet absolute velocity C_2 and relative velocity W_2 reach high and

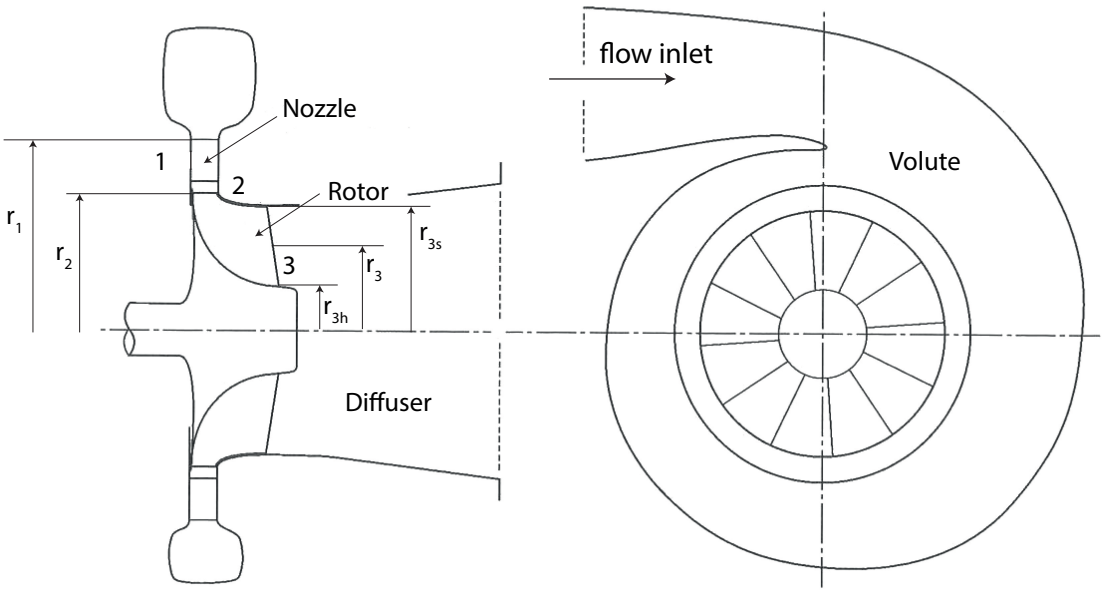

Figure 1.1: Side (left) and circumferential (right) view of a radial inflow turbine (adapted from [19]).

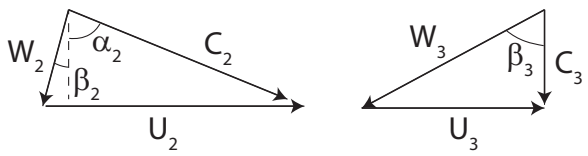

Figure 1.2: Velocity triangles for a radial inflow turbine.

low values, respectively. This is obtained when the flow angle α_2 is large and the relative velocity is directed radially inward. Similarly, axial discharge and large β_3 are to be realized to minimize C_3 and maximize W_3, respectively. The contribution to the extracted work deriving from the rotodynamic effect (i.e., variation of the peripheral velocity) increases as the radius ratio r_2/r_3 increases.

A parameter of interest in radial turbine design practice is the power ratio ($s_{\mathcal{W}}$) which is the ratio between the specific work ($s_{\mathcal{W}}$) and the total enthalpy at the machine inlet

$$s_{\mathcal{W}} = \frac{\mathcal{W}}{h_{01}} \tag{1.2}$$

Starting from the total-to-static efficiency (η_{ts}) definition and considering Eq. (1.2), the pressure ratio p_{01}/p_3 can be written as

$$\frac{p_{01}}{p_3} = \left(1 - \frac{s_{\mathcal{W}}}{\eta_{ts}}\right)^{-\frac{\gamma}{\gamma-1}} \tag{1.3}$$

Accordingly, power ratios in the range $0.15 < s_{\mathcal{W}} < 0.25$ correspond to $2 < p_{01}/p_3 < 3$ for typical values of efficiency (80-90%) and when traditional fluids are considered.

Moreover, since the specific work is

$$\mathcal{W} = c_p T_{01} s_{\mathcal{W}} \tag{1.4}$$

the expansion of hot combustion gases ($T_{01} = 1000$ K) with a typical power ratio $s_{\mathcal{W}} = 0.2$ corresponds to a specific work of approximately 300 kJ/kg.

Optimum intervals for the specific speed (n_s) and velocity ratio ($\nu_s = U_2/(2\Delta h_{0s})^{0.5}$) are

$$\boxed{n_s = 0.3 - 0.7 \qquad \nu_s = 0.55 - 0.77} \tag{1.5}$$

Figure 1.3 shows the expansion process across a radial turbine in the enthalpy-entropy diagram and the nomenclature of the thermodynamic states adopted in this Chapter.

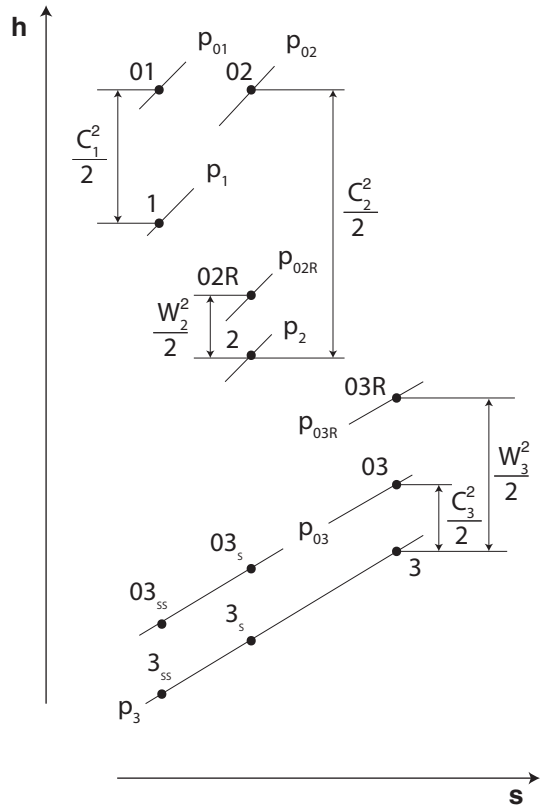

Figure 1.3: Thermodynamic expansion process across a radial inflow turbine in the enthalpy-entropy diagram.

1.2 Design of the rotor inlet

This Section deals with the design of the rotor inlet following Whitfield and Baines [27] design guidelines. The absolute flow angle (α_2) is related to the power ratio ($s_{\mathcal{W}}$), relative flow angle (β_2) and Mach number (M_2) in order to calculate the α_2 value which leads to the minimum M_2. Values of α_2 in the range $\alpha_2 = 65 - 70°$ are found. Then, the blade stagnation Mach number (M_{0u}) is related to the design specifications and to M_2 and it is shown that for high efficiency turbines $0.7 < M_{0u} < 0.75$. Finally, the

inlet relative Mach number M_{2R} is expressed as a function of the previously defined parameters.

1.2.1 Minimum inlet Mach number

A common design guideline for the rotor inlet is to choose the absolute and relative flow angles in order to achieve the smallest absolute Mach number [27]. The tangential velocity can be written in the form

$$C_{u2} = U_2 + W_{u2} = U_2 + C_{u2}\frac{\tan\beta_2}{\tan\alpha_2} \tag{1.6}$$

Considering no exit swirl (i.e., $C_{u3} = 0$) and multiplying by C_{u2}/C_2^2, Eq. (1.6) is reduced to

$$\sin^2\alpha_2\left(1 - \frac{\tan\beta_2}{\tan\alpha_2}\right) = u \tag{1.7}$$

in which the quantity $u = U_2 C_{u2}/C_2^2$ is directly related to the design specifications. In fact, it can be easily demonstrated that

$$u = \frac{U_2 C_{u2}}{C_2^2} = \frac{s_{\mathcal{W}}/(\gamma-1)}{M_{02}^2} \tag{1.8}$$

where $s_{\mathcal{W}}$ is the power ratio (see Eq. (1.2)) and M_{02} is the stagnation Mach number at rotor inlet

$$M_{02} = \frac{C_2}{a_{02}} = \frac{M_2}{\left(1 + \frac{\gamma-1}{2}\right)^{0.5}} \tag{1.9}$$

Further, dividing Eq. (1.7) by $\cos^2\alpha_2$ and remembering the identity $1/\cos^2\alpha_2 = \tan^2\alpha_2 + 1$, gives

$$\boxed{\left(\frac{M_2^2}{1+\frac{\gamma-1}{2}M_2^2} - \frac{s_{\mathcal{W}}}{\gamma-1}\right)\tan^2\alpha_2 - \frac{M_2^2}{1+\frac{\gamma-1}{2}M_2^2}\tan\beta_2\tan\alpha_2 - \frac{s_{\mathcal{W}}}{\gamma-1} = 0} \tag{1.10}$$

For given values of $s_{\mathcal{W}}$, M_2 and β_2 the quadratic Equation (1.10) can be solved for $\tan\alpha_2$. Figure 1.4 shows the solution of Eq. (1.10) for selected values of $s_{\mathcal{W}}$ and β_2 with $\gamma = 1.4$.

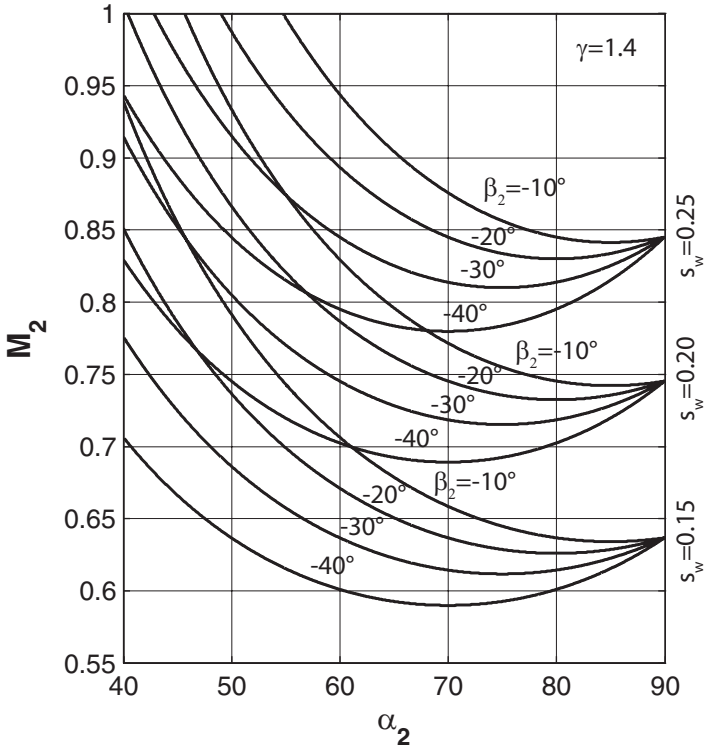

Figure 1.4: Rotor inlet Mach number (M_2) as a function of the absolute flow angle (α_2) for selected values of the relative flow angle (β_2) and power coefficient ($s_{\mathcal{W}}$).

For a given power ratio ($s_{\mathcal{W}}$) and relative flow angle (β_2), the minimum of each curve is sought next.

By equating to zero the first derivative of M_{02}^2 with respect to $\tan\alpha_2$ resulting from Eq. (1.10) it follows that the the absolute flow angle $\alpha_{2|M_2=M_{2min}}$ leading to the minimum inlet Mach Mach number is

$$\tan\alpha_{2|M_2=M_{2min}} = \frac{-1-\cos^{-1}\beta_2}{\tan\beta_2} \tag{1.11}$$

Being the right-hand-side of Eq. (1.11) equal to $\tan(\pi/2+\beta_2/2)$ it follows

$$\boxed{\alpha_{2|M_2=M_{2min}} = \frac{\pi}{2}+\frac{\beta_2}{2}} \tag{1.12}$$

The value of the corresponding minimum inlet Mach number (M_{2min}) for assigned $s_{\mathcal{W}}$, β_2 and γ is found by including the optimum α_2 value (Eq. (1.12) into Eq. (1.10). It results

$$M_{2min} = \left(\left(\frac{2s_{\mathcal{W}}}{\gamma-1}\right)\frac{\cos\beta_2}{1+(1-s_{\mathcal{W}})\cos\beta_2}\right)^{0.5} \tag{1.13}$$

Figure 1.5 shows that the optimum α_2 values (i.e., $\alpha_{2|M_2=M_{2min}}$) fall in the range

$$\boxed{\alpha_2 = 60-80^\circ} \tag{1.14}$$

Figure 1.5 plots Eq. (1.13) and shows the dependency of M_{2min} on the power ratio $s_{\mathcal{W}}$ for some rotor inlet flow angles β_2. Note that M_{2min} slightly depends on β_2.

1.2.2 Blade stagnation and relative Mach number

The definition of power ratio may be recast as

$$\frac{U_2}{a_{01}}\frac{C_{u2}}{a_{01}} = \frac{s_{\mathcal{W}}}{\gamma-1} \tag{1.15}$$

so that

$$M_{0u} = \frac{U_2}{a_{01}} = \frac{s_{\mathcal{W}}}{\gamma-1}\frac{a_{01}}{a_2}\frac{a_2}{C_2\sin\alpha_2} \tag{1.16}$$

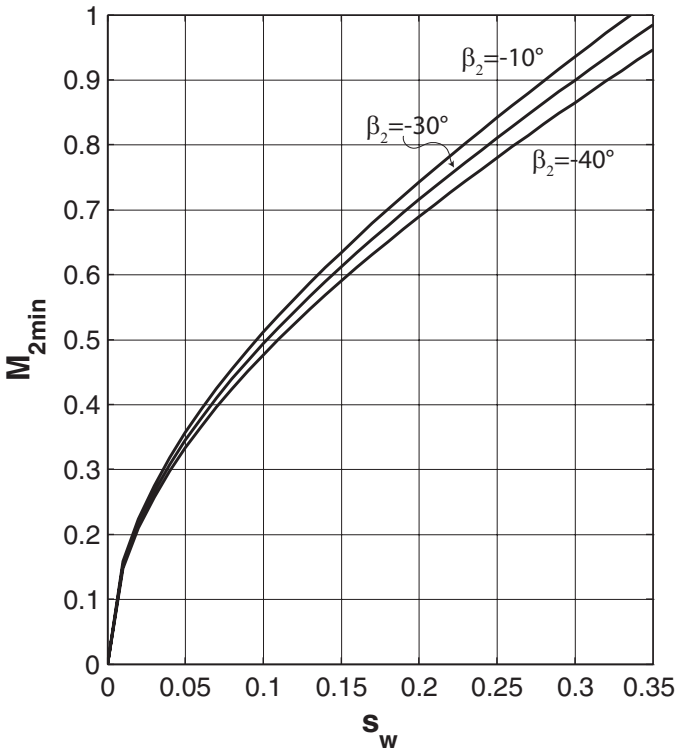

Figure 1.5: Minimum inlet Mach number (M_{2min}) as a function of the power ratio ($s_{\mathcal{W}}$) for selected values of the relative flow angle β_2.

Since the total enthalpy across the nozzle is constant, Eq. (1.16) is further rearranged as

$$\boxed{M_{0u} = \frac{s_{\mathcal{W}}}{\gamma - 1} \frac{\left(1 + \frac{\gamma-1}{2} M_2^2\right)^{0.5}}{M_2 \sin \alpha_2}} \tag{1.17}$$

For assigned $s_{\mathcal{W}}/(\gamma - 1)$, relative flow angle β_2 and Mach number M_2, Eq. (1.10) can be solved for α_2 and, in turn, the blade Mach number M_{0u} can be calculated with Eq. (1.17). Figure 1.6 shows the blade stagnation Mach numbers as a function of M_2 and for various power ratios at fixed β_2. The importance of Fig. 1.6 is made clear if it is compared to the experimental performance data collected in Fig. 1.7, which shows the total-to-static efficiencies of several radial turbines measured by [30]. Since the spouting velocity ($C_0 = (2(h_{01} - h_{3ss}))^{0.5}$) can be written as

$$C_0 = \left(2 c_p T_{01} \frac{s_{\mathcal{W}}}{\eta_{ts}}\right)^{0.5} \tag{1.18}$$

the stagnation blade Mach number can be related to the ratio U_2/c_0 by

$$M_{0u} = \frac{U_2}{C_0} \left(\frac{2 s_{\mathcal{W}}}{(\gamma - 1)\eta_{ts}}\right)^{0.5} \tag{1.19}$$

Thus, turbines with reasonably low power ratios (e.g., $s_{\mathcal{W}} = 0.15$) which achieve the highest efficiency level ($\eta_{ts} = 0.9$) at $U_2/C_0 = 0.7$ (see Fig. 4.45) are characterized by $M_{0u} = 0.7$; whereas, if ($\eta_{ts} = 0.8$) is considered, then $M_{0u} = 0.75$. In brief, turbines with low power ratio and blade Mach number in the range

$$\boxed{M_{0u} = 0.7 - 0.75} \tag{1.20}$$

are expected to operate in the region of the highest efficiency.

Similarly to M_{0u}, the relative Mach number at rotor inlet $M_{2R} = W_2/a_2$ can be calculated as a function of $s_{\mathcal{W}}$, γ, M_2 and β_2. In fact, trivial trigonometric considerations lead to

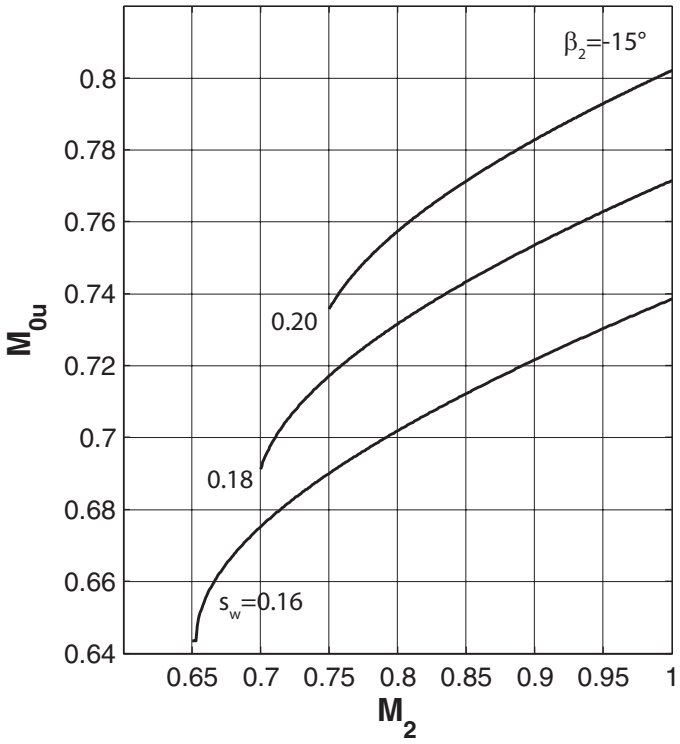

Figure 1.6: Blade stagnation Mach number (M_{0u}) as a function of the inlet Mach number M_2 for selected power ratios and relative flow angle.

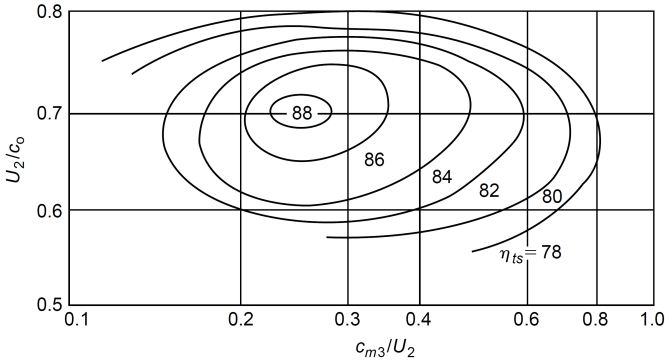

Figure 1.7: Total-to-static efficiency chart from the data of Rodgers and Gleiser. Figure reproduced from [29]

.

$$M_{2R} = -M_u \sin\beta_2 + (M_2^2 - M_u^2 \cos^2\beta_2)^{0.5} \tag{1.21}$$

where the term $M_u = U_2/a_2$ can be calculated by

$$M_u = \frac{s_{\mathcal{W}}}{\gamma - 1} \frac{1 + \frac{\gamma-1}{2} M_2^2}{M_2 \sin\alpha_2} \tag{1.22}$$

Figure 1.8 plots Eq. (1.21) for fixed β_2 and provides an immediate indication of the allowed degree of acceleration through the rotor channel to avoid choking occurrence.

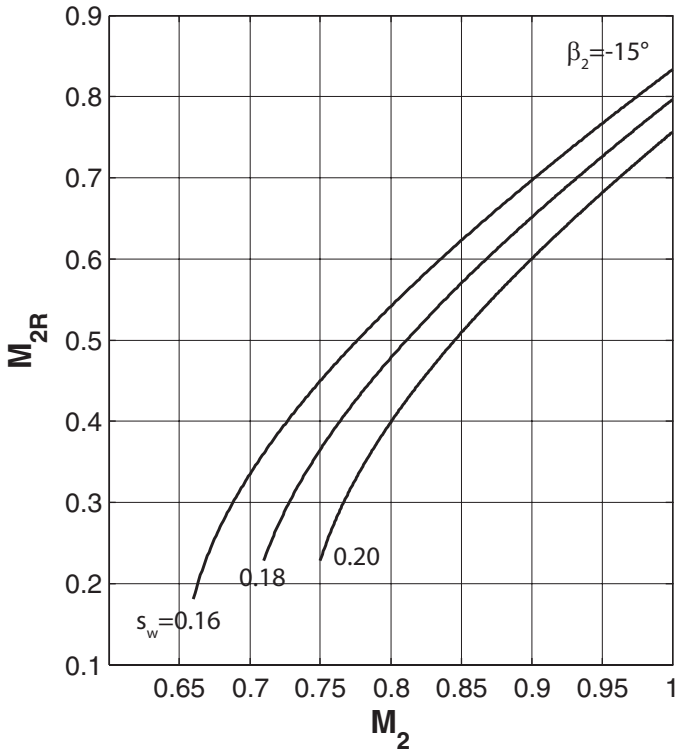

Figure 1.8: Relative inlet Mach number (M_{2R}) as a function of the inlet Mach number M_2 for selected power ratios and relative flow angle.

1.3 Design of the rotor outlet

This Section focuses on the design of the rotor outlet. A relationship between the relative Mach number at the rotor shroud (M_{3Rs}) and the exit

Mach number (M_3) is derived and the choice of M_3 in order to minimize M_{3Rs} is discussed. Then, the radius ratio r_{3s}/r_2 and the blade height-to-radius ratio b_2/r_2 are calculated as a function of the design specifications. Optimum incidence considerations and the resulting criterion for the choice of the relative inlet flow angle close the Section.

1.3.1 Minimum exit Mach number

In the rotor outlet section, the shroud is the position where the highest relative flow velocities and, in turn, loss phenomena occur. Accordingly, a possible design criterion for the rotor outlet is to choose the absolute Mach number in order to minimize the relative Mach number at the shroud. A relationship between these two variables is derived in the following.

If the rotor discharge is axial, the mass balance for the rotor outlet section is

$$\dot{m} = \rho_3 c_3 A_3 = \rho_3 c_3 \pi r_{3s}(1-k^2) \tag{1.23}$$

where $k = r_{3h}/r_{3s}$ is the ratio between the hub and shroud radii at rotor outlet. The use of the perfect gas law and sound speed at state 01 allow to recast Eq. (1.23) in the form

$$\Phi = \frac{p_3}{p_{01}}\left(\frac{T_{01}}{T_3}\right)^{0.5} M_3 \frac{u_{3s}^2}{U_2^2}(1-k^2) \tag{1.24}$$

being for the sake of brevity $\Phi = \dot{m}/(\rho_{01} a_{01} \pi_2^2)$.

Further, starting from $U_{3s}^2 = W_{3s}^2 - C_3^2$, the ratio U_{3s}/U_2 can be expressed as

$$\frac{U_{3s}^2}{U_2^2} = \frac{M_{3Rs}^2 - M_3^3}{M_{0u}^2}\frac{T_3}{T_{01}} \tag{1.25}$$

Accordingly, the mass balance (Eq. (1.24)) when solved for M_{3Rs} gives

$$M_{3Rs}^2 = M_3^2 + \frac{\Phi M_{0u}^2}{1-k^2}\frac{1}{M_3}\left(1+\frac{\gamma-1}{2}\right)^{0.5}\left(\frac{p_{01}}{p_3}\right)\left(\frac{T_{01}}{T_{03}}\right)^{0.5} \tag{1.26}$$

Finally, being

$$\frac{p_{01}}{p_3} = \left(1-\frac{s_{\mathcal{W}}}{\eta_{ts}}\right)^{-\gamma/(\gamma-1)} \qquad \frac{T_{01}}{T_{03}} = (1-s_{\mathcal{W}})^{-1} \tag{1.27}$$

and defining B as

$$B = \frac{\Phi M_{0u}^2}{1-k^2}\frac{p_{01}}{p_3}\left(\frac{T_{01}}{T_{03}}\right)^{0.5} \tag{1.28}$$

the relative Mach number at the rotor shroud becomes

$$\boxed{M_{3Rs}^2 = M_3^2 + B\left(\frac{1}{M_3^2} + \frac{\gamma-1}{2}\right)^{0.5}} \tag{1.29}$$

This form is particularly useful because it establishes a straightforward relationship between M_3 and M_{3Rs} in which only design specifications (i.e., $s_{\mathcal{W}}$, η_{ts}) or variables depending on them (i.e., M_{0u}, see Eq. (1.17)) appear.

Figure 1.9 plots Eq. (1.29) for different values of $\phi_f = \Phi M_{0u}^2/(1-k^2)$ and constant values of power ratio and efficiency. Within these assumptions, it indicates that M_3 should fall in the range 0.2-0.4.

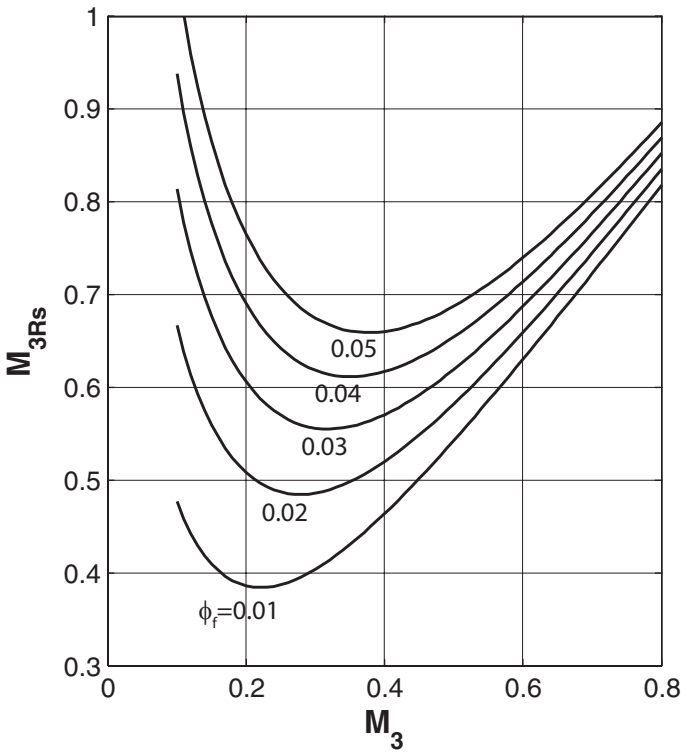

Figure 1.9: Relative Mach number (M_{3Rs}) as a function of the parameter B. It is assumed $p_{01}/p_3 = 2$ and $\eta_{ts} = 0.85$.

In addition, once M_3 and M_{3Rs} are defined, the relative flow angle at

the rotor shroud β_{3s} can be calculated by

$$\cos\beta_{3s} = \frac{M_3}{M_{3Rs}} \tag{1.30}$$

1.3.2 Shroud-to-inlet radius ratio and blade height-to-inlet radius ratio

The radius ratio at rotor outlet (r_3/r_2) can be related to the relative velocity ratio across the rotor (W_3/W_2), absolute flow angle at rotor inlet (α_2) and relative flow angle at rotor outlet (β_3). In the following analysis it is assumed that the angle β_3 changes with radius such that the exit velocity C_3 is constant along the blade span.

From the velocity triangle it is

$$\sin|\beta_3| = \frac{U_3}{W_3} \tag{1.31}$$

which is recast, being $U_3 = U_2 r_3/r_2$, in the form

$$\frac{r_3}{r_2} = \frac{W_3}{W_2}\frac{W_2}{U_2}\sin|\beta_3| \tag{1.32}$$

Trigonometric considerations on the inlet velocity triangle allow to recast Eq. (1.32) as

$$\frac{r_3}{r_2} = \frac{W_3}{W_2}\frac{\cos\alpha_2}{\sin(\alpha_2-\beta_2)}\sin|\beta_3| \tag{1.33}$$

In case the α_2 which minimizes the Mach number M_2 is selected (i.e., $\alpha_2 = \pi/2 + \beta_2/2$, see Eq. (1.12)) then the radius ratio reduces to

$$\boxed{\frac{r_3}{r_2} = \frac{W_3}{W_2}\frac{\sin|\beta_3|}{\tan\alpha_2}} \tag{1.34}$$

At the shroud radius it is

$$\boxed{\frac{r_{3s}}{r_2} = \frac{W_{3s}}{W_2}\frac{\sin|\beta_{3s}|}{\tan\alpha_2}} \tag{1.35}$$

Equations (1.34) and (1.35) are suitable to calculate the radius ratio because α_2 and β_3 (or β_{3s}) can be evaluated by Eqs. (1.12) and (1.30),

respectively. Clearly, an assumption on the velocity ratio has to be made. Recommended values of W_3/W_2 [31] and W_{3s}/W_2 [27] are

$$\boxed{\frac{W_3}{W_2} = 2 \qquad \frac{W_{3s}}{W_2} = 2.5} \tag{1.36}$$

The blade height-to-radius ratio (b_2/r_2) is calculated starting from the area ratio A_2/A_3 in the form

$$\frac{b_2}{r_2} = \frac{A_2}{A_3}\frac{1-k^2}{2}\left(\frac{r_{3s}}{r_2}\right)^2 \tag{1.37}$$

The conservation of the mass flow between stations 2 and 3 allows to write A_2/A_3 in terms of the so-called flow functions

$$\frac{A_3}{A_2} = \frac{F_2\cos\alpha_2}{F_3}\left(\frac{T_{03}}{T_{02}}\right)^2\frac{p_{02}}{p_{03}} = \frac{F_2\cos\alpha_2}{F_3}\left(\frac{T_{03}}{T_{02}}\right)^2\frac{p_{02}}{p_{01}}\frac{p_{01}}{p_3}\frac{p_3}{p_{03}} \tag{1.38}$$

where F depends only on M and γ.

The second law $Tds = dh - vdp$ can be used to evaluate the entropy change between states $2s$ and 2. By integrating the second law along the isobaric line p_2 and the constant stagnation temperature line $T_{01} = T_{02}$, the equivalence of the resulting entropy change gives

$$\frac{p_{02}}{p_{01}} = \frac{T_{2s}}{T_2}^{\frac{\gamma}{\gamma-1}} \tag{1.39}$$

Being $\zeta_N = (h_2 - h_{2s})/(0.5C_2^2)$ the nozzle loss coefficient, the pressure ratio p_{02}/p_{01} is written as

$$\frac{p_{02}}{p_{01}} = \left(1 - \zeta_N\frac{\gamma-1}{2}M_2^2\right)^{\frac{\gamma}{\gamma-1}} \tag{1.40}$$

Finally, by including Eqs. (1.40) and (1.27) in Eq. (1.38) a useful form of the area ratio depending on design specifications is obtained

$$\frac{A_3}{A_2} = \frac{F_2\sin\alpha_2}{F_3}\left(1 - \frac{s_{\mathcal{W}}}{\eta_{ts}}\right)^{-\frac{\gamma}{\gamma-1}}(1-s_{\mathcal{W}})^{0.5}\left(\frac{1-\zeta_N\frac{\gamma-1}{2}M_2^2}{1+\frac{\gamma-1}{2}M_3^2}\right)^{\frac{\gamma}{\gamma-1}} \tag{1.41}$$

1.3.3 Optimum incidence and relative flow angle

The dominant effect in the rotor inlet region is the tangential turning of the flow and the resulting negative incidence at design operation. In standard applications the most uniform flow distributions were found to be at a relative inlet angle (accounted from radial direction) in the range -20 to $-40°$. Lower angles result in a flow separation at the leading edge of the suction surface and a strong recirculation occurs in the full extent of this surface. On the other hand, higher angles lead to flow separation and recirculation at the pressure surface leading edge. The cause of the flow movement across the passage from the suction to the pressure surface is that as the flow moves inward the blade speed U decreases more rapidly than the tangential velocity C_t. Accordingly, the direction of the relative velocity moves towards the direction of the peripheral velocity, that is towards the pressure surface.

A simple way to take into account these phenomena in the preliminary design phase is to use the so-called slip factor σ. It relates the optimum incidence velocity triangle to the velocity triangle at zero incidence condition (superscript '), as shown in Fig. 1.10 (U and C_m are the same).

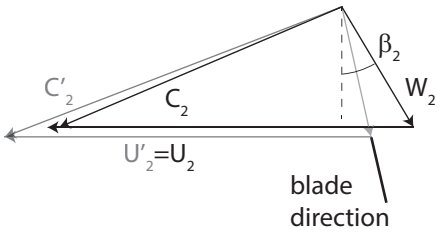

Figure 1.10: Velocity triangles for the definition of the slip factor.

The slip factor is defined as

$$\sigma = 1 - \frac{C'_{t2} - C_{t2}}{U_2} \tag{1.42}$$

and it depends, in its simplest formulations, on the rotor blade number Z (see, e.g., Stanitz: $\sigma = 1 - 0.63\pi/Z$). If the blades are radial, the

previous Equation becomes

$$\sigma = \frac{C_{t2}}{U_2} \tag{1.43}$$

and trivial trigonometric considerations on the velocity triangle allows to write

$$\frac{C_{t2}}{U_2} = \frac{\tan \alpha_2}{\tan \alpha_2 - \tan \beta_2} \tag{1.44}$$

For minimum inlet Mach number condition (i.e., $\alpha_2 = \pi/2 + \beta_2/2$) Eq. (1.44) reduces to

$$\frac{C_{t2}}{U_2} = \cos \beta_2 \tag{1.45}$$

Thus, from Eqs. (1.43) and (1.45) and using Stanitz slip factor it is possible to obtain a criterion for the choice of the relative flow angle

$$\boxed{\cos \beta_2 = 1 - \frac{0.63\pi}{Z}} \tag{1.46}$$

Chapter 2

Design guidelines for axial flow turbines

This Chapter focuses on the fundamentals of traditional steam axial flow turbines and it is aimed at providing a general presentation of the different turbine configurations along with the design guidelines commonly followed in the steam turbine design practice ([32], [28], [33]).

Section 2.1 outlines the fundamental thermodynamic concepts in energy conversion across a turbine stage and shows how the purpose of obtaining high specific work reflects on the velocity triangles shapes and row configuration. The non-dimensional parameters commonly used in the design and performance analysis of turbine stages (i.e., flow and loading coefficient and reaction) are recalled in Section 2.2 and their influence on both stage geometry and performance is examined. In particular, reaction is particularly useful to classify two kinds of turbine stage: action (Section 2.3, 2.4 and 2.5 referring to pure impulse, velocity compounded and pressure compounded impulse stage, respectively) and reaction (Section 2.6) turbine stage. In the former the whole available enthalpy drop is used to accelerate the fluid in the nozzle and no pressure drop occurs in the rotor row. Conversely, in the latter part of the available enthalpy drop is used to

accelerate the fluid also in the rotor. A common scheme is used to illustrate the main features of action and reaction stages: (i) general architecture, velocity triangles and expansion in the h-s chart, (ii) efficiency calculation as a function of the design parameters and (iii) design guidelines.

Subsequently, Section 2.7 shows how stages are assembled in the action-reaction multistage turbines, which represents the most common turbine configuration in steam power plants as it allows to overcome the limitations about the minimum volumetric flow rate at the inlet and to efficiently manage the off-design operation.

Section 2.8 deals with some criteria to split the available enthalpy drop among the turbine stages and, in turn, determine the stages number along with the mean diameter and the blade height for each stage. The discussed criteria are: (i) constant blade span to mean diameter ratio and (ii) constant hub diameter. The analytical derivation of well-known design tools in preliminary turbine design practice (i.e., the loading coefficient-flow coefficient chart and the specific speed-specific diameter diagram) closes the Chapter.

2.1 General concepts of energy transfer

A turbine stage consists of a nozzle followed by a rotor, as depicted in Fig. 2.1. The inlet to the stage is station 1, the outlet from the stator or the inlet to the rotor is station 2 and the outlet from the rotor is station 3. Flow angles are referred to the axial direction and are positive when they are in the direction of the blade motion (e.g. in Fig. 2.1 the absolute flow angle α_1 is negative as the corresponding velocity tangential projection C_{t1}). With this sign convention the specific work delivered by an axial turbine stage can be expressed in terms of velocities by the Euler equation for turbomachinery

$$\boxed{\mathcal{W} = U(C_{t2} - C_{t3}) = U(W_{t2} - W_{t3})} \tag{2.1}$$

where U, C and W are the peripheral, absolute and relative velocities, respectively. The subscripts t and m denote the tangential and meridional component of the corresponding vector. If $C_m = W_m$ is constant across the stage, Eq. (2.1) can be rearranged as

$$\mathcal{W} = UC_m(\tan\alpha_2 - \tan\alpha_3) = UC_m(\tan\beta_2 - \tan\beta_3) \tag{2.2}$$

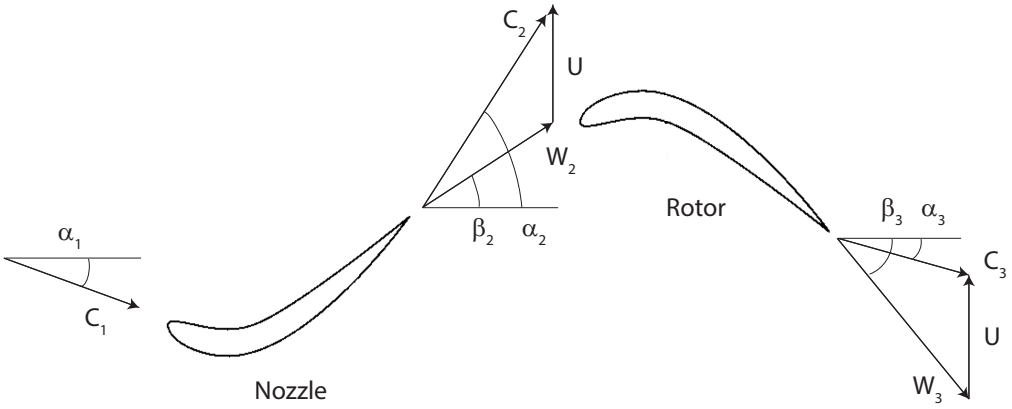

Figure 2.1: Velocity triangles for a turbine stage.

In the following axial turbines stage are analyzed assuming that the flow conditions at a mean radius, i.e., the meanline, represent the flow at all radii. This simplification provide a reliable approximation of the actual flow if (i) the blade height to rotor tip diameter is low (e.g., $r_h/r_t > 0.4$, where r_h and r_t are the hub and tip rotor radii) and (ii) the flow is invariant along the circumferential direction.

The aim of a turbine stage is, for given U, to obtain an high specific work $\mathcal{W}$ with a high efficiency. High specific work requires high deflection ϵ in the rotor ($\epsilon_R = \beta_2 - \beta_3$): a typical value is 70° and rarely exceeds 90° for heavily loaded blades. High rotor deflections require in turn that the stator deflects the absolute stream in the opposite direction (compare W_2 and W_3 directions in Fig. 2.1). Hence, the rotor deflects the relative stream in the

opposite direction of U, whereas the stator deflects the absolute stream in the direction of U. As the stator turns the absolute velocity toward the direction of rotation, the stator outlet velocity C_2 is higher than C_1, leading to a drop in the static enthalpy

$$h_1 - h_2 = \frac{1}{2}(C_2^2 - C_1^2) \tag{2.3}$$

Eq. (2.3) rearranged in the form

$$\boxed{(u_1 - u_2) + (p_1 v_1 - p_2 v_2) = \frac{1}{2}(C_2^2 - C_1^2)} \tag{2.4}$$

highlights that the increase in kinetic energy ($1/2(C_2^2 - C_1^2)$) across the stator comes from a decrease of the internal energy ($u_1 - u_2$) and from the difference in the flow work ($p_1 v_1 - p_2 v_2$). In particular, $p_1 v_1$ is the work done by the fluid just upstream the control volume on the adjacent fluid to push it inside the control volume; $p_2 v_2$ is the work done by the fluid inside the control volume on the adjacent fluid to push it outside the control volume. Necessarily, the variation of internal energy and the difference in the flow work have the same sign, as can be easily demonstrated by assuming ideal gas behavior

$$du = c_V dT \tag{2.5}$$

$$d(pv) = RdT \tag{2.6}$$

where c_V is the specific heat at constant volume and R is the ideal gas constant. The ratio of these contributions to the increase of the kinetic energy across the stator is ($c_v = R/(\gamma - 1)$)

$$\boxed{\frac{du}{d(pv)} = \frac{1}{\gamma - 1}} \tag{2.7}$$

where $\gamma = c_P/c_V$. The variation of the ratio expressed by Eq. (2.7) is equal to 3 for $\gamma = 1.33$ (steam) and progressively increases as γ decreases

reaching 10 for $\gamma = 1.1$ (typical for high molecular mass organic fluids). Thus, for organic fluids the increase in kinetic energy across the stator mainly derives from the drop in internal energy.

In the rotor the fluid is directed back toward the axis and reduces its absolute kinetic energy. The specific work is

$$\mathcal{W} = h_{02} - h_{03} = h_2 - h_3 + \frac{1}{2}(C_2^2 - C_3^2) \tag{2.8}$$

Again, by expanding the enthalpy terms

$$\boxed{\mathcal{W} = (u_2 - u_3) + (p_2 v_2 - p_3 v_3) + \frac{1}{2}(C_2^2 - C_3^2)} \tag{2.9}$$

and the ratio between the contribution to the delivered work from the variation of internal energy $(u_2 - u_3)$ and flow work $(p_2 v_2 - p_3 v_3)$ is still expressed by Eq. (2.7).

2.2 Turbine stage design parameters

The preliminary design of a turbine stage usually starts with the choice of three non-dimensional parameters which allow the designer to define the shape (i.e., flow angles) of the velocity triangles. These non-dimensional parameters are the *flow coefficient* (ϕ), *loading coefficient* (Ψ) and *reaction* (R or χ).

The flow coefficient ϕ is defined as the ratio between the meridional flow velocity (C_m) to the blade speed (U)

$$\boxed{\phi = \frac{C_m}{U}} \tag{2.10}$$

A stage with low ϕ leads to flow angles close to tangential direction and vice versa. The mass flow rate is proportional to ϕ for fixed geometry and rotational speed.

The stage loading coefficient Ψ is the ratio of the stagnation enthalpy change through the stage to the square of the blade speed. For an axial stage recalling the Euler equation

$$\boxed{\Psi = \frac{h_{01} - h_{03}}{U^2} = \frac{C_{t2} - C_{t3}}{U}} \tag{2.11}$$

A stage with high Ψ means large flow turning and, in turn, highly skewed velocity triangles. Generally, designs with high stage loading are preferable, because they limit the stage number to produce a required work output. On the other hand, higher blade loading means higher losses across the expansion due to the increased flow turning (see Section 2.9).

Loading and flow coefficient allows to obtain a Euler turbine equation in a dimensionless form starting from Eq. (2.2)

$$\Psi = \phi(\tan\alpha_2 - \tan\alpha_3) \tag{2.12}$$

or, equivalently

$$\Psi = \phi(\tan\beta_2 - \tan\beta_3) \tag{2.13}$$

The stage reaction is defined in at least two different ways: the kinematic (R) and the thermodynamic (χ) reaction

$$\boxed{R = \frac{W_3^2 - W_2^2}{(C_2^2 - C_3^2) + (W_3^2 - W_2^2)} = \frac{h_2 - h_3}{h_1 - h_3} = 1 - \frac{h_1 - h_2}{h_1 - h_3}} \tag{2.14}$$

$$\boxed{\chi = \frac{h_2 - h_{3s}}{(h_1 - h_{1s}) - (h_2 - h_{3s})}} \tag{2.15}$$

In general terms, the same turbine stage has different values of the kinematic and thermodynamic reaction. As a design parameter the reaction is an indicator of the velocity triangle asymmetry, thus it provide a fairly direct indication about the blade geometry and it is therefore the most suited parameter to classify different turbine styles.

2.3 Impulse stage

In an impulse stage no pressure drop occurs across the rotor because the whole available enthalpy drop is converted in kinetic energy at nozzle outlet. Both the specific work and the total-to-static efficiency may be related to different design parameters: the characteristic velocity ratios $X = U/(C_2 \sin \alpha_2)$ and $\nu = U/c_0$ or the loading coefficient Ψ. The values of these parameters leading to the maximum turbine efficiency provide indications for an optimum stage design. They are $X \approx 0.5$, $\nu \approx 0.47$ and $\Psi \approx 2$.

2.3.1 Construction features

An impulse stage consists of a set of nozzles and a row of blades. The entire pressure drop takes place in the nozzle so that the pressure is maintained constant across the rotor row. Consequently, assuming an irreversible process across the rotor, the cinematic reaction of an impulse stage is slightly negative

$$h_3 > h_2 \rightarrow R = \frac{h_2 - h_3}{h_1 - h_3} < 0 \tag{2.16}$$

Instead, the thermodynamic reaction χ is null because there is no isentropic enthalpy drop across the rotor (i.e., state 2 and 3s coincide as shown in Fig. 2.3).

As in the nozzle the whole available enthalpy drop is used to accelerate the fluid, it is not unusual the adoption of converging-diverging nozzles to reach supersonic speeds. Moreover, the equiangular rotor blades (i.e., $\beta_2 = -\beta_3$), assume the typical bucket shape, because at the design condition metal angles are close to the flow ones.

Figure 2.2 shows the velocity triangles for a real impulse stage with equiangular rotor blades. It can be seen that rotor diffusion ($W_2 > W_3$) occurs across the rotor row. This aspect should be carefully taken into

account because the resulting adverse pressure gradient (i.e., the pressure increases in the direction of the flow) coupled with the typical turbine fluid deflection may give rise to boundary layer separation and corresponding efficiency losses.

The expansion process is sketched on the enthalpy-entropy diagram in Fig. 2.3: nozzle outlet state (2) and isentropic rotor outlet state (3s) coincide as they lie on the same pressure line.

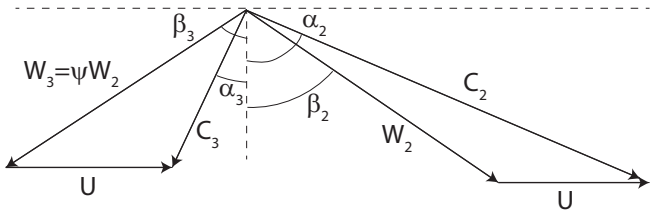

Figure 2.2: Velocity triangles for a real impulse stage with equiangular rotor blades (W_3 must be lower than W_2).

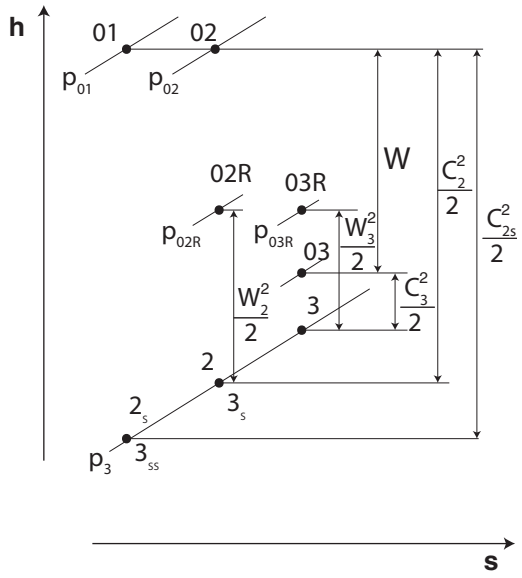

Figure 2.3: Enthalpy-entropy diagram for an impulse stage turbine.

2.3.2 Analytical expressions of work and efficiency versus design parameters

In this Section the expressions for the specific work $\mathcal{W}$ and the total-to-static efficiency η_{ts} are derived. Irreversibilities are accounted by means of velocity coefficients: φ for the nozzle and ψ for the rotor.

$$\varphi = \frac{C_2}{C_{2s}} = \frac{1}{(1+\zeta_N)^{0.5}} \tag{2.17}$$

$$\psi = \frac{W_3}{W_{3s}} = \frac{W_3}{W_2} = \frac{1}{(1+\zeta_R)^{0.5}} \tag{2.18}$$

The equivalence $W_{3s} = W_2$ in Eq. (2.18) is a direct consequence of the absence of pressure drop across the rotor (i.e., $p_2 = p_3 \rightarrow$ state $3 \equiv 3s$).

The work extracted by an axial machine is

$$\mathcal{W} = U(C_2 \sin\alpha_2 - C_3 \sin\alpha_3) \tag{2.19}$$

Considering the rotor outlet velocity triangle and the definitions provided by Eq. (2.18)

$$C_3 \sin\alpha_3 = \psi W_2 \sin\beta_3 + U \tag{2.20}$$

whereas for the rotor inlet

$$C_2 \sin\alpha_2 = W_2 \sin\beta_2 + U \tag{2.21}$$

By substituting W_2 from Eq. (2.21) in Eq. (2.20) and the resulting expression of $C_3 \sin\alpha_3$ in Eq. (2.19), the work expression can be rearranged in

$$\mathcal{W} = U(C_2 \sin\alpha_2 - U)\left(1 - \psi\frac{\sin\beta_3}{\sin\beta_2}\right) \tag{2.22}$$

Introducing the speed ratio between the peripheral speed and the tangential absolute velocity at rotor inlet

$$\boxed{X = \frac{U}{C_2 \sin\alpha_2}} \tag{2.23}$$

and assuming equiangular rotor blades ($\beta_2 = -\beta_3$), the final expression for the work becomes

$$\boxed{\mathcal{W} = C_2^2 \sin^2 \alpha_2 X(1-X)(1+\psi)} \tag{2.24}$$

The total-to-static efficiency η_{ts} follows immediately from its own definition by embedding the work expression of Eq. (2.22)

$$\eta_{ts} = \frac{w}{h_{01} - h_{2s}} = \frac{C_2^2 \sin^2 \alpha_2 X(1-X)\left(1 - \psi \frac{\sin\beta_3}{\sin\beta_2}\right)}{\frac{C_2^2}{2\varphi^2}} \tag{2.25}$$

For equiangular rotor blades ($\beta_2 = -\beta_3$) it reduces to

$$\boxed{\eta_{ts} = 2\varphi^2 \sin^2 \alpha_2 X(1-X)(1+\psi)} \tag{2.26}$$

The performance of the stage has been related up here to the characteristic speed ratio $X = U/(C_2 \sin\alpha_2)$ (see for example Eq. (2.26)). However, it might be useful to relate the performance of the stage to other parameters frequently used in turbine design practice: the loading coefficient (Ψ) and the isentropic velocity ratio (ν).

By including in the definition of loading coefficient (Eq. (2.11)) the work expression deduced in Eq. (2.24) it results

$$\boxed{\Psi = \frac{(1-X)(1+\psi)}{X}} \tag{2.27}$$

The isentropic velocity ratio (ν) is the ratio between the peripheral speed U and the spouting velocity C_0 (which is the velocity at the end of an isentropic expansion from the total inlet condition of the fluid to the outlet static pressure)

$$\nu = \frac{U}{C_0} = \frac{U}{(2(h_{01} - h_{3ss}))^{0.5}} \tag{2.28}$$

As $h_{01} - h_{3ss} = 1/2C_{2s}^2$, referring to the definitions of $\varphi = C_2/C_{2s}$ and $X = U/(C_2 \sin\alpha_2)$ it follows

$$h_{01} - h_{3ss} = \frac{1}{2\varphi^2} \frac{U^2}{\sin^2 \alpha_2 X^2} \tag{2.29}$$

and, in turn, Eq. (2.28) becomes

$$\boxed{\nu = \varphi \sin \alpha_2 X} \tag{2.30}$$

Equation (2.30) establishes a direct relationship between the two velocity ratio X and ν.

2.3.3 Design guidelines

The guidelines for an optimum design of an impulse stage are essentially represented by those values of non-dimensional design parameters which maximize the efficiency expression deduced in Section 2.3.2.

When the rotor velocity coefficient ψ is assumed independent of X, the parabolic work trend in Fig. 2.4 is obtained (see Eq. 2.24). The maximum work $\mathcal{W}_{max}$ and efficiency is achieved for

$$\boxed{X_{opt} = 0.5} \tag{2.31}$$

and it is

$$\mathcal{W}_{max} = \mathcal{W}_{|X=0.5} = C_2^2 \sin^2 \alpha_2 \frac{1}{4}(1 + \psi) \tag{2.32}$$

It is remarkable to note that, under the hypothesis of constant ψ, the X value leading to the maximum work extraction or total-to-static efficiency is independent of the rotor loss coefficient.

Similarly to the specific work, when the rotor loss coefficient ψ is constant, a parabolic η_{ts} trend with X is obtained. The maximum efficiency lies again on $X = 0.5$ and it is equal to

$$\eta_{ts,max} = \eta_{ts|X=0.5} = \frac{1}{2}\varphi^2 \sin^2 \alpha_2 (1 + \psi) \tag{2.33}$$

Figure 2.5 shows the trend of η_{ts} for two different values of the nozzle outlet angle α_2 in case the dependency of the loss coefficient ψ on X is taken into account. In general terms, for fixed C_2 and α_2, an increase of X results in a decrease of (i) the rotor turning and in turn of the losses (i.e.

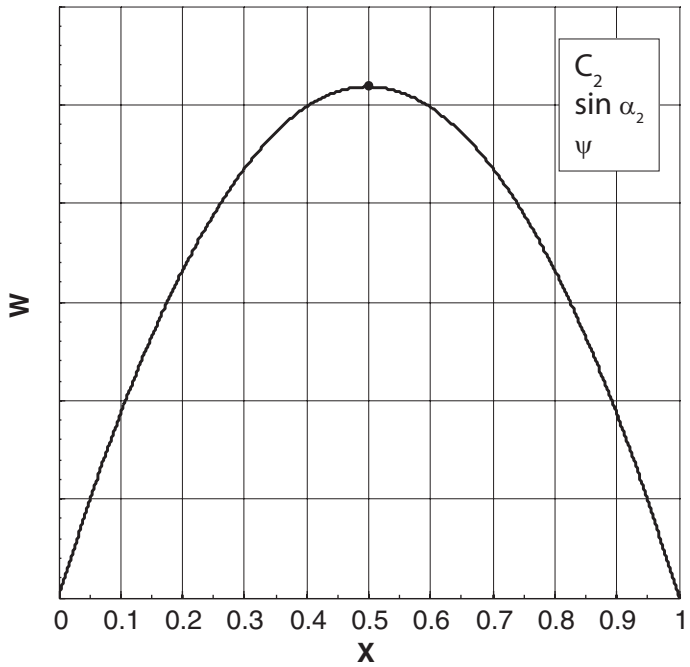

Figure 2.4: Specific work extracted by an impulse stage with equiangular rotor blades and fixed rotor loss coefficient.

ψ increases and ζ_R decreases) and (ii) the inlet relative velocity W_2. Consequently, the enthalpy loss in the rotor $h_3 - h_{3s}$ decreases as X increases

$$h_3 - h_{3s} = (1 - \psi^2)\frac{W_2^2}{2} \tag{2.34}$$

The discharge kinetic energy, which is a loss for a total-to-static efficiency, is minimum for $X = 0.5$ (i.e., axial discharge) in the ideal case ($\psi = 1$). Thus, for the real case ($\psi < 1$ and variable with X) the minimum kinetic loss is located not too far from $X = 0.5$. All the above considerations would lead to an optimum X slightly over 0.5 as reported in Fig. 2.5.

However, when the parasitic losses (disk friction, partialization) are considered, it is convenient to adopt small rotors because both disk friction and partialization losses are proportional to the wheel diameter. In practice, $X \approx 0.45$ is chosen in real impulse stage, because the partialization losses in off design operation rapidly increase with the peripheral

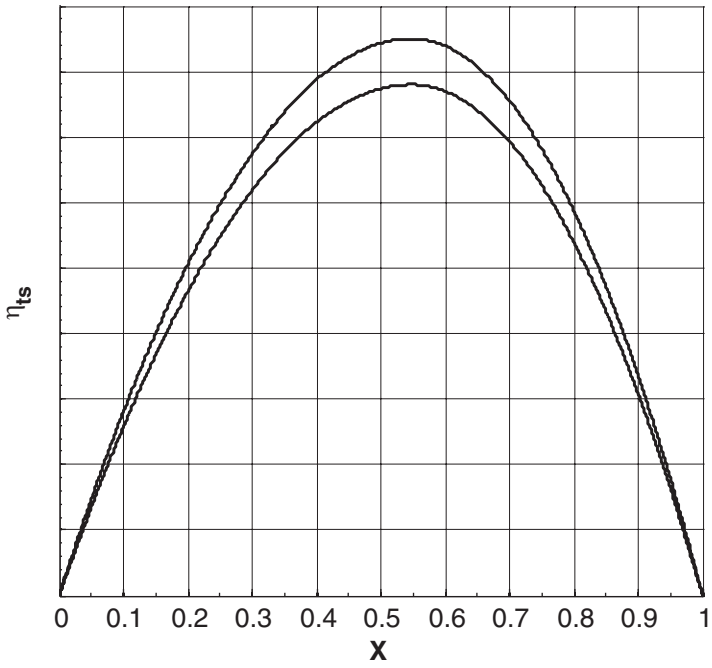

Figure 2.5: Total-to-static efficiency of an impulse stage with equiangular rotor blades and variable rotor loss coefficient.

speed U. In this way, the decrease of η_{ts} with respect to its maximum value is still limited, but it is outweighed by the lower partialization losses.

As regards the optimum loading coefficients (Ψ), Eq. (2.27) evaluated for the optimum $X_{opt} = 0.5$, gives

$$\Psi_{opt} = \Psi_{|X=0.5} = 1 + \psi \tag{2.35}$$

Equation (2.35) states that the optimum loading coefficient for an impulse stage is approximately (being $\psi \leq 1$)

$$\boxed{\Psi_{opt} \approx 2} \tag{2.36}$$

Instead, the optimum ν is

$$\boxed{\nu_{opt} \approx 0.47} \tag{2.37}$$

when $\varphi = 0.95$ and $\alpha_2 = 80°$ are assumed in Eq. (2.30)).

2.3.4 Impulse turbine limitations

Centrifugal stresses are predominant on the blades and disks of a turbine and they depend on the square of the peripheral velocity U. For the condition $X = 0.5$ resulting in both maximum work $\mathcal{W}$ and η_{ts}

$$U_{opt} = 0.5 C_2 \sin \alpha_2 \tag{2.38}$$

By considering a typical total-to-static enthalpy drop Δh_{ts} for steam application in the order of 1000 kJ/kg and assuming a total-to-static efficiency equal to 0.84 and a nozzle outlet angle α_2 equal to 70°, it follows

$$U_{opt} = 0.5 \left(2 \Delta h_{ts} \eta_{ts}\right)^{0.5} \sin \alpha_2 = 600 \text{ m/s} \tag{2.39}$$

which is very much higher than the maximum allowable speed imposed by materials (in the order of $300 - 350$ m/s). Moreover, the high velocity at nozzle outlet would certainly cause unacceptable losses. Thus, the single stage impulse turbine cannot be used with the typical enthalpy drops available in steam power plants unless an X ratio strongly lower than the optimum one is chosen.

2.4 Velocity compounded impulse stage

A velocity compounded impulse stage consists of an impulse turbine followed by a series of nozzle and rotor rows which progressively reduce the swirl velocity component. Compared to the impulse stage, it can efficiently manage higher enthalpy drops because it achieves its best efficiency point at a lower peripheral velocity. The optimum values of the design parameters for a two row arrangement are $X \approx 0.24$ and $\nu \approx 0.22$. Although the increase of the rows number leads to a reduction in the optimum peripheral velocity, configurations with more than three rows are rarely used.

2.4.1 Construction features

A velocity compounded impulse stage represents a possible solution when high available enthalpy drop would require too high peripheral velocity to operate efficiently. Despite this configuration includes more than one fixed and rotor row (usually two) it is commonly referred as "stage". The steam passes through an impulse stage where occurs the whole pressure drop and then enters in a stator row composed of equiangular vanes. They redirect the fluid towards the second rotor for a further work extraction and so on.

Figure 2.6 shows the expansion in the enthalpy-entropy chart.

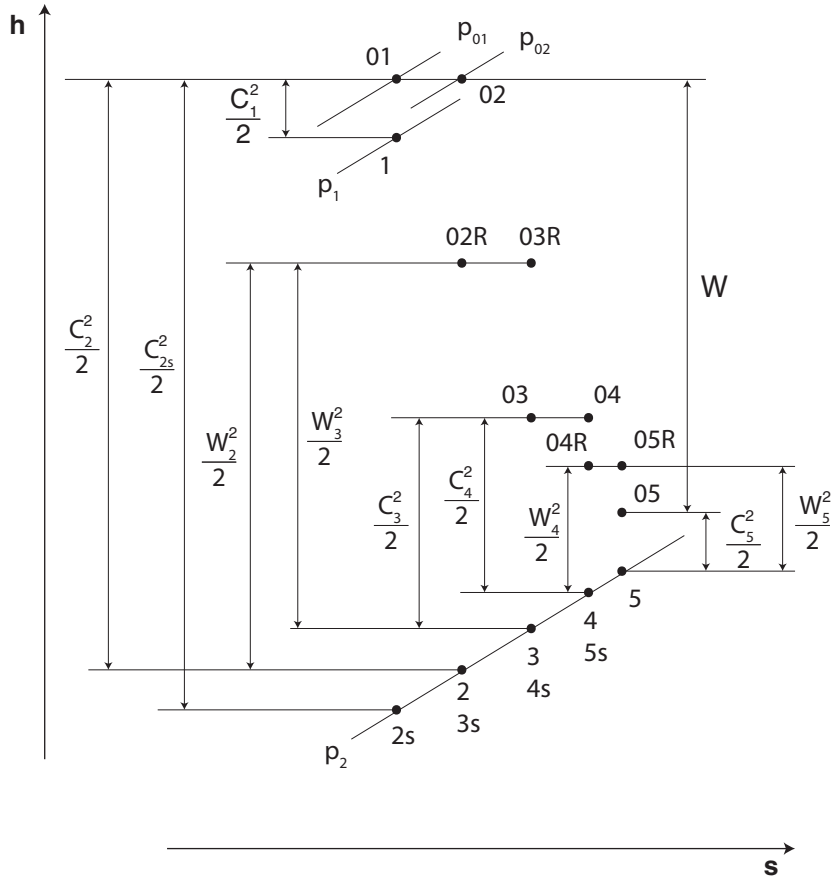

Figure 2.6: Enthalpy-entropy diagram for a two stage velocity compounded impulse turbine.

2.4.2 Analytical expressions of work and efficiency versus design parameters

This Section is aimed at evaluating the expressions of the specific work and total-to-static efficiency for a velocity compounded stage with symmetrical blades

$$\beta_2 = -\beta_3 \qquad \alpha_3 = -\alpha_4 \qquad \beta_4 = \beta_5 \tag{2.40}$$

and real rows, whose loss coefficient for the first rotor (ψ'), second rotor (ψ'') and stator (ψ_N) are

$$\psi' = \frac{W_3}{W_{3s}} = \frac{W_3}{W_2} \tag{2.41}$$

$$\psi'' = \frac{W_5}{W_{5s}} = \frac{W_5}{W_4} \tag{2.42}$$

$$\psi_M = \frac{C_4}{C_{4s}} = \frac{C_4}{C_3} \tag{2.43}$$

The velocity triangles are sketched in Fig. 2.7.

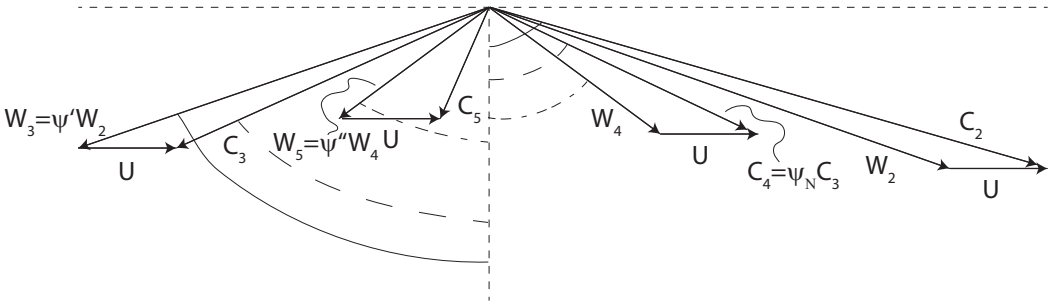

Figure 2.7: Velocity triangles for a real velocity compounded stage. Angles with the same graphical notation are equal.

The total work $\mathcal{W}$ is the sum of the two rotor contributions $\mathcal{W}_{12}$ and $\mathcal{W}_{22}$ and, recalling Eq. (2.24), is

$$\mathcal{W} = \mathcal{W}_{12} + \mathcal{W}_{22} = U(C_2 \sin\alpha_2 - U)(1 + \psi') + U(C_4 \sin\alpha_4 - U)(1 + \psi'') \tag{2.44}$$

The expression $C_4 \sin\alpha_4$ can be re-written in terms of loss coefficients and kinematic variables at nozzle outlet

$$C_4 \sin\alpha_4 = \psi_R(\psi'(C_2 \sin\alpha_2 - U) - U) \tag{2.45}$$

Thus, Eq. (2.44) becomes

$$\mathcal{W} = U\left(((1+\psi') + \psi_N\psi'(1+\psi''))\, C_2 \sin\alpha_2 - ((1+\psi') + \psi_N\psi'(1+\psi'') + (1+\psi'')(1+\psi_N))\, U\right) \tag{2.46}$$

and including the speed parameter $X = U/(C_2 \sin\alpha_2)$ it turns into

$$\mathcal{W} = (X((1+\psi')+\psi_R\psi'(1+\psi'')) - X^2((1+\psi')+\psi_R\psi'(1+\psi'')+(1+\psi'')(1+\psi_R)))C_2^2 \sin^2\alpha_2 \tag{2.47}$$

Since for the single stage impulse turbine, the velocity loss coefficients ψ', ψ'' and ψ_N depends on the deflection and, in turn, on the speed ratio $X = U/(C_2 \sin\alpha_2)$ the probable values $\alpha_2 = 76°$, $\psi' = 0.86$, $\psi_R = 0.9$ and $\psi'' = 0.93$ are assumed [32]. Accordingly, Eq. (2.47) becomes

$$\boxed{\mathcal{W} = 3.35X(1-2.1X)C_2^2 \sin\alpha_2^2} \tag{2.48}$$

Consequently, the total-to-static efficiency is recast as

$$\boxed{\eta_{ts} = \frac{\mathcal{W}}{C_2/(2\varphi^2)} = 6.7X(1-2.1X)\varphi^2 \sin^2\alpha_2} \tag{2.49}$$

2.4.3 Design guidelines

Specific work and total-to-static efficiency expression (see Section 2.4.2, Eqs. (2.48) and (2.49)) are null for $X = 0$ and $X = 0.48$ and are maximum for

$$\boxed{X_{opt} = 0.24} \tag{2.50}$$

Differently from the single stage configuration, the optimum value of the velocity characteristic ratio X depends on the velocity loss coefficient.

The optimum design parameter $X_{opt} = 0.24$ can be converted in terms of velocity ratio by means of Eq. (2.30), where $\varphi = 0.95$ and $\alpha_2 = 80°$ are supposed

$$\boxed{\nu_{opt} = 0.22} \tag{2.51}$$

Figure 2.8 shows the total-to-static efficiency for an impulse (Eq. (2.26)) and velocity compounded impulse stage (Eq. (2.49)) with equiangular blades for different velocity ratios (X) and nozzle outlet angles (α_2). The velocity coefficient for the single stage arrangements ψ is set equal to the stator velocity coefficient of the two stage arrangement ψ_N. With these assumptions the efficiency ratio of the two configurations at the respective best efficiency points is

$$\frac{(\eta_{ts,max})_{Z=2}}{(\eta_{ts,max})_{Z=1}} = \frac{0.8\varphi^2 \sin^2 \alpha_2}{0.5\varphi^2 \sin^2 \alpha_2 (1+\psi)} = 0.842 \tag{2.52}$$

The efficiency of the velocity compounded turbine is lower than the pure impulse arrangement because (i) losses in the first rotor are higher due to the higher deflection and (ii) there are also the additional losses in the stator and in the second rotor.

To further investigate the effect of the velocity compounding staging on the optimum design parameter when more that two row are put in series, ideal rows (i.e., $\psi = \varphi = 1$) are considered hereafter for the sake of simplicity. As the discharge kinetic energy is the only considered loss source, the condition of maximum total-to-static efficiency is achieved for no swirl discharge component at rotor outlet. Accordingly, velocity triangles indicate that the optimum peripheral velocity U_{opt} needed for no discharge swirl is

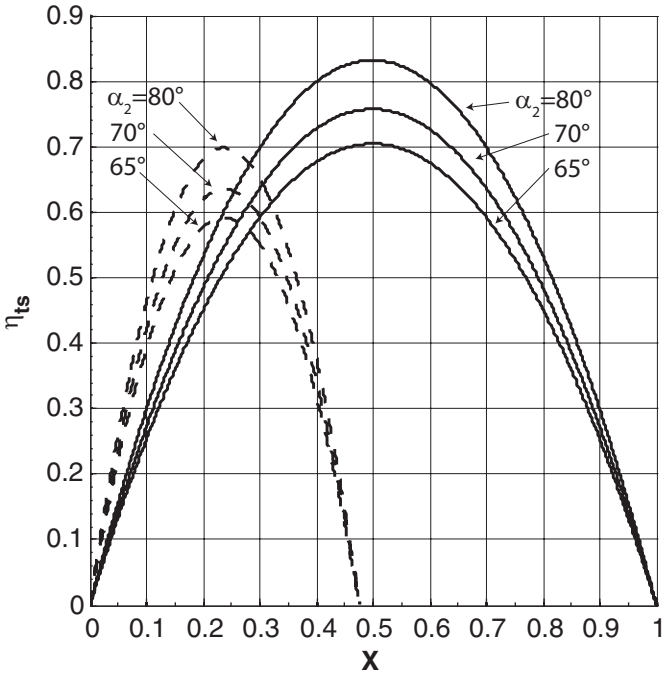

Figure 2.8: Total-to-static efficiency versus X velocity ratio for different nozzle outlet angles (65, 71, 80) for a single (right) and double stage (left) impulse turbine elaborating the same enthalpy drop. The assumed loss coefficients for the single impulse turbine are $\phi = 0.95$ (nozzle) and $\psi = 0.9$ (rotor); for the double impulse turbine they are $\phi = 0.95$ (nozzle), $\psi' = 0.86$ (first rotor), $\psi_s = 0.9$ (stator) and $\psi'' = 0.93$ (second rotor).

$$U_{opt} = \frac{C_2 \sin \alpha_2}{4} \tag{2.53}$$

which corresponds to an optimum velocity ratio

$$X_{opt} = \frac{U}{C_2 \sin \alpha_2} = \frac{1}{4} \tag{2.54}$$

The work for the maximum efficiency operation (which is also the maximum work) is

$$\mathcal{W}_{max} = \mathcal{W}_{|X=0.25} = \frac{1}{2} C_2^2 \sin^2 \alpha_2 = 8U^2 \tag{2.55}$$

($6U^2$ from the first stage and $2U^2$ from the second).

Extending Eqs. (2.53), (2.54) and (2.55) to Z stages arrangement

$$U_{opt} = \frac{C_2 \sin \alpha_2}{2Z} \tag{2.56}$$

$$\boxed{X_{opt} = \frac{U}{C_2 \sin \alpha_2} = \frac{1}{2Z}} \tag{2.57}$$

$$\mathcal{W}_{max} = \frac{1}{2} C_2^2 \sin^2 \alpha_2 = 2Z^2 U^2 \tag{2.58}$$

Thus, Eq. (2.58) indicates that the ratio between (i) the maximum work extracted by a turbine with Z ideal and equiangular rows ($\mathcal{W}_{Zvd}$) and (ii) the maximum work extracted by an ideal and equiangular single row impulse turbine ($\mathcal{W}_{1vd}$) is

- Z^2, when U is the same;
- unitary, when the nozzle outlet velocity $C_2 \sin \alpha_2$ is the same.

A velocity compounded arrangement is advantageous because requires a lower optimum peripheral velocity U_{opt} in accordance with Eq. (2.56).

Figure 2.9 compares the ideal velocity triangles and the work of an impulse turbine (part a) to a two row velocity compounded stage for equal

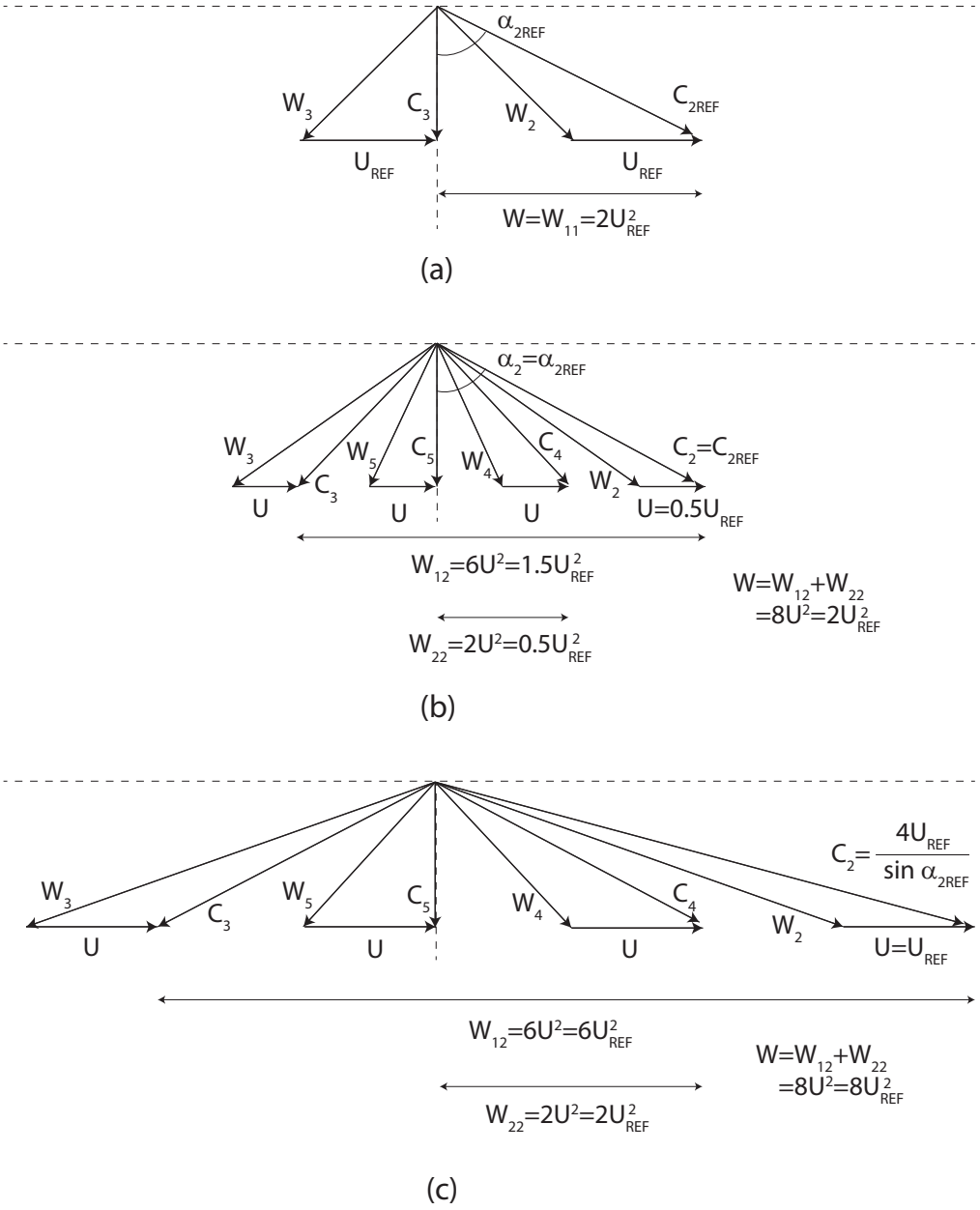

Figure 2.9: Comparison between single stage impulse turbine velocity triangles (a) and two stage velocity compounded impulse turbine with equal $C_2 \sin \alpha_2$ (b) and equal U (c). Ideal and equiangular rows and maximum work operation are assumed.

Table 2.1: Main parameters for velocity compounded ideal turbines at optimum efficiency point for fixed $C_2 \sin\alpha_2$.

	w_{1max}	w_{2max}	w_{3max}	w_{ratio}	u_{opt}	X_{opt}
$Z=1$	$\frac{1}{2}C_2^2\sin^2\alpha_2$	–	–	1	$\frac{1}{2}C_2\sin\alpha_2$	$\frac{1}{2}$
$Z=2$	$\frac{3}{8}C_2^2\sin^2\alpha_2$	$\frac{1}{8}C_2^2\sin^2\alpha_2$	–	3 : 1	$\frac{1}{4}C_2\sin\alpha_2$	$\frac{1}{4}$
$Z=3$	$\frac{5}{18}C_2^2\sin^2\alpha_2$	$\frac{3}{18}C_2^2\sin^2\alpha_2$	$\frac{1}{18}C_2^2\sin^2\alpha_2$	5 : 3 : 1	$\frac{1}{6}C_2\sin\alpha_2$	$\frac{1}{6}$

nozzle outlet velocity $C_2 \sin\alpha_2$ (part b) and peripheral velocity U (part c). All the designs refer to the maximum work (or efficiency) operation.

Velocity compounded stages composed by more than three rows are not convenient because the relative contribution to the total work provided by the farthest rows is rather low. In fact, after some tedious algebra, the work extracted by the n^{th} ideal and equiangular rotor wheel (that is independent of the turbine stage number) can be expressed by

$$\mathcal{W}_n = 2U(C_2\sin\alpha_2 - U) - 4(n-1)U^2 \tag{2.59}$$

whereas the maximum work $\mathcal{W}_{nZmax}$ extracted by the n^{th} ideal and equiangular rotor wheel of a Z row stage turbine is deduced by substituting Eq. (2.57) in Eq. (2.59)

$$\mathcal{W}_{nZmax} = C_2^2\sin^2\alpha_2\left(\frac{2(Z-n)+1}{2Z^2}\right) \tag{2.60}$$

Table 2.1 summarizes the effect of the row number Z on the work distribution and optimum velocity ratio.

2.5 Pressure compounded impulse stage

A sequence of impulse stages put in series constitutes the pressure compounded impulse stage. Each fixed row elaborates a fraction of the available enthalpy drop. The optimum design parameters values are the same of

the impulse stage ($X_{opt} = 0.5$), but, for fixed enthalpy drop, the optimum peripheral velocity is $Z^{-0.5}$ times smaller. Instead, for fixed peripheral velocity the pressure compounded stage allows for an efficient exploitation of an enthalpy drop Z times greater than the impulse stage.

2.5.1 Construction features

A pressure compounded impulse stage represents a further viable option when facing with available enthalpy drop which would require an impulse stage arrangement with an excessive optimum tangential speed.

Two or more impulse rows are arranged in series to reduce the optimum peripheral speed and the steam is expanded partially in each of the nozzles until the reaching of the discharge pressure. No pressure drop occurs across each rotor.

2.5.2 Analytical expressions of work and efficiency versus design parameters

The total-to-total efficiency is the proper metric for the performance evaluation, independently of the effective recovery of the discharge kinetic energy

$$\eta_{tt} = \frac{\mathcal{W}}{h_{01} - h_{02s}} \tag{2.61}$$

It has already been shown in Eq. (2.24) that the work extracted by an impulse stage with equiangular rotor blades (i.e., $\beta_2 = -\beta_3$) is

$$\mathcal{W} = C_2^2 \sin^2 \alpha_2 X(1 - X)(1 + \psi) \tag{2.62}$$

By using the definition of nozzle velocity coefficient, the denominator of Eq. (2.61) can be conveniently re-written as

$$h_{01} - h_{02s} = \frac{C_2^2}{2\varphi^2} - \frac{C_3^2}{2} \tag{2.63}$$

Thus, the stage efficiency is updated

$$\eta_{tt} = \frac{2\varphi^2 \sin^2 \alpha_2 X(1-X)(1+\psi)}{1-\varphi^2\left(\frac{C_3}{C_2}\right)^2} \tag{2.64}$$

The velocity ratio C_3^2/C_2^2 is then rearranged

$$\frac{C_3^2}{C_2^2} = \frac{1}{C_2^2}(U^2 + W_3^2 + 2W_3 U \sin\beta_3) = \frac{1}{C_2^2}(U^2 + \psi^2 w_2^2 + 2\psi W_2 U \sin\beta_3) \tag{2.65}$$

and including in Eq. (2.65) the expression $W_2^2 = U^2 + C_2^2 - 2C_2 U \sin\alpha_2$ and $W_2 = (C_2 \sin\alpha_2 - U)/\sin\beta_2$ it becomes

$$\frac{C_3^2}{C_2^2} = \psi^2 + X \sin^2\alpha_2((1+\psi)^2 X - 2\psi(1+\psi)) \tag{2.66}$$

Accordingly, the final expression of the total-to-total efficiency results in

$$\boxed{\eta_{tt} = \frac{2\varphi^2 \sin^2 \alpha_2 X(1-X)(1+\psi)}{1-\varphi^2(\psi^2 + X \sin^2\alpha_2((1+\psi)^2 X - 2\psi(1+\psi)))}} \tag{2.67}$$

To avoid any ambiguity, it is useful to point out that Eq. (2.67) expresses the performance of a single couple nozzle-rotor of the pressure compounded arrangement. The derivation of an analytical formulation of the efficiency of the entire pressure compounded stage consisting in more than one row, would be impractical and it is therefore omitted.

2.5.3 Design guidelines

The considerations on the optimum design parameters values of the pressure compounded stage are the same of the impulse stage (see Section 2.3) because the pressure compounded arrangement is essentially a sequence of impulse stages. Obviously, for equal enthalpy drop, the nozzle outlet velocity of the pressure compounded stage is lower than the impulse stage, because the nozzle converts into kinetic energy only a fraction of the available enthalpy drop.

As the total-to-total stage efficiency do not account for the kinetic energy losses, the optimum velocity ratio X_{opt} in Eq. (2.67) is slightly

higher than the one maximizing the total-to-static efficiency, leading to $X_{opt} > 0.5$. Nevertheless,

$$\boxed{X \approx 0.5} \tag{2.68}$$

is chosen in practice because it guarantees lower parasitic losses (e.g. disk friction loss which rapidly increases with X) in the face of a very limited decrease of the efficiency.

In the following the pressure compounded stage with Z rows (subscript Zpd, pd stands for pressure drops) is compared both with the impulse stage and the velocity compounded stage. It is assumed that (i) the available enthalpy drop is equally divided among the Z rows, (ii) rotor rows are equiangular and (iii) working conditions are optimum (X_{opt}=0.5).

For the pressure compounded impulse stage

$$U_{Zpd} = \frac{C_2 \sin\alpha_2}{2} = \varphi \frac{\sin\alpha_2}{2} \left(\frac{2(h_{01} - h_{2s})_{Zpd}}{Z} \right)^{0.5} \tag{2.69}$$

where $(h_{01} - h_{2s})_{Zpd}$ is the isoentropic enthalpy drop inlet/outlet of the turbine and C_2 is the nozzle outlet velocity.

Similarly, for the impulse stage

$$U_{1pd} = \varphi \frac{\sin\alpha_2}{2} (2(h_{01} - h_{2s})_{1pd})^{0.5} \tag{2.70}$$

Accordingly (see Eqs. (2.69) and (2.70)),

- for equal nozzle outlet angle (α_2), nozzle loss coefficient (φ) and peripheral velocity (U) it is

$$\boxed{\frac{(h_{01} - h_{2t})_{Zpd}}{(h_{01} - h_{2t})_{1pd}} = Z} \tag{2.71}$$

  that is the pressure compounded stage allows an efficient exploitation of an enthalpy drop Z times greater than the impulse stage.

- for equal available enthalpy drop ($(h_{01} - h_{2s})_{Zpd} = (h_{01} - h_{2s})_{1pd}$)

$$\boxed{\frac{U_{Zpd}}{U_{1pd}} = \frac{1}{Z^{0.5}}} \tag{2.72}$$

that is the optimum peripheral velocity of the pressure compounded stage is $Z^{-0.5}$ times the impulse stage.

When the velocity triangles of pressure compounded stage are similar to those of the impulse stage, Eq. (2.72) can be extended in the form

$$\frac{U_{Zpd}}{U_{1pd}} = \frac{C_{Zpd}}{C_{1pd}} = \frac{\mathcal{W}_{Zpd}}{\mathcal{W}_{1pd}} = \frac{1}{Z^{0.5}} \tag{2.73}$$

The specific losses in the nozzle (L_n) and in the rotor row (L_r) of the impulse stage are

$$(L_n + L_r)_{1pd} = \left(\frac{1}{\varphi^2} - 1\right)\left(\frac{C_2^2}{2}\right)_{1pd} + (1 - \psi^2)\left(\frac{W_2^2}{2}\right)_{1pd} \tag{2.74}$$

whereas in the pressure compounded stage they are Z times those occurring in the impulse stage

$$(L_n + L_r)_{Zpd} = \left(\frac{1}{\varphi^2} - 1\right)\left(\frac{C_2^2}{2}\right)_{Zpd} + (1 - \psi^2)\left(\frac{W_2^2}{2}\right)_{Zpd} \tag{2.75}$$

Assuming equal velocity coefficients and considering Eq. (2.73), it results

$$\frac{(L_n + L_r)_{1pd}}{(L_n + L_r)_{Zpd}} = 1 \tag{2.76}$$

Thus, in spite of the higher number of rows in a pressure compounded stage, the total loss amount is almost the same being velocities proportionally lower. On the other hand, in the pressure compounded stage the discharge kinetic energy loss is $1/Z$ times that of the impulse stage.

With respect to the comparison with the velocity compounded stage (subscript Zvd stands for velocity drop) whose optimum velocity ratio is $X_{opt} = 1/(2Z)$ (refer to Section 2.4) it is

$$(h_{01} - h_{2s})_{Zvd} = \frac{2U_{Zvd}^2}{\varphi^2 \sin\alpha_2^2} Z^2 \tag{2.77}$$

Accordingly (see Eqs. (2.69) and (2.77)),

- for equal nozzle outlet angle (α_2), nozzle loss coefficient (φ) and peripheral velocity (U) it is

$$\boxed{\frac{(h_{01} - h_{2t})_{Zpd}}{(h_{01} - h_{2t})_{Zvd}} = Z} \tag{2.78}$$

  that is the pressure compounded stage is more suitable to exploit high enthalpy drops with a limited number of stages. However, pressure compounded arrangement can achieve higher turbine efficiency because of the reheat factor effect and the reduced discharge kinetic energy losses.

- for equal available enthalpy drop ($(h_{01} - h_{2s})_{Zpd} = (h_{01} - h_{2s})_{Zvd}$)

$$\boxed{\frac{U_{Zvd}}{U_{1vd}} = \frac{1}{Z}} \tag{2.79}$$

  that is the optimum peripheral velocity of the pressure compounded stage is Z^{-1} times the velocity compounded stage.

2.6 Reaction stage

Differently from an impulse stage, in a reaction stage a fraction of the available enthalpy drop occurs in the rotor. The 50% reaction stage is the most diffused reaction arrangement because it is characterized by symmetric blade profiles. Its optimum design parameters are: $X_{opt} \approx 1$, $\Psi_{opt} \approx 1$

and $\nu_{opt} \approx 0.90$. Differently from the impulse stage, the technological constraints on the minimum inlet blade height cannot be overcome by partialized operation, thus a limitation on minimum swallowable volumetric flow rate exists.

2.6.1 Construction features

In a reaction stage a pressure/enthalpy drop occur both across the nozzle and rotor row. When kinematic and thermodynamic reaction are equal to 50%, nozzle and rotor velocity triangles and, in turn, corresponding blade profiles are symmetric.

Reaction stages with equal cinematic (R, see Eq. (2.14)) and thermodynamic reaction (χ, see Eq. (2.15)) are largely employed in power plants, being particularly favorable from a practical point of view. According to the respective definitions, the cinematic and thermodynamic reactions are equal when

$$\psi = \phi \qquad W_3 = C_2 \qquad C_3 = W_2 \qquad C_3 = C_1 \tag{2.80}$$

and the resulting common value is $R = \chi = 0.5$.

The condition $\psi = \phi$ requires in turn equal fluid deflections in the nozzle and rotor row, that is

$$\alpha_3 = -\beta_2 \qquad \alpha_2 = -\beta_3 \tag{2.81}$$

In brief, a stage with $R = \chi = 0.5$ is characterized by symmetric velocity triangles (see Fig. 2.10) and makes possible the use of the same blade profiles in the stator and in the rotor with obvious reduction of manufacturing costs. Figure 2.11 shows the expansion in the enthalpy-entropy chart.

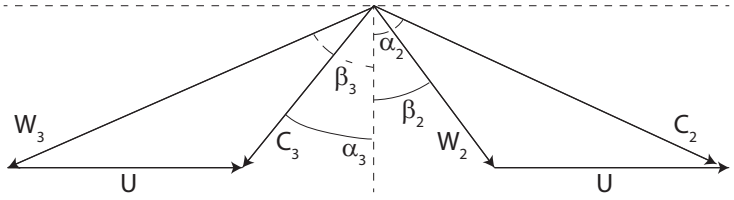

Figure 2.10: Velocity triangles for a reaction stage with $R = \chi = 0.5$.

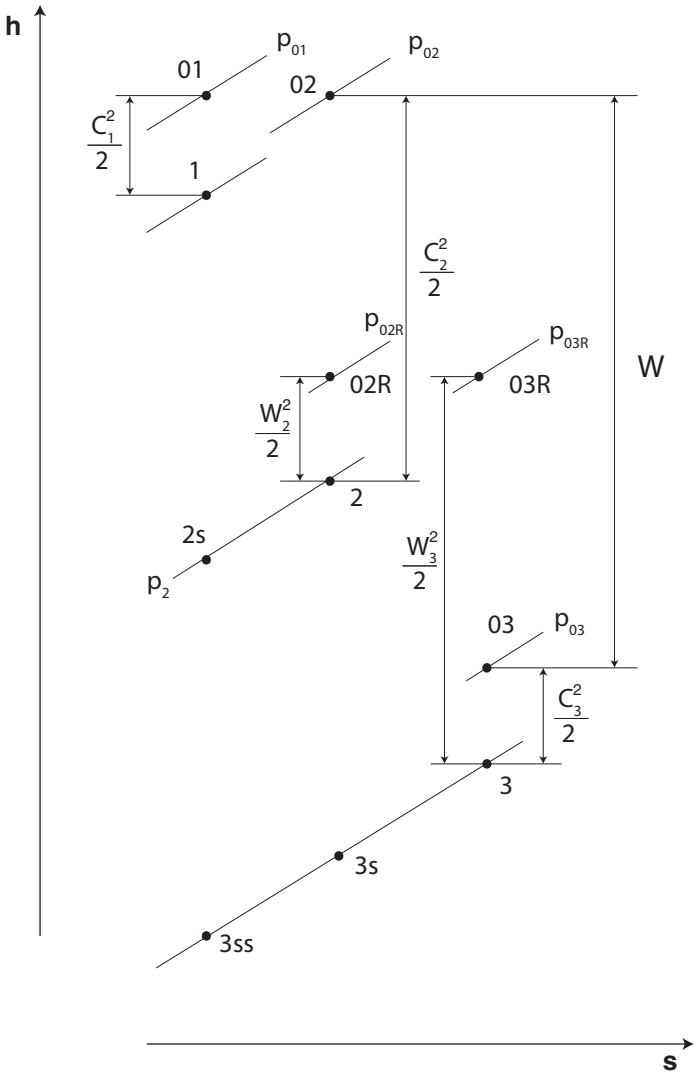

Figure 2.11: Enthaply-entropy diagram for a 50% reaction stage.

2.6.2 Analytical expressions of work and efficiency versus design parameters

This Section is aimed at evaluating the expressions of the specific work and total-to-total efficiency for a 50% reaction stage.

The specific work extracted by the stage may be written as

$$\mathcal{W} = U(C_2 \sin\alpha_2 - C_3 \sin\alpha_3) = U(2C_2 \sin\alpha_2 - U) \tag{2.82}$$

and introducing the velocity ratio $X = U/(C_2 \sin\alpha_2)$

$$\boxed{\mathcal{W} = C_2^2 \sin\alpha_2^2 X(2-X) = U^2 \frac{2-X}{X}} \tag{2.83}$$

As regards the efficiency, the total-to-total enthalpy isentropic enthalpy drop $h_{01} - h_{03ss}$ is conveniently recast as follows

$$h_{01} - h_{03ss} = h_{01} - h_{3ss} - \frac{C_1^2}{2} = h_{01} - h_{2s} + h_{02R} - h_{3s} - \frac{C_3^2}{2} - \frac{C_1^2}{2} \tag{2.84}$$

From the velocity coefficients definitions

$$h_1 - h_{2s} = \frac{C_2^2}{2\varphi^2} - \frac{C_1^2}{2} \tag{2.85}$$

$$h_2 - h_{3s} = \frac{C_2^2}{2\psi^2} - \frac{C_1^2}{2} \tag{2.86}$$

it follows ($C_1 = W_2$)

$$h_{01} - h_{2s} = \frac{C_2^2}{2\varphi^2} \tag{2.87}$$

$$h_{02R} - h_{3s} = \frac{C_2^2}{2\psi^2} \tag{2.88}$$

Accordingly, Eq. (2.84) becomes

$$h_{01} - h_{03ss} = \frac{C_2^2}{2\varphi^2} + \frac{C_2^2}{2\phi^2} - \frac{C_3^2}{2} - \frac{C_1^2}{2} \tag{2.89}$$

As in a 50% reaction stage $\varphi = \psi$ and $C_1 = C_3$ the total-to-total enthalpy drop may be simplified as

$$h_{01} - h_{03ss} = \frac{C_2^2}{\varphi^2} - C_3^2 \tag{2.90}$$

and the total-to-static efficiency η_{tt} turns into

$$\eta_{tt} = \frac{h_{01} - h_{03}}{h_{01} - h_{03ss}} = \frac{\varphi^2 \sin^2 \alpha_2 X(2-X)}{1 - \frac{1}{2}\varphi^2 \frac{C_3^2}{C_2^2}} \tag{2.91}$$

By considering for the rotor inlet triangle the geometric identity

$$W_2^2 = C_2^2 + U^2 - 2C_2 U \sin \alpha_2 \tag{2.92}$$

it results ($W_2 = C_3$)

$$\frac{C_3^2}{C_2^2} = 1 + \sin^2 \alpha_2 X^2 - 2X \sin^2 \alpha_2 \tag{2.93}$$

and, in turns, the final expression of the total-to-total efficiency for a normal 50% reaction stage becomes

$$\boxed{\eta_{tt} = \frac{\varphi^2 \sin^2 \alpha_2 X(2-X)}{1 - \frac{1}{2}\varphi^2 (1 - \sin^2 \alpha_2 X(2-X))}} \tag{2.94}$$

Similarly to the impulse stage the velocity ratio X can be related to the loading coefficient Ψ by embedding the work expression deduced in Eq. (2.83) in the definition of loading coefficient (Eq. (2.11))

$$\boxed{\Psi = \frac{2-X}{X}} \tag{2.95}$$

2.6.3 Design guidelines

The identification of the design parameters values which maximize the work and efficiency expressions (Section 2.6) provide an indication for an optimum design of the reaction stage.

For fixed $C_2 \sin \alpha_2$, the X value leading to the maximum work extraction is

$$\boxed{X_{opt} = 1} \tag{2.96}$$

and the correspondent work is

$$\mathcal{W}_{max} = \mathcal{W}_{|X=1} = C_2^2 \sin^2 \alpha_2 = U^2 \tag{2.97}$$

The efficiency η_{tt} (Eq. (2.94)) trend with X is symmetric with respect to $X = 1$ when the velocity coefficient are constant. However, the velocity coefficients depend on X and they decrease (i.e. more losses) as the deflection increases, so that the best efficiency lies between $X = 1 - 1.33$. Nevertheless, configurations with $X = 0.8 - 1$ are chosen in real practice because they allow to manage higher enthalpy drops with a slight reduction in efficiency.

The optimum loading coefficient corresponding to $X_{opt} = 1$ is approximately one half of the impulse stage and it is deduced from Eq. (2.95)

$$\boxed{\Psi_{opt} = 1} \tag{2.98}$$

Instead, the optimum velocity ratio is

$$\boxed{\nu_{opt} \approx 0.90} \tag{2.99}$$

2.6.4 Limitations on the minimum inlet volumetric flow rate

Differently from an impulse stage, a reaction stage cannot be partialized due to the pressure drop across the rotor. As a consequence the design of a reaction stage might be unfeasible when the inlet volumetric flow rate is too low, because it would require an excessively short blade ([32],[34]). Therefore, it exists a minimum allowable rotor inlet volumetric flow rate $\dot{V}_{2min}$.

The smaller the power, or the higher the enthalpy drop or the lower the specific volume, the lower the rotor inlet volumetric flow rate

$$\dot{V}_{2I} = \frac{P}{\eta(h_{0A} - h_{Bs})} v_{2s} \tag{2.100}$$

where subscripts A and B denote the inlet and the outlet of the turbine and η is the turbine total-to-static efficiency (including parasitic losses).

The volumetric flow rate equation can be recast to highlight the influence of cinematic parameters on the design [32]. In particular

$$\dot{V}_{2I} = \zeta_1 \pi D_m b_2 C_2 \cos\alpha_2 \tag{2.101}$$

and, including the trivial identities (i) $\pi D_m = 60u/n$ (n in rotation per minute), (ii) $C_2 \cos\alpha_2 = U/(X1 \tan\alpha_2)$ and (iii) $w = U^2(2-X)/X$ (valid only for $R = 0.5$ reaction stages) it results

$$\boxed{\dot{V}_2 = \frac{60}{n}\zeta_2 b_2 \frac{w}{2-X}\frac{1}{\tan\alpha_2}} \tag{2.102}$$

Equation (2.102) allows the evaluation of the minimum inlet volumetric mass flow rate $\dot{V}_{2min}$ once the proper values (identified by the superscript $*$) of the variables are fixed. In detail, the requirements for

- limiting the stage number based on techno-economic considerations suggests a minimum value of the enthalpy drop per stage $w*$;
- avoiding low stage and, in turn, turbine efficiency imposes $X^* > 0.4 - 0.5$;
- fulfilling manufacturing constraints lead to $b_2^* > 25 - 30$mm and $\alpha_2^* < 76 - 78°$.

Thus, Eq. (2.102) evaluated for the star values provides an indication whether or not the volumetric flow rate deduced from the design specifications (Eq. 2.100) might be swallowed by a 50% reaction stage.

2.7 Impulse-reaction multistage turbines

Multistage turbines are needed when the high available enthalpy drop would lead to unfeasible or inefficient single stage configurations, that is

when the optimum design parameters of single stage turbines result, as instance, in excessive peripheral speeds. The main advantage of impulse-reaction multistage turbine arrangement relies on the possibility of partializing the first impulse stage which in turn allow (i) acceptable blade height even for low volumetric flow rate and (ii) an effective management of off-design operation (no throttling). Moreover, the higher the stage number, the lower the optimum peripheral speed.

In Section 2.6.4 it has been shown that both technical and fluid dynamic considerations define the minimum volumetric flow rate swallowed by a reaction stage. In case the available volumetric flow rate is lower than this limiting value, a velocity compounded impulse stage is placed before the reaction stages series. This configuration is very common in turbine technical practice and it is called "impulse-reaction turbine". In fact, the velocity compounded impulse stage can be largely partialized to permit the discharge of rather low volumetric flow rate until an adequately high volumetric flow rate is reached before the subsequent reaction stages. However, impulse-reaction turbines are used in power generation also when the volumetric flow rate would technically allow the simple reaction stage arrangement. The reason of this choice is two-fold. Firstly, the velocity compounded configuration is particularly useful in off design operation, because it is possible to partialize the first nozzle row to reduce the mass flow rate and, in turn, the power without introducing irreversibilities before the turbine (e.g., throttling). Secondly, the stress on the reaction turbine section is lower due to (i) the remarkable pressure drop across the impulse stage nozzle and (ii) the progressive pressure reduction in the flow direction. In fact, the maximum work and the enthalpy drop across a reaction stage is slightly lower than in an impulse stage, because, in the latter the work is $\mathcal{W} \approx 7u^2$ (see Eq. (2.48) evaluated for $X_{opt} = 0.24$), whereas in the former the work is U^2 (see Eq. 2.97).

2.8 Enthalpy drop splitting among turbine stages

The choice of the stage number in the multistage turbine design is a key problem. Only turbines composed of 50% reaction stages are considered here and methodologies to estimate (i) the stage number for assigned available enthalpy drop and (ii) the mean diameter and the blade height for each rotor row inlet are outlined. Two criteria are commonly used in the technical practice ([32], [34]): (i) constant blade to mean diameter ratio and (ii) constant hub diameter. The former is suitable for high pressure turbine section, whereas the latter fits to medium-low pressure section. Regardless of the design criterion, iterative procedures are needed.

2.8.1 Constant rotor inlet blade height to mean diameter ratio design criterion

The assumption of constant blade height to mean diameter ratio for all turbine stages

$$\boxed{\frac{b_2}{D_{m2}} = constant} \tag{2.103}$$

implies larger rotor toward the lower pressure with increasing blade root diameter and is typical of the high pressure section in multistage turbines.

The specific work of a turbine stage is

$$\mathcal{W} = \Delta h + \frac{C_1^2}{2} - \frac{C_3^2}{2} = \Psi U^2 \tag{2.104}$$

and equivalently

$$\Delta h = \left(\Psi + \frac{1}{2}\left(\frac{C_3^2}{U^2} - \frac{C_1}{U^2}\right)\right) U^2 = k_1 u^2 \tag{2.105}$$

where the constant quantity $k_1 = \Psi + 0.5(C_3^2/U^2 - C_1^2/U^2)$ is equal for all the stages as they have similar velocity triangles.

The volumetric flow rate $\dot{V}_2$ entering in the generic rotor row is (b_2 and ζ are the blade height and the blockage factor, respectively)

$$\dot{V}_2 = \dot{m} v_2 = \zeta \pi D_{m2} b_2 C_2 \sin\alpha_2 \frac{1}{\tan\alpha_2} \tag{2.106}$$

Including $D_{m2} = 2U/\omega$, $C_2 \sin\alpha_2 = U/X$ (ω and X are equal for all the stages) in Eq. (2.106), it results for the specific volume

$$v_2 = \frac{4\pi\zeta b_2}{\dot{m}\omega^2 D_{m2} X \tan\alpha_2} U^3 \tag{2.107}$$

In accordance with Eq. (2.103), Eq. (2.107) becomes

$$v_2 = k_2 u^3 \tag{2.108}$$

where $k_2 = (4\pi\zeta b_2)/(\dot{m}\omega^2 D_{m2} X \tan\alpha_2)$ is constant for all the stages.

Finally, Eqs. (2.105) and (2.108) lead to the fundamental relationship

$$\boxed{\Delta h = \frac{k_1}{k_2^{2/3}} v_2^{2/3} = k_3 v_2^{2/3}} \tag{2.109}$$

which states that the criterion of constant rotor inlet blade height to mean diameter ratio (Eq. (2.103)) requires, in turn, that the ratio between the enthalpy drop across a stage and the corresponding specific volume at rotor inlet power of 2/3, be the same for all the stages (Eq. 2.109).

The next step in the multistage turbine design is the estimation in the h-s chart of a first attempt expansion line which connects the static state at the outlet of the first rotor row (state $3I$ in Fig. 2.12, known from the first stage design) to the static state at the turbine discharge (state B in Fig. 2.12).

For the sake of simplicity a straight line is assumed. With regard to state B identification, the total enthalpy at turbine discharge (h_{0B}) is calculated from the energy balance

$$h_{0A} - h_{0B} = w = (h_{0A} - h_{0Bs}) \overline{\eta}_{ts} \mu \tag{2.110}$$

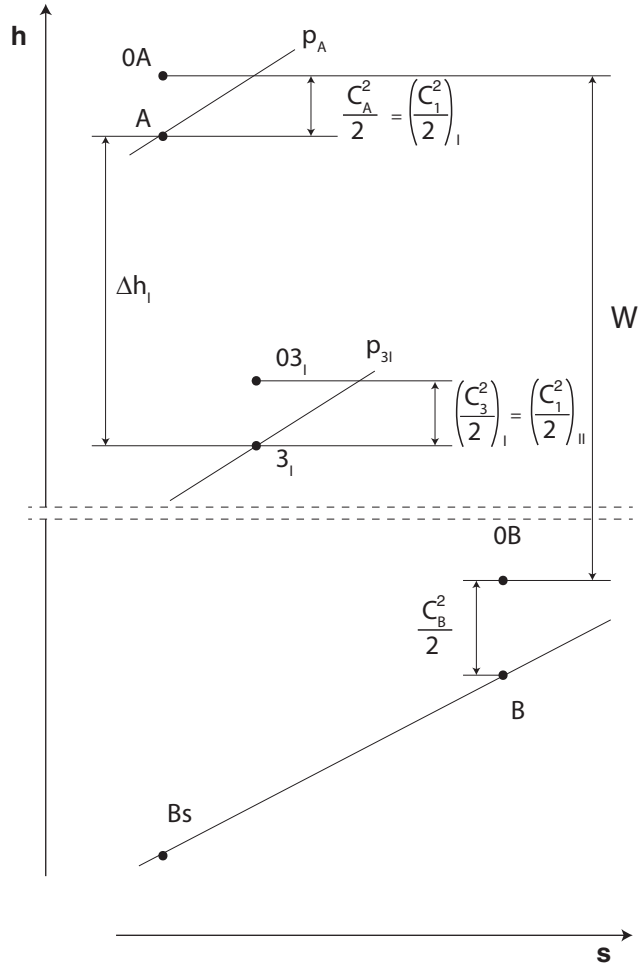

Figure 2.12: First attempt expansion line construction in the h-s diagram.

where the total-to-static mean stage efficiency ($\overline{\eta}_{ts}$) and the reheat factor μ are assumed by the designer. As (i) the variation of kinetic energy across a stage is proportional to the work of that stage and (ii) the inlet velocity into a stage is equal to the outlet velocity of the previous stage, it results after some algebra

$$\frac{C_B^2}{2} = \frac{C_A^2}{2}\left(\left(\frac{C_3^2}{2}\right)_I - \frac{c_A^2}{2}\right)\frac{\mathcal{W}}{\mathcal{W}_I} \tag{2.111}$$

Accordingly, the static state B is defined by the pressure p_B (which is a design specification) and by the static enthalpy $h_B = h_{0B} - c_B^2/2$ (Eqs. (2.110) and (2.111)).

Figure 2.13 illustrate the implementation of the design rule $b_2/D_{ms} = const.$ (Eq. (2.103)). It shows in the h-v diagram the curve labeled $v^{2/3}$ built from the first attempt straight expansion line previously drawn in the h-s diagram. At first, the triangle ABC corresponding to the first stage design is drawn out. Later, the triangle BDE similar to ABC and with the point E on the curve $v^{2/3}$ is built: it identifies on the x-axis the static enthalpy drop of the second stage (Δh_{II}) and the rotor inlet state (point E). This simple graphical construction is equivalent to solve the following system

$$\frac{(\Delta h)_{II}}{(\Delta h)_I} = \frac{(v_2)_{II}^{2/3}}{(v_2)_I^{2/3}} \tag{2.112}$$

$$\frac{(h_2)_{II} - (h_3)_I}{(h_3)_{II} - (h_3)_I} = \frac{1}{2} \tag{2.113}$$

$$(h_2)_{II} = f((v_2)_{II}) \tag{2.114}$$

Equation (2.112) directly derives from Eq. (2.109), Eq. (2.113) is the reaction definition and Eq. (2.114) represents the first attempt expansion line.

The first stage design has to be repeated until the discharge static enthalpy resulting from the graphical construction is sufficiently similar to the previously calculated value h_B. Moreover, the first attempt straight expansion line in the h-s chart has to be progressively corrected and, accordingly, the correspondent $v^{2/3}$ line in the h-v chart has to be updated.

Once convergence is obtained, the rotor inlet diameter $(D_{m2})_j$ and blade height $(b_2)_j$ of the j-th stage are calculated from Eq. (2.108)

$$(D_{m2})_j = \left(\frac{(v_2)_j}{(v_2)_I}\right)^{1/3} (D_{m2})_I \tag{2.115}$$

$$(h_2)_j = \left(\frac{(v_2)_j}{(v_2)_I}\right)^{1/3} (h_2)_I \tag{2.116}$$

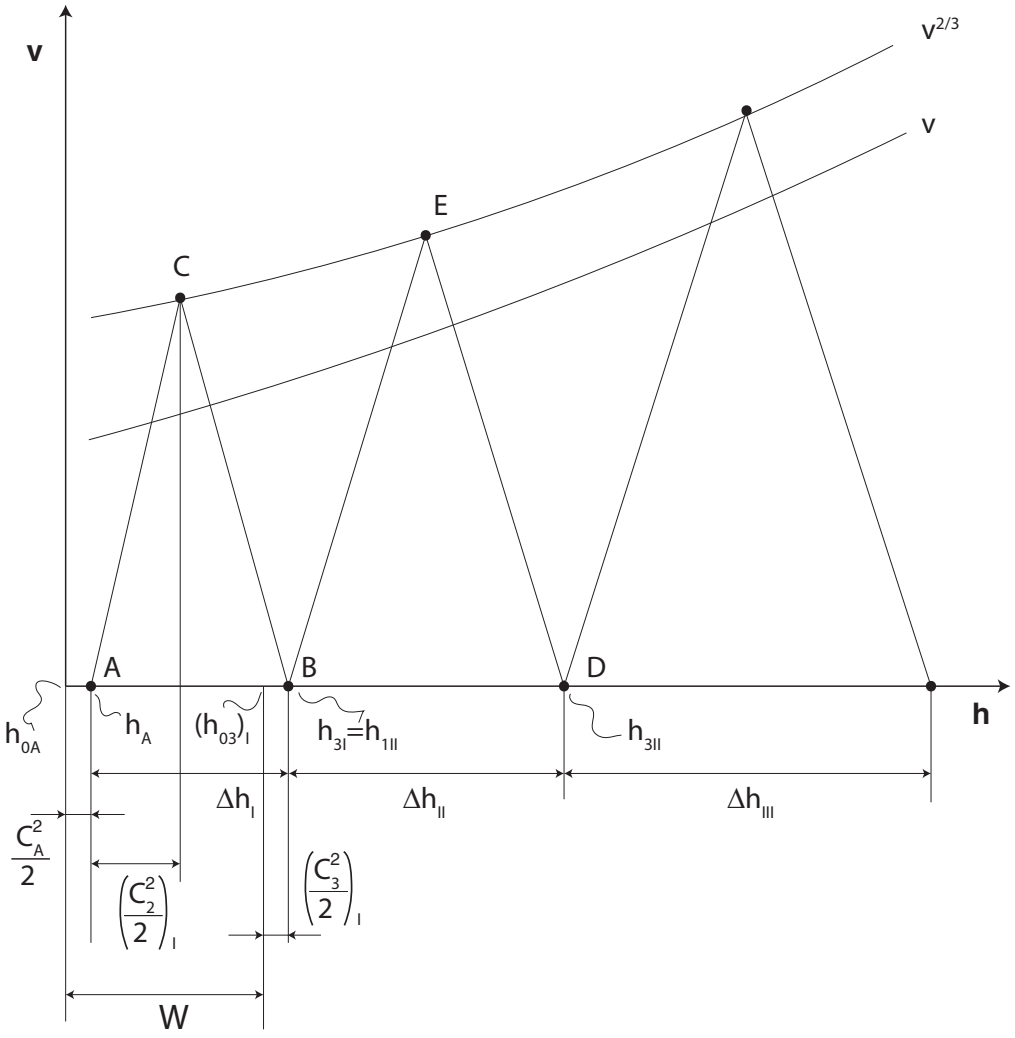

Figure 2.13: Enthalpy drop splitting and stage number determination according to the constant blade height to mean diameter ratio design criterion ($b_2/D_{m2} = constant$).

2.8.2 Constant blade root diameter design criterion

A constant blade root diameter (D_h) design

$$\boxed{D_h = constant} \tag{2.117}$$

is preferred in the medium-low pressure turbine section because it limits the mean diameter and the increase of the blade span in the final part of the expansion, even for dramatic specific volume variations.

Equation (2.105) is recast in the form

$$\Delta h = k_1 \omega^2 \frac{(D_h + b_2)^2}{4} = k_4 (D_h + b_2)^2 \tag{2.118}$$

being $U = \omega(D_h + b_2)/2$ and $k_4 = \Psi + 1/8(C_3^2/U^2 - C_1^2/U^2)\omega^2$

and Eq. (2.106) after some rearrangements leads to

$$v_2 = \frac{\zeta \pi \omega}{2\dot{m} X \tan \alpha_2} b_2 (D_h + b_2)^2 = k_5 b_2 (D_h + b_2)^2 \tag{2.119}$$

being $k_5 = (\zeta \pi \omega)/(2\dot{m} X \tan \alpha_2)$

Thus, Eqs. (2.118) and (2.119) give the fundamental relationship

$$\boxed{\frac{v_2}{\Delta h} = \frac{k_4}{k_5} b_2} \tag{2.120}$$

which states that the criterion of constant hub diameter (Eq. (2.117)) requires, in turn, that the ratio between the rotor inlet specific volume divided by the product between the stage enthalpy drop and the blade height be the same for all the stages (Eq. (2.120)).

Similarly to the procedure outlined in Section 2.8.1 it is necessary to suppose an expansion line in the h-s chart and to design in advance the first stage (hence $(b_2)_I$, k_4, k_5 are known and the triangle ABC may be drawn in Fig. 2.14). Then, a set of b_2 is chosen and the corresponding values of (i) Δh (Eq. (2.118)), (ii) v_2 (Eq. (2.119)) and (iii) h (from the supposed expansion line) are calculated. Accordingly, the function $\Delta h = f''(h)$ is

defined and triangles similar to ABC are identified along with the enthalpy drop of each stage (Δh_j).

The rotor inlet blade height $(b_2)_j$ of the j-th stage is calculated from Eq. (2.120)

$$(b_2)_j = \frac{(v_2/\Delta h)_j}{(v_2/\Delta h)_I}(b_2)_I \tag{2.121}$$

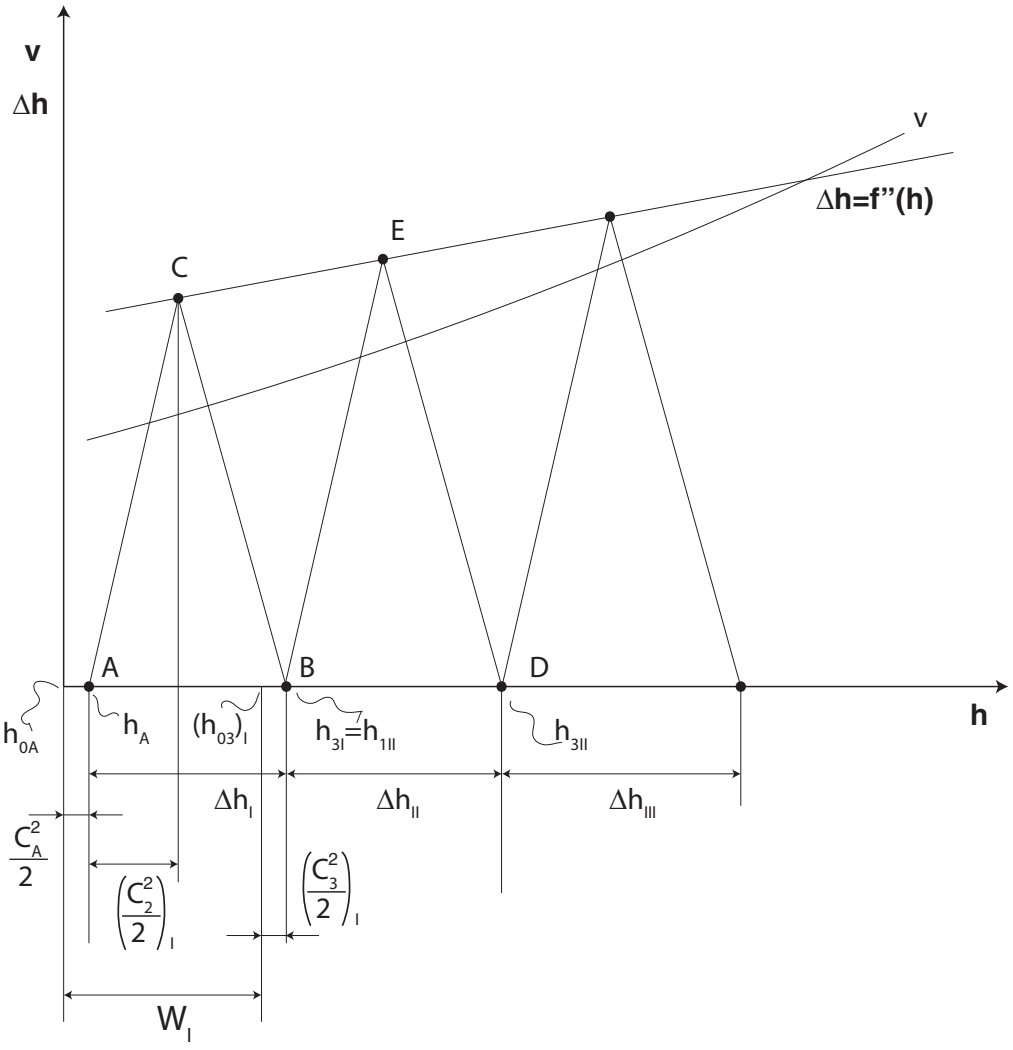

Figure 2.14: Enthalpy drop splitting and stage number determination according to the constant hub diameter design criterion ($D_h = constant$).

2.9 Stage efficiency charts

Efficiency charts correlate the achievable stage efficiency to the most significant design parameters. They are a very useful tool for the preliminary design because, starting from the optimum values of the design parameters, allow the determination of the optimum geometry. The well-known $\psi - \phi$ chart (also known as Smith chart) and the $n_s - d_s$ diagram (also known as Balje diagram) are analytically built here and the optimum intervals of the design parameters are identified.

2.9.1 Normal stage

When dealing with multistage axial flow turbines it is desirable to maintain similar mean velocity triangles in all stages. For this purpose (i) the axial velocity and (ii) the mean blade radius must remain constant and (iii) the flow angles at the outlet of each stage must be equal to those at the inlet. Obviously, as the density decreases during the expansion, requirement (i) implies the blade height must be continuously increased. So, the requirements for a normal (or repeating) stage are [29]

$$\boxed{C_m = const \qquad r = const \qquad \alpha_1 = \alpha_3} \tag{2.122}$$

It is noteworthy that the above conditions are the same adopted when dealing with the reaction stage (see Section 2.6). Despite these hypotheses unavoidably bring about a lack of generality, they allow to obtain simple relationships between the stage design parameters (ϕ, ψ, R) and the flow angles, as demonstrated below.

Due to the constant axial velocity assumption (Eq. (2.122)) the static enthalpy drop across the stator is

$$h_1 - h_2 = \frac{1}{2}(C_{t2}^2 - C_{t1}^2) = \frac{1}{2}C_m^2(\tan^2\alpha_2 - \tan^2\alpha_1) \tag{2.123}$$

and for $C_1 = C_3$ (consequence of $C_m = const.$ and $\alpha_1 = \alpha_3$)

$$h_1 - h_3 = h_{01} - h_{03} = \psi U^2 \tag{2.124}$$

By substituting Eqs. (2.123) and (2.124) into the definition of R (Eq. (2.14))

$$R = 1 - \frac{\phi^2}{2\Psi}(\tan^2 \alpha_2 - \tan^2 \alpha_3) \tag{2.125}$$

which, by the inclusion of Ψ from the non dimensional Euler equation (2.12) reduces to

$$R = 1 - \frac{\phi}{2}(\tan \alpha_2 + \tan \alpha_3) \tag{2.126}$$

The absolute flow angles may be expressed as function of the design parameters by means of Eqs. (2.12) and (2.126)

$$\boxed{\tan \alpha_3 = \frac{1 - R - \Psi/2}{\phi} \qquad \tan \alpha_2 = \frac{1 - R + \Psi/2}{\phi}} \tag{2.127}$$

Since the relative stagnation enthalpy is constant in the rotor and the axial velocity is assumed constant

$$h_2 - h_3 = \frac{1}{2}(W_{t3}^2 - W_{t2}^2) = \frac{1}{2}C_m^2(\tan^2 \beta_3 - \tan^2 \beta_2) \tag{2.128}$$

When Eqs. (2.128) and (2.124) are embedded in the definition of reaction (2.14), it results

$$R = \frac{\phi^2}{2\Psi}(\tan^2 \beta_3 - \tan^2 \beta_2) \tag{2.129}$$

Including Ψ from the non dimensional Euler equation (2.13) into Eq. (2.129) gives

$$R = -\frac{\phi}{2}(\tan \beta_3 + \tan \beta_2) \tag{2.130}$$

The relative flow angles may be expressed as function of the design parameters by means of Eqs. (2.130) and (2.13)

$$\boxed{\tan \beta_3 = -\frac{R + \Psi/2}{\phi} \qquad \tan \beta_2 = -\frac{R - \Psi/2}{\phi}} \tag{2.131}$$

Hence, all the flow angles ($\alpha_1 = \alpha_3, \alpha_2, \beta_2, \beta_3$) are determined for assigned design parameters (Ψ, ϕ, R) according to Eqs. (2.127) and (2.131). From a mathematical point of view, Eqs. (2.127) and (2.131) represent a system of four equations in seven variables, therefore any three of them may be specified and the remaining four calculated.

A remarkable result can be obtained by considering Eqs. (2.12) and (2.126)

$$\Psi = 2(1 - R - \phi \tan \alpha_3) \tag{2.132}$$

It shows that to obtain a high stage loading (Ψ), the reaction (R) should be low and the inter-stage swirl angle should be as large as possible.

2.9.2 $\Psi - \phi$ efficiency charts

This Section is aimed at deriving a relationship between the stage total-to-total efficiency (η_{tt}) or total-to-static efficiency (η_{ts}) and the design parameters (Ψ, ϕ and R).

Figure 2.15 shows an irreversible expansion in the enthalpy-entropy plane (states 1 to 3) and the corresponding notation .

The total-to-total efficiency is

$$\eta_{tt} = \frac{h_{01} - h_{03}}{h_{01} - h_{03ss}} \tag{2.133}$$

which can be conveniently rearranged in the form

$$\frac{1}{\eta_{tt}} - 1 = \frac{h_{03} - h_{03ss}}{h_{01} - h_{03}} = \frac{h_3 - h_{3ss}}{\mathcal{W}} + \frac{C_3^2 - C_{3ss}^2}{2\mathcal{W}} \tag{2.134}$$

and

$$\frac{1}{\eta_{tt}} - 1 = \frac{(h_3 - h_{3s}) + (h_{3s} - h_{3ss})}{\mathcal{W}} + \left(1 - \frac{C_{3ss}^2}{C_3^2}\right) \frac{C_3^2}{2\mathcal{W}} \tag{2.135}$$

As the rotor loss coefficient is

$$\zeta_R = \frac{h_3 - h_{3s}}{\frac{1}{2} W_3^2} \tag{2.136}$$

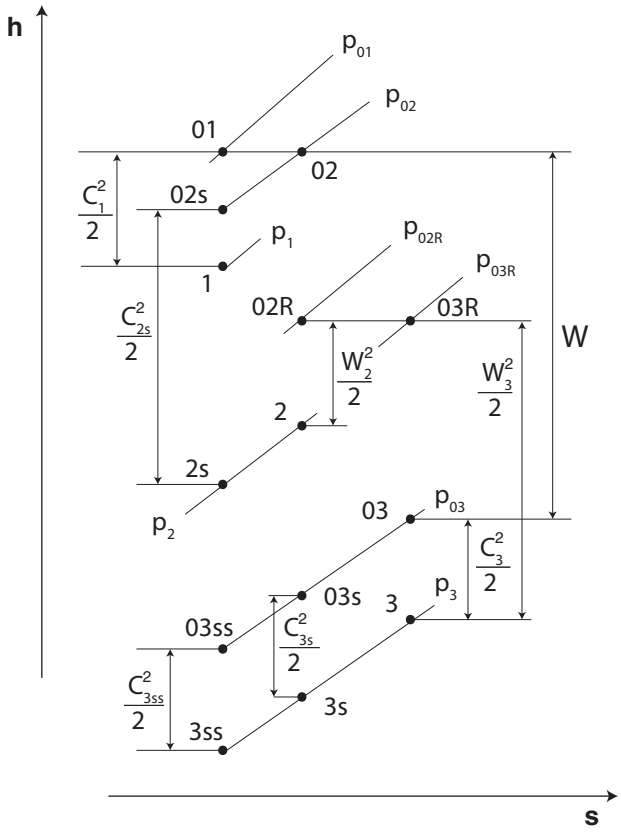

Figure 2.15: Thermodynamic states for expansion across an axial turbine stage.

it follows

$$h_3 - h_{3s} = \frac{1}{2}\zeta_R W_3^2 \tag{2.137}$$

By integrating the Gibbs equation ($Tds = dh - vdp$) along the isobar p_3 from state $3ss$ to $3s$ and, similarly, along the isobar p_2 from state $2s$ to 2 the relationships

$$s_2 - s_1 = c_P \ln \frac{T_{3s}}{T_{3ss}} \tag{2.138}$$

$$s_2 - s_1 = c_P \ln \frac{T_2}{T_{2s}} \tag{2.139}$$

are found. They lead to

$$\frac{T_{3s}}{T_{3ss}} = \frac{T_2}{T_{2s}} \tag{2.140}$$

and, after subtracting one from each side and multiplying by c_P

$$h_{3s} - h_{3ss} = \frac{T_{3ss}}{T_{2s}}(h_2 - h_{2s}) \tag{2.141}$$

Introducing the nozzle loss coefficient ζ_N

$$\zeta_N = \frac{h_2 - h_{2s}}{\frac{1}{2}C_2^2} \tag{2.142}$$

it follows

$$h_{3s} - h_{3ss} = \frac{T_{3ss}}{T_{2s}}\frac{1}{2}\zeta_N C_2^2 \tag{2.143}$$

Finally, by substituting the enthalpy differences from Eqs. (2.137) and (2.143) into Eq. (2.135) and considering $T_{3ss}/T_{2s} = T_{3s}/T_2$ (Eq. (2.140)) and $C_{3ss}^2/C_3^2 = T_{3ss}/T_3$ (being $M_3 = M_{3ss}$), the expression of the efficiency becomes

$$\frac{1}{\eta_{tt}} - 1 = \frac{1}{2\mathcal{W}}\left(\zeta_R W_3^2 + \frac{T_{3s}}{T_2}\zeta_N C_2^2 + \left(1 - \frac{T_{3ss}}{T_3}\right) C_3^2\right) \tag{2.144}$$

Equation (2.144) is frequently simplified in the form

$$\frac{1}{\eta_{tt}} - 1 = \frac{1}{2\mathcal{W}}\left(\zeta_R W_3^2 + \zeta_N C_2^2\right) \tag{2.145}$$

Moreover, since $C_m = W_3 \cos\beta_3 = C_2 \cos\alpha_2 = C_3 \cos\alpha_3$, Eq. (2.144) and its approximated version Eq. (2.145) are equivalent to

$$\frac{1}{\eta_{tt}} - 1 = \frac{\phi^2}{2\Psi}\left(\frac{\zeta_R}{\cos^2\beta_3} + \frac{T_{3s}}{T_2}\frac{\zeta_N}{\cos^2\alpha_2} + \left(1 - \frac{T_{3ss}}{T_3}\right)\frac{1}{\cos^2\alpha_3}\right) \tag{2.146}$$

and

$$\frac{1}{\eta_{tt}} - 1 = \frac{\phi^2}{2\Psi}\left(\frac{\zeta_R}{\cos^2\beta_3} + \frac{\zeta_N}{\cos^2\alpha_2}\right) \tag{2.147}$$

Recalling the fundamental trigonometric identity

$$\cos^2 x = \frac{1}{1 + \tan^2 x} \tag{2.148}$$

Eqs. (2.127) and (2.131) provide

$$\cos^2\alpha_2 = \frac{\phi^2}{\phi^2 + (1 - R + \Psi/2)^2} \qquad \cos^2\beta_3 = \frac{\phi^2}{\phi^2 + (R + \Psi/2)^2} \tag{2.149}$$

hence, Eq. (2.147) can be recast as

$$\boxed{\eta_{tt} = \left(1 + \frac{\phi^2}{2\Psi}\left(\frac{\zeta_R}{\frac{\phi^2}{\phi^2+(R+\Psi/2)^2}} + \frac{\zeta_N}{\frac{\phi^2}{\phi^2+(1-R+\Psi/2)^2}}\right)\right)^{-1}} \tag{2.150}$$

Equation (2.150) represents a notable result because it establishes a direct relationship between the shape of the velocity triangles (represented by the triplet $\Psi - \phi - R$) and the efficiency.

Assuming the loss coefficients are constant when varying ϕ and Ψ the optimum loading coefficient Ψ_{opt} is given by

$$\Psi_{opt} = 2\left(\frac{\phi^2 + R^2 + \zeta_N/\zeta_R(\phi^2 + (1-R)^2)}{1 + \zeta_N/\zeta_R}\right)^{0.5} \tag{2.151}$$

Figure 2.16 plots Eqs. (2.150) and (2.151) for $R = 0.5$ and $\zeta_N = \zeta_R = 0.09$. The iso efficiency lines pattern depends on the shape of the velocity triangles, which, in turn, are determined by Ψ, ϕ and R. The irreversibilities are accounted by the loss coefficients ζ_N and ζ_R. They depend essentially on the amount of turning, but their influence on the

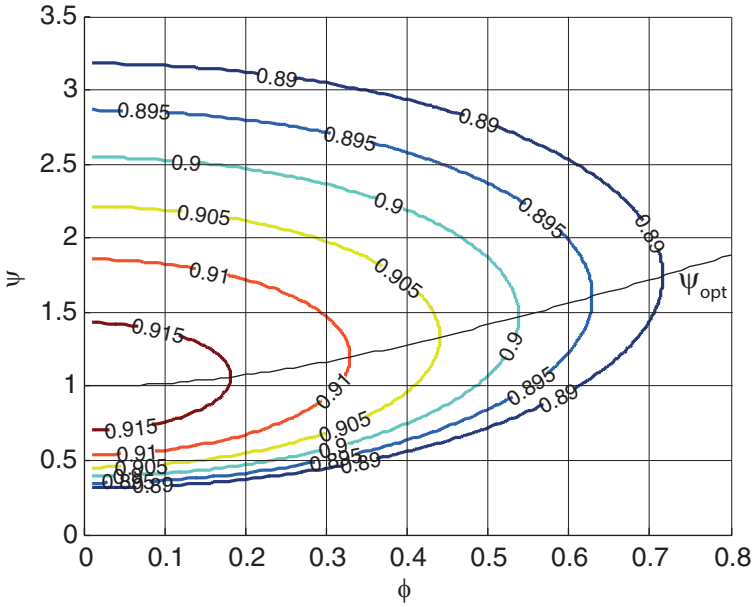

Figure 2.16: Total-to-total efficiency for a $R = 0.5$ normal stage with $\zeta_N = \zeta_R = 0.09$. Line of optimum loading coefficients is also shown.

shape of the efficiency contours is not as important as the influence of the flow angles. This claim can be easily verified by including the actual loss coefficient evaluated by Soderberg correlation [29]. Soderberg loss correlation is extremely simple, because the ζ loss coefficient depends only on the flow turning ϵ (angles are in degrees)

$$\zeta = 0.04 + 0.06\,(\epsilon/100)^2 \tag{2.152}$$

Equation (2.152) refers to a blade height-to-axial chord ratio equal to 3 and Reynolds number equal to 10^5. The resulting total-to-total stage efficiency (Eq. (2.150)) is visualized in Fig. 2.17 for $R = 0$ and $R = 0.5$. It indicates that for a stage with $R = 0.5$ maximum total-to-total efficiency corresponds to loading and flow coefficients rather low. Higher loading coefficients and, in turn, higher specific works can be achieved with acceptable efficiency by stages having $R = 0$.

It is also possible to obtain analogous relationships for the total-to-

static efficiency. In particular, similarly to Eqs. (2.144) and (2.145) the exact and approximate estimations of the total-to-static efficiency are

$$\frac{1}{\eta_{ts}} - 1 = \frac{1}{2\mathcal{W}} \left(\zeta_R W_3^2 + \frac{T_{3s}}{T_2} \zeta_N C_2^2 + C_3^2 \right) \tag{2.153}$$

$$\frac{1}{\eta_{ts}} - 1 = \frac{1}{2\mathcal{W}} \left(\zeta_R W_3^2 + \zeta_N C_2^2 + C_3^2 \right) \tag{2.154}$$

Equation (2.154) is recast as

$$\boxed{\eta_{ts} = \left(1 + \frac{\phi^2}{2\Psi} \left(\frac{\zeta_R}{\frac{\phi^2}{\phi^2+(R+\Psi/2)^2}} + \frac{\zeta_N}{\frac{\phi^2}{\phi^2+(1-R+\Psi/2)^2}} + \frac{1}{\frac{\phi^2}{\phi^2+(1-R-\Psi/2)^2}} \right) \right)^{-1}} \tag{2.155}$$

It shows that the maximum η_{ts} are achieved at $\Psi = 2$ and $\Psi = 1$ for $R = 0$ and $R = 0.5$, respectively. Both these configurations (i.e., $\Psi = 2$, $R = 0$ and $\Psi = 1$, $R = 0.5$) correspond to axial flow discharge.

In brief, the previous outcomes suggest the following design guidelines.

- In the design of a single stage turbine the criterion is to maximize the total-to-static efficiency and to choose a reaction ≈ 0 to ensure high loading coefficients and, in turn, high specific work. Moreover, $R \approx 0$ allows the turbine partialization in off design operation.

- In the design of an intermediate stage, two different criteria might be considered. The first is the maximization of the total-to-total efficiency by means of symmetrical blade rows and with a not too low (to avoid high stage number) loading coefficient. Accordingly, stages with $R = 0.5$ and $\Psi \approx 1$ are selected. The second is the limitation of the stage number. Consequently, higher loading and flow coefficient are chosen ($\Psi = 1.2 - 2.5$ and $\phi = 0.6 - 1$) having reaction lower than 0.5.

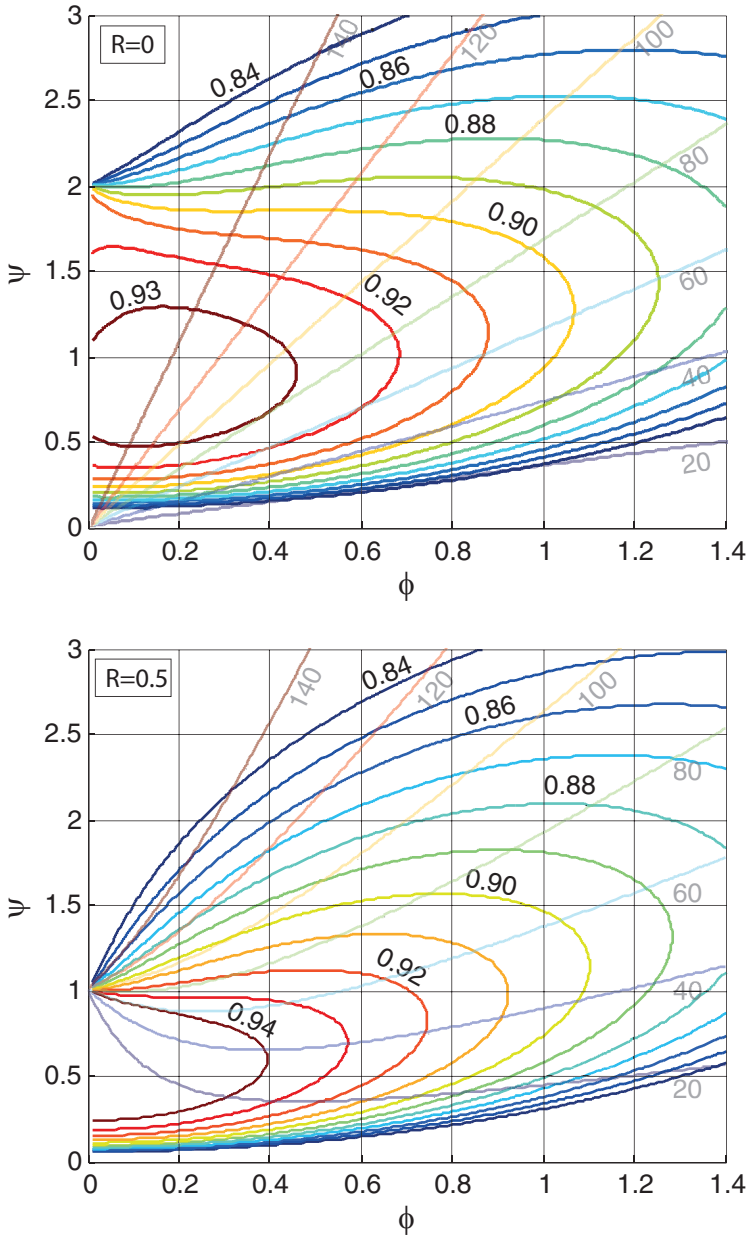

Figure 2.17: Total-to-total efficiency (Eq. (2.150)) for a normal stage with 0 and 0.50 reaction. Loss coefficients ζ_N and ζ_R are estimated by Soderberg correlation (Eq. (2.152)). Rotor turnings are shown with opaque lines.

2.9.3 $n_s - d_s$ diagram

This Section summarizes the procedure developed by Balje [35] to build the specific speed (n_s) - specific diameter (d_s) efficiency diagram for axial turbine stage.

The aim of the procedure is the determination of the optimum geometry and, in turn, the maximum efficiency of an axial turbine stage, for given specific speed and specific diameter. The estimation of the losses across the expansion uses a simplified version of the boundary layer theory and empirical relationships (see [35]). Model variables can be classified in two groups: (i) fixed level input variables (Table 2.2) and (ii) optimizing variables (Table 2.3). The fixed level input variables are kept constant and are not optimized, because the efficiency is a monotonic function of each of these variables. Instead, the optimizing variables are geometric ratios or angles which may be chosen independently in order to maximize the efficiency. Obviously each optimizing variable is varied within an upper and lower limit imposed by technical or physical feasibility considerations.

Table 2.2: Fixed level variables.

α_1	90
k_I	1
$\frac{t_{bN}}{h}$	0.02
$\frac{t_{bR}}{h}$	0.02
$\frac{s}{h}$	0.02
$\frac{\Delta}{D}$	0.02

Figure 2.18 shows the stations nomenclature and the meridional channel geometry: a constant nozzle and rotor blade height (h) is assumed. Figure 2.19 shows the expansion in the h-s diagram and the corresponding notation.

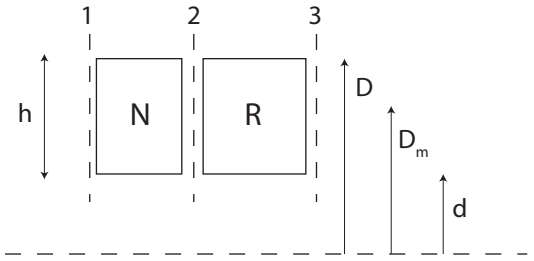

Figure 2.18: Stations nomenclature and meridional channel geometry.

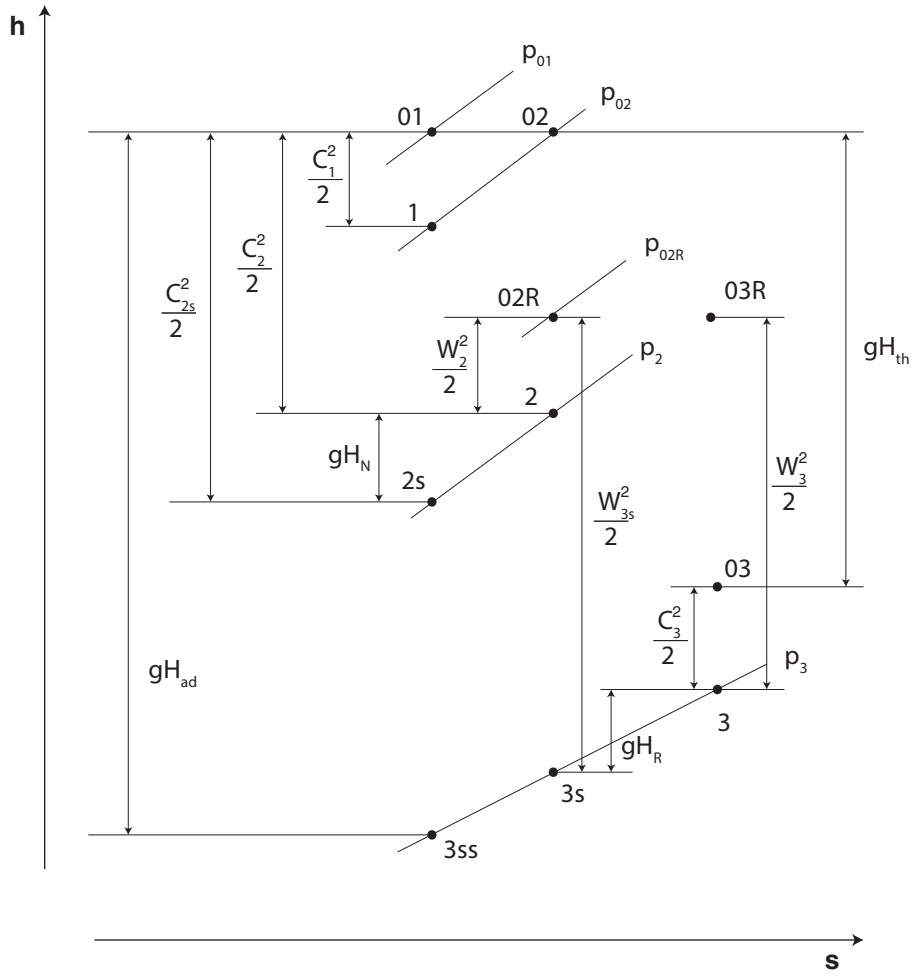

Figure 2.19: Thermodynamic states of the expansion across an axial turbine stage.

Table 2.3: Optimizing variables and their upper and lower bounds.

	min value	max value
α_2	15	60
β_3	5	90
$\frac{h}{D}$	0.0001	0.35
$\frac{c_N}{D}$	0.02	0.35
$\frac{c_R}{D}$	0.02	0.35

Some fundamental hypotheses should be explicitly stated before illustrating the procedure: (i) all the stage designs collected in the chart have the same Reynolds flow regime; (ii) working fluid density does not vary across the rotor, thus, compressibility effects are not accounted for.

The procedure can be summarized in the following steps:

1. Choice of a $n_s - d_s$ couple and choice of a first set of guess values of the optimizing variables.

2. Calculation of the flow factor ϕ_3

$$\phi_3 = \frac{c_{m3}}{u_p} = \frac{2}{\pi}\frac{1}{n_s d_s^3}\frac{1}{\delta(1-\delta)^{0.5}} \tag{2.156}$$

   where $\delta = h/D(1 - h/D)$.

3. Calculation of the real relative rotor outlet flow angle β_{3e} accounting for the deviation due to clearance losses

$$\beta_{3e} = \beta_3 + \Delta\beta_{cl} \tag{2.157}$$

   and of the absolute rotor outlet flow angle α_3

$$\alpha_3 = \arctan\left(\frac{1}{\cot\beta_{3e} - \frac{1}{\phi_3}}\right) \tag{2.158}$$

   Note that, angles β_2, β_3 and α_3 are accounted from the opposite direction of the peripheral speed, whereas α_2 is accounted from the same direction of the peripheral speed.

4. Calculation of the theoretical head coefficient q_{th}:

$$q_{th} = \frac{gH_{th}}{u_p^2} = \phi_3(k_I \cot\alpha_2 + \cot\alpha_3) \tag{2.159}$$

gH_{th} is the real total-to-static enthalpy drop. As reported in Table 2.2 $k_I = C_{m2}/C_{m3} = 1$.

5. Calculation of the nozzle loss coefficient q_N:

$$q_N = \frac{gH_N}{u_p^2} = \frac{1}{2}\left(\frac{\zeta_N}{1-\zeta_N}\right)\left(\frac{k_I\phi_3}{\sin\alpha_2}\right)^2 \tag{2.160}$$

where the term gH_N denotes the difference between the nozzle outlet static enthalpy (h_2) and the nozzle outlet isentropic static enthalpy (h_{2s}). The nozzle loss coefficient ζ_N is

$$\zeta_N = \frac{h_2 - h_{2s}}{\frac{C_{2s}^2}{2}} = \frac{gH_N}{\frac{c_{2s}^2}{2}} = \frac{gH_N}{\frac{C_2^2}{2} + gH_N} \tag{2.161}$$

6. Calculation of the rotor loss coefficient q_R:

$$q_R = \frac{gH_R}{u_p^2} = \frac{1}{2}\left(\frac{\zeta_R}{1-\zeta_R}\right)\left(\frac{\phi_3}{\sin\beta_{3e}}\right)^2 \tag{2.162}$$

where the term gH_R denotes the difference between the rotor outlet static enthalpy (h_3) and the rotor outlet isentropic static enthalpy (h_{3s}). The rotor loss coefficient ζ_R is

$$\zeta_R = \frac{h_3 - h_{3s}}{\frac{w_{3s}^2}{2}} = \frac{gH_R}{\frac{w_{3s}^2}{2}} = \frac{gH_R}{\frac{W_3^2}{2} + gH_R} \tag{2.163}$$

7. Calculation of the kinetic energy loss coefficient q_{ex}:

$$q_{ex} = \frac{C_3^2/2}{u_p^2} = \frac{1}{2}\left(\frac{\phi_3}{\sin\alpha_3}\right)^2 \tag{2.164}$$

8. Calculation of the disk friction loss coefficient q_d:

$$q_d = \frac{C_d\,(1-2h/D)^5}{8\pi\delta\phi_3} \tag{2.165}$$

where C_d is the disk friction coefficient.

9. Calculation of the adiabatic head coefficient q_{ad} in two different ways:

$$q_{ad1} = \frac{gH_{ad}}{u_p^2} = q_{th} + q_N + q_R + q_{ex} \tag{2.166}$$

where gH_{ad} is the isentropic total-to-static enthalpy drop.

$$q_{ad2} = \frac{gH_{ad}}{u_p^2} = \frac{4}{n_s^2 d_s^2} \frac{1}{1-2\delta} \tag{2.167}$$

gH_{ad} is the isentropic total-to-static enthalpy drop. Generally, the first guess set of the optimizing variables will result in different values of the head coefficient q_{ad} (Eqs. (2.166) and (2.167)), because the optimizing variables do not simultaneously satisfy the continuity equation. Thus, a constraint which ensure the equality of the two expression of q_{ad} must be implemented in the model (see point 12 below).

10. Evaluation of the total-to-static efficiency:

$$\eta_{ts} = \frac{h_{01} - h_{03}}{h_{01} - h_{3ss}} = \frac{q_{th} - q_d}{q_{ad1}} \tag{2.168}$$

11. Calculation of the nozzle and rotor Reynolds numbers

$$Re_N = \frac{l_N C_2}{\nu_3} \tag{2.169}$$

$$Re_R = \frac{l_R W_3}{\nu_3} \tag{2.170}$$

where l is the camberline length.

12. Evaluation of the function (s) to be minimized

$$s = 1 - \eta + P_N + P_R + P_q \tag{2.171}$$

where

$$P_N = \begin{cases} 0 & \text{if } Re_N \geq 4 \times 10^4 \\ 10^{-8}(4 \times 10^4 - Re_N)^2 & \text{if } Re_N < 4 \times 10^4 \end{cases}$$

$$P_R = \begin{cases} 0 & \text{if } Re_R \geq 4 \times 10^4 \\ 10^{-8}(4 \times 10^4 - Re_R)^2 & \text{if } Re_R < 4 \times 10^4 \end{cases}$$

$$P_q = 10 \left(\frac{q_{ad_{max}}}{q_{ad_{min}}} \right)^2 \tag{2.172}$$

The functions P are "penalty functions" which are added to the objective function (i.e., $1-\eta$) to embed the constraints in the objective function. These constraints are used here (i) to avoid flow regimes with a low Reynolds number ($Re < 4 \times 10^4$) in which the loss equations cannot provide reliable estimations; (ii) to close iteration loops (equality of the two expression of q_{ad}).

13. Update of the optimizing variables and new evaluation of the function s until the minimum is found.

14. Calculation of the dependent variables degree of reaction (R) and blade number (Z):

$$R = \frac{gH_{ad} - (gH_N + C_2^2/2)}{gH_{ad}} = 1 - \frac{q_N}{q_{ad}} - \frac{\left(\frac{k_I \phi_p}{\sin \alpha_2}\right)^2}{2q_{ad}} \tag{2.173}$$

$$Z_N = \frac{\pi(1-2\delta)^{0.5}}{\frac{c_N}{D}\left(\frac{t}{c}\right)_N} \tag{2.174}$$

$$Z_R = \frac{\pi(1-2\delta)^{0.5}}{\frac{c_R}{D}\left(\frac{t}{c}\right)_R} \tag{2.175}$$

The resulting specific speed - specific diameter efficiency diagram for an axial turbine stage is shown in Fig. 2.20. It highlights that the optimum specific speed and specific diameter intervals are

$$\boxed{n_s = 0.45 - 1.8} \tag{2.176}$$

$$\boxed{d_s = 2 - 4} \tag{2.177}$$

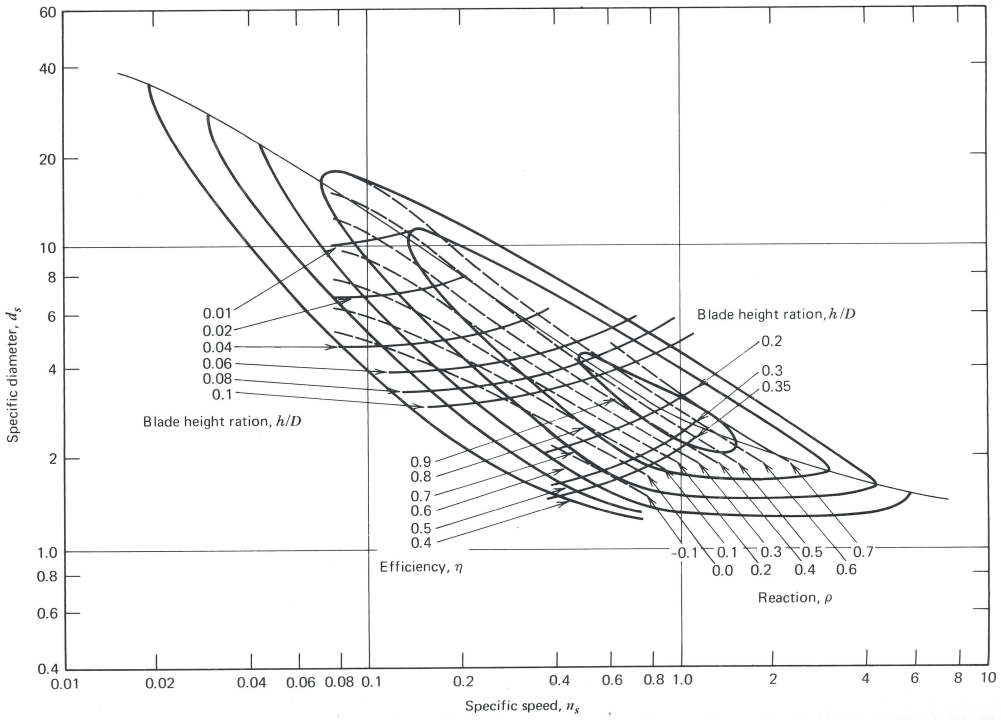

Figure 2.20: Total-to-static efficiency diagram for an axial stage (from [23]).

Chapter 3

Flow similarity of turbines handling non traditional fluids

The very first step of the basic design of a turbomachine is to determine shape, diameter and rotating speed which fulfill the main design specifications (i.e., at least, flow rate and available specific work) while keeping the highest efficiency. The use of similarity laws simplifies this problem and allows to extend the results obtained on a machine to another one of the same shape. The dimensional analysis can be used to deduce the similarity laws: it reduces the number of variables influencing the turbomachine behavior by grouping them in dimensionless products.

It is demonstrated that the efficiency of a specific turbine type (i.e., of fixed shape) driven by a real gas depends on seven dimensionless variables (specific speed, specific diameter, technological parameter, Mach number, Reynolds number, fundamental derivative of gas dynamics and compressibility factor) that is, the equivalence of these variables ensures the achievement of full flow similarity (Section 3.1).

Then, some rearrangements of the similarity parameters and approximations are introduced in order to obtain a functional relationship which is more useful when facing turbine design and performance estimation prob-

lems in the wider context of the whole ORC system optimization and less dependent on the fluid nature (Section 3.2). The final result shows that the maximum efficiency achievable by turbines of optimized shape can be correlated to the so-called "size parameter" and volumetric flow ratio. A map collecting turbine efficiency data in this form can be conveniently embedded in optimization tools of an ORC power cycle.

Finally, real data of radial inflow turbines operating with air are used to build the corresponding size parameter - volumetric flow ratio efficiency map (Section 3.3).

3.1 Full flow similarity for turbines of very different size handling real gas

The basic approach used in the following to group the relevant design and operation variables into dimensionless parameters well suited to solve the design problem is an extension of the similarity approach suggested by Balje [23].

It is observed that the variables which strongly affect the net power (P) of a turbine handling a *real* compressible medium can be collected in the following categories:

1. *Turbomachine size*: outer diameter of the turbine runner/wheel (d);

2. *Turbomachine stage arrangement*: number of stages (n);

3. *Turbomachine stages shape*: blade height (B_n), chord (l_n) and all the geometric variables which, along with the diameter, define the shape of each turbomachine stage and the arrangement of its components. These variables can be divided by the outer diameter d to obtain a series of dimensionless ratios that are independent from both the manufacturing technology and the size of the turbine, and can be

collected in a m*n-length vector $(B_1/d, B_2/d, ..., B_n/d, l_1/d, l_2/d, ..., l_n/d, ..., l_{m1}/d, l_{m2}/d, ..., l_{mn}/d)$;

4. *Technological features*: surface roughness (ϵ), leading and trailing edge thicknesses (t_l, t_e), blade clearance (δ) etc., i.e., all the details not considered in item 3 but required to define rigorously the real geometry of the turbine. As per the turbine shape variables, all these geometrical variables can be collected in the r-length vector $\bar{\epsilon} = (\epsilon, t_l, t_e, \delta, ..., t_r)$. It is assumed here that all the $\bar{\epsilon}$ components are known when the value of one of them is defined. This is because at a first approximation, for a given manufacturing process all these variables keep the same proportion to each other being not affected by number and relative size of the turbine stages. The reason why the geometrical variables are split into shape and technological variables is that the same shape can be obtained by a different technology depending on size and/or manufacturing costs.

5. *Turbomachine control variables*: mass flow rate ($\dot{m}$) and angular speed (ω). The multi-shaft arrangement is not considered here as a practical issue for present ORC turbines application;

6. *Plant/thermodynamic variables*: available specific work (Δh_{0s}), total speed of sound at turbine inlet (a_{01}) and isentropic mass density at turbine outlet (ρ_{2s}).

7. *Molecular properties of the working fluid*: kinematic viscosity (ν), compressibility factor (Z) and isentropic variation of the sound speed against the gas mass density ($(\partial a_{01}/\partial \rho)_s$). Both the last two terms are needed to account for deviations from the perfect gas behavior. In particular, Z is related to the force between two adjacent molecules as function of the distance between their centers (being repulsive when the distance is small - i.e., $Z > 1$ - and attractive when the

distance is high - i.e., $Z < 1$) [36], whereas $(\partial a_{01}/\partial\rho)_s$ fully describes the behavior of a compressible gas [37].

Thus, the net power of any turbine type (fully described by the stages number and dimensionless vector introduced in item 3) can be expressed as

$$P = f\left\{d, \bar{\epsilon}, \dot{m}, \omega, \Delta h_{0s}, a_{01}, \rho_{2s}, \nu, (\partial a_{01}/\rho)_s, Z\right\} \tag{3.1}$$

The Buckingham's (or Π) theorem [38] applied to the present physical system that involves 3 fundamental dimensions (i.e., length, mass and time, being the heat transfer processes neglected) states that the thermo-fluid dynamics of a turbine at steady state operation is fully described by 7 dimensionless groups.

The design specifications Δh_{0s}, $\dot{m}$ and mass density at turbine discharge ρ_{2s} are the three "repeating variables" chosen here to fulfill the requirements stated in [38] for the repeating variables and obtain the following dimensionless form of Eq. (3.1)

$$\Pi_0 = f\left\{\Pi_1, \Pi_2, \Pi_3, \Pi_4^I, \Pi_5, \Pi_6, \Pi_7\right\} \tag{3.2}$$

where Π_0 to Π_3 groups in Eq. (3.2) write

$$\Pi_0 = \frac{P}{\dot{m}\Delta h_{0s}} = \eta \quad \Pi_1 = \omega\frac{(\dot{m}/\rho_{2s})^{0.5}}{\Delta h_{0s}^{0.75}} = n_s \quad \Pi_2 = d\frac{\Delta h_{0s}^{0.25}}{(\dot{m}/\rho_{2s})^{0.5}} = d_s$$
$$\Pi_3 = \frac{\epsilon\Delta h_{0s}^{0.25}}{(\dot{m}/\rho_{2s})^{0.5}} = \tau \tag{3.3}$$

The first three parameters in Eqs. (3.3) are the turbine efficiency (η), specific speed (n_s) and diameter (d_s), respectively. Note that n_s and d_s appear explicitly here because of the choice made for the repeating variables. Other choices are suggested in the literature in the study of turbomachine operation, where, in addition to ρ_{2s}, the rotational speed and volumetric

flow rate usually replace Δh_{0s} and $\dot{m}$, being the former two "fixed constraints" [39]. The group Π_3 is strictly related to the capability of the machine tools to reach a high quality (i.e., low roughness ϵ) of the surface for a given "size" of the machine. Accordingly, in the following it will be referred to as "technological parameter" (τ).

The remaining dimensionless groups in Eq. (3.2) are

$$\Pi_4^I = \frac{a_{01}}{\Delta h_{0s}^{0.5}} \quad \Pi_5 = \frac{\nu}{\Delta h_{0s}^{0.25}(\dot{m}/\rho_{2s})^{0.5}} \quad \Pi_6 = \left(\frac{\partial a_{01}}{\partial \rho}\right)_s \frac{\rho_{2s}}{\Delta h_{0s}^{0.5}} \quad \Pi_7 = Z \tag{3.4}$$

Note that the choice made here for the repeating variables is straightforward in the design of turbomachines.

The dimensionless groups can be recast in alternative groups obtained by combinations of product of powers of the original Π_i, as stated by Buckingham [38]. Thus, a recast of some of the previous Π_i terms is presented in the following to obtain other dimensionless groups commonly used in turbomachines design practice.

In particular, being

$$\Pi_4^I = \Pi_1 \Pi_2 \left(\frac{\omega d}{a_{01}}\right)^{-1} \tag{3.5}$$

Π_4^I can be replaced by the machine Mach number (Ma), i.e.,

$$\Pi_4^I = \frac{\omega d}{a_{01}} = Ma \tag{3.6}$$

In a similar manner

$$\Pi_5 = \Pi_1 \Pi_2^2 \left(\frac{\omega d^2}{\nu}\right)^{-1} \tag{3.7}$$

and Π_5 can be replaced by the machine Reynolds number (Re), i.e.,

$$\Pi_5 = \frac{\omega d^2}{\nu} = Re \tag{3.8}$$

Finally, Π_6 can be replaced by

$$\Gamma = 1 + \Pi_6 = 1 + \frac{\rho_{2s}}{a_{01}} \left(\frac{\partial a_{01}}{\partial \rho} \right)_s \tag{3.9}$$

to make explicit the dependence of efficiency on the so-called fundamental derivative of gas dynamics (Γ) [37].

Thus, each turbine type handling a *real* gas and featuring a given "technological parameter" (τ) achieves the maximum value of efficiency (η^*) for a specific pair (n_s, d_s), and for the corresponding values of the machine Mach number (Ma^*) and machine Reynolds number (Re^*), i.e.,

$$\eta^* = f\left\{n_s, d_s, \tau, Ma^*, Re^*, \Gamma, Z\right\} \tag{3.10}$$

where the superscript * stands for value at best efficiency operation.

Note that Eq. (3.10) is the result of a problem formulation that is more general than the original one suggested by Balje [23] and most suited to the study of organic fluid turbines. In fact, Balje [23]

- assumes the gas is perfect ($Z = 1$ and $\Gamma = (\gamma + 1)/2$) and incompressible ($Ma = 0$);
- fixes the "technological parameter" by choosing defined values for the $\bar{\epsilon}$ vector components-to-diameter ratio;
- fixes a lower limit for the camberline Reynolds number ($Re > 4 \times 10^4$) and does not take into account the effect of Re on the loss coefficients, i.e., Re effect is neglected.

If the space of the ORC turbines is restricted to machines featuring optimized specific speed and diameter, (i.e., to the best machine designs), Eq. (3.10) becomes

$$\eta^* = f\left\{\tau, Ma^*, Re^*, \Gamma, Z\right\} \tag{3.11}$$

3.2 Rationale of the performance maps "Size Parameter (SP)-Volumetric Flow Ratio (VR)"

Equation (3.11) clearly states that two turbines of the same type are characterized by similar flow conditions and, in turn, same efficiencies if *all* the variables in its right-hand-side are equal. However, some rearrangements and approximations can be made in order to obtain a functional relationship which is (i) more practical when facing turbine design and performance estimation problems in the wider context of the optimization of the thermodynamic cycle in which the turbine is placed and (ii) less dependent on the fluid nature. Each of the following Sections introduces a modification in the full flow similarity relationship deduced in Section 3.1 till the achievement of the functional form used in the efficiency charts presented in Chapter 5.

3.2.1 Scale effect: the role of the size parameter

It has already been observed in Section 3.1 that the technological features influence the machine performance and the achievement of similar flow conditions requires that the technological parameter in Eq. (3.11) is constant.

However, when a machine shape is scaled the technological features cannot scale with the same ratio due to manufacturing and technical constraints, causing a departure from similar flow conditions. For instance, as most machines are manufactured with the same techniques (e.g., casting) or the same machine tools, wall roughness ϵ is typically of the same order of magnitude. So, absolute roughness is approximately constant and relative roughness tends to decrease with the machine actual size. Further, the radial clearance to blade span ratio is higher in smaller machines because

it is technically unfeasible to realize clearances lower than a limiting value and the contact between rotating parts and casing must be avoided in any case (thermal expansion of materials have to be carefully taken into account). Moreover, some parts (e.g., blades tips) have a minimum thickness imposed by stress considerations and/or production technique.

For all the above reasons, the technological parameter τ cannot be neglected especially when turbines of considerably different size are analyzed. The technological parameter can be written as

$$\tau = \frac{\epsilon}{SP} \tag{3.12}$$

where

$$SP = \frac{\dot{V}_{2s}^{0.5}}{\Delta h_{0s}^{0.25}} \tag{3.13}$$

stands for the size parameter firstly introduced by Macchi and Perdichizzi [24] to quantify the size of the machine in terms of the design specifications, Δh_{0s} and $\dot{V}_{2s}$. They calculated up to 9% efficiency drop for axial-flow turbines handling organic fluids passing from SP=0.20 to 0.0.01 m.

The manufacturing technology fixes the quality level of the technological features (see item 4 of Section 3.1). Accordingly, when a machine type is scaled down below a certain size a drop in the maximum efficiency appears. On the other hand, the continuous decrease of the technological parameter expected for machines of increasing size does not result in a corresponding continuous increase of the efficiency, once the technological features have reached their optimum level. This behavior of turbine efficiency (and performance) is commonly referred to in the literature as "scale effect" [40].

However, since the technological level fixes (at least at a first approximation) the minimum value of $\bar{\epsilon}$ vector components (see item 4 in Section 3.1), the ratio $\tau = \epsilon/SP$ that ensures the maximum turbine efficiency is defined once SP is fixed. Accordingly, the dimensionless implicit expression of maximum efficiency achievable by turbines of optimized shape

previously reported in Eq. (3.11) can also be written as

$$\eta^* = f\left\{SP, Ma^*, Re^*, \Gamma, Z\right\} \tag{3.14}$$

The advantage of this simplification is made clear in the more general framework of the thermodynamic system optimization procedures aimed at finding the best cycle parameters for the exploitation of a given heat source. In fact, since the size parameter can be calculated from variables which are obtained by the thermodynamic system optimization procedures it allows to directly take into account the size effect affecting the turbine component even during the optimization of the whole system. Note that the use of a dimensional variable alongside dimensionless similarity variables does not weaken the rigorousness of the approach but emphasizes the size parameter as the metric to account for the technological features that could not scale with the turbine shape vector $(B_1/d, B_2/d, ..., B_n/d, l_1/d, l_2/d, ..., l_n/d, ..., l_{m1}/d, l_{m2}/d, ..., l_{mn}/d)$, that is the size parameter accounts for the scale effect.

3.2.2 Compressibility and fluid type effects: the role of the volumetric flow ratio

The compressibility of the fluid is accounted in Eq. (3.14) by the Mach number (Ma) and it plays a fundamental role in the definition of the efficiency of an ORC expander due to the relatively low speed of sound and the resulting high Mach number levels. The influence of the compressibility cannot therefore be disregarded even in the preliminary design phase.

However, the Mach number is almost useless in the preliminary design phase and does not provide any direct insight about turbine design. Accordingly, a parameter accounting for the compressibility which is of immediate concern in the design of a turbine through similarity principles is searched by varying the choice of the plant-thermodynamic variables

(see item 6 in Section 3.1). This is possible because one or more of the plant-thermodynamic variables can be replaced by others provided that the selected set of variables is able to unambiguously define the thermodynamic state of the system at the inlet and outlet of the turbine. So, the total speed of sound at the inlet (a_{01}) is replaced by a thermodynamic variable such as the total density at turbine inlet (ρ_{01}) or equivalently the total pressure at turbine inlet (p_{01}). Accordingly, the dimensional analysis results in the two following alternative forms of Π_4^I in Eq. (3.2)

$$\Pi_4^{II} = \frac{\rho_{01}}{\rho_{2s}} \qquad \Pi_4^{III} = \frac{p_{01}}{\Delta h_{0s} \rho_{2s}} \tag{3.15}$$

where Π_4^{II} is the volumetric expansion ratio (VR) and Π_4^{III} can be recast in the pressure ratio (PR), which many times appears explicitly in the turbine performance maps [29]. Thus, Eq. (3.14) can be recast in the more convenient forms

$$\eta^* = f \left\{ SP, \begin{matrix} VR^* \\ PR^* \end{matrix}, Re^*, \Gamma, Z \right\} \tag{3.16}$$

The influence of the fluid type on the efficiency is explicitly taken into account by the compressibility factor (Z) and by the fundamental derivative of gas dynamics (Γ): both these variables must be the same if similar flow conditions are to be achieved. Thus, it is apparent that these requirements are not fulfilled by different fluids, that is it is not rigorously possible to use the results obtained on a turbine driven by a certain fluid to make predictions when the fluid is changed.

Nevertheless, as implicitly stated by Macchi and Perdichizzi [24] Eq. (3.16) under the hypothesis of ideal gas further simplifies to

$$\eta^* = f \left\{ SP, VR^*, Re^*, \gamma \right\} \tag{3.17}$$

In fact, the two dimensionless parameters accounting for real gas features in the general Eq. (3.16), i.e., Z and Γ, reduce to only one, namely

the specific heat ratio γ, because for the ideal gas (i) $Z = 1$ by definition, and (ii) $\Gamma \approx (\gamma+1)/2$, where $(\gamma+1)/2$ is the exact value of the fundamental derivative of gas-dynamics for a perfect gas [37].

By comparing the simulated operations of two turbines driven by two different ideal gases under the hypothesis of constant Reynolds number, Macchi and Perdichizzi [24] proved that the sensitivity of the efficiency to γ is minimized (but not eliminated) when the turbines work at equal inlet-to-outlet mass density ratio. As a consequence, the choice of VR as similarity parameter has a two-fold advantage. First, it allows to weaken the dependency on the fluid type, i.e., on γ because the same density variation (VR) even for different fluids implies similar accelerations and, in turn, not too different losses. The same is not at all true for equal pressure ratios, as the same pressure ratio on different fluids results in slightly different accelerations. Second, the volumetric expansion ratio is the real design specification when a new turbine has to be designed for a power plant as it is generally imposed by machine boundary conditions (e.g., temperature levels of the thermal source and condensing medium). Thus, Eq. (3.17) further simplifies in

$$\eta^* = f\{SP, VR^*\} \tag{3.18}$$

Within the limitations stated in the current Section (i.e., the working fluid is an ideal gas and SP fixes the optimum τ), Eq. (3.18) clearly shows that a turbine design optimized for a given fluid works with efficiency that at first approximation depends only on the size parameter, provided that (i) the volumetric expansion ratio is kept at the original optimum value VR^* in the operation at optimal n_s and d_s with different working fluids; (ii) the flow regime within the passages of the chosen optimal design is not affected by the change of the working fluid or, alternatively, Re is always high enough to make friction losses independent on the flow regime.

3.2.3 Reynolds number effect

The fulfillment of rigorous similar flow conditions requires that the Reynolds number must be held constant but a change in the size at fixed molecular properties of the working fluid always results in a variation of the Reynolds number and, in turn, in a variation of the efficiency (*Reynolds effect*). However, in most cases of practical interest the performance of a turbomachine is slightly affected by Reynolds number, i.e., a Reynolds number variation results in a negligible efficiency variation, so that Reynolds number is often disregarded. This Section discusses this practice and points out its limitations starting from fundamental fluid dynamic considerations on straight pipes.

The flow in a pipe or in the channels of a turbomachine may be *turbulent* or *laminar*. In a turbulent flow the fluid friction is caused by a transport of fluid masses and thereby of momentum crosswise to the direction of the "mean" flow. Friction stresses are controlled by inertia forces and they are proportional to the density and squared velocity of the fluid. In a laminar flow all fluid particles move along smooth lines without crossing or mixing. Friction stresses are controlled by viscous forces and they are proportional to the viscosity and the first power of the velocity, and inversely proportional to the linear dimensions. Turbulent and laminar flow regimes occur well above and well below certain critical values of the Reynolds number, respectively. In a straight pipe friction losses are well expressed in terms of frictional head h_L by the relation

$$h_L = f\frac{L}{D}\frac{V^2}{2g} \tag{3.19}$$

being V the average fluid velocity, L the length and D the diameter of the pipe. The friction factor f (also named Fanning factor) depends on both the Reynolds number and the relative roughness of the pipe. The Moody chart shows this dependency for commercial straight pipes. Abun-

dant experimental information indicate in fully turbulent flow f does not practically depends on Re, but only on the relative roughness (ϵ/D). On the other hand, in a laminar flow f is strongly proportional to Re.

A turbulent flow must become laminar in the immediate vicinity of a smooth wall, as the solid boundary prevents particles motions in the normal direction. The thin layer of laminar fluid motion in an otherwise turbulent flow is called *laminar boundary layer*. As the flow in the boundary layer is laminar, then the friction is viscosity controlled i.e., friction factor f and, in turn, losses depend on the Reynolds number. Conversely, as the flow in the remaining part of the volume is turbulent, then the friction is inertia controlled and losses do not depend on the Reynolds number. Friction phenomena are, on the whole, less Reynolds dependent when the Reynolds number is increased because the thickness of the boundary layer decreases.

Instead, within rough walls the laminar boundary layer cannot develop, that is the flow is turbulent throughout the volume. In this case, f does not depend on Re but it increases with the relative roughness because the turbulent fluctuations near the wall are proportional to the surface roughness.

When dealing with turbines of conventional size (i.e., not excessively small) channel dimensions, flow velocity and fluid viscosity levels make the flow regime turbulent. Also, flow passages can be considered as hydraulically rough, so laminar boundary layers cannot develop and friction and, in turn, corresponding losses are inertia controlled. As in this situation of complete turbulent flow, the friction factor does not vary with the Reynolds number then the Reynolds number can be practically disregarded as similarity parameter.

However, when a turbine is considerably scaled down to a relatively small size, Reynolds effects might not be fully negligible and sensibly penalize the performance. Traditionally, scale and Reynolds effects are not

explicitly separated in the literature where their cumulative effect on efficiency is accounted for by means of semi-empirical correlations the validity of which is limited to a specific turbomachine type ([41], [42], [43]). A quite general functional relationship which encompasses many models structures proposed by different authors is

$$\frac{1-\eta}{1-\eta_{ref}} = a + (1-a)\left(\frac{Re_{ref}}{Re}\right)^{n} \tag{3.20}$$

which attempts a basic and somehow arbitrary distinction between Reynolds dependent and independent losses. The coefficient a is the Reynolds independent loss fraction and the exponent n is taken to be inversely proportional to the Reynolds number to account for the decreasing influence of the viscous losses for high Reynolds values (see Capata and Sciubba [44] for a comprehensive collection of different correlations to estimate the Reynolds effect proposed in the past decades).

Since organic fluid applications sometimes demand for relative small size turbines, Reynolds effects might not be fully negligible. Nevertheless (see next Section 3.3), the size parameter itself catches also the Reynolds effect where the latter is significant on the efficiency. Accordingly, Eq. (3.18) is the best functional form for the maximum efficiency (i.e., the shape is optimized) when facing a turbomachinery design and performance estimation problem.

3.3 Size parameter - volumetric flow ratio maps: a real example

Figure 3.1 shows typical experimental charts of the adiabatic efficiency of radial inflow turbines operating with air as working fluid. In particular, Fig. 3.1a shows the variation of the design point efficiency versus specific speed (n_s), rotor outer diameter (d) and pressure ratio (PR); Fig. 3.1b gives the optimum velocity ratio ν_s for each value of the specific speed.

Within the limitations outlined in the previous Sections, these turbine maps can be arranged in the form

$$\eta^* = f(SP, VR^*) \tag{3.21}$$

to become a single efficiency map of a turbine type valid for any machine size/ expansion ratio and less sensitive to the working fluid properties.

The velocity ratio is defined as the peripheral speed (U) on the rotor outer diameter divided by the spouting velocity ($C_0 = (2\Delta h_{0s})^{0.5}$)

$$\nu_s = \frac{U}{C_0} = \frac{U}{(2\Delta h)^{0.5}} \tag{3.22}$$

For instance, a turbine with 140 mm wheel diameter, $n_s = 0.6$ and $PR = 5$ is expected to have an optimum U/C_0 equal to 0.685 and 85*(1-0.75/100)=84.4% percentage points isentropic efficiency.

By considering designs at optimum specific speed and velocity ratio, a wheel diameter reduction from 400 to 80 mm results in an 8% percentage points relative efficiency decay (from 88.8 to 80.7%) due to (i) the practical impossibility of scaling down the detailed geometry lengths with the same ratio of the diameter (scale effect) and (ii) the Reynolds effect. Similarly, an increase of the pressure ratio from 1 to 10 results in a decay of relative efficiency of 2.5% percentage points.

Design data collected in Fig. 3.1 can be conveniently re-arranged to build the corresponding relationship $\eta = f(SP, VR)$. The specific diameter

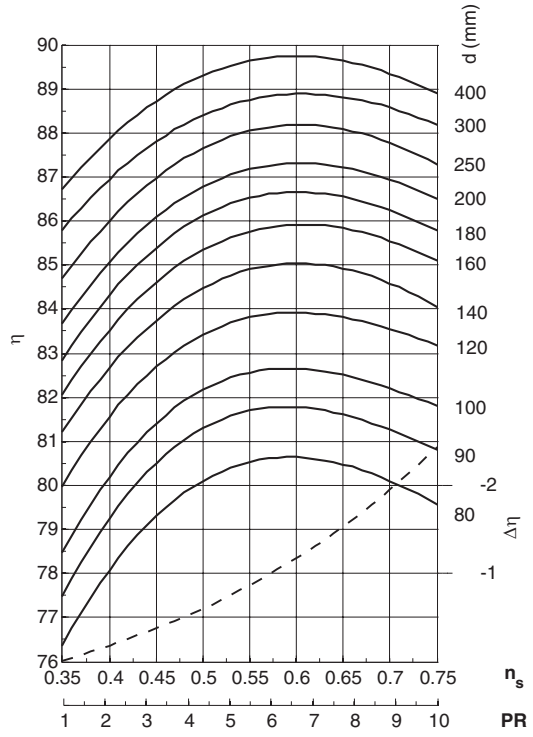

(a)

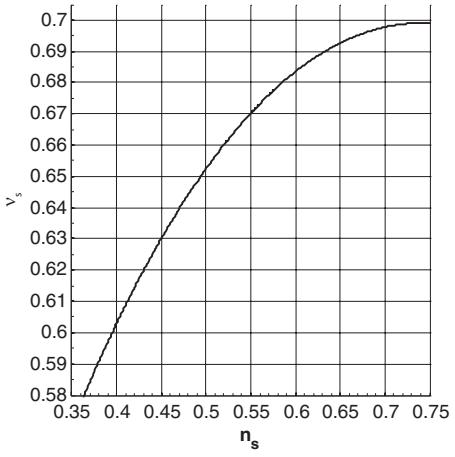

(b)

Figure 3.1: (a) Isentropic efficiency (η) variation with (i) the specific speed (n_s) and diameter (d) (solid line) and (ii) pressure ratio (PR) (dashed line); (b) Velocity ratio (ν_s) variation with the specific speed.

(d_s) is linked to the specific speed and velocity ratio by embedding the definition of n_s in Eq. (3.22)

$$d_s = 2^{1.5}\frac{\nu_s}{n_s} \tag{3.23}$$

Thus, it is

$$SP = \frac{d}{d_s} = \frac{1}{2^{1.5}} d \frac{n_s}{\nu_s} \tag{3.24}$$

The pressure ratio (PR) is converted into the isentropic volume ratio (VR) by the reversible adiabatic relationship ($\gamma = 1.4$ is used)

$$VR = PR^{\frac{1}{\gamma}} \tag{3.25}$$

For each $d-PR$ combination the turbine design with optimum $n_s-\nu_s$ is considered and the associated SP and VR are calculated by Eqs. (3.24) and (3.25), respectively. Note that irrespective of the size and the expansion ratio the optimum n_s is equal to 0.6. Figure 3.2 collects the resulting $SP - VR - \eta$ triplets and it is the plot of Equation (3.21) based on real manufacturer design charts for radial inflow turbines.

Obviously, as the wheel diameter increases, the size parameter increases, as well; the volume ratio follows the same trend of the pressure ratio. Accordingly, the efficiency increases with the machine size and decreases with the expansion ratio. Although Fig. 3.2 conveys information already present in Fig. 3.1, the former provides a more direct indication on the maximum efficiency achievable by the turbine as a function of parameters (i.e., SP and VR) strictly linked with the turbine design specifications.

Figure 3.2 shows also the Reynolds number ($\widetilde{Re}$) variations. The Reynolds number ($\widetilde{Re}$) refers to the wetted area and the meridional velocity at inlet section of the rotor. It can be roughly estimated that the Reynolds number is one-twentieth of the machine Reynolds number (Re). Machines Reynolds numbers are calculated using manufacturer data of Fig. 3.1 by

$$Re = \frac{2\nu_s(\Delta h_{0s})^{0.5} d}{\nu} \tag{3.26}$$

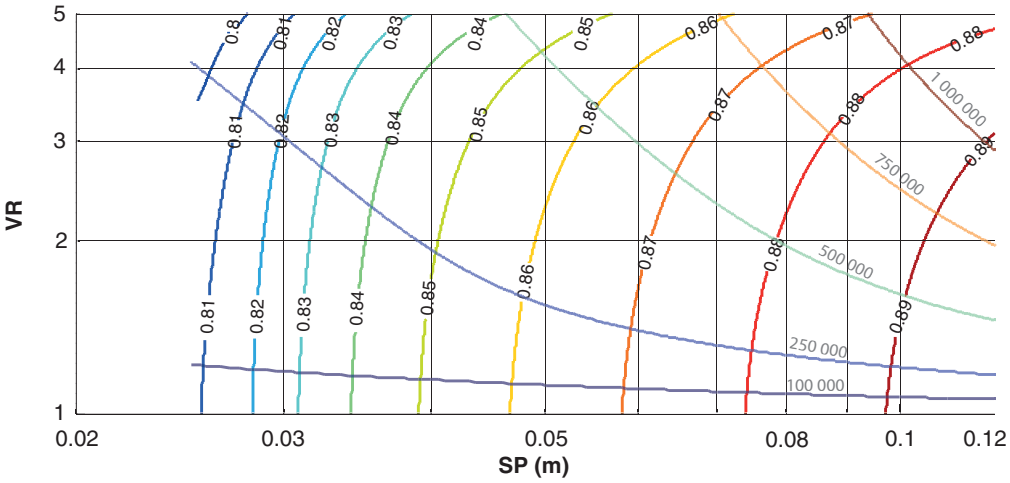

Figure 3.2: Efficiency and Reynolds number variation with SP and VR calculated from data of Fig. 3.1 ($n_s = 0.6$).

where $\Delta h_{0s} = c_p T_{2s}(PR^{\frac{\gamma-1}{\gamma}} - 1)$ is the total-to-static isentropic enthalpy drop. On the basis of real turbine applications, $\nu = 1.5e-5 m^2/s$ (kinematic viscosity), $c_p = 1006 J/kgK$ and $T_{2s} = 288K$ are assumed.

Equation (3.17) clearly shows that the scale effect differs from the Reynolds number effect although some authors (e.g., [41] and [40]) prefer to avoid a strict distinction between these two effects. This choice is questionable from a rigorous theoretical perspective but it is supported by the practical applications where the fluid (i.e., the kinematic viscosity) is fixed. So, the change of the turbine size results in a change of the Reynolds number that most of the times cannot be counterbalanced by the rotational speed. In other words, the turbine size and the Reynolds number cannot vary independently from each other but are somehow correlated.

Other information can be obtained looking at Fig. 3.2. In the lower range of SP ($SP \leq 0.03$ m), the turbine efficiency is mainly affected by SP only: this is the region dominated by the scale effect and changes of VR and Re have only minor effects on efficiency. The small size of the turbine

does not allow high values of the Reynolds number even at the highest VR.

In the medium range of SP ($0.03\,\text{m} \leq SP \leq 0.1\,\text{m}$) the turbine efficiency is affected by both SP and VR: iso-efficiency lines and iso-Re lines form a roughly orthogonal grid in the SP-VR plane (i.e., iso-efficiency lines are roughly the directions of Re steepest gradient). This confirms that also in this SP range the effect of Reynolds number on turbine efficiency is by far lower than the influence of VR and SP: a proper combination of VR and SP pairs permits to keep constant the turbine efficiency for any change of the Reynolds number. VR is important also when it is low, indicating that the losses due to compressibility effects are relevant within the medium range of SP.

In the higher range of SP ($SP \geq 0.1$ m), the turbine efficiency appears to be affected mainly by VR: iso-efficiency lines and iso-Re lines bend progressively towards the horizontal direction. It is likely that these iso lines overlap the iso-VR lines becoming parallel to each other at very high SP. At very high SP, compressibility effects dominate the turbine efficiency behavior and limit the range of variability of the Reynolds number, especially at lower VR values.

Finally, in the very high range of VR ($VR>>5$), it is likely that iso-Re lines bend towards the vertical direction (becoming iso-SP lines), whereas iso-efficiency lines bend towards the horizontal direction (becoming iso-VR lines): the very high VR range is dominated by compressibility effects also at low SP values. These latter fix the value of the Reynolds number and the turbine efficiency is ruled by losses due to compressibility.

The qualitative findings of this discussion on the effect of VR and SP parameters on the turbine efficiency are quite general within the variability range considered for the two parameters, because they are based on experimental data of real turbines. On the other hand, working fluids different from air show different values of the Reynolds number, and likely a change in the role of the Reynolds effect on the turbine losses. Nevertheless, it is

worth noting that (i) it is unlikely that the qualitative trends showed here notably change for different fluids following the ideal gas behavior; (ii) the sensitivity of turbine efficiency to the Reynolds number value will be lower than that reported in Fig. 3.2 if the turbine operates with a working fluid having molecular complexity higher than air (being Re higher). Thus, it can be concluded that SP also accounts also for the Reynolds effect when the turbine size and operation lead to efficiency that is mostly affected by the variation of the Reynolds number. This leads to conclude that the quasi-similarity statement summarized by Eq. (3.21) is the oversimplified derivation from the similarity law that permits to extend efficiency data of a specific turbine type designed for a given fluid to the operation with another fluid with the maximum accuracy allowed by such minimum number of independent parameters, provided that the specific speed and specific diameter are the optimum ones.

An attempt to relax the ideal gas constraint that tarnishes the extension of SP-VR maps derived from a specific fluid to another one could be to admit (i) a variable and non-unity distribution of the compressibility factor with the minor requirement of not very different Z values at corresponding turbine operation with different working fluids, and (ii) a contextual slight variation of the fundamental derivative of gas dynamics Γ. Item (ii) seems a quite acceptable constraint relaxation, as already stated within the text surrounding Eq. (3.17), whereas, item (i) requires further comments (see Chapter 5).

In any case, efficiency SP-VR maps can be conveniently embedded in optimization tools of an ORC power cycle that want to exploit the actual turbine technology available for traditional fluids. This practice which moves towards an integrated design of the ORC system and its turbine avoids arbitrary assumptions on turbine performance and assures that the real turbine is able to obtain the thermodynamic states at the inlet and outlet of the turbine resulting from the optimization procedure.

Efficiency predictions resulting from the models developed in this work will be presented in this form.

Chapter 4

Methodology: design of radial and axial turbines for ORCs

The previous Chapter concluded that the SP-VR maps are best suited to ORC design and optimization. In order to obtain such maps, a method of analysis of axial and radial turbines is required. First, this method should provide reliable results and must allow the execution of a huge number of simulations to characterize different turbomachines designs. Second, the entire set of designs must be filtered to obtain the optimal solutions for each set of design specifications. Finally, these tasks must be repeated for several organic fluids.

At present, CFD is not a viable tool to reach the final objective of this thesis in a reasonable time, and the only analysis approach that is believed to be suited to this work is a mean line model. The more detailed, reliable and widespread mean line model in the literature was suggested by Balje [35]. This model allows for the computation of the well-known $n_s - d_s$ charts [23] that are the common starting point for the preliminary design of turbomachines. One of the features at the basis of Balje's model success is that it leaves some degrees of freedom in the choice of the turbomachine geometry details allowing for the sensitivity study of their effect on the

efficiency. This is apparent by looking at any Balje chart (see Fig. 2.20). However, in the models used to build the $n_s - d_s$ charts for compressible flow turbomachines, differently from those used for hydraulic machines, Balje introduced some major constraints. In particular, both the Mach and Reynolds numbers are fixed at specific values. These constraints are not very relevant for traditional fluid applications, but are unacceptable for ORC turbines. Moreover, the specific molecular properties of each organic fluid cannot be disregarded. Finally, the relatively very small size of several ORC turbines requires to account for the scale effect (SP) that usually plays a secondary role in turbomachinery handling traditional fluids. In this work, the degrees of freedom of almost all the secondary geometrical features of a turbomachine design are fixed at optimal design values taken from the literature to make the present turbomachine models capable to focus on the fundamental parameters for ORC applications: SP, VR, fluid molecular properties (and Reynolds number).

The models are based on algebraic equations derived from the fundamental conservation laws of fluid mechanics and thermodynamics (i.e., conservation of momentum, mass and energy) complemented by real molecular properties of each fluid and loss correlations to consider the irreversibility losses in the turbine flow (Section 4.2). After a detailed presentation and discussion of loss correlations (Sections 4.3 to 4.5), the structure and the sequential resolution procedure of the model are presented with the aid of several flowcharts showing the skeleton of the scripts implemented in Matlab® and how they are coupled with the Refprop fluid properties database (Sections 4.6 and 4.7). A discussion on model criticalities concerning the reliability of a mean line model and the inherent limitations of loss correlations closes the Chapter (Section 4.8).

4.1 Introduction

The turbine mean line model assumes that the flow field is everywhere uniform and unidirectional, that is the values of the flow variables at the mean line (i.e., mid span of the blade) are representative of the actual flow field in the fluid flow sections perpendicular to the mean line. This approximation disregards all three-dimensional effects existing in the real flow field that are are considered only in the loss correlations for their contribution to energy losses.

Although through flow or CFD models would certainly result in a more reliable estimation of performance in the face of a strong computational effort, they go beyond the scope of this work. The turbine analysis by means of viscous, three-dimensional CFD techniques does not represent an alternative methodology to a mean line analysis but it is a subsequent phase in the overall turbomachinery design process because it requires the knowledge of detailed blade shapes and principal geometric parameters, which are made available by the mean line model. Thus, a realistic and potentially efficient preliminary design obtained by a mean line model is a precondition for the design of a high efficiency ORC turbine.

A mean line design approach is therefore chosen here, as this work focuses on the preliminary design and analysis of a large variety of organic fluid turbines differing for arrangement (i.e., radial inflow or axial), design specifications (i.e., mass flow rate and enthalpy drop) and basic dimensionless design parameters (i.e., specific speed and velocity ratio for the radial turbines and loading coefficient, flow factor and reaction for the axial ones).

In the lumped-parameter approach typical of a mean line analysis, the irreversibilities are accounted for by loss coefficients: they allow to the real flow conditions to be evaluated starting from the loss free scenario. The main portion of this Chapter deals with the choice of the loss correlations embedded in the models. Several alternative correlations available in the

open literature are presented and discussed for both the radial inflow and axial turbine analysis.

The models built in this work are derived from those proposed by Aungier [45], who validated them for turbines handling traditional fluids. The author is aware that models based on empirical correlations originally developed for traditional fluids and validated against steam or gas flows might be unreliable, and that a validation against experimental data is mandatory. However, to the author's knowledge, in the open literature there are not experimental data of optimized ORC turbines that can support this validation.

Only a partial validation of the models was performed by comparing the results of the radial turbine model with performance data of the radial turbines in the Stillwater geothermal power plant (Nevada (USA)) [46]. The predicted efficiency closely agrees with the measured one (see Section Critical Remarks in Chapter 5) for the design values of size parameter and volumetric flow ratio. Although very limited, this successful validation may suggest that also the axial turbine model (that shares the origin with the radial turbine model) could provide reliable predictions. On the other hand, the search for the optimum designs requires that some geometrical parameters are allowed to vary. So, in the axial turbine model several design conditions of the Aungier's [45] original design procedure have been relaxed to obtain a model sensitive to the variations of some major geometrical features

4.2 Model structure

The mean line models are formulated with a lumped-parameter approach and calculate the flow variables at few selected stations of the cascade (inlet, outlet and, for the radial turbine, mid) disregarding the detailed three dimensional shape of the blade. Velocity diagrams, size,

angular speed, blade heights and number, flow sections and estimated efficiency level are the main outcomes of the mean line model. The efficiency estimation is made possible by the inclusion in the model of loss correlations expressed as function of the blade row inlet and exit velocity triangles and only the overall geometric features.

Turbine mean line models are based on few algebraic equations resulting from fundamental conservation laws of fluid mechanics and thermodynamics expressed into a form suitable for the analysis of turbomachines. In particular, they are

- *Conservation of mass*

$$\dot{m} = \rho c \cos\alpha A(1 - bf) \tag{4.1}$$

where $\dot{m}$ is the mass flow rate through a blade passage, $\cos\alpha$ is the meridional velocity component, A is the geometric flow area and bf is a blockage factor due to blade surface and endwall boundary layers. If A_1 and A_2 are the areas at stations 1 and 2 along a passage, respectively, then

$$\dot{m} = \rho_1 c_1 \cos\alpha_1 A(1 - bf_1) = \rho_2 c_2 \cos\alpha_2 A(1 - bf_2) \tag{4.2}$$

since there is no accumulation of fluid within the control volume.

- *Conservation of energy*

The steady flow energy equation for a turbine through which flow enters at position 1 (nozzle inlet) and leaves at position 3 (rotor outlet) is

$$q - w = h_{03} - h_{01} \tag{4.3}$$

where q is the specific heat exchange through the turbine boundaries and $h_{03} - h_{01}$ is the variation of the total (or stagnation) specific

enthalpy ($h_0 = h + 0.5c^2$) across the turbine. Note that in Eq. (4.3) the contribution of the potential energy is neglected as it is usually small and since turbine flow processes are adiabatic then $q = 0$.

The application of energy conservation to the nozzle control volume gives

$$h_{01} - h_{02} = 0 \tag{4.4}$$

that is the total enthalpy is constant because stationary blade row does not transfer any work from the fluid.

Indeed, for the rotor control volume the specific work w is

$$w = h_{02} - h_{03} \tag{4.5}$$

- *Conservation of momentum*

For one-dimensional steady flow which enters the rotor control volume at radius r_2 with tangential velocity c_{t2} and leaves at radius r_3 with tangential velocity c_{t3}, the vector sum τ of the moments of all external forces acting on the rotor is

$$\tau = \dot{m}(r_2 c_{t2} - r_3 c_{t3}) \tag{4.6}$$

which states that the torque on the rotor is equal to the net time rate of efflux of angular momentum from the control volume.

The specific work $\mathcal{W}$ can therefore be written in terms of the so-called Euler's turbine equation as

$$\mathcal{W} = \frac{\tau\omega}{\dot{m}} = u_2 c_{t2} - u_3 c_{t3} = \frac{c_2^2 - c_3^2}{2} + \frac{u_2^2 - u_3^2}{2} + \frac{w_3^3 - w_2^2}{2} \tag{4.7}$$

The Euler equation (Eq. (4.7)) and the energy conservation for the rotor (Eq. (4.5)) result in

$$h_{02} - u_2 c_{t2} = h_{03} - c_{t3} \tag{4.8}$$

that is the quantity $h_0 - uc_t$ is constant across a rotor streamline. This function is commonly named rothalpy, a contraction of rotational stagnation enthalpy. Trivial trigonometric allows to recast Eq. (4.8) in the form

$$h_2 + \frac{w_2^2}{2} - \frac{u_2^2}{2} = h_3 + \frac{w_3^2}{2} - \frac{u_3^2}{2} \tag{4.9}$$

where the quantity $h_{0R} = h + w^2/2$ is the relative stagnation enthalpy. Accordingly, the relative stagnation enthalpy is constant through the rotating blade row if the blade speed is constant, i.e., the streamline radius does not vary.

The solution of the flow field within a mean line model ultimately consists in determining the values of the flow variables (velocity, enthalpy, density, etc.) which fulfill the above mentioned balance equations of mass, energy and momentum. However, the model resolution requires, in turn, the availability of further Equations which allow to define

- fluid properties to describe the thermodynamic behavior of the working medium. In this work they are evaluated by the program Refprop [47] which is based on the most accurate pure fluid and mixture models currently available. It implements three models for the thermodynamic properties of pure fluids: equations of state explicit in Helmholtz energy, the modified Benedict-Webb-Rubin equation of state, and an extended corresponding states (ECS) model. Viscosity is modeled with either fluid-specific correlations or in some cases the friction theory method. Since in this work only pure substances are considered, a thermodynamic state is completely determined by specifying two independent thermodynamic properties; other properties are then function of these independent properties through the equation of state.

  The calculation of fluid properties using the ideal gas equation of

state in place of interrogating real fluid properties libraries is improper when dealing with organic fluids, especially if the expansion starts not too far from the fluid critical point where compressibility factors may significantly deviate from unity.

- irreversibilities across each turbine component. This is done using total pressure loss coefficients which are estimated through loss correlations as a function of the main geometric and cinematic variables. An extensive survey on loss coefficient rationale and estimation is given in Sections 4.3 to 4.4.

- relationships among the flow velocities in the absolute and relative frame of reference

$$c_t = w_t + u \tag{4.10}$$

$$c^2 = u^2 + w^2 - 2uw_t \tag{4.11}$$

where c, w and u indicate the absolute, relative and peripheral velocity, respectively.

4.3 Loss coefficients

The analysis of a turbomachine and the estimation of the resulting performance is a really tough issue because it involves complex three dimensional, viscous, unsteady and irreversible flows occurring in both stationary and rotating boundaries. On the other hand, efficiency is one of the most relevant parameter for most turbomachines and the evaluation of the irreversibilities arising in the flow plays a fundamental role because the latter can be equated to a certain amount of lost work and thus a loss in efficiency. In general terms, the increase of the entropy in the flow across a turbomachine is the consequence of several phenomena: skin friction on

the blade surfaces, viscous and turbulent dissipative mechanisms of vortices and shocks, vortices that cause some parts of the fluid to move in directions other than the principal one, fluid leakage in the gap between the blade tip and the shroud, etc. As all these mechanisms reduce the useful work they are commonly referred as losses.

The direct mathematical treatment of local losses is not trivial because involves the solutions of the Navier-Stokes equations with a suitable turbulence model. Moreover, for viscous layers and vortices the interest is usually focused on overall or integrated losses rather than local losses. Thus, what is commonly done in turbomachinery engineering (at least in a preliminary design phase) is to use an ideal flow model which takes into account the effects of the irreversibilities by means of loss coefficients. In other words, loss coefficients allow to determine the real flow conditions starting from those which would be obtained in case the irreversibilities were absent (i.e., the flow was ideal).

According to Japikse and Baines [48] loss coefficients can be broadly grouped according to the methods adopted to define them in the following categories.

- Gross (or bulk overall) loss coefficients. They are fixed numbers or very simple functions of few overall fundamental performance parameters and strongly depend on the experimental dataset used to determine their values. They provide reasonable estimates only in the range where data exist, so they are unfit to explore the effect of geometry modifications on the expected performance. Gross loss coefficients do not give any insights about the physics of the phenomenon which underneath the loss mechanism.

- Correlated coefficients. By the use of test data taken from a subset of similar machines, loss coefficients are correlated to key design parameters in place of overall performance parameters. The bigger

the size of the experimental dataset, the higher the coefficients reliability. Correlated coefficients should be applied only to families of machines with similar characteristics or, at most, they can be carefully used to investigate the effects of limited geometry changes on the performance.

- Fundamental (or physically based) coefficients. They attempt to reproduce the actual physical processes in the flow: each basic loss-generating process within the flow field (e.g. friction, secondary flows, etc.) is accounted separately by a loss coefficient and modeled as a function of the fundamental geometric, cinematic and thermo-fluid dynamic parameters. Then, these loss coefficients are summed together to get the overall loss coefficient and, in turn, the real flow conditions. However, it must be borne in mind that, whilst the partition of the global loss mechanism in more fundamental loss-generating processes reduces a complex problem to smaller proportions, it is artificial because loss-generating processes interact and influence each other. Compared to the previous categories these coefficients are the most suitable for design purposes because they should be able to predict with good accuracy the performance of turbines other than those for which they were developed; nevertheless, few empirical input (i.e., tuning constants) are still required to calibrate the loss modeling system with respect to the experimental findings and to indirectly account for possible lacks in the flow modeling.

In turbomachine engineering practice loss coefficients are usually defined on velocity/enthalpy or pressure basis. In the following the most relevant definitions for nozzle and rotor are collected and they are related to each other.

Figure 4.1a shows an expansion process across a nozzle from the initial state 1 to the final state 2; state $2s$ is the isentropic (or ideal) final state

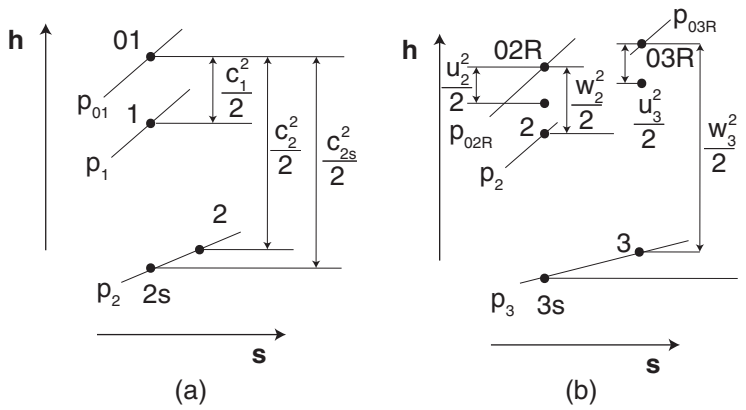

Figure 4.1: Expansion process across a (a) nozzle and (b) rotor.

and lies on the same isobar line of state 2. The velocity loss coefficient (ϕ) compares the real discharge flow velocity to the ideal one

$$\phi = \frac{c_2}{c_{2s}} = \left(\frac{h_{01} - h_2}{h_{01} - h_{2s}}\right)^{0.5} \tag{4.12}$$

The enthalpy loss coefficient (ζ) is often defined as

$$\zeta = \frac{h_2 - h_{2s}}{h_{01} - h_2} = \frac{h_2 - h_{2s}}{c_2^2/2} \tag{4.13}$$

or, more rarely, if the isentropic total-to-static enthalpy drop is considered, as

$$\zeta' = \frac{h_2 - h_{2s}}{h_{01} - h_{2s}} = \frac{h_2 - h_{2s}}{c_{2s}^2/2} \tag{4.14}$$

Equations (4.12), (4.13) and (4.14) allow to calculate the real discharge enthalpy value (h_2) which is higher than the ideal one (h_{2s}) because the difference $h_2 - h_{2s}$ is not used to accelerate the fluid to the ideal velocity discharge value c_{2s}.

Simple rearrangements permit to interrelate the above definitions

$$\zeta = \frac{h_2 - h_{2s}}{\phi^2 \frac{c_{2s}^2}{2}} = \frac{\zeta'}{\phi^2} = \frac{\zeta'}{1 - \zeta'} \qquad \zeta = \frac{1}{\phi^2} - 1 \qquad \phi = \left(\frac{1}{1 - \zeta'}\right)^{0.5} \tag{4.15}$$

Total pressure loss coefficient (Y) is usually preferred by English authors and the most diffused definition is (see, e.g., Horlock [49] for a comprehensive list of the possible variations)

$$Y = \frac{p_{01} - p_{02}}{p_{02} - p_2} \tag{4.16}$$

from which the total outlet pressure and, in turn, the outlet thermodynamic state can be determined. Under the hypothesis of ideal gas behavior it is possible to analytically relate the enthalpy loss coefficient ζ (Eq. (4.13)) and total pressure loss coefficient (Eq. (4.16)). It results

$$\zeta = \frac{2}{(\gamma-1)M_2^2}\left(1 - \left(\frac{1}{1+Y} + \frac{Y}{1+Y}\frac{1}{(1+Y)\left(1+\frac{\gamma-1}{2}M_2^2\right)^{\frac{\gamma}{\gamma-1}} - Y}\right)^{\frac{\gamma-1}{\gamma}}\right) \tag{4.17}$$

where γ and M_2 denote the specific heat ratio and the outlet Mach number, respectively. Equation (4.17) for $M_2 \leq 0.4$ is well approximated by

$$\zeta = \frac{Y}{1 + \frac{\gamma}{2}M_2^2} \tag{4.18}$$

Similarly, loss coefficients ζ' and Y can be related by relationships analogous to Eq. (4.17) and (4.18) (see [32] for the details).

A number of turbomachine designers (e.g., Balje [50] and Rodgers [51]) prefer to use loss coefficients based on the stagnation enthalpy loss ($h_{02} - h_{02s}$, being the state 02s on the total pressure isobar line p_{02} and $s_{02s} = s_1$), non-dimensionalized by the tip speed u of the rotor which follows the nozzle

$$\Delta q = \frac{h_{02} - h_{02s}}{u^2} \tag{4.19}$$

Figure 4.1b shows an expansion process across a rotor from the initial state 2 to the final state 3; state $3s$ is the isentropic (or ideal) final state and lies on the same isobar line of state 3. Subscript R stands for relative frame of reference. The velocity loss coefficient (ψ) compares the real relative discharge flow velocity to the ideal one

$$\psi = \frac{w_3}{w_{3s}} = \left(\frac{(h_{02R} - h_3) + \left(\frac{u_3^2}{2} - \frac{u_2^2}{2}\right)}{(h_{02R} - h_{3s}) + \left(\frac{u_3^2}{2} - \frac{u_2^2}{2}\right)}\right)^{0.5} \tag{4.20}$$

The enthalpy loss coefficient (ζ) is

$$\zeta = \frac{h_3 - h_{3s}}{h_{02R} - h_3 + \frac{u_3^2}{2} - \frac{u_2^2}{2}} = \frac{h_3 - h_{3s}}{w_3^2/2} \tag{4.21}$$

whereas, if the isentropic total-to-static enthalpy drop is considered, it is

$$\zeta' = \frac{h_3 - h_{3s}}{h_{02R} - h_{3s} + \frac{u_3^2}{2} - \frac{u_2^2}{2}} = \frac{h_3 - h_{3s}}{w_{3s}^2/2} \tag{4.22}$$

It is also

$$\zeta = \frac{\zeta'}{1 - \zeta'} = \frac{1}{\psi^2} - 1 \tag{4.23}$$

Note that Eqs. (4.21) and (4.22) are applicable to rotors of both axial and radial turbines. In the former case being $u_2 = u_3$ they assume simpler expressions. On the other hand, different expressions have to be used for the total pressure loss coefficient depending on the machine arrangement. In particular, for the axial rotors it is

$$Y = \frac{p_{02R} - p_{03R}}{p_{03R} - p_3} \tag{4.24}$$

whereas for the radial ones (see [45])

$$Y = \frac{p_{03Rs} - p_{02R}}{p_{02R} - p_2} \tag{4.25}$$

with $p_{03Rs} = f(h_{03R}, s_2)$.

The relationships which interrelate ζ and Y can be obtained from Eqs. (4.17) and (4.22) by subscripts mutation.

4.4 Loss evaluation for the radial turbine

The building of a reliable loss model for radial inflow turbines in terms of fundamental loss coefficients is inherently more difficult compared to axial turbines. In fact, differently from what is commonly done in the study of axial turbines, the large amount of test data available for stationary cascades cannot be profitably used in the analysis of radial turbines because

in the latter case the flow field is deeply influenced by both the radius change and the pressure distribution caused by rotation. As a result, the open literature does not provide any comprehensive and well-validated performance prediction model for this type of machines. Nevertheless, in the market there are commercially available software (see Rital ®) which implement proprietary performance analyses for radial inflow turbines.

In this work the loss modeling system proposed by Aungier has been used in the analysis of radial inflow turbines because

- i) most of the loss correlations are formulated specifically for the radial inflow applications and are not adapted from axial flow turbine and centrifugal compressor engineering practice;

- ii) it attempts to estimate the loss amount starting from a quite general physical modeling of each loss mechanisms (e.g., the use of a simplified boundary layer analysis for the passage losses);

- iii) it limits (but not excludes) the use of experimentally derived tuning constant whose applicability to turbines of very different size might be questionable;

- iv) consistently with a mean line analysis the loss calculation considers not only the geometric and kinematic parameters at the inlet and outlet of each turbine component (as commonly done by several authors) but also at the mid station;

- v) it was originally formulated to address radial inflow turbines applications in the energy market and it is relatively recent so it can be argued that it took stock of the previous findings accumulated over the years.

Losses in each turbine component (i.e., volute, nozzle, annulus and rotor) are estimated by means of total pressure loss coefficient (Y) depending

on kinematic and geometrical parameters. Total pressure loss coefficients are used (see Section 4.6) to calculate the total pressure at the outlet of each component and, in turn, the entropy increase across the turbine. In the following the loss correlations implemented in this work are shown and they are briefly compared to other loss models (especially for the rotor) proposed by different authors in the past decades.

As commonly done in the literature, the loss correlations are grouped by turbine component because loss phenomena and the equations to model them are different depending on the turbine component. The reason of such diversity relies on the considerably different geometries and, in turn, flow fields of turbine components (e.g., nozzle and rotor). In the following, the notation used in the Equations for the calculation of the pressure loss coefficients (Y) follows this scheme: subscripts v, n, a, r stand for volute, nozzle, annulus and rotor, respectively; subscripts 1, 2 and 3 indicate the inlet, mid and outlet station, whereas subscript 0 denotes the corresponding total state.

4.4.1 Volute

The total pressure loss coefficient in the volute (Y_v) is defined by:

$$Y_v = \frac{p_{01v} - p_{03v}}{p_{03v} - p_{3v}} \tag{4.26}$$

This coefficient is expressed as the sum of two components: the profile loss (Y_{pv}) and the circumferential distortion loss (Y_θ):

$$Y_v = Y_{pv} + Y_{\theta v} \tag{4.27}$$

Profile loss coefficient of each turbine component, is calculated according to a simplified boundary layer analysis, which, according to Aungier's experience, has been found to be particularly effective for radial inflow turbines. In particular, the profile loss coefficient for the volute (Y_{pv}):

$$Y_{pv} = \frac{2\Theta_v + \Delta_v^2}{(1-\Delta_v)^2} \tag{4.28}$$

where $\Theta_v = 2(\theta_{wv}/b_{3v})$ and $\Delta_v = 2(\delta^*_{wv}/b_{3v})$.

The estimation of the boundary layer "momentum thickness" (θ_{wv}) requires the calculation of the skin friction coefficient (c_{fv}, which depends, in turn, on Reynolds number and relative roughness), the average density throughout the volute (ρ_{avev}), the flow path length (L_v) and the flow velocities at the three stations (1, 2 and 3):

$$\theta_{wv} = c_{fv}\rho_{avev}\left[\left(\frac{C_{1v}}{C_{3v}}\right)^5 + 2\left(\frac{C_{2v}}{C_{3v}}\right)^5 + 1\right]\frac{L_v}{8\rho_{3v}} \tag{4.29}$$

The "displacement thickness" (δ^*_{wv}) can be directly obtained from θ_{wv} by multiplication for the shape factor ($H = 1.2857$), because it is assumed that the boundary layer shape factor for the 1/7th power law velocity applies.

The circumferential distortion loss (Y_θ) accounts for mixing losses associated with circumferentially non-uniform angular momentum imposed at the volute exit:

$$Y_{\theta v} = \left(\left(\frac{r_{1v}C_{1v}}{r_{3v}} - C_{t3v}\right)/C_{3v}\right)^2 \tag{4.30}$$

In this study the volute is designed to maintain uniform angular momentum in the circumferential direction so this loss is null ($Y_{\theta v} = 0$).

A common approach followed by other authors is to calculate the friction loss by means of conventional pipe flow correlations with Reynolds number for fully turbulent flow. For instance, Kastner and Bhinder [52] and Rogo [53] evaluate the friction loss in terms of enthalpy loss coefficient

$$\Delta q = 4c_f\frac{L}{D}\frac{(\bar{c}/u_{1r})^2}{2} \tag{4.31}$$

where Δq is the loss coefficient based on total enthalpy loss and non-dimensionalized by the rotor tip speed (u_{1r}), $4c_f = 0.054(\bar{c}D/\nu)^{-0.25}$ is

the turbulent friction factor, $\bar{c}$ is the mean velocity and L and D are the equivalent hydraulic length and diameter, respectively. However, the evaluation of skin friction coefficient in Eqs. (4.29) and (4.31) is in any case questionable, because most of the available correlations refer to flow in straight pipes of constant area. An attempt to overcome this issue is made by Japikse [54] through the relationship $c_f = k(1.8e5/Re)^{0.2}$, where the constant k may vary in the wide range $0.005 - 0.02$.

According to the author knowledge, there are no correlations to estimate the secondary losses caused by recirculation and cross flows in the volute.

4.4.2 Nozzle

The total pressure loss coefficient in the nozzle (Y_n) is defined by:

$$Y_n = \frac{p_{01n} - p_{03n}}{p_{03n} - p_{3n}} \tag{4.32}$$

This coefficient can be expressed as the sum of two loss contributions, namely the profile loss (Y_{pn}) and the incidence loss (Y_{incn}):

$$Y_n = Y_{pn} + Y_{incn} \tag{4.33}$$

The profile loss is calculated from the boundary layer theory as

$$Y_{pn} = \frac{2\Theta_n + \Delta_n^2}{(1 - \Delta_n)^2} \tag{4.34}$$

where

$$\Theta_n = 1 - \left[1 - 2\left(\frac{\theta_{wn}}{b_{wn}}\right)\right]\left[1 - \left(\frac{\theta_{bsn}}{b_{bn}} + \frac{\theta_{bpn}}{b_{bn}}\right)\right] \tag{4.35}$$

$$\Delta_n = 1 - \left[1 - 2\left(\frac{\delta^*_{wn}}{b_{wn}}\right)\right]\left[1 - \left(\frac{\delta^*_{bsn}}{b_{bn}} + \frac{\delta^*_{bpn}}{b_{bn}}\right)\right] \tag{4.36}$$

In Equations 4.34 and 4.35 three "momentum thicknesses" appear which are related to the wall of the nozzle (θ_{wn}), the blade suction side

of the nozzle (θ_{bsn}) and the blade pressure side (θ_{bpn}). The dimensional lengths used at the denominator are:

$$b_{bn} = esse_{3n} \sin \beta_{3n} \tag{4.37}$$

$$b_{wn} = b_{3n} \tag{4.38}$$

Note that θ_{bsn} and θ_{bpn} calculation follows Eq. (4.29) but the blade surface fluid velocity on suction c_{2bsn} and pressure side c_{2bsn} are required in the mid station to include the influence of the blade loading effect on the blade surface boundary layer calculation. The average difference in velocity on the two blade surfaces (Δc_n) is given by Stokes's theorem for irrotational flows, that is the integration about any closed path of the velocity component tangent to the path is identically equal to zero

$$\Delta c_n = 4\pi \left| r_{3n} C_{t3r} - r_{1n} C_{t1r} \right| / (L_n NN) \tag{4.39}$$

where L_n is the nozzle flow path length. It is assumed that this difference Δc_n could be subdivided in equal parts between the two sides of the blades, so

$$c_{2bsn} = c_{2n} + \frac{\Delta c_n}{2} \tag{4.40}$$

$$c_{2bpn} = c_{2n} - \frac{\Delta c_n}{2} \tag{4.41}$$

The incidence loss is:

$$Y_{incn} = \sin^2(\alpha_{1n} - \alpha^*_{1n}) \frac{p_{01n} - p_{1n}}{p_{03n} - p_{3n}} \tag{4.42}$$

and it is proportional to the difference between the actual flow angle α_{1n} and the optimum one α^*_{1n}.

When the flow regime at nozzle outlet is supersonic post-expansion shock waves occur. In the absence of guidelines the author estimated the

associated losses using the following correlation borrowed from axial flow cascades (see Aungier [45]):

$$Y_{exn} = \left(\frac{M_{3n} - 1}{M_{3n}} \right)^2 \tag{4.43}$$

which is added to the nozzle total pressure loss calculated at sonic conditions.

$$Y_{n|M_{3n}>1} = Y_{n|M_{3n}=1} + Y_{exn} \tag{4.44}$$

The number of published studies on nozzle performance is very limited and, in any case, with little supporting data often referring to a fixed turbine size. Accordingly, their application to turbines of very different size may be questionable.

Rodgers [51] suggests the following expression for nozzle loss

$$\zeta_n = \frac{0.05}{Re_b^{0.2}} \left(\frac{3 \tan \alpha_{3n}}{s/c} + \frac{s \cos \alpha_{3n}}{b} \right) \tag{4.45}$$

where $\zeta_n = (h_{3n} - h_{3ns})/(h_{01n} - h_{3n})$ is the static enthalpy loss coefficient ($h_{3ns} = f(p_{3n}, s_{1n})$), s is the vane spacing, b_n and c_n are the nozzle blade height and chord length, respectively and the Reynolds number is based on nozzle blade height and outlet velocity. This formulation highlights that losses increases with the pitch-to-chord ratio and blade height-to-pitch ratio as the wetted area is increased; the inverse dependency on the Reynolds number takes into account the effect of the friction coefficient (which is not explicitly taken into account). Note that flow angles in Eq. (4.45) refer to the radial direction.

Balje [50] accounts the nozzle losses in terms of total enthalpy loss coefficient using a frictional pipe formulation based on hydraulic length and diameter. Even less general is Benson's model [55] which correlates the nozzle loss coefficient to the reduced mass flow rate: the higher the reduced mass flow rate, the lower the losses.

4.4.3 Vaneless annular passage

The total pressure loss coefficient in the annulus (Y_a) is defined by:

$$Y_a = \frac{p_{01a} - p_{03a}}{p_{03a} - p_{3a}} \tag{4.46}$$

This is the sum of two components, the profile loss (Y_{pa}) and the entrance loss (Y_{ina}):

$$Y_a = Y_{pa} + Y_{ina} \tag{4.47}$$

The profile loss is calculated from the boundary layer theory as

$$Y_{pa} = \frac{2\Theta_a + \Delta_a^2}{(1 - \Delta_a)^2} \tag{4.48}$$

where $\Theta_a = 2(\theta_{wa}/b_{3a})$ and $\Delta_a = 2(\delta^*_{wa}/b_{3a})$.

In the equations above the "momentum thickness" (θ_{wa}) and "displacement thickness" (δ^*_{wa}) are estimated using an analogous procedure to that described for the volute (see 4.29).

The entrance loss coefficient accounts for the abrupt area contraction loss (see Benedict et al. [56]) applied to the meridional component of the velocity head:

$$Y_{ina} = \left[\left(\frac{A_{1a}}{A_{3a}} - 1\right)^2 \sin\alpha_{1a}\right]^2 \frac{p_{01a} - p_{1a}}{p_{03a} - p_{3a}} \tag{4.49}$$

On the other hand, Whitfield and Baines [27] suggest to estimate the passage losses of the annulus by the same loss models of the volute (e.g., Eq. (4.31)) since the volute and the annulus are both stationary components in which unguided swirling flows occur.

4.4.4 Rotor

The overall loss coefficient in the rotor has a different definition compared to the previous components because it refers to the relative framework:

$$Y_r = \frac{p_{03Rsr} - p_{03Rr}}{p_{03Rr} - p_{3r}} \tag{4.50}$$

with $p_{03Rsr} = f(h_{03Rr}, s_{1r})$.

It is estimated by calculating the following loss contributions: profile (Y_{pr}), incidence (Y_{incr}), blade loading (Y_{blr}), hub-to-shroud loading (Y_{hsr}), clearance (Y_{clr}):

$$Y_r = Y_{pr} + Y_{incr} + Y_{blr} + Y_{hsr} + Y_{clr} \tag{4.51}$$

The profile loss is given by:

$$Y_{pr} = \frac{2\Theta_r + \Delta_r^2}{(1 - \Delta_r)^2} \tag{4.52}$$

$$\Theta_r = 1 - \left[1 - 2\left(\frac{\theta_{wr}}{b_{wr}}\right)\right]\left[1 - \left(\frac{\theta_{bsr}}{b_{br}} + \frac{\theta_{bpr}}{b_{br}}\right)\right] \tag{4.53}$$

$$\Delta_r = 1 - \left[1 - 2\left(\frac{\delta^*_{wr}}{b_{wr}}\right)\right]\left[1 - \left(\frac{\delta^*_{bsr}}{b_{br}} + \frac{\delta^*_{bpr}}{b_{br}}\right)\right] \tag{4.54}$$

Like in the nozzle, three "momentum thicknesses" are defined to account for the flow condition at the wall, blade suction surface and blade pressure surface. The dimensional lengths used at the denominator are:

$$b_{br} = esse_{3r} \sin \beta_{3r} \tag{4.55}$$

$$b_{wr} = b_{3r} \tag{4.56}$$

The same hypotheses of the nozzle about the blade loading distribution are made in the rotor analysis.

Some authors do not distinguish between skin friction losses caused by shear forces on the passage solid surface and blade loading losses due to cross-stream or secondary flow (blade losses are also referred as secondary losses). The reason of this choice is three-fold: (i) the difficult of experimentally measuring these effects separately in radial turbomachines; (ii) friction and secondary losses are both viscous, boundary layer effects; (iii) maintain a simple formulation in view of the uncertainties which are inherent to a 1D analysis. Basically, two alternative approaches are proposed

in the literature: mean kinetic energy formulation and frictional loss formulation. As instance, Futral and Wasserbauer [57] model belongs to the former category and it is based on the meridional component of kinetic energy at rotor inlet and the total kinetic energy at the outlet

$$\Delta q = \frac{k(c_{m1r}^2 + w_{3r}^2)}{2u_{1r}^2} \tag{4.57}$$

where k is an experimentally determined coefficient whose value obviously originates from the available test data.

Frictional loss formulations have the same structure of Eq. (4.31) and are affected by analogous uncertainties on the friction coefficient. Nevertheless, Moustapha et al. [19] has recently proposed a correlation in the form

$$\Delta q = \frac{1}{u_{1r}^2} k \left(\frac{L}{D} + 0.68 \left(1 - \left(\frac{r_{or}}{r_4} \right)^2 \frac{\cos \beta_{or}}{b_{or}/c_r} \right) \right) \frac{w_{1r}^2 + w_{3r}^2}{2} \tag{4.58}$$

where the throat section (subscript "or") is considered instead of the discharge one. The first term in brackets accounts for frictional losses. The mean passage hydraulic length (L) is the mean of two quarter circle based on the rotor inlet and exit, whereas the hydraulic diameter (D) is the mean of the inlet and exit hydraulic diameters. The second term in brackets takes into account secondary flow losses: it increases with the mean radius variation and it is inversely proportional to the blade height-to-chord ratio. As usual, the constant k is experimentally determined and its value is doubled for rotors where the shroud line has a small radii of curvature because the risk of flow separation near the blade tips is higher.

The incidence loss is:

$$Y_{incr} = \sin^2 \left(\alpha'_{1r} - \alpha'^{*}_{1r} \right) \frac{p_{01r} - p_{1r}}{p_{03r} - p_{3r}} \tag{4.59}$$

α'_{1r} is the actual relative flow angle and α^*_{1r} is the optimum rotor inlet flow angle. Both these angles have to be accounted from radial direction.

The latter is estimated using the relationship

$$\tan \alpha'^{*}_{1r} = \frac{\sigma u_{1r} - c_{m1r} \cot \beta_1 - u_{1r}}{c_{m1r}} \tag{4.60}$$

where σ is the slip factor. It is defined as

$$\sigma = 1 - \frac{c'_{t1r} - c^*_{t1r}}{u_{1r}} \tag{4.61}$$

where c'_{t1r} refers to the velocity triangle which follows the blade direction.

The slip factor estimation proposed by Aungier mainly follows the model of Wiesner [58] but a corrective factor for rotors with low blade solidity is accounted for. Alternative forms for the calculation of the slip factor and, in turn, the optimum incidence angle are equally valid (see, e.g., Stanitz [59]). In any case, all the models for the slip factor estimation were originally developed for power-absorbing machines but they can be extended to turbine rotors, all velocity directions being reversed.

Note that, the incidence loss corresponds to the difference of the tangential component kinetic energy of the actual relative flow and that in optimum incidence conditions (i.e., superscript *). This choice is commonly accepted in the literature and it was originally proposed by Futral and Wasserbauer [57] and developed and tested at a later time by various NASA researchers and by Jensen [60]. Regardless of the physical meaning of the model, a better agreement with experimental data is observed by Wasserbauer and Glassman [61] when the exponent is increased to 3 for positive incidences.

The blade loading (or secondary flow) loss accounts for cross-stream or secondary flows and is estimated by

$$Y_{blr} = \frac{1}{24} \left[\frac{\Delta W}{W_{3r}} \right]^2 \tag{4.62}$$

where ΔW is the relative velocity difference between suction and pressure surface which is calculated according to the procedure already outlined in the nozzle analysis.

The hub to shroud loading loss accounts for the secondary flows produced by the pressure gradient in the hub-to-shroud direction

$$Y_{hsr} = \frac{1}{6}\left(\frac{\kappa_m b_{3r} W_{2r}}{W_{3r}\sin\alpha_{3r}}\right) \tag{4.63}$$

where κ_m is the mean curvature of the meridional channel.

Blade loading loss and hub to shroud loss coefficients are computed as mixing losses and are adapted from the impeller performance analysis for centrifugal compressors of Aungier [62]. The absolute flow angle in the hub to shroud loss accounts for the higher exit flow profile distortion in turbine impellers compared to centrifugal compressors.

The blade clearance loss due to to the leakage from the rotor blade pressure to suction surfaces across the clearance gap between the rotor and its shroud is estimated by:

$$Y_{clr} = \frac{\dot{m}_{cl}}{\dot{m}}\frac{\Delta p}{p_{03Rr} - p_{3r}} \tag{4.64}$$

where $\dot{m}_{cl}$ is the clearance gap leakage mass flow rate between adjacent vanes defined by

$$\dot{m}_{cl} = \rho_{aver} u_{cl} L_r N_r \delta_c \tag{4.65}$$

and δ_c is the clearance gap.

The physical basis of this loss model is explained in the following. The power (P) extracted by the turbine can be written as

$$P = \omega T = \omega r_{aver} N_r b_{aver} L_r \Delta p \tag{4.66}$$

where T is the torque, the subscript *aver* stand for averaged rotor quantity, L_r is the rotor path length and Δp is the pressure difference between blade suction and pressure side. Since it is also $P = \dot{m}\Delta h_0$, it results

$$\Delta p = \frac{\dot{m}(r_{1r} c_{t1r} - r_{3r} c_{3r})}{r_{aver} b_{aver} N_r L_r} \tag{4.67}$$

The fluid velocity through the clearance gap u_{cl} is linked to the pressure difference Δp by

$$\Delta p_{cl} = 1.5\frac{1}{2}\rho_{aver} u_{cl}^2 \tag{4.68}$$

where the coefficient 1.5 is determined by comparison with experiments.

Thus, from Eq. (4.68) it is

$$u_{cl} = 0.816 \left(\frac{2\Delta p}{\rho_{aver}} \right)^{0.5} \tag{4.69}$$

The clearance gap leakage mass flow rate ($\dot{m}_{cl}$) is by continuity

$$\dot{m}_{cl} = \rho_{aver} \delta_c L_r u_{cl} N_r \tag{4.70}$$

Finally, being the loss power due to the clearance mass flow rate ($\dot{m}\Delta h_{0cl}$) equal to the pumping power across the clearance ($\dot{m}_{cl}\Delta p/\rho_{aver}$), the total pressure loss coefficient of Eq. (4.64) is obtained.

Several studies for the estimation of clearance losses influence on radial turbines have been proposed in the literature (e.g., [63], [64] and [65]). They agree that the radial clearance in the exducer region is more important compared to the axial clearance in the rotor inlet region but there is considerable disagreement in the estimation of losses (see Moustapha et al. [19] for a quantitative comparison). Rodgers [51] suggests a very simple loss correlation in terms of efficiency decrease

$$\Delta\eta_{tt} = 0.1\delta_c/b_{3r} \tag{4.71}$$

where the loss is proportional to the ratio of the radial clearance (δ_c) to the outlet blade height (b_{3r}). Similarly, Krylov and Spunde [63] correlated the efficiency penalty to the radial clearance to inlet blade height and to the rotor radius ratio. Spraker [66] modeled the leakage flow as a shear flow assuming that the velocity varies linearly between the wall and the tip from zero to the local blade speed, respectively. This model is very similar to Aungier's one but the calculation of the leakage flow velocity is slightly different. Moustapha et al. [19] suggested to estimate the leakage mass flow rate in terms of axial and radial leakage gaps by assuming a simplified straight line rotor shroud contour and equal leakage flow and blade speed velocity.

Finally the disk friction loss is given in terms of enthalpy drop by:

$$\Delta h_{0df} = \frac{1}{4}\frac{C_M \rho_{aver} \omega^3 r_{1r}^5}{\dot{m}} \tag{4.72}$$

where the torque coefficient (C_M) is calculated according to the approach by Daily and Nece [67] (as very often done in the literature) with minor modifications. The torque coefficient C_M for the two faces of the disk is defined as

$$C_M = \frac{2M}{\rho_{aver} \omega^2 r_{1r}^5} \tag{4.73}$$

and its value is determined against experimental data.

In particular, these authors identify four flow regimes that may occur in the enclosed rotating disk: (i) laminar, merged boundary layers; (ii) laminar, separate boundary layers; (iii) turbulent, merged boundary layers; (iv) turbulent, separate boundary layers. The torque coefficient is calculated for each of the four flow regimes as a function of the disk-housing clearance to rotor radius ratio (Δ/r_{1r}) and the disk Reynolds number: the higher one identifies the relevant flow regime. This C_M value is used in Eq. (4.73) if the disk Reynolds number is lower than a limiting Reynolds number where roughness first become significant, i.e., the flow is smooth. On the other hand, if the disk Reynolds number is higher than a limiting Reynolds number beyond which the flow is fully turbulent, the torque coefficient to be used in Eq. (4.73) depends on both Δ/r_{1r} and the relative surface roughness. In this case it is accounted by an experimental correlation which is slightly different from that reported in the work of Daily and originally proposed by Aungier in [45].

Note that the disk friction losses are considered as external losses, so they do not influence the flow field inside the expander.

4.5 Loss evaluation for the axial turbine

Several loss prediction methods for axial turbines have been formulated over the past sixty years starting from tests on stationary cascades or direct measurements on turbine stages. The best known and well documented loss system is that of Ainley and Mathieson [68] (AM) which has been extensively used for many years to predict the performance of conventional blades turbines in both design and off-design operation. Later, as technical capabilities have improved and the availability of experimental data has increased the AM model was modified/integrated by Dunham and Came [69] in 1970 originating the so-called AMDC performance system. In 1981, AMDC model was modified, in turn, by Kacker and Okapuu [70] (KO model) and by Moustapha et al. [71]. It has to be borne in mind that the basic architecture of the AM model has been maintained by the cited authors and revisions over the years were aimed at achieving a better agreement with new experimental data and extending the model applicability. This was achieved by changing tuning constants or by taking into account the influence of flow/geometric variables which were originally assumed fixed or, at most, variable in a narrow range.

Other significant open literature loss models to predict the overall performance of axial turbine stages are those by Craig and Cox [72], Traupel [73] and Denton [74]. There are also some works specifically devoted to the prediction of some individual loss components (see e.g. Dunham [75], Lakshminarayana [76] and Yaras and Sjolander [77]).

In this work the loss system of Aungier [45] for axial turbine performance evaluation is chosen because it

- (i) is basically derived from the well-established AM, DC and KO models and thus it benefits from their previous findings, critically compares their results and improves their predictions;

- (ii) is specifically extended to treat modern high-pressure ratio turbines and the corresponding severe operating conditions;

- (iii) explicitly considers the effects on profile losses of surface roughness which might be important for small size turbines;

- (iv) it imposes asymptotic superior limits on some loss terms (e.g., secondary, shock and post-expansion losses) to avoid, differently from other methods, absurd predictions and permits, at least, more likely results.

Losses are estimated in terms of total pressure loss coefficients (Y) and it is assumed that the total pressure loss coefficient through the blade rows is the sum of several terms representing specific loss sources: profile (Y_p), secondary (Y_s), trailing edge (Y_{te}), post expansion (Y_{ex}), shock (Y_{sh}) and, for rotating rows only, clearance losses (Y_{cl}).

$$Y = Y_p + Y_s + Y_{te} + Y_{ex} + Y_{sh} + Y_{cl} \tag{4.74}$$

Although in this Section loss equations are written for a fixed row (i.e., stator) they are still valid for a rotor provided that relative flow angles (α') are substituted for absolute ones (α). When using the following Equations flow angles must be expressed as

$$\alpha_1 = 90 + \arctan(c_{t1}/c_m) \tag{4.75}$$

$$\alpha_2 = 90 - \arctan(c_{t2}/c_m) \tag{4.76}$$

$$\alpha'_2 = 90 - \arctan(w_{t2}/c_m) \tag{4.77}$$

$$\alpha'_3 = 90 + \arctan(w_{t3}/c_m) \tag{4.78}$$

The output of the loss model is the total pressure loss coefficient of the stator (Y_N) and rotor (Y_R), respectively defined by

$$Y_N = \frac{p_{01} - p_{02}}{p_{02} - p_2} \tag{4.79}$$

$$Y_R = \frac{p_{02R} - p_{03R}}{p_{03R} - p_3} \tag{4.80}$$

where subscripts 1, 2, 3 refer to nozzle inlet, rotor inlet (or nozzle outlet), and rotor outlet, respectively.

In the following, the equations of Aungier loss system are presented and briefly compared to AM, DC and KO models to highlight similarities and differences; for each loss term a phenomenological description of the loss generating mechanisms and the physical rationale of some correlations is provided, as well.

4.5.1 Profile loss (Y_p)

Profile (or skin friction) loss is the loss which arises from the growth of the blade surface boundary layers and the attendant surface friction effects. It depends on the blade area in contact with the fluid, surface finish, Reynolds and Mach flow number in the passage and geometry of the airfoil. The profile loss coefficient suggested by Aungier is a modified form of the well-established Ainley-Mathieson [68] model. It can be represented as

$$Y_p = k_{mod}\, k_{inc}\, k_p\, k_{Re}\, k_M \left(\left(Y_{p1} + \xi^2 \big(Y_{p2} - Y_{p1}\big)\right) \left(\frac{5t_{max}}{c}\right)^{\xi} - \Delta Y_{te} \right) \tag{4.81}$$

The terms Y_{p1} and Y_{p2} are profile loss coefficients for a stator blade with an axial approach flow and for an impulse blade, respectively. They give the profile loss for a nominal blade thickness ($t/c = 0.2$), zero incidence, low Mach number ($M \leq 0.6$) and a nominal Reynolds number in terms of the pitch-to-chord ratio and exit angle ($Re = 2 \times 10^5$). It is apparent from Y_{p1} and Y_{p2} plots (see [68]) that (i) the profile loss is larger for impulse

blades compared to stator blade and (ii) the trend of profile loss versus pitch-to-chord ratio exhibits a minimum which is not too far from the optimum pitch-to-chord ratio according to well-known Zweifel criterion [78]. Item (i) and the increase of the losses with the pitch-to-chord ratio is mainly a consequence of the higher surface area in impulse blades and in high pitch-to-chord ratio blades (i.e., higher deviations or higher chords means higher area) whereas for small chord blades the beneficial effect due to area reduction is compensated by the larger suction surface diffusion losses, resulting in a rise of the overall loss.

Basic terms Y_{p1} and Y_{p2} are combined together to get the loss of the reaction blade according to interpolation scheme

$$Y_{p1} + \xi^2(Y_{p2} - Y_{p1}) \tag{4.82}$$

where

$$\xi = \frac{90 - \beta_1}{90 - \alpha_2} \tag{4.83}$$

The AM model includes in the profile loss term the trailing edge loss assuming $t_2 = 0.02s$, where t_2 and s are the trailing edge thickness and blade pitch respectively. Since in Aungier model the trailing edge loss is evaluated separately, the term ΔY_{te} subtracts this loss accounted with Eq. (4.98) for $t_2 = 0.02s$. The factor involving t_{max}/c (t_{max} is the maximum blade thickness) takes into account the effect of t_{max}/c values different from the reference one (i.e., 0.2): the higher the ratio, the higher the loss.

Factors k_i in Eq. (4.81) are corrections to the basic profile loss for Mach number, Reynolds number etc. different from those on which test data were performed and for off-design incidence angles. In particular:

- k_{mod} is an experience factor suggested by Kacker and Okapuu [70] to account for superior performance of more designs compared to those considered by Ainley and Mathieson [68] in the Fifties. A value of

0.67 is suggested by the authors. However, it would be reasonable to use a lower coefficient for contemporary turbines.

- k_{inc} is a correction for off-design incidence effects which depends on the ratio between the actual incidence and the stalling incidence: the higher the absolute value of this ratio, the higher the corrective factor. The stalling incidence is a function of the exit flow angle (α_2), factor ξ (Eq. (4.83)) and pitch-to-chord ratio. However, as in this work only design operation is considered k_{inc} does not influence the expected performance.

- k_p is a correction for compressibility effects on channel flow acceleration. A consequence of the compressibility of the working fluid is that the flow in the passage between two adjacent blades is subjected to a larger acceleration when the outlet Mach number is increased. Accordingly, the boundary layer becomes thinner and the risk of flow separation reduces. Since the original Ainley and Mathieson [68] loss model is based on low speed cascade test ($M_2 \leq 0.2$), the estimated performance might be too pessimistic when high expansion ratio turbines are analyzed. Kacker and Okapuu [70] suggest an expression of k_p which depends on inlet-to-outlet Mach number ratio ($X = M_1/M_2$) and on the outlet Mach number (M_2): losses decreases (i.e., k_p decreases) as both these parameters increase. Aungier [45] uses the same model structure but replaces M_1, M_2 and $X = M_1/M_2$ with

$$\tilde{M}_1 = (M_1 + 0.566 - |0.566 - M_1|)/2 \tag{4.84}$$

$$\tilde{M}_2 = (M_2 + 1 - |M_2 - 1|)/2 \tag{4.85}$$

$$\tilde{X} = 2\tilde{M}_1/(\tilde{M}_1 + \tilde{M}_2 + \left|\tilde{M}_2 - \tilde{M}_1\right|) \tag{4.86}$$

This modification to Kacker and Okapuu [70] model imposes an upper limit to these variables (i.e., $M_1 \leq 0.566$, $M_2 \leq 1$ and $X \leq 1$) to avoid very low unrealistic k_p values in severe operating conditions, while maintaining quite similar results in the remaining cases. The correction factor for compressibility effects is

$$k_p = 1 - (1 - k_1)\tilde{X}^2 \tag{4.87}$$

where

$$k_1 = 1 - 0.625(\tilde{M}_2 - 0.2 + \left|\tilde{M}_2 - 0.2\right|) \tag{4.88}$$

- k_{Re} is used to account for Reynolds number effects when the Reynolds numbers are different from those on which the experimental cascade tests are based. Reynolds number correction is based on friction models which estimate the variation of the skin friction coefficient with the blade chord Reynolds number Re_c evaluated at the discharge flow conditions.

  Three flow regimes are identified: laminar ($Re_c \leq 10^5$), transition ($10^5 \leq Re_c \leq 5 \times 10^5$) and turbulent ($Re_c \geq 5 \times 10^5$).

  In the transition regime it is assumed $k_{Re} = 1$ because friction models cannot estimate the complex variations of the skin friction coefficient and, in turn, k_{Re} without a detailed knowledge of the blade shape. Furthermore, experimental cascade tests refer to Reynolds number levels (i.e., $Re_c = 200000$) which lie in this transitional regime.

  In the laminar region k_{Re} is higher than unit to account for a general thickening of the laminar boundary layers and a gradual increase of separated laminar flow regions. It is based on the laminar skin

friction model

$$k_{Re} = \left(\frac{1 \times 10^5}{Re_c}\right)^{0.5} \tag{4.89}$$

In the turbulent region the evaluation of k_{Re} is less straightforward because the effect of surface roughness e has to be considered. To this end, a critical blade Reynolds number Re_r is introduced which is defined as the ratio between chord and surface roughness multiplied by a factor of 100

$$Re_r = 100\frac{c}{e} \tag{4.90}$$

If $Re_c \leq Re_r$ the surface roughness is not significant and the correction factor is dependent only on Re_c

$$k_{Re} = \left(\frac{log_{10}(5 \times 10^5)}{log_{10}Re_c}\right)^{2.58} \tag{4.91}$$

If $Re_c \geq Re_r$ and $Re_r \geq 5 \times 10^5$

$$k_{Re} = \left(\frac{log_{10}(5 \times 10^5)}{log_{10}Re_r}\right)^{2.58} \tag{4.92}$$

whereas, if $Re_c \geq Re_r$ and $Re_r \leq 5 \times 10^5$

$$k_{Re} = 1 + \left(\left(\frac{log_{10}(5 \times 10^5)}{log_{10}Re_r}\right)^{2.58} - 1\right)\left(1 - \frac{5 \times 10^5}{Re_c}\right) \tag{4.93}$$

This model is quite similar to that of Kacker and Okapuu [70], although the latter considers slightly different intervals for the flow regimes, suggests a more severe correction at low Reynolds number and especially does not consider the influence of the surface roughness in the turbulent flow. Reynolds correction of Kacker and Okapuu [70] model are

$$k_{Re} = \left(\frac{Re_c}{2 \times 10^5}\right)^{-0.4} \qquad Re \leq 2 \times 10^5 \tag{4.94}$$

$$k_{Re} = 1 \qquad 2 < \times 10^5 Re \leq 10^6 \tag{4.95}$$

$$k_{Re} = \left(\frac{Re_c}{10^6}\right)^{-0.2} \qquad Re > 10^6 \tag{4.96}$$

The AMDC model simply suggests to use the multiplicative factor $(Re/2 \times 10^5)^{-0.2}$ to penalize small turbines where low Reynolds flow regime could occur and disregards the influence of the surface roughness. Instead, the method of Craig and Cox [72] is one of the few which considers the effects of surface roughness on the Reynolds correction.

Note that, according to Aungier model the influence of Reynolds number on k_{Re} for very high Reynolds number (i.e., $Re_c \geq 10^7$) is weaker than in KO and AMDC models but in accordance with Craig and Cox findings. Thus, Reynolds number correction which disregard the influence of surface roughness might lead to unreliable results, especially when dealing with high-pressure ratio turbines and when dealing with a variety of sizes.

- k_M is the Mach number correction as originally proposed by the AM model and it depends on the ratio of the pitch to the suction surface radius of curvature s/R_c and the discharge Mach number M_2: the higher s/R_c and M_2, the higher k_M, i.e., the higher the loss

$$k_M = 1 + (1.65(M_2 - 0.6) + 240(M_2 - 0.6)^4)(s/R_c)^{3M_2 - 0.6} \tag{4.97}$$

Note that the Mach number range is limited to $0.6 \leq M_2 \leq 1$ when applying Eq. (4.97).

4.5.2 Trailing edge loss (Y_{te})

The trailing edge loss coefficient is computed as an expansion loss through an abrupt area enlargement and is obviously proportional to the squared area ratio. The effective passage width after the mixing is estimated as $s \sin \beta_g$ because it is assumed that the discharge flow angle is

approximately equal to the gauging angle β_g ($\sin\beta_g = o/s$, where o is the blade throat); on the other hand, the passage width before the mixing is reduced by the trailing edge thickness to yield $s\sin\beta_g - t_2$. Accordingly, assuming no density change across the area enlargement it is

$$Y_{te} = \left(\frac{t_2}{s\sin\beta_g - t_2}\right)^2 \tag{4.98}$$

Kacker and Okapuu [70] performed an extensive survey of cascade results and correlated the trailing edge loss coefficients in terms of enthalpy to the ratio between the trailing edge thickness and the blade throat. Similarly to what is done for the profile losses, they produced distinct correlations for stator blades with an axial approach flow and for an impulse blades: the latter have lower loss coefficients due to the thinner boundary layers. For blades other than the two basic types, trailing edge losses are interpolated in a manner similar to profile losses.

4.5.3 Secondary flow loss (Y_s)

The secondary flow are vortices due to the lower fluid velocities in the endwall boundary layers than in the mainstream and the curvature of the passage which cause some parts of the fluid to move in different directions than the principal direction of the flow. Secondary flows create a momentum deficit and a low momentum fluid redistribution through the passage, i.e., a loss. Japikse and Baines [48] recognize three vortex type depending on the part of the blade passage in which they originate. Trailing edge vortices at the trailing edge of the blade, cascade vortices in the blade passage generated as the endwall boundary layers roll up under the action of the cross-passage pressure gradient and corner vortices near the blade leading edge.

The secondary flow loss coefficient Y_s accounts for cross-stream or secondary flows (i.e., vortices) and its formulation was originally proposed by

Ainley and Mathieson [68] and subsequently modified over the years by different authors (e.g., Dunham and Came [69] and Kacker and Okapuu [70]) in respect of some details while conserving the overall structure which is commonly accepted today. Also the loss coefficient formulation of Aungier is very similar to the AMDC model as revised by Kacker and Okapuu but some modifications are introduced to extend the range of applicability and to avoid too pessimistic loss estimations in severe operating conditions.

The basic secondary flow loss coefficient $\widetilde{Y}_s$ is calculated as

$$\widetilde{Y}_s = 0.0334 F_{AR} Z \frac{\cos \alpha_2}{\cos \beta_1} \tag{4.99}$$

The loading factor Z, as originally introduced by Ainley, is

$$Z = \left(C_L \frac{c}{s} \right)^2 \frac{\sin^2 \alpha_2}{\sin^3 \alpha_m} \tag{4.100}$$

where α_m is the mean flow angle and C_L is the lift coefficient

$$C_L = 2(\cot \alpha_1 + \cot \alpha_2) \frac{s}{c} \sin \alpha_m \tag{4.101}$$

These Equations highlight that the secondary flow losses are proportional to the flow turning because the vortices which cause the loss are created by a normal pressure gradient acting on fluid in the endwall boundary layer. The higher the turning, the more intense the pressure gradient, the higher the strength of vortices and cross-stream flows.

The factor F_{AR} in Eq. (4.99) is an aspect ratio (h/c) correction aimed at improving predictions at low aspect ratios. Secondary flow losses increase as the ratio h/c decreases because on blades of low aspect ratio the secondary flow effects are limited to endwall regions and the flow at midspan is nearly uniform, whereas on small aspect ratios blades secondary flows influence a greater proportion of the passage. So,

$$F_{AR} = c/h \; if \; h/c \geq 2 \tag{4.102}$$

$$F_{AR} = 0.5(2c/h)^{0.7} \; h/c < 2 \tag{4.103}$$

$$F_{AR} = \begin{cases} c/h & if \quad h/c \geq 2 \\ 0.5(2c/h)^{0.7} & if \quad h/c < 2 \end{cases}$$

Note that F_{AR} values predicted by Eq. (4.103) are less pessimistic in the lower aspect ratio range compared to the estimations of Dunham and Came [69] and Kacker and Okapuu [70], whereas almost identical results are obtained for high h/c ratios. The secondary flow loss coefficient is given by

$$Y_s = k_{Re} k_s \left(\frac{\widetilde{Y_s}^2}{1 + 7.5\widetilde{Y_s}^2} \right)^{0.5} \tag{4.104}$$

The expression in the square root in Eq. (4.104) imposes an asymptotic upper limit on the preliminary estimate of about 0.365 to avoid excessive values of this loss in extreme conditions. Two corrective factors are included in Eq. (4.104): k_{Re} and k_s. The former is the same Reynolds number correction used for profile losses; the latter is a modified form of the compressibility correction suggested by Kacker and Okapuu [70] and it is necessary because the compressibility has an effect on the acceleration of the flow next to the endwalls, and hence on the secondary losses. It is

$$k_s = 1 - (1 - k_p) \frac{(b/h)^2}{1 + (b/h)^2} \tag{4.105}$$

where b is the axial chord and k_p is the same corrective factor used in the profile loss estimation. The term at the denominator in Eq. (4.105) limits k_s for cases where b/h is very large.

4.5.4 Shock loss (Y_{sh})

The shock loss considers the possible formation of shock waves at highly curved blade leading edges near the hub in subsonic flow regimes. This is

because the radial variations of gas conditions imposed by radial equilibrium result in higher local acceleration near the hub and, in turn, higher hub Mach numbers than those at the mean line. A preliminary estimate $\widetilde{Y_{sh}}$ of the shock loss coefficient is given by

$$\widetilde{Y_{sh}} = 0.8X_1^2 + X_2^2 \tag{4.106}$$

where X_1 linearly depends on the inlet Mach number ($X_1 = M_1 - 0.4$) and X_2 considers the possibility of flow diffusion which may be met at far off-design operating conditions. An asymptotic upper limit of unity is imposed in the actual shock loss coefficient calculation

$$Y_{sh} = \sqrt{\frac{\widetilde{Y_{sh}}^2}{1 + \widetilde{Y_{sh}}^2}} \tag{4.107}$$

Instead, according to KO model the Mach number correction for an ideal gas is

$$Y_{sh} = \frac{r_h}{r_t} 0.75(M_{1h} - 0.4)^{1.75} \frac{p_1}{p_2} \frac{1 - \left(1 + \frac{\gamma-1}{2} M_1^2\right)^{\frac{\gamma}{\gamma-1}}}{1 - \left(1 + \frac{\gamma-1}{2} M_2^2\right)^{\frac{\gamma}{\gamma-1}}} \tag{4.108}$$

where subscripts h and t stand for hub and tip, respectively. The presence of the ratio r_h/r_t in Eq. (4.108) results in lower penalization as the blade height increases being the shock wave a local phenomenon.

4.5.5 Supersonic expansion loss (Y_{ex})

The supersonic expansion loss accounts for shock waves which occur when the flow at the discharge of a blade row is over-expanded to supersonic Mach numbers. The correlation suggested by Aungier is original and does not represent an improvement of other authors previous findings and it is

$$Y_{ex} = \left(\frac{M_2 - 1}{M_2}\right)^2 \tag{4.109}$$

The literature offers very few models for the estimation of this loss component and their results are particularly uncertain due to the severe lack of cascade tests of adequate quality and the inherent difficulty to model such complex flow phenomena through a mean line analysis.

Dunham and Came [69] proposed to account for supersonic expansion losses by a multiplier on the profile loss coefficient

$$k = 1 + 60(M_2 - 1)^2 \tag{4.110}$$

but the same authors admitted that their model is quite arbitrary and not supported by solid experimental evidences. Kacker and Okapuu [70] have doubts about the reliability of Eq. (4.110) because it is independent from the blade exit angle and, in turn, ignores the limit loading of airfoils but they do not offer any valid alternative method. In addition, as highlighted by Aungier, Eq. (4.110) gives unreliable results for high Mach numbers which are typical in organic fluid applications and it is questionable to expect that the supersonic expansion loss should depend on the profile losses as it has a different nature.

4.5.6 Blade clearance loss (Y_{cl})

The blade clearance loss is due to the tip flow which goes through the clearance between the blade tip and the casing from the pressure side to the suction side of the blade. The loss is caused by (i) the mixing of the leakage flow with the main flow near the suction surface and downstream of the blade and (ii) the formation and viscous/turbulent dissipation of leakage vortices along with their interaction with the main flow. The main factors influencing the tip leakage loss are the clearance gap size, the pressure difference between the pressure and suction surface and the rotor configuration (shrouded or unshrouded).

The method suggested by Aungier for the calculation of the blade clear-

ance loss coefficient for unshrouded blade rows (which are those here considered) is the same as Dunham and Came

$$Y_{cl} = 0.47 Z \frac{c}{h} \left(\frac{\delta}{c} \right)^{0.78} \tag{4.111}$$

where δ is the clearance, Z is the loading parameter as defined by Eq. (4.100) and c/h is the chord-to-blade span ratio. This model derives, in turn, from that originally suggested by Ainley and Mathieson [68] but in the latter the loss coefficient is calculated as a linear function of the tip clearance instead of power function.

4.6 Model resolution for radial turbine

The design and performance prediction of the radial inflow turbine (RIT) is carried out by a Matlab® script developed by the author coupled with Refprop fluid properties database.

Figure 4.2 shows at a glance the global architecture of the model and highlight the starting and ending points of the procedure. The model is composed of two main routines, namely the "design routine" and the "operation routine" (bold font in Fig. 4.2).

The design routine determines the RIT geometry starting from the specifications dictated by the thermodynamic analysis (total inlet state, mass flow rate and discharge static pressure), the designer choices on specific speed and velocity ratio and some first guess values to initialize the calculations. Instead, the performance routine evaluates the flow field in the RIT and the resulting efficiency using the geometry and the total inlet state and discharge pressure as inputs. The final design of a RIT requires several cascaded runs of the design and performance routines to update the guess values used in the design run (see recirculation arrow in Fig. 4.2), till convergence.

In the following Sections both the design and the operation routines recalled in bold in Fig. 4.2 are sequentially presented in detail. Several flowcharts support the explanation of each of them to show step-by-step the equations, the main assumptions and where they are used and the different cases which could be faced. In particular, Section 4.6.1 illustrates the design of the expander components, whereas Section 4.6 shows how the operation routine works to solve the flow field. In the latter, particular attention is paid on two issues which require several iterative loops and the activation from time to time of different blocks of instruction: (i) the calculation of the mass flow rate (see Section "Calculation of the mass flow rate matching the specified turbine outlet pressure"), (ii) the management of the choking flow operation (see Section "Solution of the flow field when chocking occurs").

4.6.1 Design routine

As shown in Fig. 4.2 the input data for the design routine are: (i) the turbine inlet state (p_{01}, T_{01}), the turbine outlet pressure (p_5) and the mass flow rate of the working fluid ($\dot{m}$), given by the thermodynamic analysis; (ii) the couple specific speed (n_s) - velocity ratio (ν_s); (iii) first guess values for some variables (total-to-static efficiency η_s, total pressure at rotor inlet p_{04}, total density at rotor outlet ρ_{05}) and (iv) some kinematic/geometrical assumptions (e.g., null tangential velocity at rotor outlet, blade thickness, etc.). Obviously, (iii) do not influence the final design of the turbine (i.e., the exit from Fig. 4.2 is the same), but only lengthen or shorten the execution time for the search of convergence. The flowcharts of Figs. 4.4 to 4.6 show the inputs and the model equations in the exact order they are implemented in the Matlab® code.

Figure 4.3 depicts the meridional view of the inflow radial turbine and the nozzle showing the relevant geometrical parameters using the notation

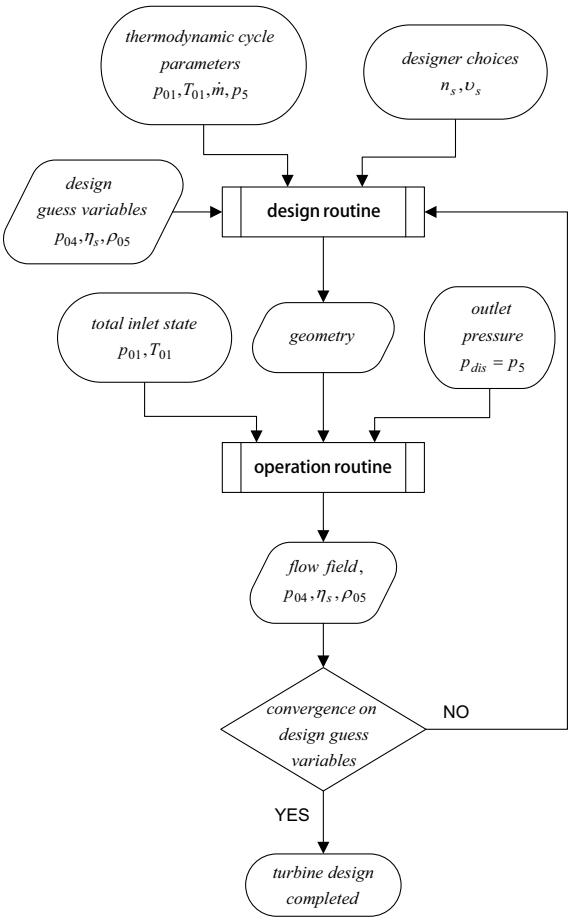

Figure 4.2: General model architecture for the design and the operation analysis of a radial inflow turbine.

employed in the design routine.

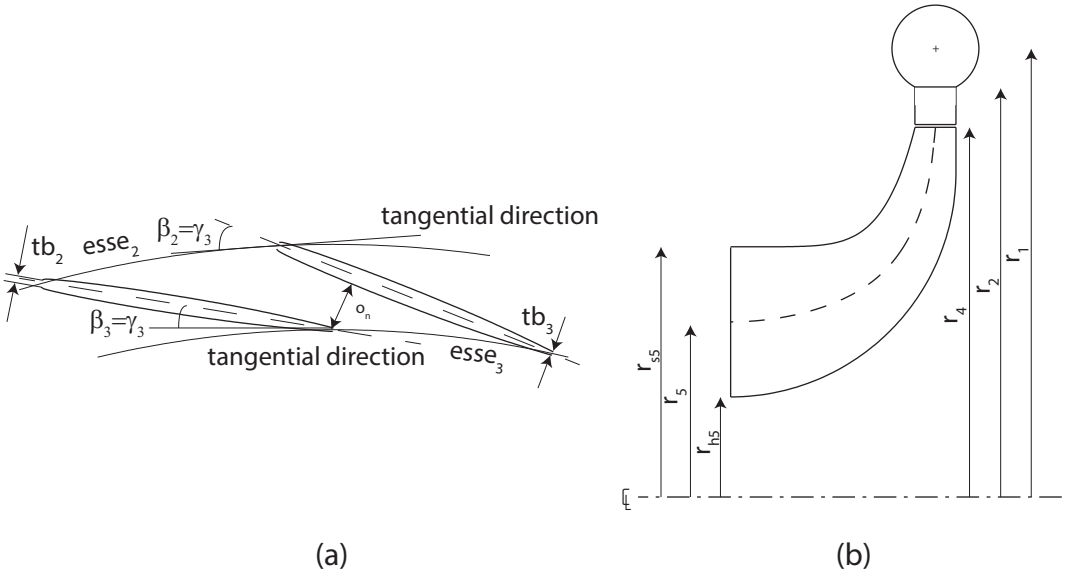

Figure 4.3: Radial inflow turbine: (a) nozzle geometry; (b) meridional view of the radial inflow turbine.

Rotor inlet

The various steps in the design of the rotor inlet station are outlined in Fig. 4.4. The combined choice of specific speed (n_s) and velocity ratio (ν_s) gives the rotational speed (ω) and turbine diameter (D_4). The Euler equation provides the tangential absolute velocity at rotor inlet (C_{t4}) required to achieve the desired specific work assuming a zero swirl at turbine exit ($C_{t5} = 0$). The absolute angle at rotor inlet (α_4) is estimated by a correlation with n_s predicting higher flow angles at higher n_s values (see [45]). Accordingly, the meridional velocity (C_{m4}), relative velocity (W_4) and the overall velocity triangle at turbine inlet can be calculated. The static enthalpy at rotor inlet (h_4) can be directly calculated from the total enthalpy, which is constant in the stator (i.e., $h_{01} = h_{04}$), and the absolute velocity (C_4). By combining the information on h_4 and p_{04} (a guess variable at the beginning of the design), the thermodynamic state at ro-

tor inlet is fully defined. The flow angle α_4 is also used to evaluate the optimum number of rotor blades (Nr) by using a correlation available in [45], which gives a higher number of blades at lower α_4. The rotor inlet blade height (b_4) directly derives from the continuity equation, taking into account the inlet metal blockage factor (k_{b4}), which needs an assumption on the blade thickness (t_{b4}).

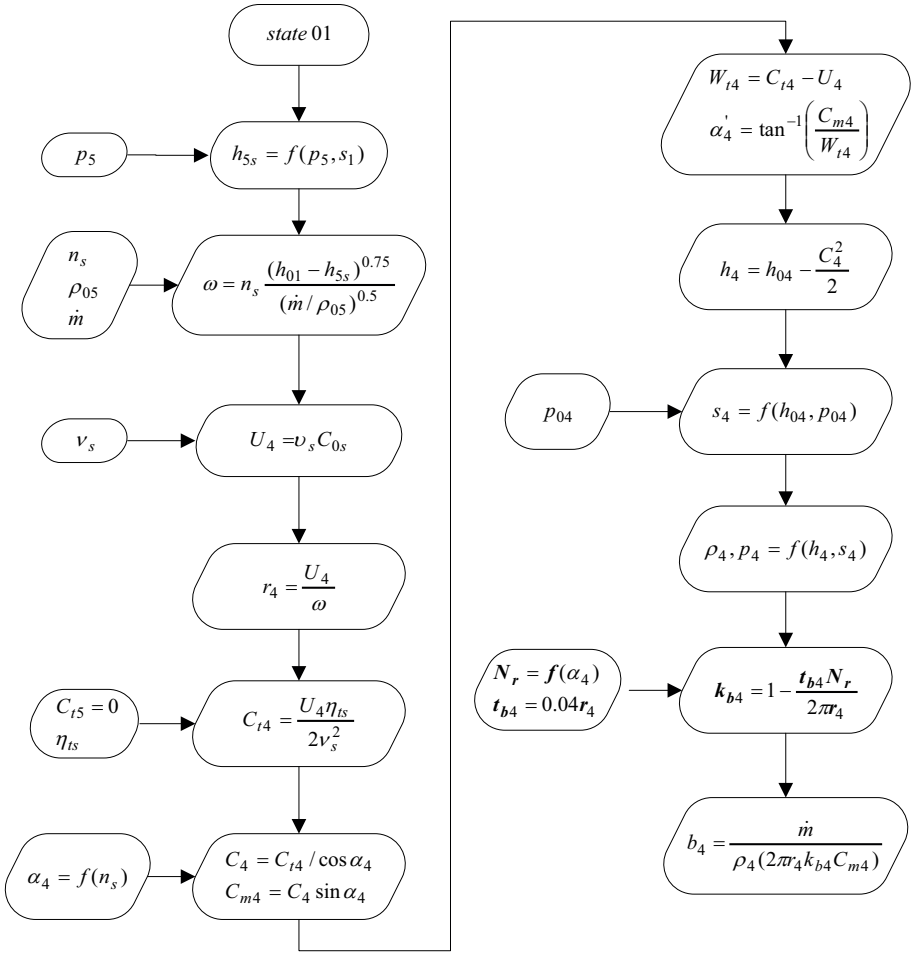

Figure 4.4: Design of the rotor inlet.

Rotor outlet

The steps in the design of the rotor outlet station and the meridional channel are shown in the flowchart of Fig. 4.5.

The design starts from the basic assumptions of a nearly constant

meridional velocity throughout the rotor and zero exit swirl. From the guess value of turbine efficiency (η_s), the total enthalpy at rotor outlet can be calculated and, in turn, the static enthalpy (h_5). So, all the thermodynamic variables at rotor exit can be calculated, being the discharge pressure (p_5) a design specification. The exit hub radius (r_{h5}) is simply estimated as a percentage of the rotor inlet radius, whereas the exit shroud radius (r_{s5}), which is obtained by the continuity equation, requires an iterative mass balance to converge on the outlet blockage factor (k_{b5}). By simply calculating the rotor exit radius (r_5) as mathematical average of the hub and shroud radii, the velocity triangle at rotor exit is fully defined. In case the blockage at rotor exit is too high (i.e., $k_{b5} < 0.50$), the number of blades is progressively reduced and all variables depending on N_r must be consequently recalculated.

The geometry of the rotor outlet must fulfill the two main constraints (see, e.g., [27], [45]) related to the maximum shroud radius, in order to avoid an excessive curvature of the meridional channel ($r_{s5} < 0.7r_4$), and the minimum hub radius for the shaft ($r_{h5} > 0.4r_{s5}$). A third constraint ($A_5/A_4 < 2.5$) is added in this study to limit the significant increase of the flow passage area from turbine inlet to outlet dictated by the high density variation. In fact, this may cause flow separation and the generation of span-wise velocity components, which can be detected only by a detailed 3D CFD study. All these constraints (Table 4.1) concur to the reduction of the flow discharge passage area and, in turn, to the increase of the meridional velocity at rotor outlet (C_{m5}). This adjustment causes an increase of the relative flow angle which sets the blade angle (β_5) at rotor exit. As the overriding majority of turbine designs considered in this study shows subsonic relative flow conditions at rotor outlet, the rotor throat width (o_5) can be directly evaluated from the blade pitch ($esse_5$) by continuity between throat and exit sections. Instead, if supersonic flow conditions occur, further calculations are needed, as shown in upper right blocks in

Table 4.1: Constraints in the sizing of the rotor outlet station.

maximum shroud radius	$r_{s5} < 0.7r_4$
minimum hub radius	$r_{h5} < 0.4r_{s5}$
maximum increase of the flow passage area	$A_5/A_4 < 2.5$

Fig. 4.5. Finally, the axial length of the rotor (Δz_r) is directly obtained from the blade height at rotor outlet.

The rotor hub contour is designed to minimize passage curvature effects by using the largest circular-arc that is compatible with the rotor dimensions previously obtained. A power-law relation parametric with ξ (see paragraph 10.6 in [45]) allows the definition of the shroud contour in order to achieve a passage area on the mean quasi-normal (A_m) that is approximately equal to the average of the rotor inlet and outlet passage areas. Straight-line element blades are adopted. Blade angle distributions (β) along the meridional coordinate for hub, shroud and mid-line can be calculated from the corresponding camberline blade angle distributions (θ).

Nozzle

All the calculations required to design the nozzle are shown in detail in Fig. 4.6 and are summarized in the following.

The passage width is assumed constant throughout the nozzle and equal to the blade height at rotor inlet. The tangential absolute velocity at nozzle outlet (C_{t3}) is simply obtained by the conservation of the angular momentum in the annulus. As the blade loading criterion proposed by Aungier [45] ($k_{load} = 1$), which determines the optimum number of nozzle blades (N_n), involves variables which will be known only at the end of the design procedure, it is necessary to repeat the design procedure for a set of nozzles having different N_n (in the range 18-33). Moreover, guess values for blade blockage (k_{b3}), fluid density (ρ_3) and blade setting angle (γ_3) are

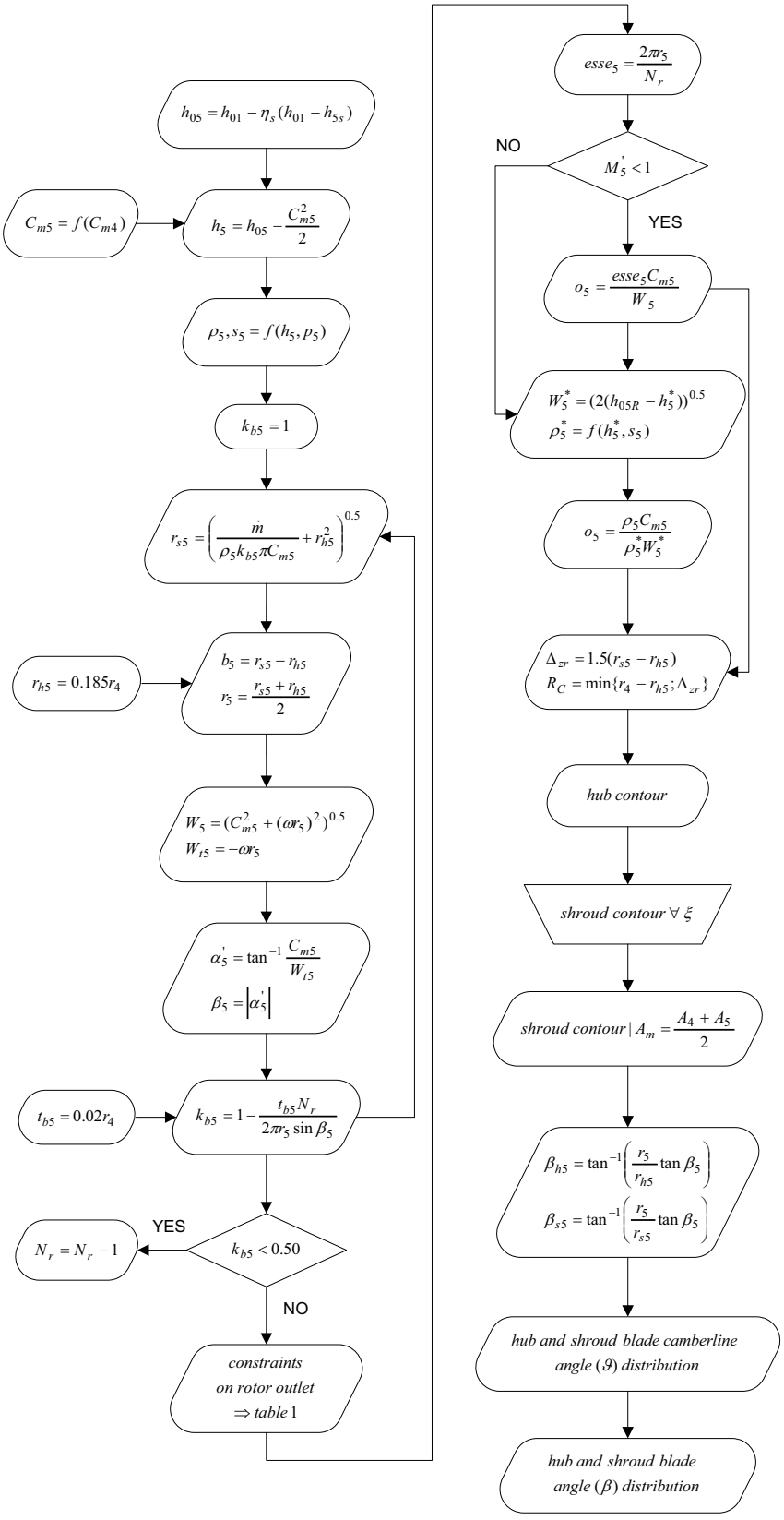

Figure 4.5: Design of rotor outlet and meridional channel.

required to initialize the calculations and updated until convergence (see Fig. 4.6).

Supersonic flow regimes often occur at nozzle outlet due to the high tangential absolute velocity and the low speed of sound typical of high molecular weight fluids. When the Mach number at nozzle outlet (M_3) is higher than one, the nozzle is choked and sonic flow conditions (star superscript) take place at the throat (o_3). The nozzle throat width o_3 is calculated from the pitch ($esse_3$) and the throat-to-pitch ratio $(o/esse)_3$, where the latter derives from the mass flow conservation between throat and exit section. The chord of the nozzle blades follows from a direct assumption on the pitch-to-chord ratio (0.75).

Nozzle blades are designed by imposing an elementary thickness distribution on a straight line camberline (see paragraph 10.9 in [45]). Only a specific value of the setting angle (γ_3) yields the throat width o_3 calculated above. Thus, an iterative method is needed to graphically obtain the desired value of the throat width. After a first guess value of γ_3 is chosen, two consecutive blades are drawn and the measured o_3 is used to obtain a new estimate of $\gamma 3$ until convergence (i.e., $\bar{o}_3 = o_3$).

The setting angle is used to calculate the radius (r_2) and blade angle (β_2) at nozzle inlet. The inlet flow angle (α_2) slightly differs from the blade angle by the optimum incidence angle (i_n) (see [24]). Finally, the nozzle fulfilling a constraint on minimum γ_3 ($> 3°$) and satisfying the optimum blade loading condition is selected. Similarly to nozzle outlet, the velocity triangle and thermodynamic state are determined through an iterative mass balance.

4.6.2 Performance routine

In this Section the general features of the performance routine are first described. Then the procedure used to solve the flow field in each ex-

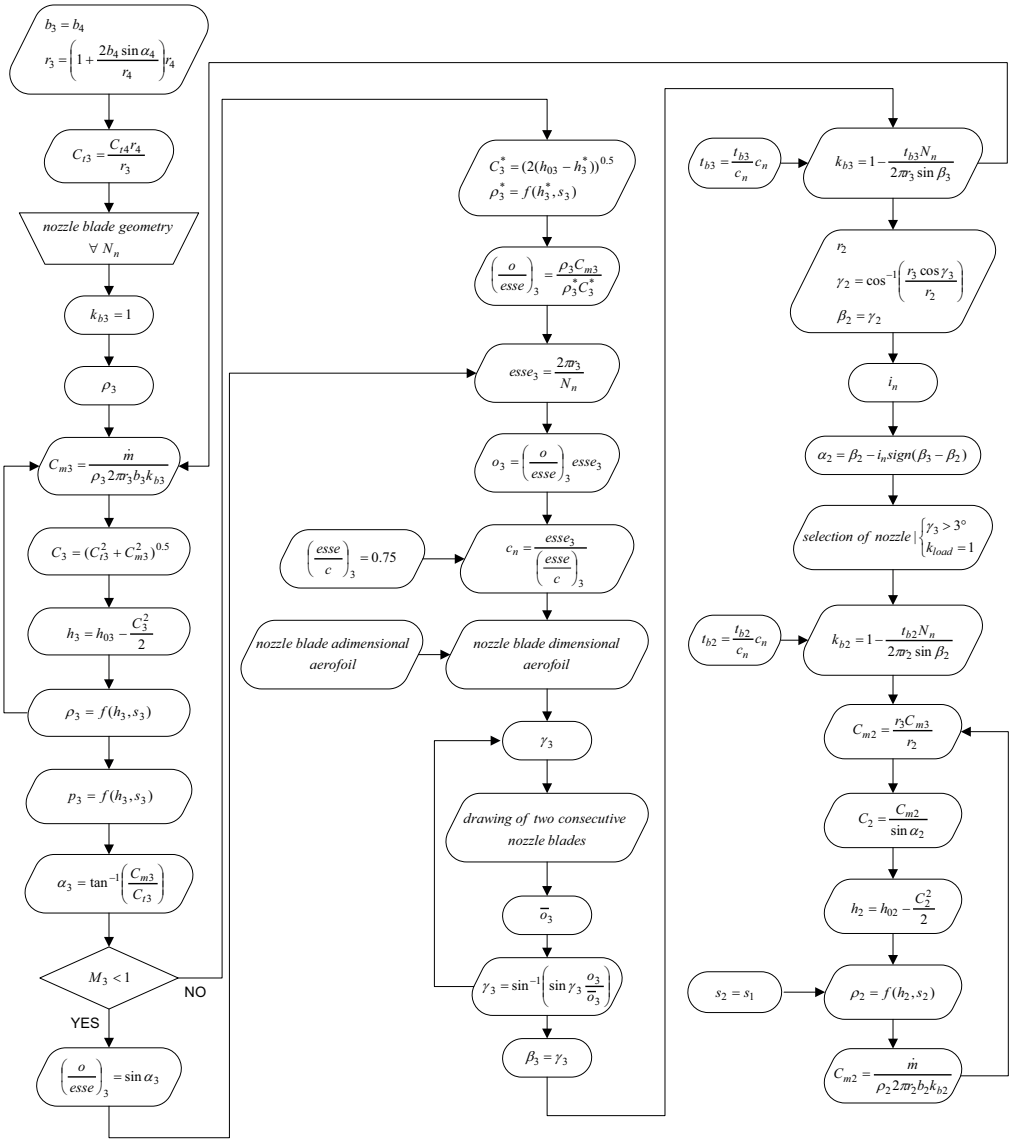

Figure 4.6: Design of the nozzle.

pander component is summarized and shown in detailed flowcharts; the procedure for the calculation of the mass flow rate matching the specified turbine outlet pressure is presented, as well. Finally, some strategies which were applied to solve specific calculation issues (e.g., choked operation) are presented. Although these routines are outlined individually for clarity's sake, they are strongly interrelated each other. Several flow charts provide the quantitative formulation of the analysis and help the reader to understand the hierarchical and strongly non linear structure of the code and the several iterative loops during the search of the solution.

The performance routine is the code section which solves the flow field along the mean line in each expander component (volute, nozzle, annulus, rotor) and finally calculates the expander efficiency (η_s). It uses as input data: (i) the geometry defined by the design routine, (ii) the total inlet state at turbine inlet (p_{01}, T_{01}) and (iii) the specified static pressure at rotor outlet (p_{dis}) (see Fig. 4.2). Although this routine may potentially be used to investigate off design operation by varying the total expander inlet state and/or the rotor discharge pressure (p_{dis}), it is used in this work to predict the flow field and the turbine efficiency at design conditions. Accordingly, the input variables p_{01}, T_{01} do not differ from those specified in the design routine and p_{dis} is the design discharge pressure ($p_{dis} = p_5$).

Unlike the design routine, which calculates only the inlet and outlet stations of each component, the performance routine solves the flow field at three stations: inlet (subscript 1), mid (2) and outlet (3) for a better analysis of the flow field and, in turn, a more accurate prediction of the losses. The irreversibilities along the expansion process are quantified by total pressure loss coefficients (Y, see Section 4.4) which are taken into account when solving stations 3 only, since no entropy increase is assumed between stations 1 and 2. However, the loss estimate depends on the geometrical and kinematic parameters of all three stations.

Iterative mass balances are widely used in the code to solve the flow

field. They follow this recurrent scheme: a guess value of static density is first assumed to calculate the velocity from the continuity equation. This allows the evaluation of the static enthalpy from the known total state (static frame) or rothalpy (relative frame) and, in turn, the static pressure and density by means of the equation of state. The new calculated density value updates the guess value and is backward used in the mass balance inside a loop, until convergence on the desired mass flow rate is reached.

It is to be borne in mind that in the performance routine the mass flow rate ($\dot{m}$) is not given (as it is instead in the design routine), but rather calculated. In fact, for assigned turbine geometry and total conditions at stage inlet, there is only one specific value of mass flow rate resulting in the specified rotor outlet static pressure (p_{dis}). This value slightly differs, yet it is generally close to that assumed in the design routine, due to minor effects which are disregarded in the definition of the overall turbine geometry.

Volute

Figure 4.6.2 shows the various steps in the evaluation of the volute performance; subscript v stands for "volute". The total state at volute inlet (i.e., the stage inlet) is known. The passage area (A_{1v}) and mean radius (r_{1v}) at station 1 are known from the design routine. Using a guess value of density (ρ_{1v}) the absolute velocity (C_{1v}) and static enthalpy (h_{1v}) can be calculated. So, a new value of density can be calculated from the two state variables (h_{1v}, s_{1v}), which updates the previous one until convergence.

The tangential velocity at station 2 (C_{t2v}) is calculated from the conservation of angular momentum.

Station 3 is the annular passage at volute exit (i.e., nozzle inlet). At this station both the radius and passage width are known from the design routine so that the passage area (A_{3v}) can be easily calculated. The so-

lution of the flow field in the volute proceeds with the calculation of the overall loss coefficient (Y_v) (see Section 4.4.1). By using the definition of total pressure loss, the total pressure at volute outlet (p_{03v}) is calculated. So, the entropy and all static variables at volute exit can be obtained. The volute analysis is completed when the convergence on the mass flow rate (ϵ is the tolerance) is reached.

Nozzle

Fig. 4.8 shows the flowchart to evaluate the performance of the nozzle. The nozzle geometry is specified at the inlet, mid-passage and outlet from the design routine. The tangential velocity at nozzle inlet (C_{t1n}) is equal to the tangential velocity at volute outlet (C_{t3v}). A first guess nozzle inlet density (ρ_{1n}) is assumed to calculate the meridional velocity (C_{m1n}) and, in turn, the static enthalpy (h_{1n}). A new value of density is calculated from the couple (h_{1n}, $s_{1n} = s_{3v}$) which updates the previous one till convergence. So, the velocity triangle at nozzle inlet is defined and the flow angle (α_{1n}) can be calculated.

A guess value is assumed for density at station 2 (ρ_{2n}) to calculate C_{m2n}. The velocity C_{2n} is calculated by assuming that the flow angle is equal to the blade angle ($\alpha_{2n} = \beta_{2n}$). Accordingly, the static enthalpy (h_{2n}) and all the static properties at station 2 can be obtained (being $s_{2n} = s_{1n}$). After reaching convergence, station 2 is solved.

Then, guess values are assumed for the density (ρ_{3n}) and pressure (p_{3n}) at nozzle outlet which allows the velocity (C_{3n}) and static density (h_{3n}) to be calculated. The solution of the flow field in the nozzle proceeds with the calculation of the overall loss coefficient (Y_n) (see Section 4.4.2). The profile loss is calculated by using the main geometrical features of the nozzle, the fluid velocities and the number of blades. The post-expansion loss accounts for shock losses occurring at supersonic flow conditions often experienced by organic fluids. From the definition of total pressure loss

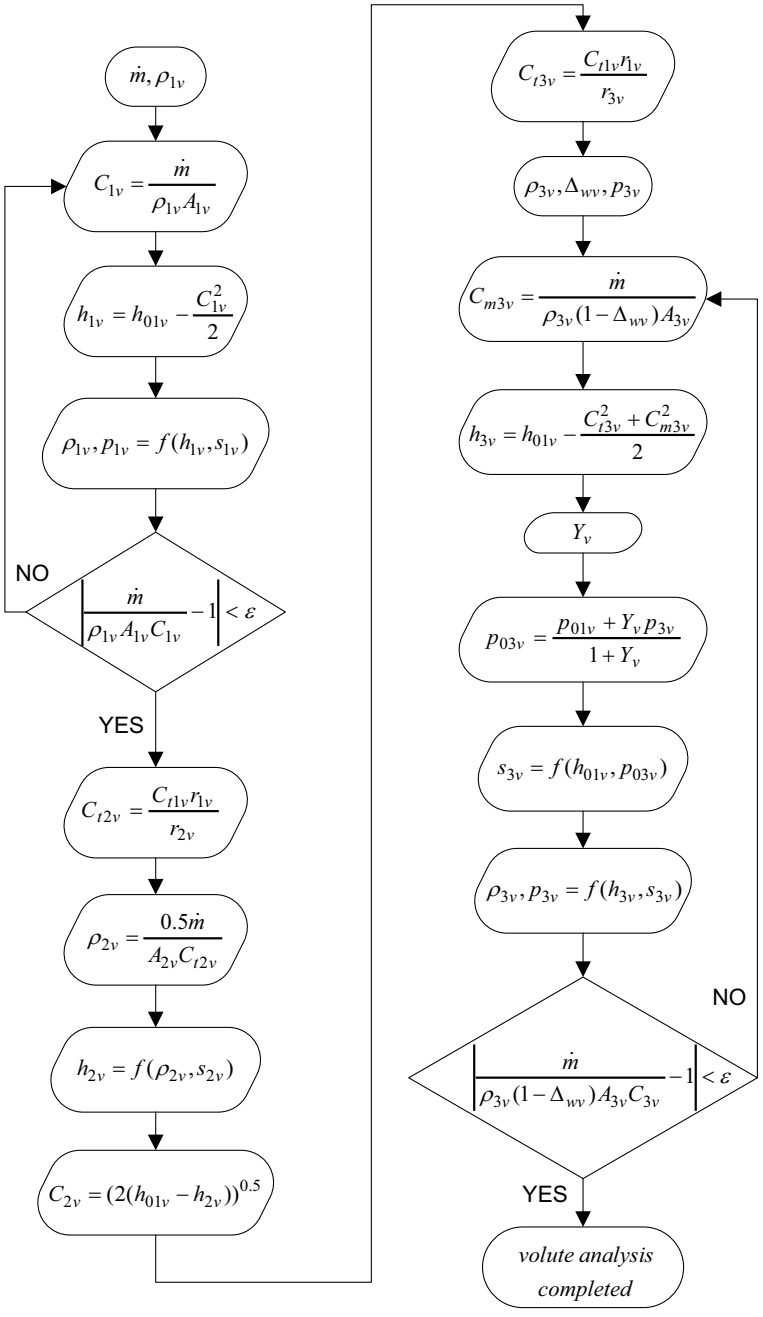

Figure 4.7: Operation of the volute.

coefficient the total pressure at nozzle outlet (p_{03n}) can be directly calculated. Consequently, the entropy and all the remaining static properties at nozzle outlet are obtained. At subsonic flow conditions the nozzle design is terminated when the convergence on ρ_{3n} and p_{3n} is reached. Instead, if the nozzle is choked (i.e., the two inequalities in the lower right part of the flowchart in Fig. 4.8 are verified) further steps are needed to achieve the solution, which are described in Section "Solution of the flow field when chocking occurs" (i.e., the flowchart continues in Fig. 4.12).

Annulus

The analysis for the vaneless annular passage is basically similar to the volute one. The calculation of the tangential velocity at stations 2 (C_{t2a}) and 3 (C_{t3a}) is obtained by the conservation of angular momentum. Guess values are initially assumed for the densities at each station and then adjusted until convergence. The corresponding flowchart of the annulus is not shown for brevity.

Rotor

Figure 4.9 shows all the steps required to evaluate the performance of the rotor. The rotor passage geometry is defined at the inlet, mid-passage and outlet stations from the design routine. The tangential component of absolute velocity at rotor inlet (C_{t1r}) is equal to that at annulus outlet (C_{t3a}). Rothalpy (I) is conserved through the rotor and can be directly calculated from the total enthalpy at stage inlet and C_{t1r}. The density assumption at rotor inlet (ρ_{1r}) allows the meridional velocity (C_{m1r}) to be calculated. So, the static enthalpy at rotor inlet (h_{1r}) can be obtained and, in turn, all the remaining static thermodynamic variables (being $s_{1r} = s_{3a}$). After achieving convergence on ρ_{1r} the velocity triangle at rotor inlet is fully determined. Moreover, the relative total enthalpy (h_{01Rr}) and relative

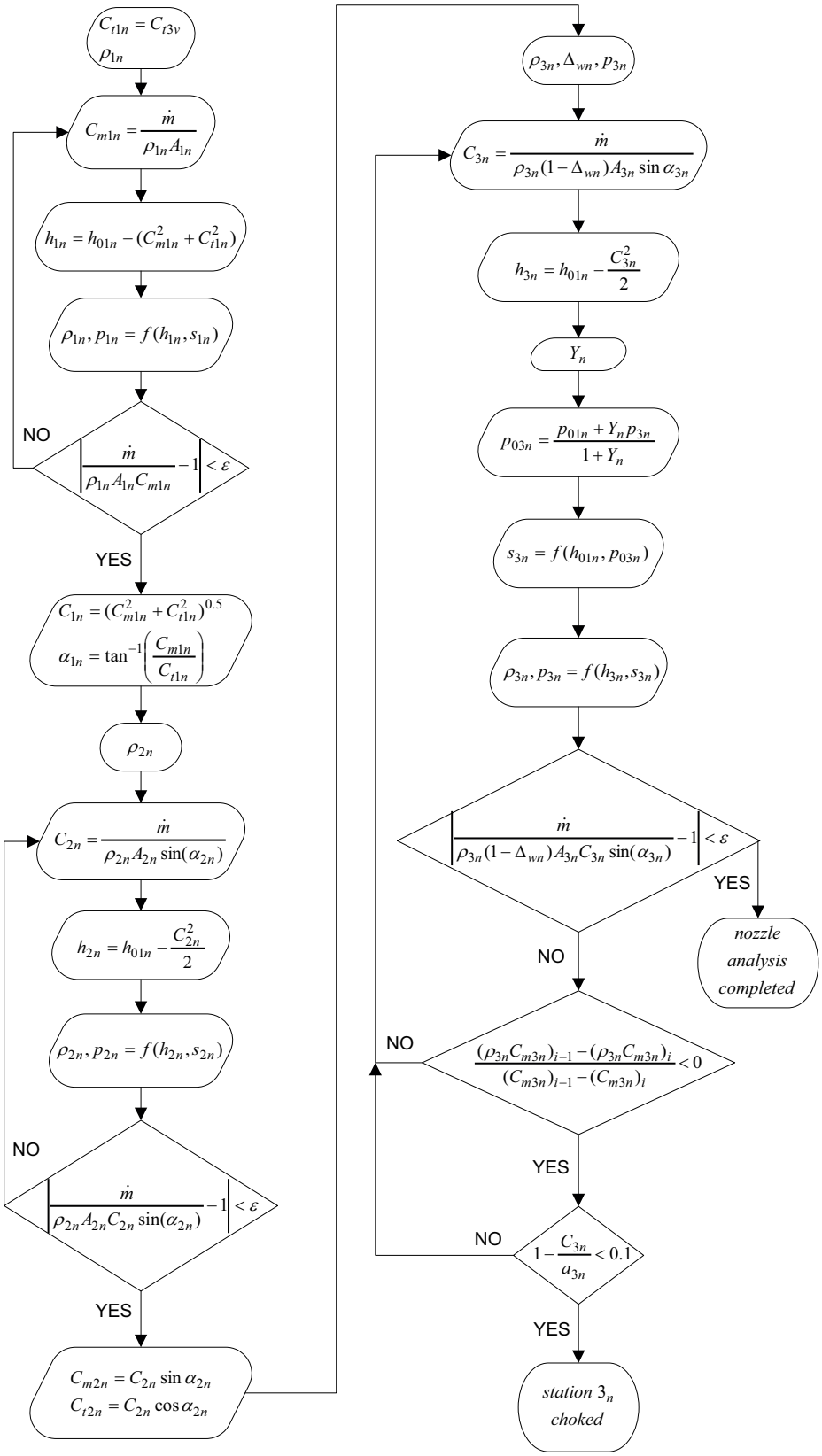

Figure 4.8: Operation of the nozzle.

total pressure (p_{01Rr}) can be calculated.

By assuming a guess value for ρ_{2r} the relative velocity and static enthalpy (h_{2r}) can be calculated. Accordingly, all the static properties at station 2 are obtained, the velocity triangle is fully defined and the total relative enthalpy and pressure can be calculated.

Finally, guess values are assumed for ρ_{3r} and p_{3r}. These allow the calculation of the relative velocity (W_{3r}) and static enthalpy at rotor outlet (h_{3r}). The solution of the flow field in the rotor proceeds with the calculation of the overall loss coefficient (Y_r) using the main geometrical features of the rotor and flow velocities (see Section 4.4.4). By the definition of total pressure loss coefficient (note that this is peculiar for the rotor) the relative total pressure at rotor outlet can be calculated (p_{03Rr}). In addition, the relative total enthalpy at rotor outlet (h_{03Rr}) can be calculated from the rothalpy and exit radius. So, the entropy at rotor outlet (s_{3r}) can be calculated which, combined with h_{3r}, gives all the remaining static properties. After the convergence on ρ_{3r} and p_{3r} is achieved a final check is done to ensure that p_{3r} is equal to the specified discharge pressure (p_{dis}). If this is not verified, the overall performance analysis is repeated for a new estimate of the mass flow rate until the final value is obtained. Instead, if the convergence on ρ_{3r} and p_{3r} cannot be achieved and the inequality describing the onset of choking is verified, the rotor is choked and further calculations are needed as described in Section "Solution of the flow field when chocking occurs".

Calculation of the mass flow rate matching the specified turbine outlet pressure

After all the expander components have been successfully analyzed in absence of choking, the static pressure at rotor outlet (p_{3r}) is calculated. Figure 4.10 shows graphically the iterative scheme used to adjust the mass flow rate up to the final convergence on the specified rotor discharge pres-

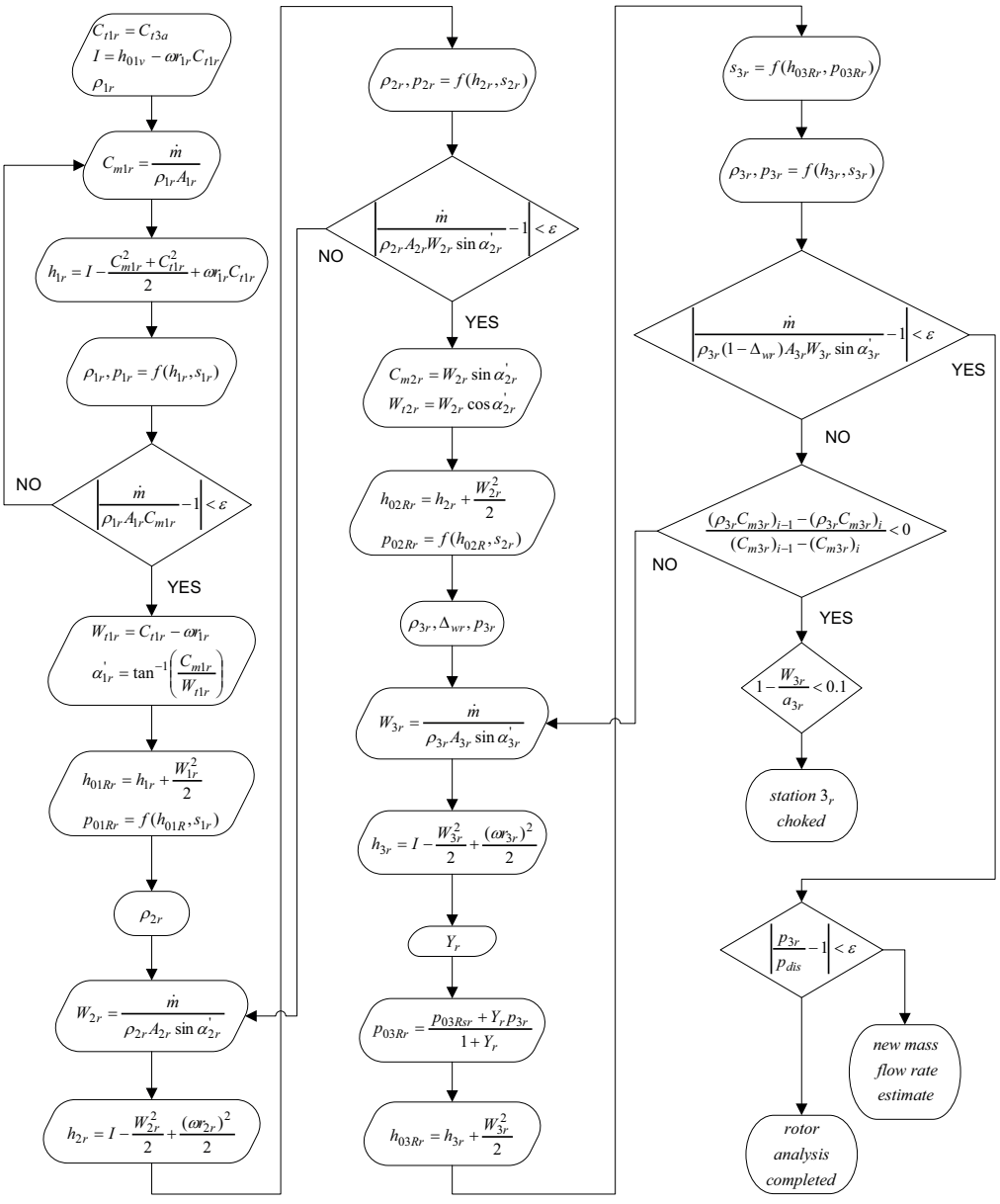

Figure 4.9: Operation of the rotor.

sure (p_{dis}). The operation routine must be repeated for all components starting from the stage inlet using a new mass flow rate: if p_{3r} turns out lower than p_{dis} then the new mass flow rate is increased and vice versa.

The new estimate of mass flow rate is obtained by applying a linearization of the turbine characteristic between the current $(p_{3r} - \dot{m})_i$ and previous $(p_{3r} - \dot{m})_{i-1}$ couple, where the blue arch is the unknown expander characteristic and the numbers indicate subsequent steps of the iterative procedure. At the beginning of the performance routine a first guess mass flow rate ($\dot{m}^I$) is chosen and results in the rotor outlet pressure (p_{3r}^I) (i.e., first operation point); the intersection between the straight line r^{0-I} passing through the origin and the point $(p_{3r}^I - \dot{m}^I)$ and the vertical straight line through p_{dis} allows the second estimate of mass flow rate ($\dot{m}^{II}$) to be obtained; accordingly, the corresponding p_{3r}^{II} is calculated (i.e., second operation point); the intersection between straight line r^{I-II} passing through the last two points of the expander characteristic (still unknown) and the vertical straight line through p_{dis} gives the third estimate of the mass flow rate ($\dot{m}^{III}$); the corresponding p_{3r}^{III} is calculated (i.e., third operation point), and so on. The iterative scheme converges on the mass flow rate $\dot{m}_{pdis}$ which gives the desired p_{dis} (red dot).

Solution of the flow field when chocking occurs

This Section outlines how the performance routine manages the turbine choking. When the iterative mass balance at nozzle or rotor outlet cannot converge, some additional calculations are to be performed as implied by the exits labels "station 3n choked" and "station 3r choked" in Figs. 4.8 and 4.9. The aim of this Section is threefold: (i) to present the criterion for the choking detection; (ii) to illustrate the interactive scheme to calculate the maximum swallowing capacity of the expander $\dot{m}_{choke}$; (iii) to show how p_{dis} is reached.

By considering two consecutive iterations (indexes $i-1$ and i) of the

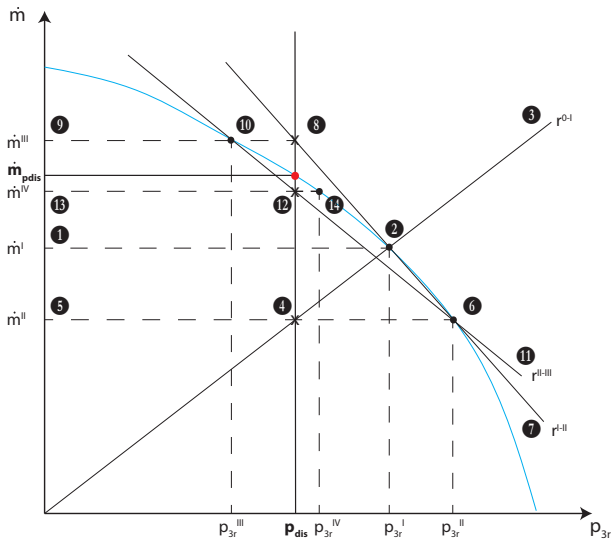

Figure 4.10: Graphical interpretation of the iterative scheme to calculate the mass flow rate leading to the specified turbine outlet pressure (p_{dis}). The blue line is the unknown turbine characteristic and the red dot is the convergence operation point.

above mentioned mass balances, it may happen that the product of density and meridional velocity ($\rho_3 C_{m3}$) decreases in spite of the gain in meridional velocity:

$$\frac{(\rho_3 C_{m3})_i - (\rho_3 C_{m3})_{i\text{-}1}}{(C_{m3})_i - (C_{m3})_{i\text{-}1}} < 0 \tag{4.112}$$

When the inequality in Eq. (4.112) is verified and the flow velocity is higher than 90% of the local speed of sound (to avoid false choking detections), the examined station is certainly choked. When choking occurs, the model iteratively seeks for the choking mass flow rate ($\dot{m}_{choke}$), which represents the maximum swallowing capacity of the expander. Figure 4.11 shows the procedure for the search of $\dot{m}_{choke}$. Let us call $\dot{m}_{max}$ and $\dot{m}_{min}$ two mass flow rates higher and lower than the searched choking mass flow rate. If using the current mass flow rate estimation ($\dot{m}$) the mass flow rate balance on the originally choked station 3 converges, then the subsequent mass flow rate estimate is increased towards $\dot{m}_{max}$. Instead, if the mass

flow rate balance ends again with a choking detection, then the subsequent mass flow rate estimate is reduced towards $\dot{m}_{min}$. In this way, the difference between $\dot{m}_{max}$ and $\dot{m}_{min}$ is progressively reduced until convergence on $\dot{m}_{choke}$. When $\dot{m}_{choke}$ is found, the post-expansion calculations outlined in the following paragraphs can be performed.

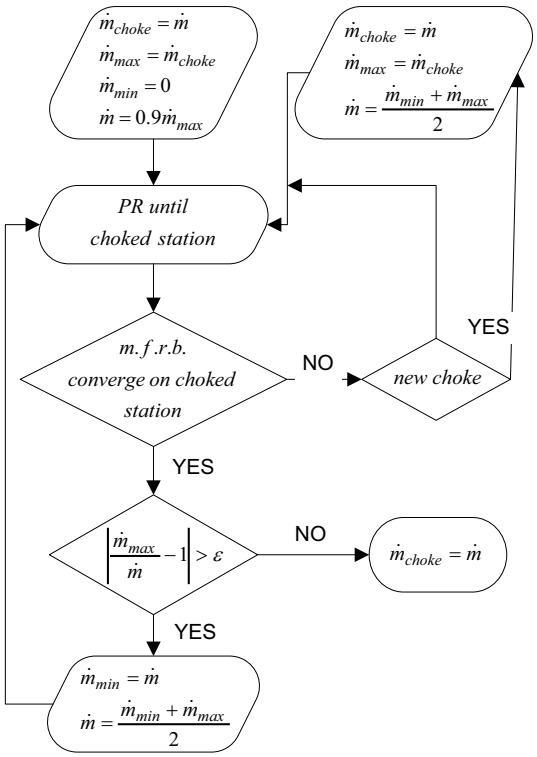

Figure 4.11: Search of $\dot{m}_{choke}$. "PR" and "m.f.r.b" stand for "performance routine" and "mass flow rate balance", respectively.

If choking at rotor outlet occurs, an irreversible post-expansion from the onset choke solution to the discharge pressure p_{dis} is considered.

When choking occurs at nozzle outlet a proper static pressure at nozzle outlet (p_{3n}) after post-expansion is searched, such that the calculated rotor outlet pressure p_{3r} matches the specified discharge pressure (p_{dis}). The convergence procedure is iterative and requires all calculations downstream the choked station 3n to be repeated for each new estimation of p_{3n} (i.e., the annulus and rotor analyses). Figure 4.12 shows all the steps involved

in the procedure where p_{max3n} and p_{min3n} are the pressures after the nozzle post-expansion resulting in p_{3r} values respectively higher and lower than p_{dis} (i.e., the target p_{3n} value falls between p_{max3n} and p_{min3n}). The static properties at nozzle outlet (h_{3n}, ρ_{3n}) are calculated from guesses for the entropy at the onset of choking (s_{3n}) and pressure (p_{3n}). Accordingly, the absolute velocity (C_{3n}) and flow angle (α_{3n}) at nozzle outlet can be calculated. Then, the total pressure loss coefficient (Y_{exn}) is calculated and, in turn, the total pressure at nozzle outlet (p_{03n}). So, a new value of s_{3n} is calculated until convergence. Note that in the flowchart p_{03n}^{ch} is the nozzle outlet total pressure at the onset of choking. The analysis proceeds with the calculation of the flow field in the annulus and rotor. If the resulting rotor outlet pressure (p_{3r}) is different from the specified discharge pressure then the first guess value of nozzle outlet pressure (p_{3n}) is consistently adjusted until convergence.

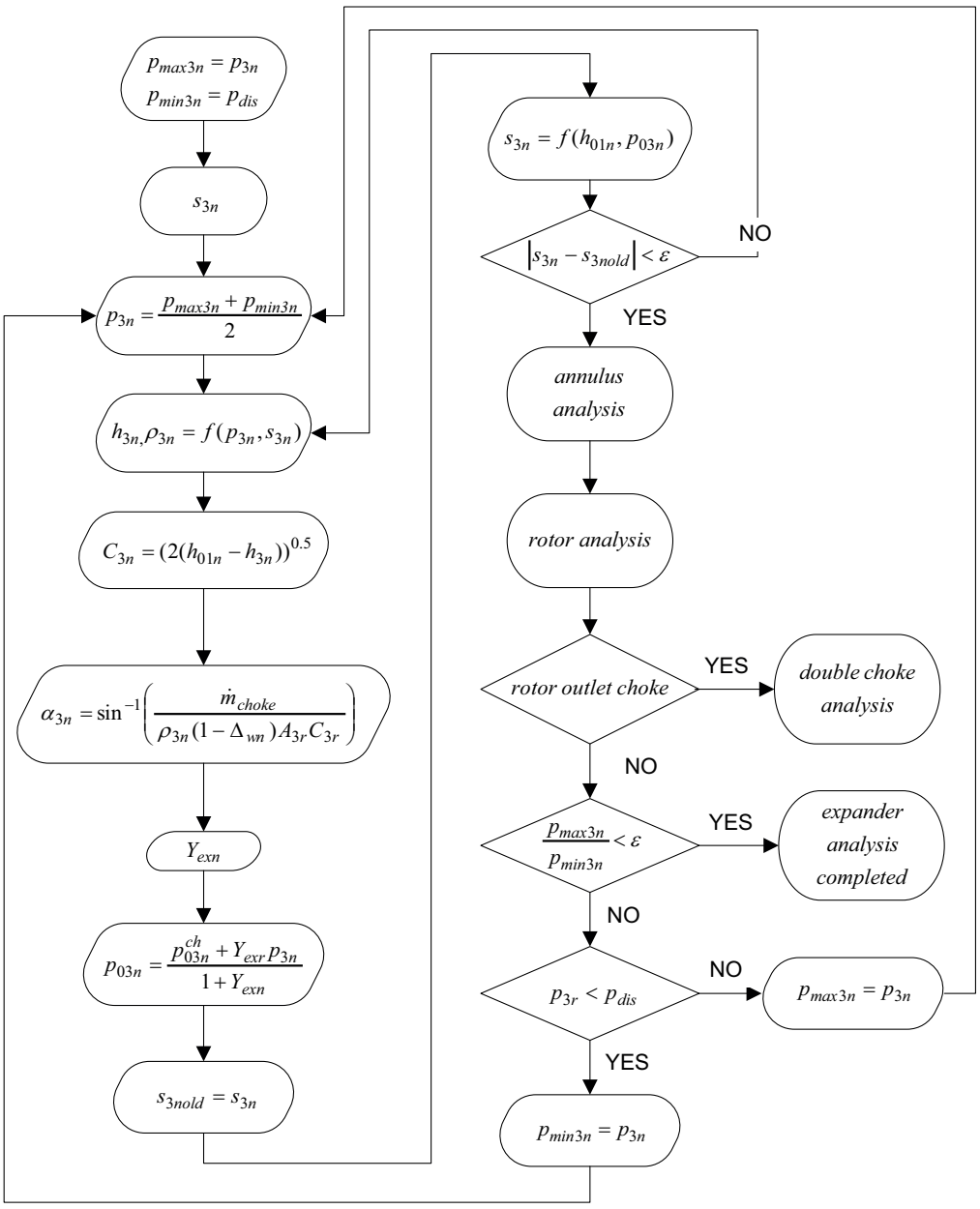

Figure 4.12: Solution of the flow field when choking occurs at nozzle outlet.

4.7 Model resolution for axial turbine

The design and performance prediction of the axial turbine is carried out by a Matlab® script developed by the author coupled with Refprop fluid properties database.

The model assumes the three requirements of a "normal" stage (named also "repeating" stage) [29]:

$$c_m = constant \qquad d = constant \qquad \alpha_1 = \alpha_3 \tag{4.113}$$

where c_m is the axial velocity, d is the root mean square diameter ($\sqrt{2(r_h^2 + r_t^2)}$), α_1 and α_3 are the absolute flow angles at stations 1 and 3. The hypothesis of constant axial velocity is consistent with the design practice commonly accepted in multistage turbines. Since the inlet flow angle does not markedly affect the stage performance [79], the choice $\alpha_1 = \alpha_3$ is not a particularly restrictive constraint. So, the stage calculated by the model can be interpreted as the generic stage of maximum efficiency of a multistage axial turbine at constant axial velocity.

A schematic of the circumferential and meridional section of the blade row is drawn in Figures 4.13 and 4.14 to highlight the main geometrical parameters calculated by the design procedure (see the flowchart in Fig. 4.15).

The flow chart in Fig. 4.15 shows the model architecture, the main equations and how they are implemented and solved sequentially. A detailed explanation of all steps for the design of the axial turbine is listed below.

1. The values of the mass flow rate ($\dot{m}$), the inlet state (p_1, T_1) and condensation pressure (p_3) are known from the thermodynamic cycle analysis, and represent design specifications, so that states 1 and the corresponding isentropic one at turbine outlet 3_{ss} are defined.

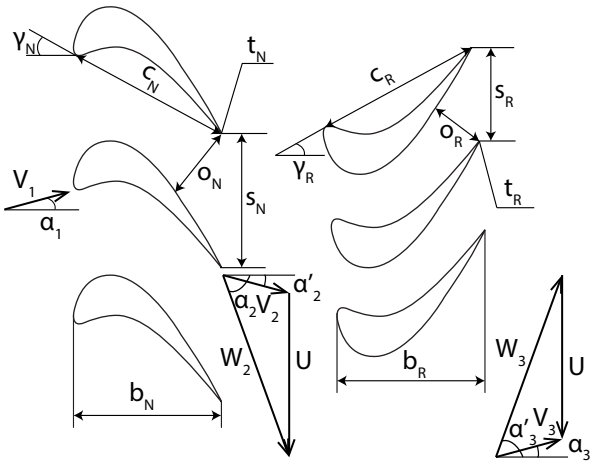

Figure 4.13: Main geometrical blade parameters.

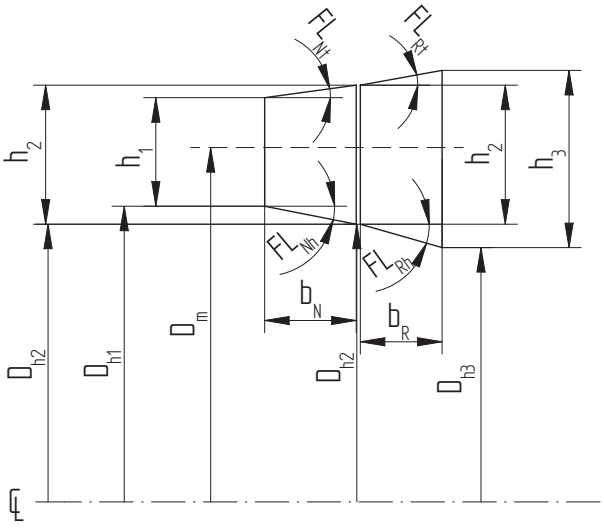

Figure 4.14: Schematic representation of turbine stage meridional channel.

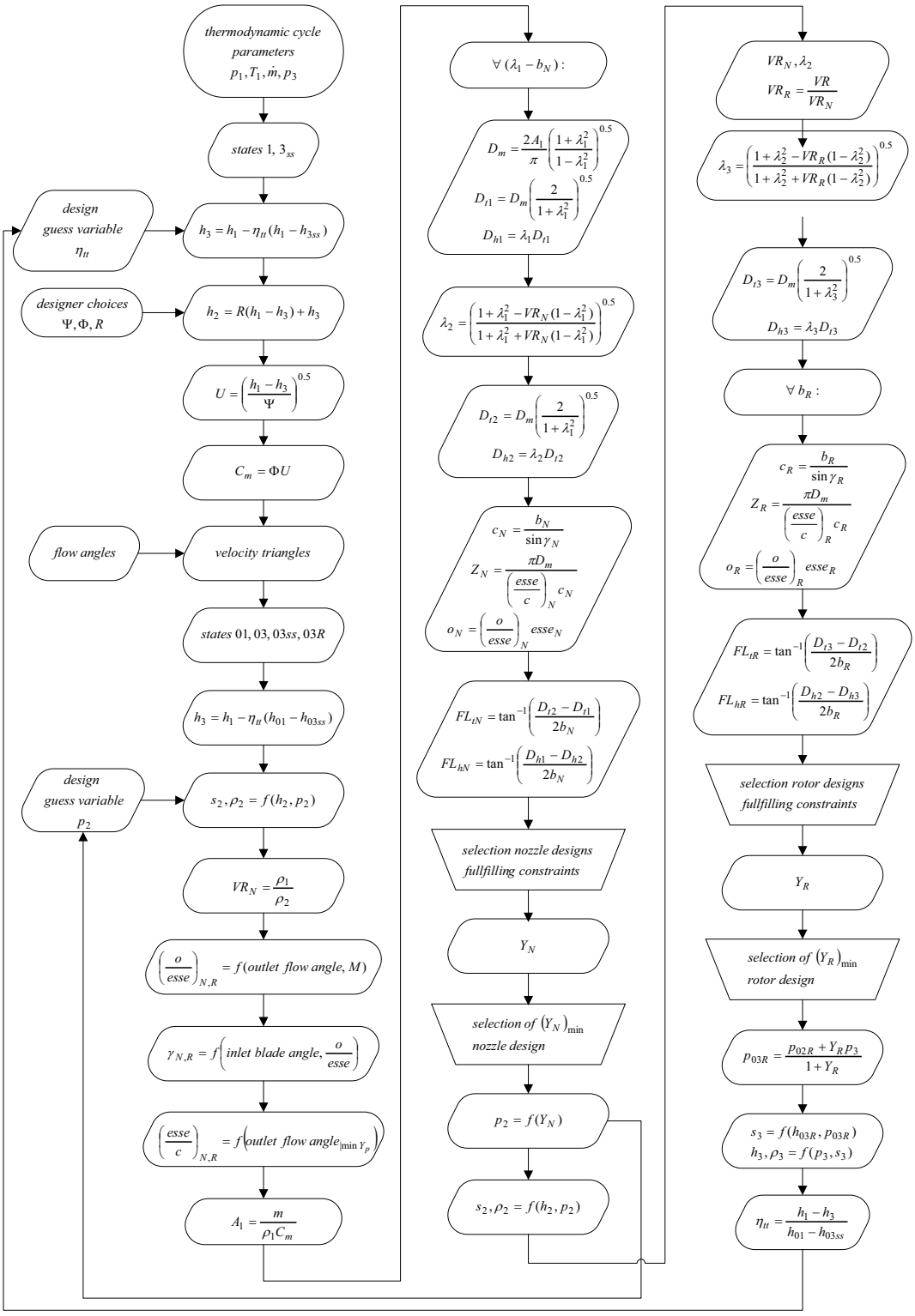

Figure 4.15: Model flowchart for the axial turbine.

2. The enthalpy h_3 is calculated by assuming a guess value of the total-to-total efficiency η_{tt}. So, the rotor outlet state is known; h_2, u and c_m are calculated from the design specifications reaction (R), loading coefficient (ψ) and flow coefficient (ϕ), respectively.

3. Loading coefficient ψ, flow coefficient ϕ and reaction R allow to calculate all absolute and relative flow angles by means of Eqs. (4.114) and (4.115):

$$\begin{cases} \tan\alpha_3 = \frac{1-R-\Psi/2}{\phi} \\ \tan\alpha_2 = \frac{1-R+\Psi/2}{\phi} \end{cases} \tag{4.114}$$

$$\begin{cases} \tan\beta_3 = -\frac{R+\Psi/2}{\phi} \\ \tan\beta_2 = -\frac{R-\Psi/2}{\phi} \end{cases} \tag{4.115}$$

4. All the velocity triangles can be obtained by means of trivial trigonometric calculations. So, the total states 01, 03, $03R$, 03_{ss} are defined and the resulting h_3 value can be used to update the calculation of h_2.

5. A first guess value for the pressure p_2 varying linearly with the reaction is chosen in order to define state 2.

6. The throat-to-pitch ($o/esse$) is calculated by means of empirical correlations as a function of the outlet flow angle and Mach number (see Aungier [45] for further details); the sweep angle (γ) is estimated as a function of the inlet blade angle and the throat-to-pitch ratio; the pitch-to-chord ratio ($esse/c$) is selected from the flow angles in order to minimize the basic profile loss coefficient (Eq. 4.82).

7. The passage area A_1 at the inlet of the stator is calculated from the mass flow rate definition. A set of couples "stator inlet hub-to-tip radius ratios ($\lambda_1 = r_{1h}/r_{1t}$ - see Fig. 4.14) - nozzle axial

chord (b_N)" is considered to calculate a wide spectrum of the following geometrical parameters: chord (c_N), root mean square diameter ($d = 2A_1/\pi\sqrt{(1-\lambda_1^2)/(1+\lambda_1^2)}$), blade span ($h_N$) (from continuity equation), blade pitch (s_N), number of blades (z_N) and throat opening (o_N). When necessary, converging-diverging nozzle vanes are considered. Unfeasible solutions in the set ($\lambda_1 - b_N$) are eliminated according to the constraints summarized in Table 4.2, among which the most binding are those associated with the flaring angle ($FL_N < 20°$) and the hub-to-tip radius ratio at rotor outlet ($\lambda_3 \geq 0.30$). The set of the remaining stator geometries are compared on the basis of the associated losses to select the best performing one: the couple ($\lambda_1 - b_N$) yielding the lowest total nozzle pressure loss coefficient (Y_N) is chosen. The blade spans (h) along the stator and rotor blade channels are then found from the continuity equation (see Fig. 4.14);

8. At this point the stator outlet pressure p_2 (previously assumed as a guess value at point 5) can be calculated from the definition of total pressure loss coefficient, being now Y_N known:

$$Y_N = \frac{p_{01} - p_{02}}{p_{02} - p_2} = \frac{p_{01} - f(h_{02}, s_2)}{f(h_{02}, s_2) - p_2} \tag{4.116}$$

where, in turn, $s_2 = f(h_2, p_2)$. So, state 2 is defined.

9. The calculation procedure of the rotor geometry and losses is similar but simpler than the stator one. In fact, the only free variable is b_R, being λ_3 ($\lambda_3 = r_{3h}/r_{3t}$ in Figure 4.14) evaluated from λ_1 (that is known from the calculations in the stator). Indeed, it can be demonstrated from the continuity equation that the hub-to-tip radius ratios of two consecutive sections i and j in a normal axial turbine stage can be linked to each other by means of the volumetric expansion ratio VR:

$$\lambda_j = \left(\frac{1 + \lambda_i^2 - VR(1 - \lambda_i^2)}{1 + \lambda_i^2 + VR(1 - \lambda_i^2)} \right)^{0.5} \tag{4.117}$$

For each value of b_R the rotor geometrical parameters (s_R, z_R, o_R, etc.) are calculated and, likewise for the nozzle, the rotor design yielding the lowest Y_R and fulfilling all the constraints is selected.

10. Starting from the definition of Y_R, p_{03R} is then calculated and used to find a new value of h_3, which updates the h_3 calculated from the η_{tt} guess at step 2;

11. A new estimate of the total-to-total efficiency is calculated using the current h_3 value. This estimate along with the current value of p_2 is used as input for the next iteration until convergence.

Table 4.2: Upper and lower bounds of the free variables in the optimization procedure.

	min value	max value
λ_1	0.30	0.95
λ_3	0.30	1
FL_N (°)	-20	20
FL_R (°)	-25	25
$(h/d)_3$	0	0.25
$\arcsin(o/s)_N$ (°)	13	60
$\arcsin(o/s)_R$ (°)	13	60
$(b/d)_N$	0	0.25
$(b/d)_R$	0	0.25
b_N (mm)	3	100
b_R (mm)	3	100
o_N (mm)	1.5	100
o_R (mm)	1.5	100
z_N	10	100
z_R	10	100

Table 4.3: Geometric parameters in (m) the rigorous similarity of which cannot be maintained at low actual turbine dimensions.

e	2×10^{-6}
δ	max(0.001 *or* 5 $\times 10^{-4}$d)
t	max(0.001 *or* 0.05 o)

4.8 Critical remarks

The loss correlations selected for the models play a fundamental role because they ultimately determine the predicted turbine efficiency value. Thus, some considerations about the limits and the degree of reliability of loss correlations are worth to be made.

It has already been observed (see Section 4.3) that loss coefficients can be used to determine the real flow conditions at the outlet of a turbomachine as a function of the inlet conditions and the ideal discharge ones. From a thermodynamic point of view, the loss coefficient is a metric of how much the real transformation across a turbomachine is far from the correspondent isentropic one.

In general terms, the creation of a loss systems requires a series of fundamental steps, which can be summarized as follows:
(i) Creation of a cascade database by collecting two and three dimensional cascade data for turbine airfoils having different geometric and aerodynamic characteristic: the higher the variety of the database, the wider the validity of the resulting loss correlation.
(ii) Detection of the main variables on which loss generating processes are believed to depend on. This variable selection makes use of further test campaigns (i.e., compare configurations which differ only in the variable being analyzed) or theoretical and physical reasoning.
(iii) development of the loss correlation. In this step it is decided how the significant variables previously detected may be conveniently linked to each other in an analytic equation. The form of the equation is the result of the application of statistical regression techniques or can be supported by physical argumentation.
(iv) test of the loss correlation against real turbine data to check the real predictive power. Note that a turbine database is required to accomplish this step. Again, the higher the size of this database, the higher the con-

fidence level of the correlation being tested.
(v) calibration of the loss correlation. The differences between predictions and real turbine data due to the inherent lacks of loss correlations are recovered by including into them empirical inputs in the form of regression coefficients to obtain a better agreement with real turbine data.

It would be naive to believe that the calculation of the flow conditions by means of loss coefficients within a mean line analysis results in a comprehensive and authentic picture of the real three dimensional flow, even when the formulation of such loss coefficient attempts to model the fundamental fluid dynamic processes.

The estimation of losses through correlations is unavoidably a strong simplification and, as such, affected by a degree of uncertainty directly arising from the procedure used to define the correlations (see item (v)) and the practical impossibility to include all of the parameters that affect the loss mechanisms. So, also in case the most significant variables are correctly identified, it is not surprising that loss correlations calibrated on different real turbine database may give rise to different loss estimation and, even more so, to different loss breakdown.

In addition, especially for radial turbines, these data sets are based on a limited number of designs originally developed for a single application, so that the use of the resulting correlations in the analysis of different configurations might be misleading. These considerations are well known to whom develop mean line models who is aware of their limitations. On the other hand, an additional and very challenging issue is related to the use of loss correlations developed for traditional fluids (e.g., steam or air) when dealing with organic fluids.

Limits in the applicability of loss correlations to unconventional fluids might arise when the loss correlation does not completely model the loss-generating phenomenon on a physical basis but resorts to numerical constants (multiplicative factors, exponents, etc.) derived through statis-

tical regression techniques on experimental database. Since these database collect the performance of turbines operating with traditional fluids, the value of these numerical constants could be influenced by the fluid nature and it is likely that the correlation is actually fluid dependent.

A further element of uncertainty derive from the estimation of losses due to high Mach number flow regimes because these loss mechanisms of utmost importance for ORC turbomachinery applications are affected by the non-ideal behavior of the working fluid. As instance, [80] has recently shown that, in contrast with the perfect gas case, the shock configuration at the trailing edge of supersonic high-pressure turbine vanes and, in turn, the related total pressure loss depend on the upstream thermodynamic state.

Only extensive experimental campaigns on cascades and turbines using organic fluids could provide solid insights to improve the reliability and predictive power of loss correlations.

Chapter 5

Results

The main outcomes of the preliminary design procedure for turbines are the geometry and the efficiency. As already explained in Chapter 4 the radial and axial turbine design models require two kinds of inputs: design specifications (i.e., mass flow rate and enthalpy drop) and design parameters. These are: the specific speed (n_s) and isentropic velocity ratio (ν_s) for radial turbines, and the loading coefficient (ψ), flow coefficient (ϕ) and reaction (R) for axial flow stages, respectively.

$$n_s = \omega \frac{\dot{V}^{0.5}}{\Delta h_{0s}^{0.75}} \qquad \nu_s = \frac{U}{(2\Delta h_{0s})^{0.5}} \tag{5.1}$$

$$\psi = \frac{h_{01} - h_{03}}{U^2} \qquad \phi = \frac{C_m}{U} \qquad R = \frac{h_2 - h_3}{h_1 - h_3} \tag{5.2}$$

Accordingly, for given design specifications a series of preliminary designs are first obtained for different combinations of design parameters. The resulting efficiencies are collected in maps as a function of the the design parameters n_s and ν_s for radial turbines, and ψ and ϕ (optimum reaction R is considered) for axial turbines, respectively.

Subsequently, design specifications are varied, and for each mass flow rate - enthalpy drop combination the optimum designs (i.e., designs with optimum n_s and ν_s for radial turbines and ψ and ϕ for axial turbines,

respectively) are selected. The corresponding values of the size parameter (SP) and volumetric flow ratio (VR) are calculated to obtain a single design point in the SP-VR map. This procedure is repeated for several combinations of the design specifications in order to span wide SP and VR intervals and, in turn, build the SP-VR map for each organic fluid considered.

Note that the condensation temperature is fixed at 33 °C for all the designs, that is, for given fluid and turbine inlet conditions, the discharge pressure and isentropic density is fixed. Thus, designs at different volumetric flow ratio VR are obtained by changing the evaporating temperature and, in turn, the enthalpy drop. Instead, variations of the size parameter SP are obtained by changing the mass flow rate.

The working fluid selected for all the radial turbine simulations is R245fa to limit the computational effort; whereas, the following eight working fluids are considered in the axial turbine simulations:

- *isobutane*, *isopentane* and *cyclopentane* (hydrocarbons commonly used in ORC [81], [4]);
- *R245fa* and *R134a* (hydrofluorocarbons having zero ODP but high GWP);
- *R1234yf*, *R1234ze(E)* and *R1234ze(Z)* (hydrofluoroolefines having both zero ODP and low GWP (< 10) and are considered the new class of refrigerants [82]).

Table 5.1 summarizes their main thermo-physical properties including the critical temperatures that range between 94.7 °C and 238.5 °C.

Finally, a stepwise regression procedure has been used to obtain a statistical correlation able to fit the eight SP-VR maps. This correlation defines a single turbine efficiency map of general validity for a variety of organic fluids that is well suited for ORC optimization.

Table 5.1: Fluid properties

Fluid	class	Tc (K)	MM (kg/kmol)	GWP	ODP
R1234yf	HFOS	367.9	114.04	4	0
R134a	HFC	374.2	102.03	1430	0
R1234ze(E)	HFOS	382.5	114.04	6	0
Isobutane	HC	407.8	58.12	3	0
R1234ze(Z)	HFOS	423.3	114.04	< 10	0
R245fa	HFOS	427.2	114.04	1030	0
Isopentane	HC	460.4	72.15	11	0
Cyclopentane	HC	511.7	70.13	11	0

5.1 New maps for the preliminary design of ORC turbines

In the following Sections the new $n_s - \nu_s$ charts developed for radial turbines, and the new ψ and ϕ charts developed for axial turbines are shown. The latter maps are analogous to the well-known Smith chart which correlate the efficiency to the design parameters.

Note that a few Celsius degrees of superheating (in the order of 5 °C) is imposed in case of expansions starting from wet vapor. It is also assumed that the kinetic energy at the rotor discharge is not recovered in the radial turbine simulations, whereas a 50% of the meridional kinetic energy component is recovered in the axial stage designs [24].

5.1.1 New $n_s - \nu_s$ efficiency maps for radial inflow turbines

Figure 5.1 shows the turbine efficiency maps $\eta = f(n_s, \nu_s)$ generated for two different design specifications: Fig. 5.1a refers to a working fluid (*R245fa*) mass flow rate of 20 kg/s and an evaporation temperature of 60 °C (which corresponds to $SP = 0.12$ m and $VR = 2.3$), whereas Fig. 5.1b refers to a much higher evaporation temperature (110 °C) and the same $\dot{m}$ (which gives approximately the same SP and $VR = 8.7$). In both maps n_s and ν_s are varied within wide intervals (0.30-0.55 and 0.50-0.80, respectively) which include the optimum. These maps allows not only to compare the effects of different design specifications in terms of volumetric flow ratio, but also to to separate the effects on turbine efficiency deriving from non-optimum n_s from those arising from non-optimum ν_s. To the author's knowledge no such 3D maps are available in the literature showing the relationship $\eta_s = f(n_s, \nu_s)$ for radial inflow turbines working with organic fluids. Instead, maps are available for turbines working with common fluids which correlate turbine efficiency with two different design parameters, namely the flow coefficient and loading coefficient (see Moustapha et al. [19]) or the specific speed and the specific diameter (see Balje [23]).

Inspection of the calculated maps shows that the predicted maximum turbine efficiency is 89.4% at low VR (Fig. 5.1a) and drops to 87.3% at high VR (Fig. 5.1b). The optimum n_s (equal to 0.425) is lower compared to the optimum range reported in the literature for common gases and it is roughly independent from the expansion ratio. Instead, the optimum ν_s is still centered on 0.65 but is markedly affected by VR: low VR values require higher ν_s and vice versa. The iso efficiency lines form rotated ellipses not aligned with the axes and tilted above the horizontal. The effect of n_s on turbine efficiency is milder compared to the effect of ν_s

as shown by the aspect ratio of the ellipse. By moving along the major axis of the ellipse (i.e., selecting designs at optimum ν_s) the efficiency at first increases, reaches a maximum and then decreases, in accordance with Rohlik [31] findings. The efficiency decay is anyhow rather low (less than 2%) and slightly higher for the high VR case. Conversely, higher deviations are obtained when ν_s deviates from the optimum.

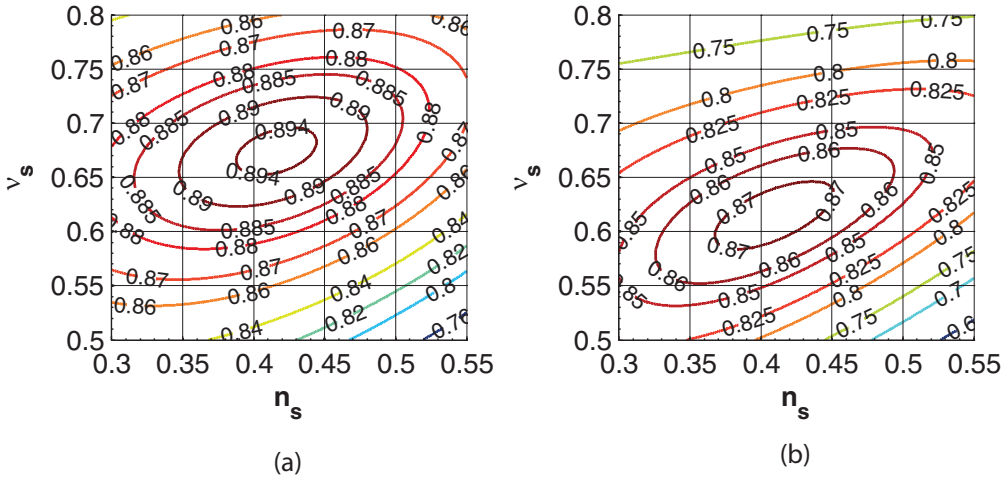

Figure 5.1: $n_s - \nu_s$ chart showing lines at constant η for $\dot{m} = 20$ kg/s (corresponding to $SP \approx 0.12$ m) at two VR values: (a) $T_{evap} = 60$ °C, corresponding to $VR \approx 2.3$, and (b) $T_{evap} = 110$ °C, corresponding to $VR \approx 9$.

Efficiency trends in the $n_s - \nu_s$ maps of Fig. 5.1 can be justified by looking at the correspondent loss breakdown reported in Figs. 5.2 and 5.3. In particular, Fig. 5.2 compares the two scenarios at low (Fig. 5.2a) and high VR (Fig. 5.2b) by considering for each n_s the corresponding optimum ν_s. Similarly, Fig. 5.3 performs the same comparison by considering for each ν_s the corresponding optimum n_s. As for the loss distribution versus the specific speed, there is a decreasing trend of the nozzle loss as n_s increases which is counter-balanced by the rising trend of the kinetic energy loss, particularly significant for high specific speed turbines. Note that both losses are comparatively higher in the high VR scenario. Losses in the vaneless components (i.e., volute and annulus) play a secondary role

in the performance determination. With regard to the ν_s effect on the loss distribution at optimum n_s, it is seen a decrease of nozzle losses as the velocity ratio increase; this effect is more pronounced in the high VR scenario. Instead, rotor losses rapidly increase at very high ν_s values, especially when VR is higher.

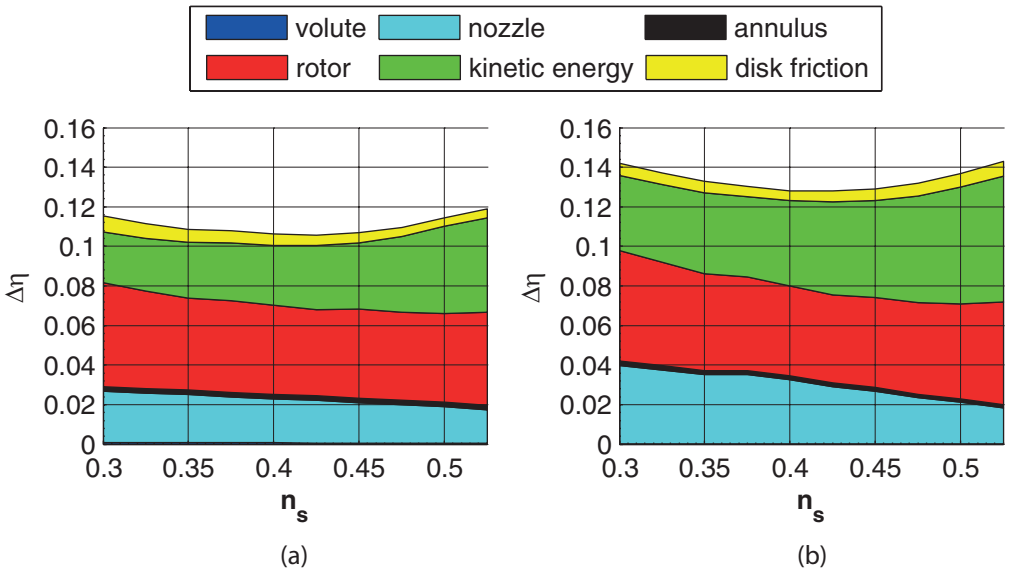

Figure 5.2: Distribution of losses versus specific speed at optimized velocity ratio for: (a) low VR scenario ($VR = 2.3$) and (b) high VR scenario ($VR = 8.7$).

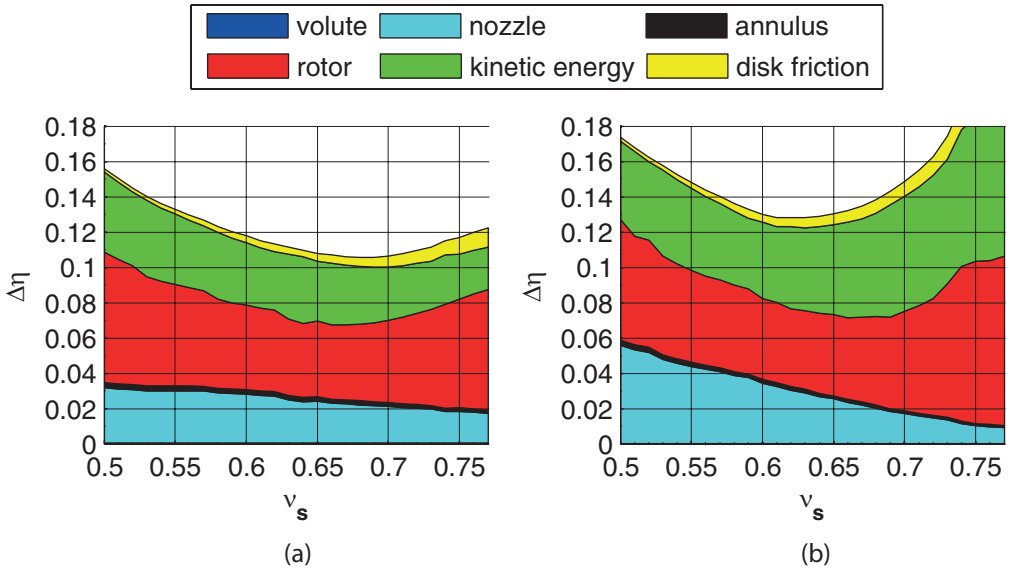

Figure 5.3: Distribution of losses versus specific speed at optimized specific speed for: (a) low VR scenario ($VR = 2.3$) and (b) high VR scenario ($VR = 8.7$).

5.1.2 New Smith charts for axial flow turbines

Figure 5.4 shows the efficiency distributions in the loading coefficient (ψ)- flow coefficient (ϕ) plane for different design specifications when *R245fa* is used: Figs. 5.4a and 5.4b refer to two extreme values of VR (1.7 and 9) and constant SP. Optimal reaction is considered and the plotted efficiency assumes that half of the axial kinetic energy at the turbine outlet is recovered.

It clearly appears that the highest efficiencies are obtained at low flow coefficients and low loading coefficients, as in the original Smith chart. High ψ values imply larger deflections which require a larger blade surface area in contact with the fluid and in turn higher friction losses. As the flow coefficient ϕ increases at constant loading coefficient, the deflection decreases but the axial velocity increases, resulting in a general velocity gain through the stage [19].

The volumetric expansion ratio has a not negligible influence on turbine efficiency. The chart in Fig. 5.4a refers to $VR \approx 1.7$ ($T_{evap} = 50$ °C) and

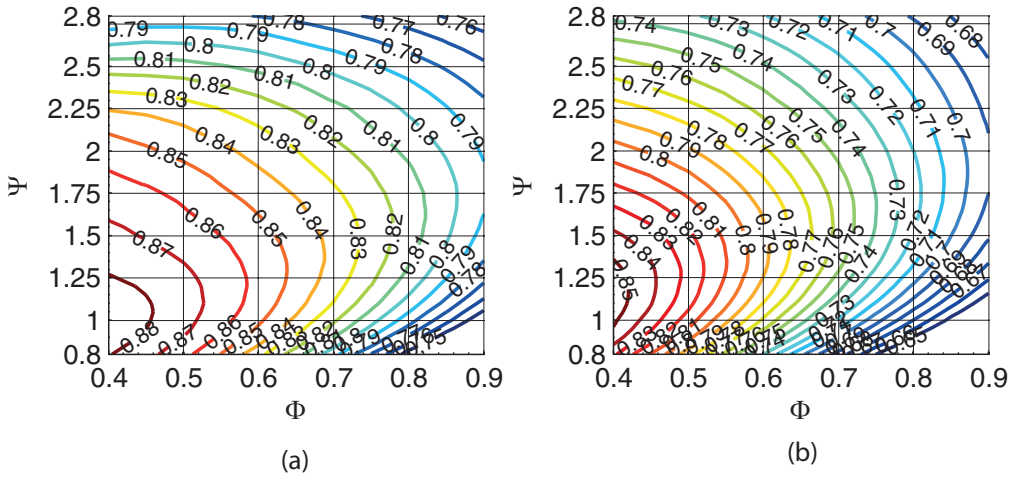

Figure 5.4: Smith charts showing lines at constant η for $\dot{m} = 50$ kg/s (corresponding to $SP \approx 0.16$ m) at two VR values: (a) $T_{evap} = 50$ °C, corresponding to $VR \approx 1.7$, and (b) $T_{evap} = 110$ °C, corresponding to $VR \approx 9$.

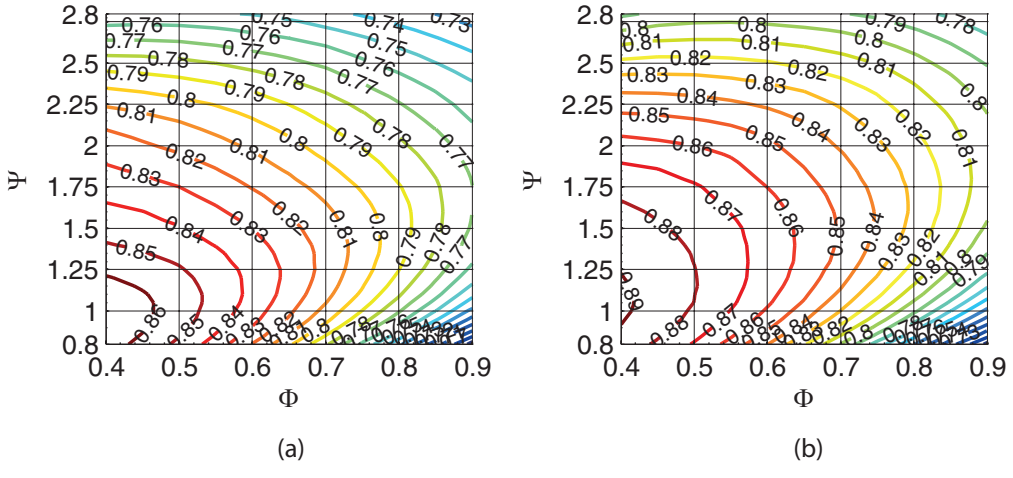

Figure 5.5: Smith charts showing lines at constant η for $T_{evap} = 50$ °C (corresponding to $VR \approx 1.7$) at two SP values: (a) $\dot{m} = 10$ kg/s, corresponding to $SP \approx 0.1$ m and (b) $\dot{m} = 150$ kg/s, corresponding to $SP \approx 0.35$ m.

shows a maximum efficiency equal to 88.7% obtained at $\phi = 0.4$ and $\psi = 1$. The chart in Fig. 5.4b refers to a much higher VR ($T_{evap} = 110$ °C), and shows a maximum efficiency equal to 85.6% which is obtained at $\phi = 0.4$ and $\psi = 1.2$. These results demonstrate that the efficiency markedly decreases and the optimum ψ slightly increases with VR.

Similarly to VR, Fig. 5.5 shows the influence of turbine size on the efficiency distribution in the $\psi - \phi$ diagram. In particular, Fig. 5.5a refers to $SP \approx 0.1$ m ($\dot{m} = 10$ kg/s) and shows a maximum efficiency equal to 86.8%; Fig. 5.5b refers to an higher SP value ($\dot{m} = 150$ kg/s) and indicates an optimum efficiency slightly over 89%.

Accordingly, a single general Smith chart cannot be representative of the wide range of operating conditions experienced by organic fluids even at moderate temperature drops. Several Smith charts ought to be considered at different values of expansion ratio and size, and used as design tools for these applications.

Inspection of kinematic parameters and optimum reaction distributions in the above Smith charts (Figs. 5.4 and 5.5) allows to draw some qualitative conclusion about the efficiency trends for fixed design specifications:

- The axial velocity ($C_m = \phi U = \phi\sqrt{(h_{01} - h_{03})/\psi} = \phi\sqrt{(h_1 - h_3)/\psi}$) rises for growing ϕ and decreasing ψ, reaching a maximum value of 150 m/s;

- The angular speed ($\omega = \sqrt{(h_{01} - h_{03})/\psi}/(0.5d)$) markedly increases with a reduction of ψ, whereas it slightly increases with ϕ;

- The optimum reaction appears to be unaffected by ϕ and mainly varies with ψ. Higher ψ requires low R in the range 0.1-0.3, which is in agreement with [24]. A low R allows to limit the secondary losses and post expansion losses in the stator. The optimum reaction in the point of maximum efficiency in Figs. 5.4a and 5.4b is 0.47 and 0.43, respectively.

Table 5.2 compares the main performance parameters and losses breakdown for two turbines having different volumetric expansion ratios in the optimum points of Figures 5.4a and 5.4b. All loss sources are shown in Table 5.2 to explain the efficiency gap between the two cases. It clearly appears that the efficiency penalties for the higher pressure ratio are due to the loss terms associated with high Mach flow regimes (in the stator they account for more than half of the total losses) which are absent for the lower pressure ratio. Indeed, the flow is supersonic both at stator and rotor outlet. Moreover, the higher secondary losses and the shock losses further reduce the efficiency. The increase of VR has two main effects on meridional geometry: i) a decrease of the aspect ratio (h/c), both in the stator and rotor, and in particular of the stator inlet blade height; ii) an increase of flaring angles to adapt the channel area to the progressive density reduction through expansion. This trend is partially balanced by a simultaneous increase of the axial chord to fulfill the upper constraint on flaring angle (25°).

Table 5.2: Comparison of the main performance parameters and losses breakdown in the optimum points of Figures 5.4a and 5.4b.

	VR	1.7			9	
	ϕ	0.4			0.4	
	Ψ	1.0			1.15	
	n_s	1.04			0.90	
	R	0.45			0.45	
	η	0.887			0.856	
	C_m	39			69.5	
	d	0.40			0.31	
	ω	488			1040	
	U	97			173	
	stator	rotor		stator	rotor	
Mach inlet	0.29	0.28		0.56	0.52	
Mach exit	0.79	0.72		1.49	1.35	
deflection	76	74		74	88	
h/c	1.57	2.54		0.44	1.0	
t/o	8.0%	8.9%		8.0%	8.1%	
δ/h		1.52%			1.44%	
flaring tip	13	16		12	18	
flaring hub	18	25		13	25	
b	0.034	0.031		0.041	0.059	
	stator	rotor	total	stator	rotor	total
profile	0.018 (33.7%)	0.016 (12.5%)	0.034 (18.8%)	0.018 (8.2%)	0.021 (7.7%)	0.038 (7.9%)
secondary	0.029 (52.4%)	0.023 (17.6%)	0.052 (27.8%)	0.054 (25.1%)	0.041 (15.2%)	0.094 (19.6%)
trailing edge	0.006 (13.9%)	0.001 (7.3%)	0.017 (9.3%)	0.008 (3.6%)	0.008 (2.8%)	0.152 (3.2%)
shock	0 (0%)	0 (0%)	0 (0%)	0.026 (12%)	0.012 (4.6%)	0.038 (7.9%)
postexpansion	0 (0%)	0 (0%)	0 (0%)	0.109 (51%)	0.066 (24.8%)	0.157 (36.5%)
clearance		0.082 (62.6%)	0.082 (44.2%)		0.12 (44.8%)	0.120 (24.9%)
total	0.056 (100%)	0.131 (100%)	0.187 (100%)	0.212 (100%)	0.264 (100%)	0.482 (100%)

5.2 Maps for the estimate of ORC turbines maximum efficiency

In the following Sections the size parameter (SP)- volumetric flow ratio (VR) maps for the working fluids reported in the introduction of this Chapter are presented and discussed in detail.

5.2.1 SP-VR map for radial inflow turbines

A radial inflow turbine map has been generated for the working fluid $R245fa$. In order to span a wide range of SP and VR (0.02-0.25 m and 2-14, respectively), the mass flow rate has been varied in the interval 1 kg/s - 100 kg/s, whereas the evaporation temperature falls in the range 50 °C-130 °C. As already explained at the beginning of this Chapter for each combination of the design specifications optimum n_s and ν_s are identified and collected in the SP-VR map reported in Fig. 5.6.

By intersecting the map with horizontal lines (constant VR) it can be easily noticed that η monotonically increases with SP due to the positive effect of the turbine size on the efficiency. The efficiency gain is approximately 3-3.5%-points in the considered range of SP. For instance, by intersecting the map at $VR \approx 2$ the turbine efficiency increases from 86.7% to 90.0%. A similar monotonic trend of turbine efficiency is not observed for VR. In particular, by intersecting the map with vertical lines (constant SP) it can be noticed that η slightly increases up to $VR = 3.6 - 4.0$ and then gradually decreases till reaching the maximum VR considered in this study (14). Thus, there is an optimum VR (slightly lower than 4.0) which maximizes the turbine efficiency. The maximum efficiency drop with VR is in the range 3-3.5%-points, regardless of the considered SP. The point in the map yielding the highest turbine efficiency (90.1%) is located at the maximum SP (= 0.25 m) and at $VR = 3.6$. Conversely, the point in the

map yielding the lowest efficiency (83.5%) is located in the upper left corner and is obtained by accounting for the combined SP and VR penalties which are roughly 3.3%-points each.

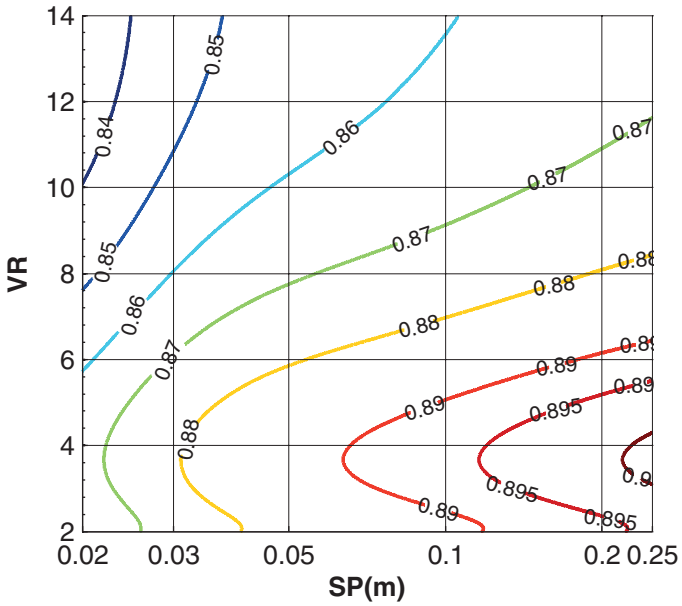

Figure 5.6: Radial turbine efficiency versus size parameter (SP) and volumetric expansion ratio (VR) at optimum n_s and ν_s.

The efficiency trend outlined in Fig. 5.6 can be further investigated by looking at the loss distribution as a function of the size parameter and volumetric flow ratio. In particular, Fig. 5.7a shows the contribution of each turbine component to the overall loss versus the size parameter for constant volumetric flow ratio ($VR = 4$), whereas Fig. 5.7b shows the loss breakdown versus the volumetric flow ratio for constant size parameter ($SP = 0.075$ m). As for the loss distribution versus SP, it can be easily seen that the losses in the rotor and in the stator gradually increase as SP decreases mainly because the increase of the clearance loss component (included in the rotor addendum) and surface roughness effects. Instead, the kinetic energy loss is almost insensitive to size variations and only a slight decrease in the lower SP range is observed. These trends are consistent with those presented in [25].

With regard to the effect of volume flow ratio variations, it can be seen that the increase of VR from 4 up to higher values is accompanied by a marked increase of nozzle and leaving kinetic energy losses. The former are due to the small blade height at nozzle outlet imposed by the relatively low volumetric flow rate in respect to that at rotor outlet. The latter is a direct consequence of the design constraint on the maximum area ratio (2.5) between rotor outlet and inlet sections: this maximum area ratio assumption limits the possibility to accommodate large volumetric flow rate variations across the rotor.

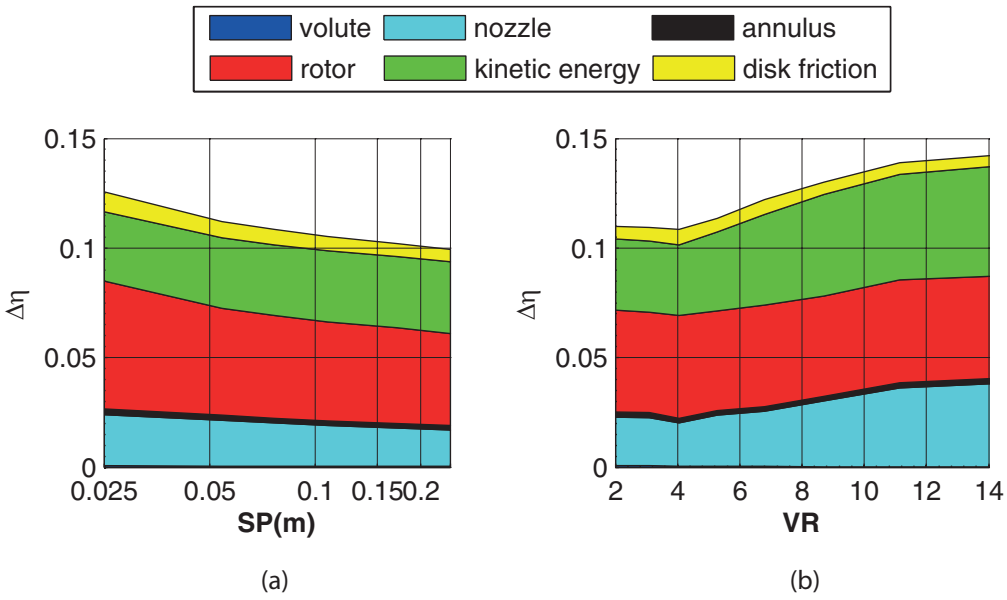

Figure 5.7: Distribution of turbine losses as a function of (a) SP (at fixed $VR = 4$); (b) VR (at fixed $SP = 0.075$ m).

Figures 5.8 and 5.9 show the rotor meridional sections for different SP values at constant VR and vice versa. The increase of SP obviously results in an increase of all turbine dimensions but the channel shape does not vary significantly with the size. The increase of VR is accompanied by (i) an increase of the passage area ratio across the rotor channel, till the maximum value compatible with the related constraint is reached and (ii) a decrease of the blade height at the inlet. Note that all the designs

considered in Fig. 5.9 feature an outlet-to-inlet radius ratio at the shroud equal to 0.7 because this is the maximum value allowed by the design procedure for this parameter (see Chapter 4).

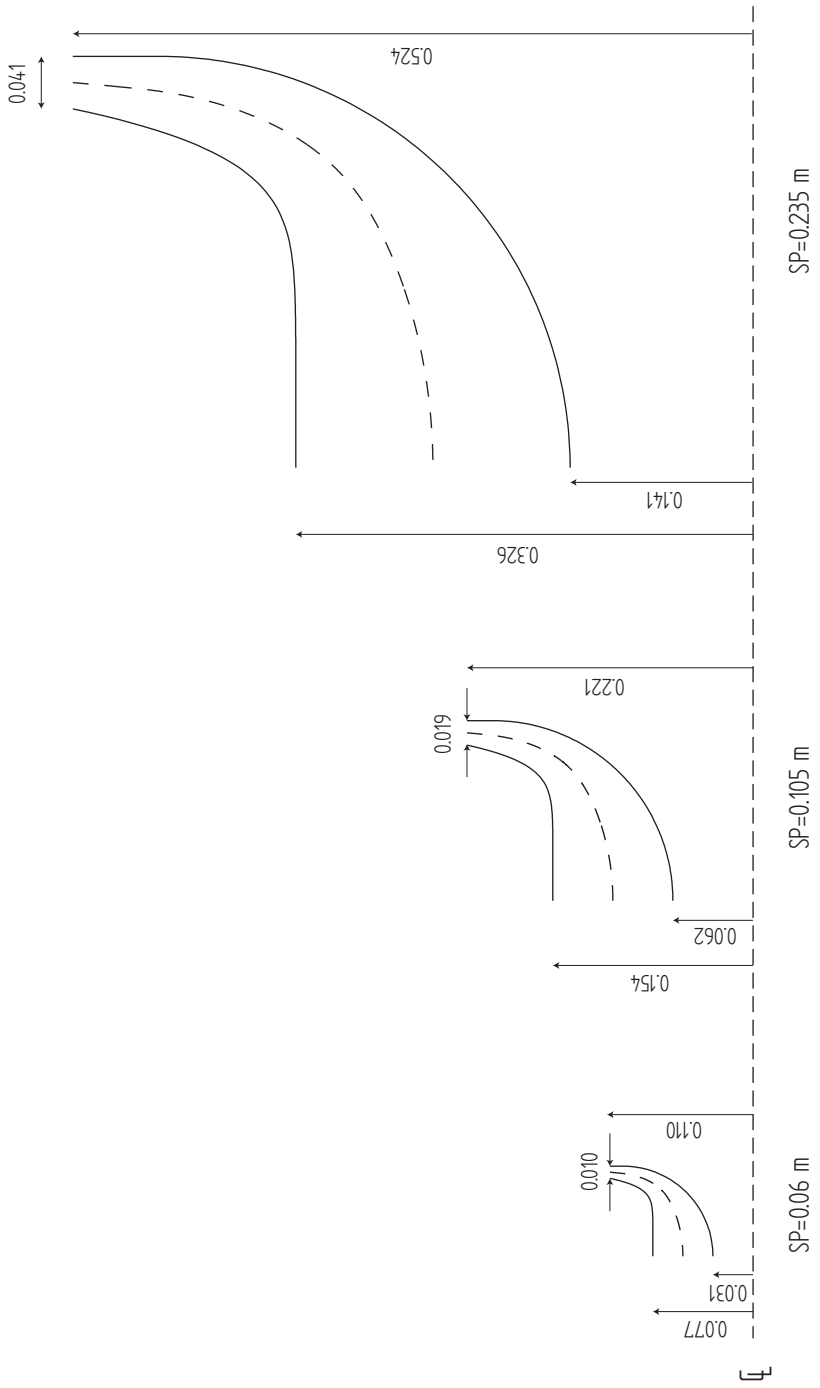

Figure 5.8: Rotor meridional sections for different SP values with constant $VR = 5.2$. Dimensions are in millimeters.

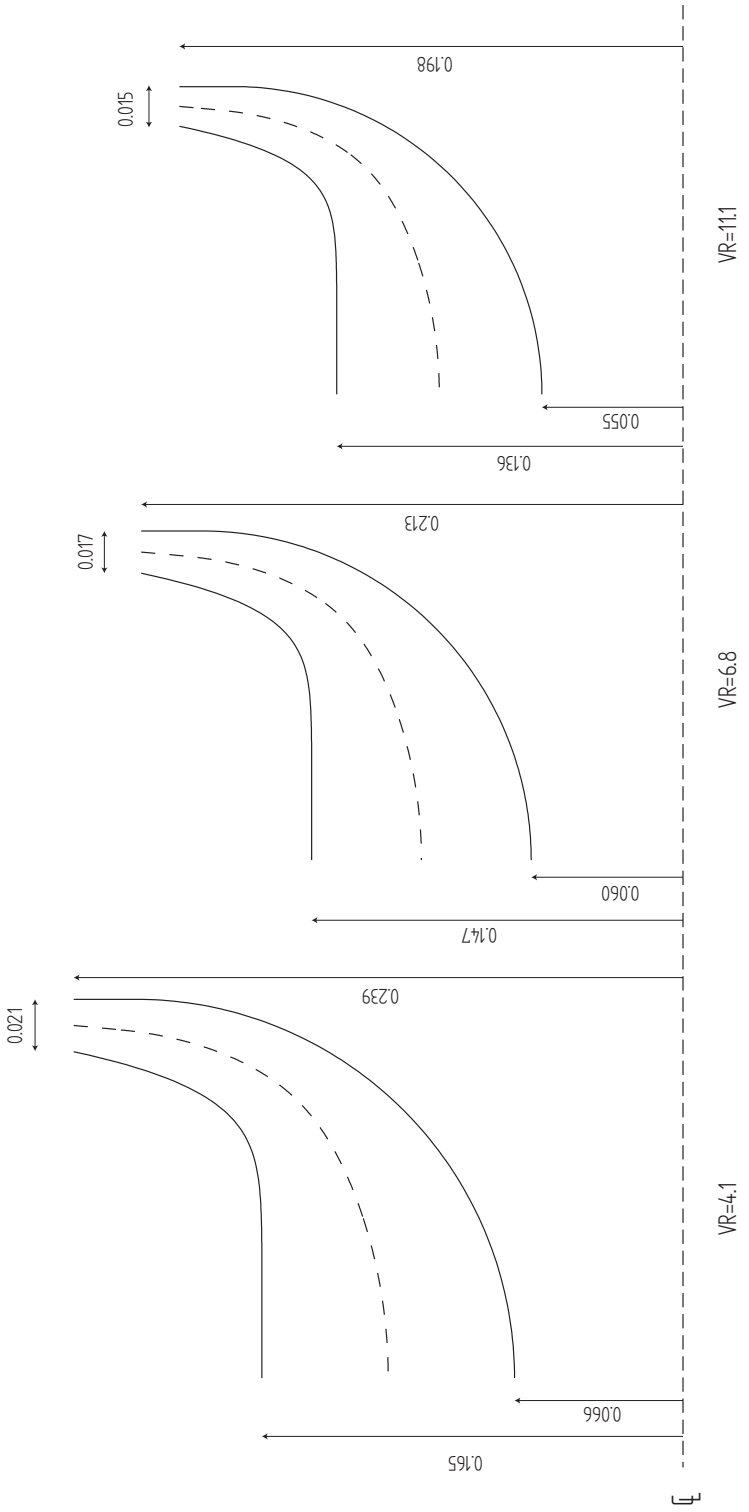

Figure 5.9: Rotor meridional sections for different VR values with constant $SP = 0.10$ m. Dimensions are in millimeters.

5.2.2 SP-VR maps for axial flow stages

This Section presents and compares the SP-VR maps for the eight organic fluids listed in the introduction of this Chapter.

Table 5.3 collects the mass flow rates and the evaporation temperature intervals used for the SP-VR maps: the evaporation temperatures are chosen in order to cover for all fluids the same volumetric expansion ratio range, whereas the mass flow rates ensure approximatively the same minimum size parameter (lower bounds) and turbine size not excessively high (upper bounds). Note that the superheating is fixed at 5 °C for all fluids but *R134a* (for this fluid it is set equal to 10 °C to avoid wet expansion because of the slightly negative slope of the saturated vapor curve). Volumetric expansion ratios higher than 6 are reached by the working fluids having lower critical temperatures (*R1234yf*, *R1234ze(Z)* and *R134a*) starting from supercritical states at turbine inlet. Higher volumetric expansion ratios are instead obtained for the other fluids (having higher critical temperature) at evaporating temperatures of about 120 °C.

Figures 5.10 and 5.11 show that the calculated turbine efficiencies for all fluids fall in the range 85 to 89% for the *SP*-*VR* values being considered. In accordance with the intervals listed in Table 5.3 *VR* is varied for all fluids between 1.6 and 9 whereas *SP* spans a range depending on fluid properties, in particular the density at turbine outlet (see last column of Table 5.3). It can be easily observed that the same general trend is followed by all fluids. Moreover, the closer the fluids class and critical temperatures, the closer the trends of the SP-VR maps. The efficiencies decrease at high *VR* and low *SP* with the exception of the very low $VR \approx\leq 2$ where the detrimental effect of increasing VRs is overcome by the favorable effect of increasing Mach number (subsonic regimes). While at low-intermediate *SP*, both *VR* and *SP* have a remarkable influence on efficiency, at high *SP* the size parameter influence is weakened so that almost horizontal

Table 5.3: Mass flow rate ($\dot{m}$) and evaporation temperature (T_{evap}) intervals to cover the size parameter and volumetric flow ratio ranges of SP-VR maps in Figs. 5.10 and 5.11; mean density values ρ_3 at rotor outlet are shown, as well.

Fluid	$\dot{m}$ interval (kg/s)	T_{evap} interval (°C)	ρ_3
R1234yf	30-150	50-110	45
R134a	20-200	50-120	39
R1234ze(E)	10-150	50-120	32
Isobutane	10-150	50-125	10
R1234ze(Z)	10-150	50-115	11
R245fa	10-150	50-110	10.5
Isopentane	5-200	50-115	3.4
Cyclopentane	2-100	50-115	1.6

iso-efficiency lines are observed. The most similar trend to the ideal gas one obtained in [24] for $\gamma = 1.1$ is achieved by *R1234yf*. This fluid has the lower critical temperature and, accordingly, the lower departure of the compressibility factor from the unit value in case of pressure values around and lower the critical one, as occurring with the condensation temperature and VR range considered here (see Fig. 5.10 for R1234yf and Fig. 5 in [24] for $0.06 \leq SP \leq 0.20$ and $2 \leq VR \leq 9$).

To easily compare the performance of the eight working fluids the iso-efficiency lines referring to 0.87 and 0.88 are superimposed in the two diagrams in Fig. 5.12. A vertical line at fixed *SP* crosses the iso efficiency lines at different *VR*. For instance, at $SP = 0.15$ m *cyclopentane* and *isopentane* give $\eta = 0.87$ at $VR \approx 4$ whereas *R1234yf* gives the same efficiency in spite of the doubled *VR*. *R1234yf* is therefore preferable to the two hydrocarbons for high expansion ratios.

Similarly, at $VR \approx 5$ *cyclopentane* and *isopentane* reach an efficiency of 0.87 at $SP \approx 0.25$ m while *R1234yf* reaches the same value at a much

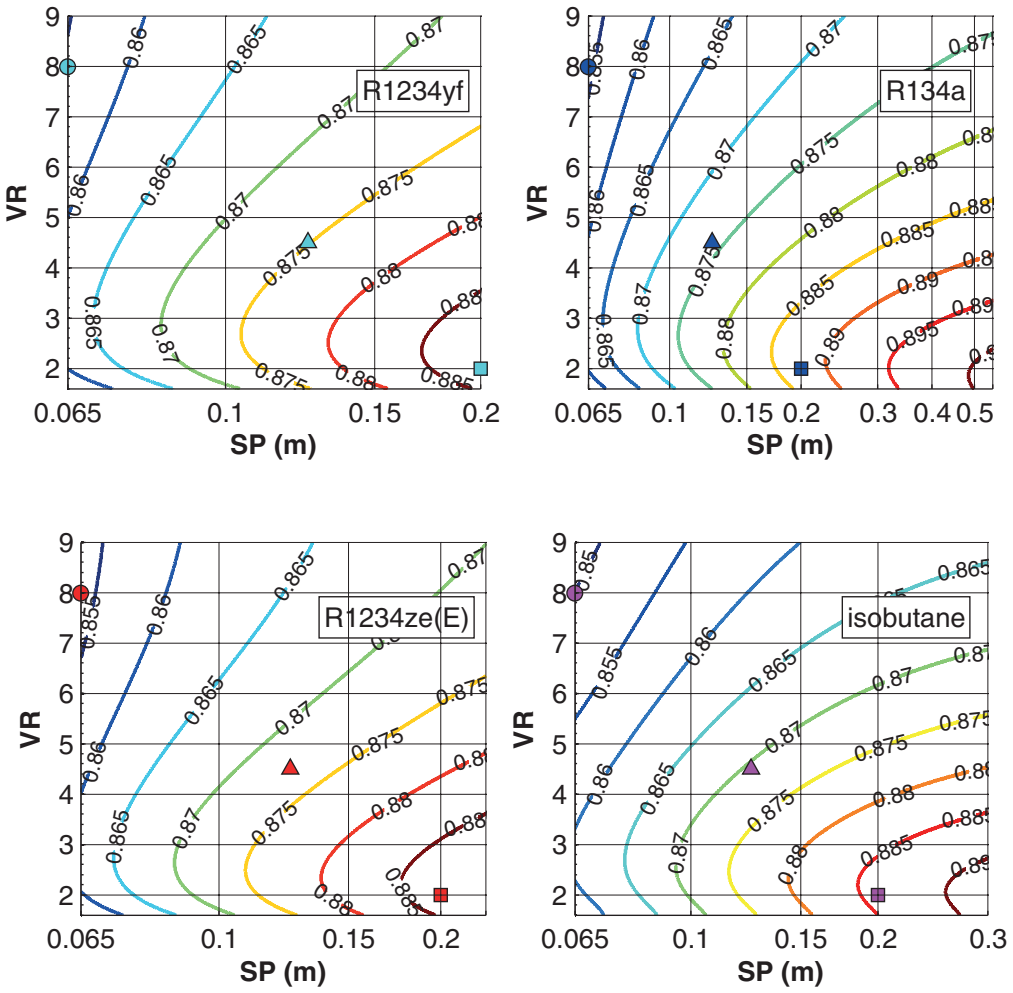

Figure 5.10: Axial turbine efficiency versus size parameter and volumetric flow ratio for different fluids (part A).

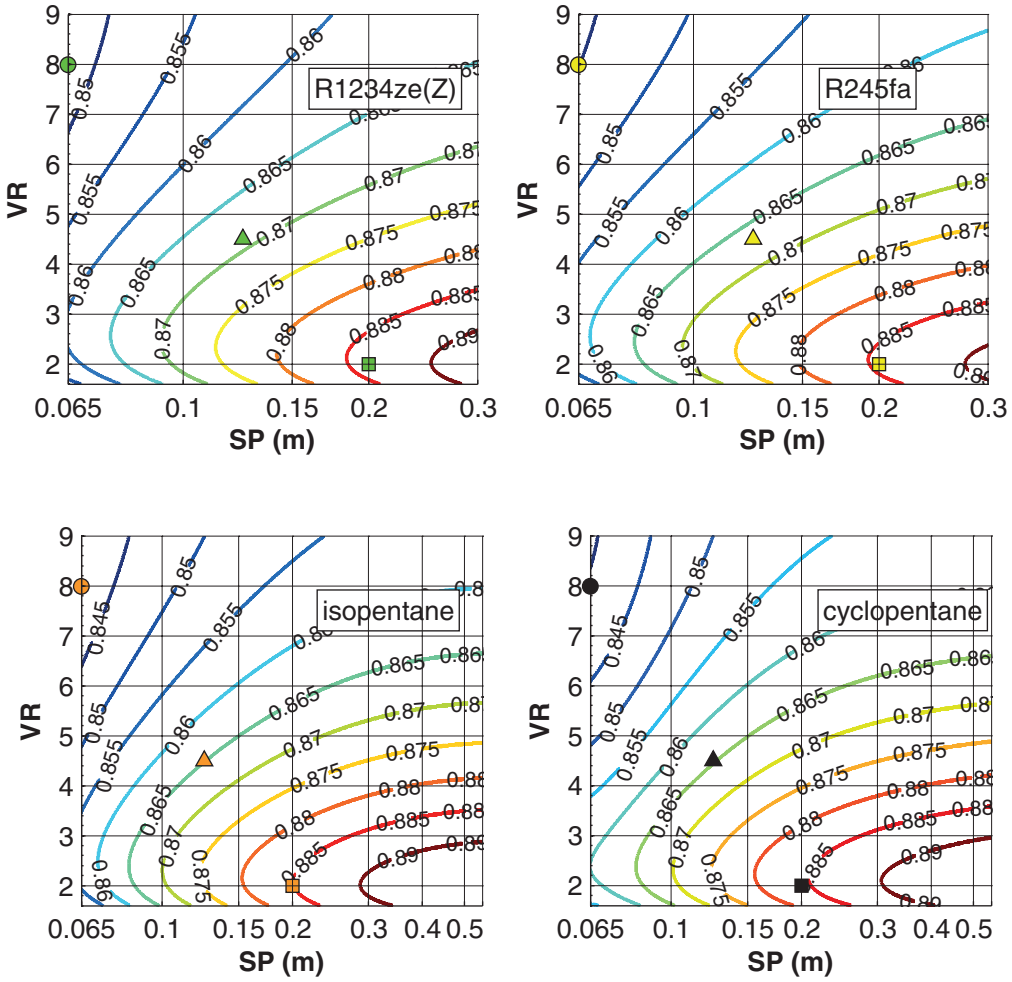

Figure 5.11: Axial turbine efficiency versus size parameter and volumetric flow ratio for different fluids (part B).

lower *SP* (0.10 m). So, *R1234yf* is preferable also for small turbine sizes.

In summary, fluids in the left upper part of Fig. 5.10 are to be preferred to those in the lower right part of Fig 5.11, being less sensitive to lower sizes and higher expansion ratios (i.e., to more severe operating conditions). So, by selecting the best fluids in descending order of *VR* or ascending order of *SP* the following ranking is obtained: *R1234yf*, *R134a*, *R1234ze(E)*, *isobutane*, *R1234ze(Z)*, *R245fa*, *isopentane* and *cyclopentane*. Note that this order follows rising critical temperatures (Table 5.1), i.e., the best fluids show the lowest T_{cr}.

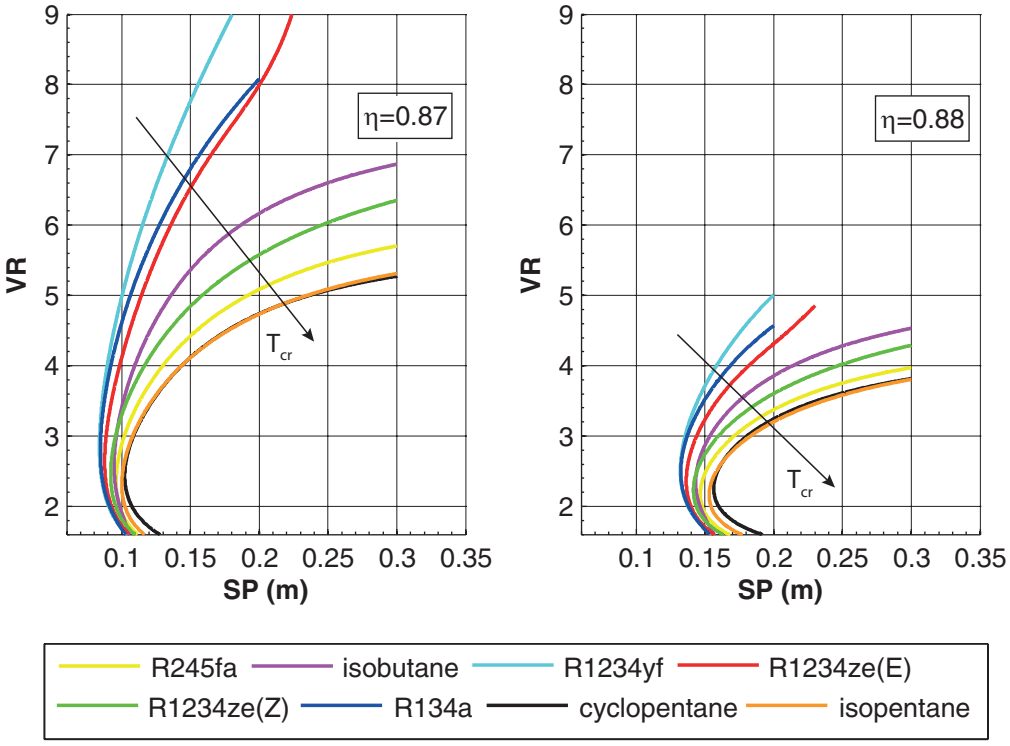

Figure 5.12: Different iso efficiency lines extracted from Figs. 5.10 and 5.11.

For any fluid at fixed *SP* increasing *VR* causes relevant losses mainly due to high velocity flow regimes whereas at fixed *VR* small turbines are disadvantaged mainly because of the higher clearance losses (Figs. 5.10 and 5.11). The main losses arising at high volumetric expansion ratios (*VR*) are the post-expansion losses and shock losses. After a deep analysis of several correlations proposed in the literature to describe these complex

phenomena within a mean line analysis, those proposed by Aungier (see Chapter 4) have been used in this work. According to these equations the effect of the Mach number is less pronounced compared to other correlations (e.g., such as that proposed in [69]) which tend to overestimate these losses at high Mach numbers. This explain the rather low difference between maximum and the minimum isentropic efficiency for all fluids when incrementing VR at fixed SP. On the other hand, the clearance losses markedly affect the efficiency at low SP. Thus, the selection of the clearance loss correlation is critical and directly affects the efficiency gap of turbines of different size. Compared to Macchi and Perdichizzi [24] it is seen that the maximum values are approximately 2% points lower in the region of high SP and low VR whereas the lowest values are 2.5% points in the region of small SP and high VR.

Table 5.4 shows the different ranges of SP that were considered for the different fluids, which primarily depend on the density ρ_3 at expander outlet (see Table 5.3), which, in turn, varies for different fluids. Accordingly, different values of the mass flow rate are needed to obtain the same value of SP for the considered eight working fluids as schematically shown by Fig. 5.13. At fixed mass flow rate, the working fluids having higher density at turbine outlet (*R1234yf* and *R134a*) give lower values of SP, and in turn reduced sizes and costs.

Figures 5.14 and 5.15 show at a glance the influence of SP and VR on the meridional sections, velocity triangles and total pressure losses breakdown, respectively. In particular, Fig. 5.14 shows that an increase of SP at VR of 4.8 mainly results in a notable increase of turbine mean diameter, flaring angles, blade spans and axial chords. For instance, moving from $SP = 0.067$ m to 0.1725 m the mean diameter increases almost by three times. The rotational speed grows towards smaller sizes to assure the optimum specific speed. Instead, no substantial changes are observed in the velocity triangles. At reduced sizes, turbine efficiency decreases due

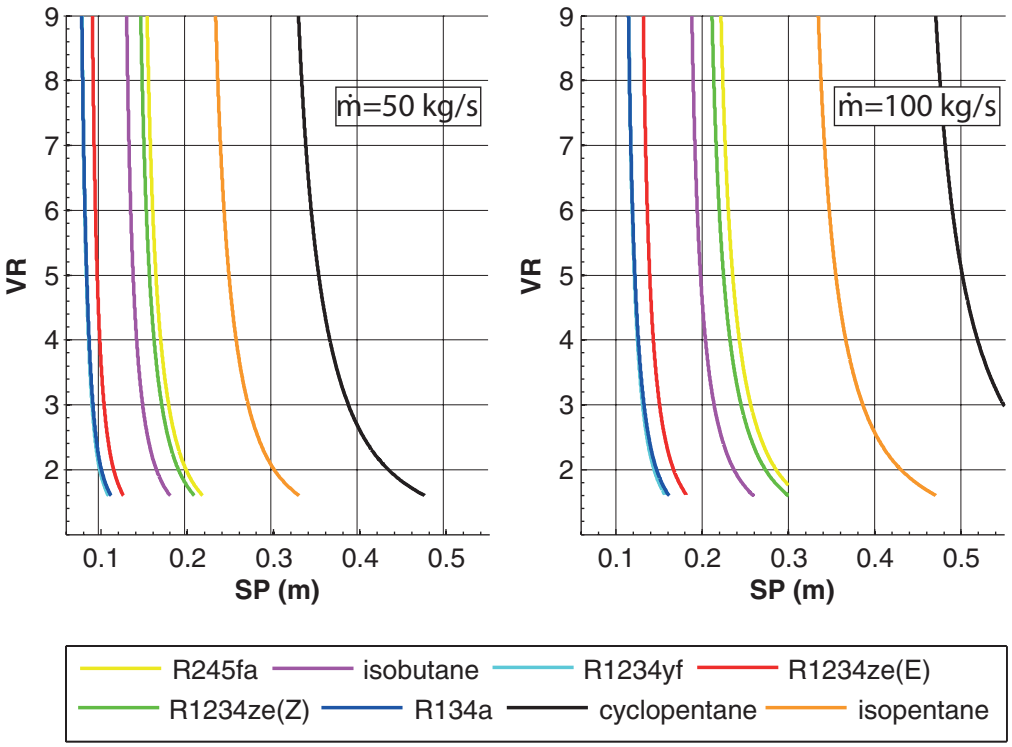

Figure 5.13: Different iso mass flow rate lines in the SP-VR plane for the eight fluids being considered.

Table 5.4: Minimum and maximum simulated *SP* values for each fluid.

Fluid	min *SP* (m)	max *SP* (m)
R1234yf	0.065	0.20
R134a	0.065	0.20
R1234ze(E)	0.065	0.23
Isobutane	0.065	0.30
R1234ze(Z)	0.065	0.30
R245fa	0.065	0.30
Isopentane	0.065	0.55
Cyclopentane	0.065	0.55

to the increase of secondary and clearance losses. The latter results from the clearance manufacturing limits.

Figure 5.15 shows that the increase of VR at $SP = 0.14$ m results in a significant decrease of stator inlet blade span due to higher inlet density along with an increase of the axial blade lengths to accommodate larger volumetric changes under the flaring angles constraints. On the other hand, both mean diameter and rotational speed increase to limit the loading coefficient. The main VR effect on the velocity triangles is a remarkable increase of all velocity modules. Thus, turbine efficiency gradually reduces because of the appearance of loss terms directly related to supersonic flow regimes (i.e., shock and post expansion losses). Furthermore, secondary losses increase as the blade height-chord ratios decrease, whereas profile losses do not vary significantly. The detrimental effect of VR on efficiency could be overcome by increasing the number of turbine stages at the expense of higher costs and more complex arrangements.

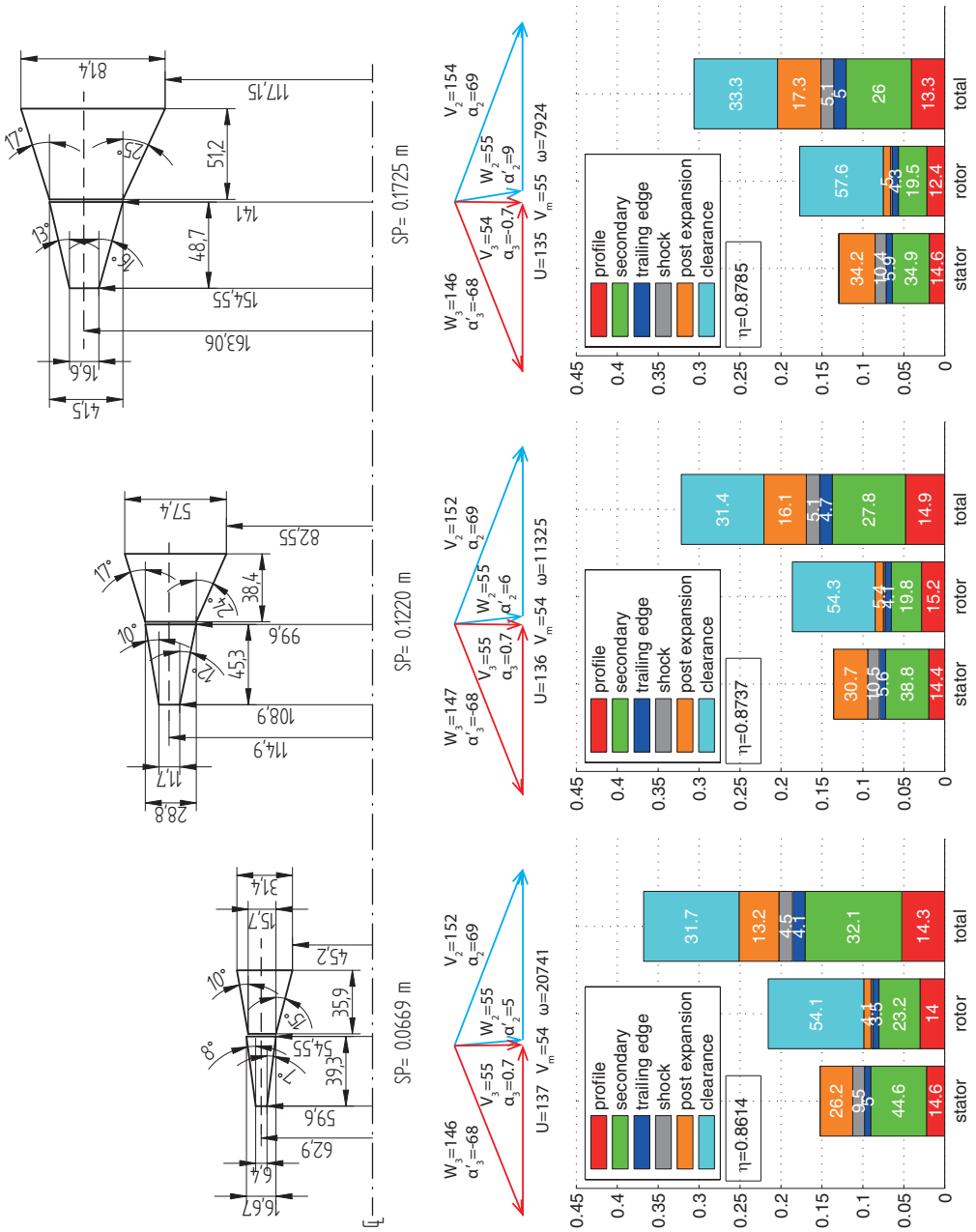

Figure 5.14: Meridional sections, velocity triangles (blue for stator and red for rotor) and total pressure loss coefficients breakdown with expander efficiency for *R1234yf* for different *SP* values with constant $VR = 4.8$. Dimensions of meridional sections are in millimeters and rotational speeds in rotations per minute. White numbers inside bars are the relative percentage weights of loss addendum.

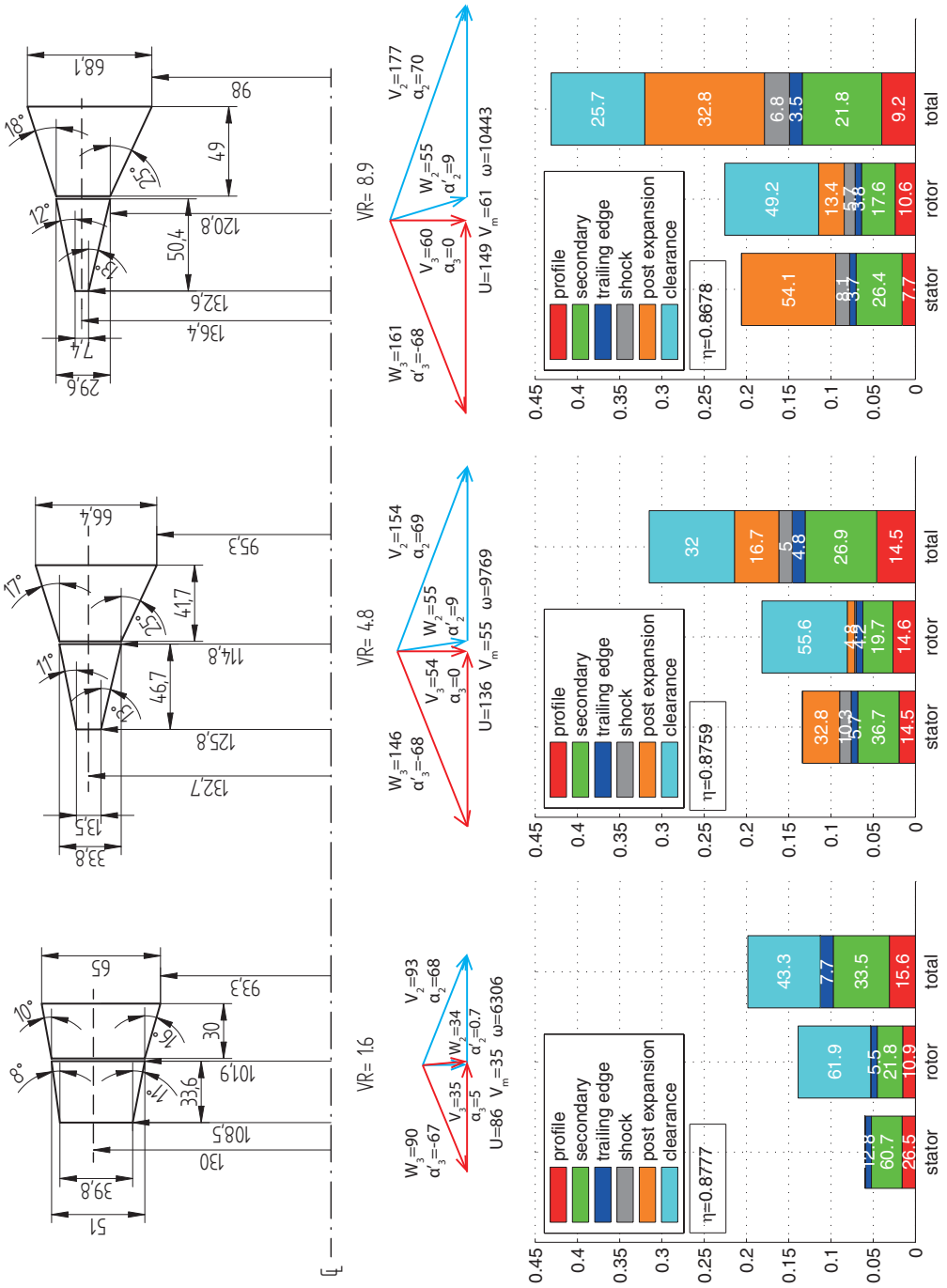

Figure 5.15: Meridional sections, velocity triangles (blue for stator and red for rotor) and total pressure loss coefficients breakdown with expander efficiency for *R1234yf* for different VR values with constant $SP = 0.14$ m. Dimensions of meridional sections are in millimeters and rotational speeds in rotations per minute. White numbers inside bars are the relative percentage weights of loss addendum.

SP-VR maps give also some insights about additional geometric/duty parameters of interest. Figure 5.16 shows very similar values of the mean diameter at the same *SP* for two different fluids (*R245fa* and *isobutane*). The turbine mean diameters linearly increase from 0.15 to 0.55 m when increasing *SP* from 0.07 to 0.30 m. A similar correspondence between mean diameter and *SP* is also found for the other fluids due to the limited variation of specific diameter, but is not reported here for brevity.

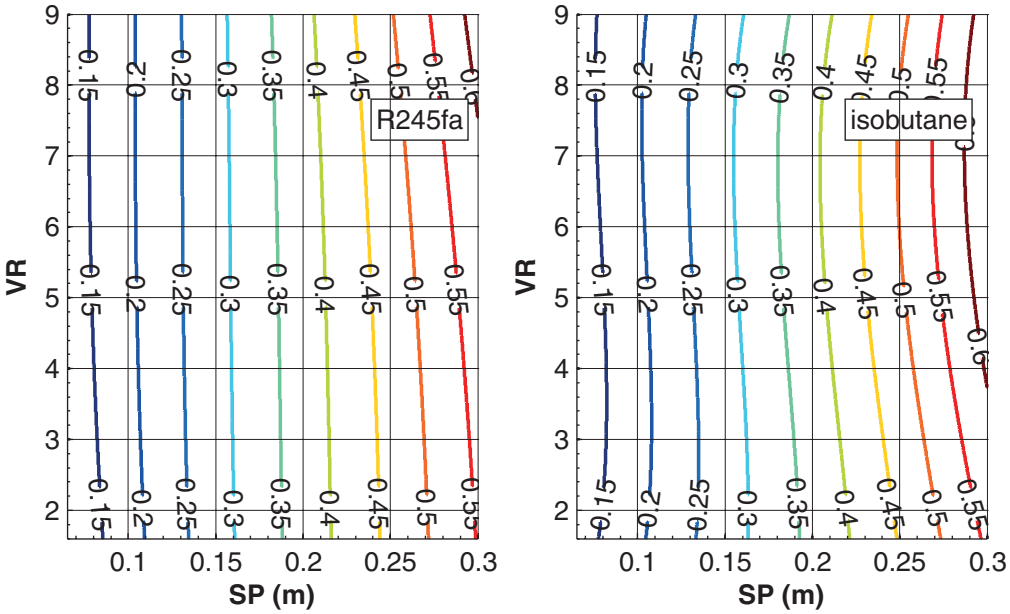

Figure 5.16: Different iso mean diameter lines in the SP-VR plane for R245fa and isobutane.

The optimal rotational speed (rpm) is shown in the *SP-VR* plane in Fig. 5.17. Turbines having high *SP* (i.e., high diameter) and low *VR* (i.e. low enthalpy drop) are characterized by lower angular velocities according to the definition of ψ:

$$\omega = \frac{2}{D_m}\sqrt{\frac{h_1 - h_3}{\psi}} \tag{5.3}$$

Rotational speeds increase from 5000 rpm at high *SP* to about 30000 rpm at low *SP*. The optimal speeds vary depending on the working fluid

(e.g., *R245fa* gives lower rotational speeds than *isobutane* in the whole field of *SP-VR* as shown in Fig. 5.17). In general working fluid associated with the lower rotational speeds are to be preferred because of the lower mechanical and electrical losses in the power generation chain.

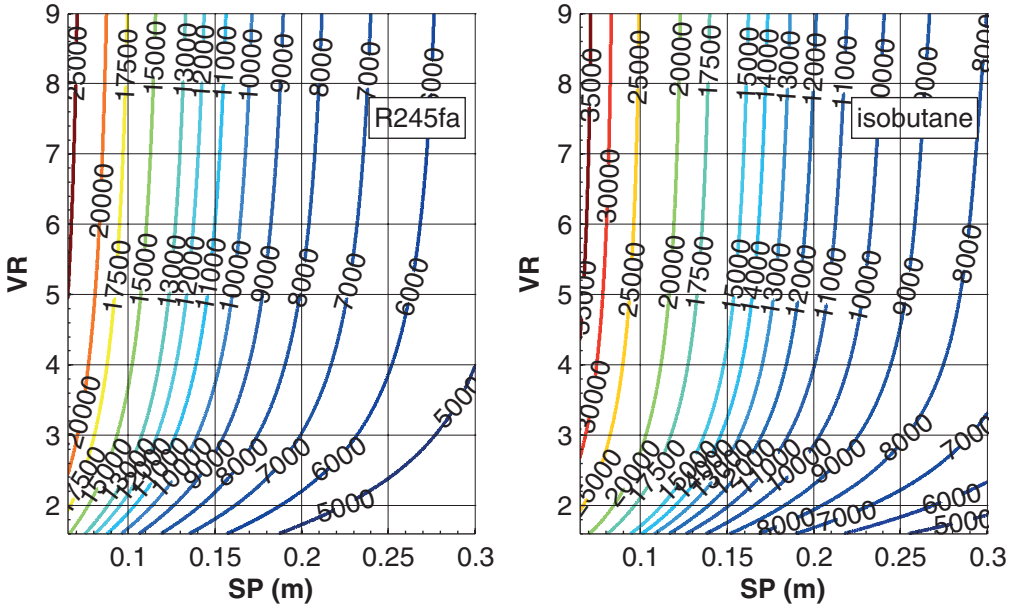

Figure 5.17: Different iso angular velocity lines in the SP-VR plane for R245fa and isobutane.

5.2.3 Multistage axial flow turbines

The *SP-VR* axial stage efficiency map is strictly valid for single-stage turbines. However, it is worth to discuss on the possibility to extend these map to the multistage arrangement. The hypotheses underlying this map (see Chapter 4) demand for constant mean diameter of the stages. In addition, the constant stages angular speed of a single shaft turbine requires a well defined split of the available specific work, as well. In this scenario, the resulting overall turbine efficiency would result from the specific-work-averaged value of the efficiency data corresponding to each stage *SP-VR* pair. However, the above restrictions also force to accept the two following approximations.

- *Kinematic approximation.* The split of the specific work across the stages reflects in differences in the flow angles at the inlet section of each fixed blade row. Actually, the same values of the exit and inlet angles of adjacent stages are possible only if the stages share the same *SP*-*VR* pair (in agreement with the repeating stage hypothesis). However, the variability of the inlet flow angle is rather limited in the entire map (angles vary in the range from about 65 to about 70°).

- *Geometrical approximation.* For example, the expansion of *R245fa* having $VR \approx 5.2$ could be obtained by means of a single-stage axial turbine having $SP = 0.16$ m working at a mean loading factor equal to 1.08. The same expansion performed with a two-stage machine would require rotors (i) working at almost equal mean loading factor (0.95 and 1.05, for the first and second stage, respectively); (ii) having a tip radius ratio between the second stage inlet and the first stage exit equal to 1.3. The corresponding $SP-VR$ pairs are 0.12-1.6 and 0.18-3.3, for the first and the second stage, respectively.

The first of these approximations is likely acceptable. Conversely, the second one should require to admit a 40% jump in the axial velocity from the first stage exit to the second stage inlet. Thus, the only reliable solution for the multistage arrangement is the availability of a specific efficiency map for each turbine of a given number of stages (i.e., one map for the two-stages turbine, one for the three-stages, and so on). This conclusion is not surprising because the stage number is a similarity variable which cannot be disregarded as reported in Chapter 3.

5.3 Generalized turbine efficiency map for ORC optimization

Maps in Figs. 5.10 and 5.11 are ordered for ascending values of critical temperature (T_{cr}): *R1234yf* has the lowest T_{cr} whereas *cyclopentane* has the highest T_{cr}. Iso efficiency lines of the same value (i.e., 0.87 and 0.88) extracted from SP-VR maps were superimposed in Fig. 5.12 to highlight the fluid influence on the efficiency: it is seen that some differences exist. So, it is attempted to catch the fluid influence by using the critical temperature as third predictor in the efficiency prediction. Three points having different *SP*-*VR* coordinates (0.065,8), (0.125,4.5), (0.20,2) are superimposed to each map of Figs. 5.10 and 5.11: they are chosen as representative of low (circle marker), medium (triangle marker) and high (square marker) efficiency regions. Efficiencies associated with all 24 marked points of Fig. 5.10 and 5.11 are collected in Fig. 5.18 to highlight any relationship between turbine efficiency and T_{cr}. It can be easily noticed that turbine efficiency increases at lower T_{cr} especially at low *SP* and high *VR*. Thus, the selection of working fluids with lower critical temperatures enables the detrimental effects on turbine efficiency deriving from low *SP* and high *VR* to be reduced. The analysis of variance demonstrates that T_{cr} (along with *SP* and *VR*) is statistically significant to predict the efficiency. So, a linear regression model between efficiency (response variable) and *SP*, *VR* and T_{cr} (predictors) is searched by applying a stepwise regression procedure to the whole set of data used to plot the efficiency maps of all the fluids being considered.

The generalized efficiency correlation is

$$\eta = \sum_{i=0}^{26} k_i X_i \tag{5.4}$$

the coefficients of which are shown in Table 5.6. Equation (5.4) fits

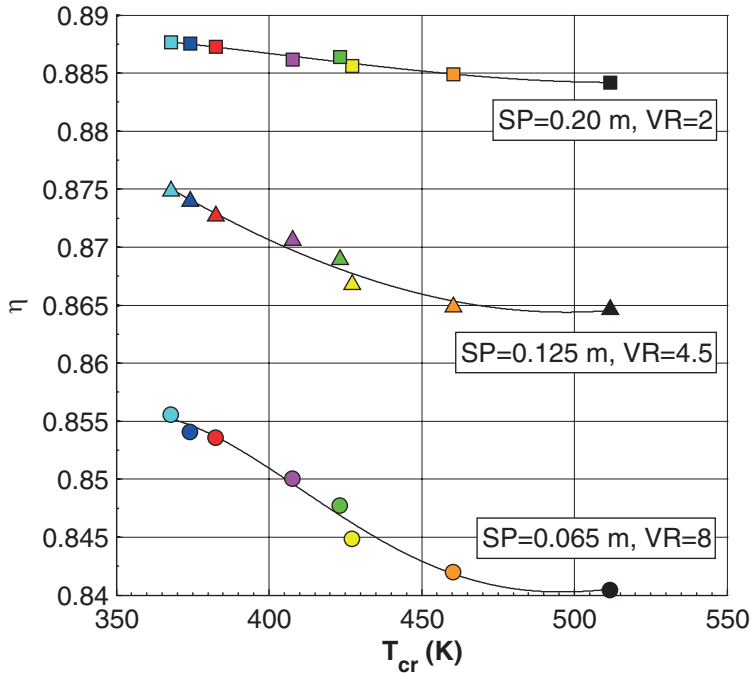

Figure 5.18: Efficiency values corresponding to three different couples SP-VR extracted from the maps of Figs. 5.10 and 5.10. Colors identify the working fluid (refer to the legend of Fig. 5.12), markers identify low (circle), medium (triangle) and high (square) efficiency regions.

Table 5.5: Upper and lower bounds of independent variables when using Eq. (5.4).

	min value	max value
SP (m)	0.065	0.20 if $367.9 \leq T_{cr} < 382.5$
		0.23 if $382.5 \leq T_{cr} < 407.8$
		0.30 if $407.8 \leq T_{cr} < 460.4$
		0.55 if $460.4 \leq T_{cr} \leq 511.7$
VR	1.60	9
T_{cr} (K)	367.9	511.7

well the turbine model output data ($R^2 = 0.993$). Standard error (SE) and p-value are reported in Table 5.6. Equation (5.4) allows not only to rapidly calculate the efficiency for the considered eight fluids but also to have a first performance estimate for any fluid having T_{cr} between *R1234yf* and *cyclopentane* ones. The boundary conditions listed in Table 5.5 are to be considered to avoid meaningless extrapolated efficiency values in the application of the generalized efficiency correlation.

Note that the calculated efficiency trends are affected by real gas effects in so far as the equations of state implemented in the fluid properties libraries predict the actual gas behavior. The critical temperature is to be interpreted as a broad indicator of fluid properties which allows to describe all the modeled *SP*-*VR* maps for axial turbine stages by means of the unique functional form $\eta^* = f(SP, VR^*, T^*_{cr})$ (the superscript * stands for value at best efficiency operation, see Chapter 3). Except for operation at very high VR^* (see, e.g. the siloxane MM ORC turbine designed in [83] in which the influence of the fundamental derivative of gas dynamics (Γ) might be not negligible), this evidence supports the validity of the quasi-similarity approach $\eta^* = f(SP, VR^*, Z)$ for optimized turbine designs, where the true similarity parameter Z is here replaced by the critical tem-

Table 5.6: Regression analysis results

i	X_i	k_i	SE_i	$p\text{-}value_i$
0	*Intercept*	0.70521	0.18264	0.00013469
1	SP	1.1963	0.25963	5.7431e-06
2	VR	-0.022219	0.03133	0.47869
3	T_{cr}	0.00041894	0.0012612	0.73995
4	SP^2	-3.7789	0.79066	2.6058e-06
5	$SP * VR$	-0.075571	0.013697	6.7691e-08
6	VR^2	-0.0089625	0.00052127	2.7176e-48
7	$SP * T_{cr}$	-0.0022818	0.0011608	0.050126
8	$VR * T_{cr}$	0.00048912	0.00021783	0.025374
9	T_{cr}^2	-5.4398e-07	2.8901e-06	0.85082
10	SP^3	3.0675	0.36211	7.1152e-16
11	$SP^2 * VR$	0.084873	0.018447	5.9152e-06
12	$SP * VR^2$	0.0054258	0.0012239	1.2489e-05
13	VR^3	0.00089835	6.0747e-05	1.1338e-38
14	$SP^2 * T_{cr}$	0.0072256	0.0036625	0.049308
15	$SP * VR * T_{cr}$	4.8573e-05	3.594e-05	0.17742
16	$VR^2 * T_{cr}$	2.055e-06	5.6586e-07	0.00032434
17	$SP * T_{cr}^2$	2.3282e-06	1.2339e-06	0.060017
18	$VR * T_{cr}^2$	-1.3485e-06	5.0075e-07	0.0074273
19	T_{cr}^3	1.7444e-10	2.1992e-09	0.93683
20	SP^4	-1.7663	0.25592	2.4708e-11
21	$SP^3 * VR$	-0.036768	0.016849	0.02977
22	$SP^2 * VR^2$	-0.0032447	0.0010874	0.0030492
23	VR^4	-3.5875e-05	2.8261e-06	1.4589e-30
24	$SP * VR^2 * T_{cr}$	-5.8154e-06	3.2231e-06	0.072063
25	$SP^2 * T_{cr}^2$	-7.5059e-06	3.7888e-06	0.048374
26	$VR * T_{cr}^3$	1.1343e-09	3.8127e-10	0.0031345

perature. Accordingly, these findings leave room for the possibility of a limited extension to different working fluids of experimental data obtained with a specific organic fluid and, so, it is possible to smooth the very strong restriction to the extension of turbine maps to different fluids theoretically stated in Chapter 3.

5.4 Critical remarks

One of the most critical aspects of this work is that the model and the resulting SP-VR efficiency maps were non subjected to a strong validation work against ORC turbines experimental data. On the other hand, it is well known that ORC turbines efficiency values and thermodynamic/geometrical data required to calculate SP and VR are not available as they are proprietary data of ORC turbine manufactures. Being unfeasible this way to validate the model, a possible alternative "validation technique" could be the comparison of SP-VR maps with the analogous maps obtained from models by other authors and available in the scientific literature (see e.g., [24], [25]).

This approach has been partially followed in the previous Sections and the matching was quite satisfactory for R1234yf. Nevertheless, this validation approach is questionable because the SP-VR maps proposed by the other authors result from different models and assumptions. For instance, the ideal gas behavior and constant Reynolds number hypotheses under the maps of [24] and [25] make not surprising that efficiency for equal SP-VR values is different from efficiency predicted by the present models. On the other hand, the improvement of turbine technology over the last decades certainly influences the turbine efficiency, i.e., the values in [24] and [25] might be pessimistic. It is believed that the only effective validation procedure is the direct comparison between the model outputs and a sufficiently large set of experimental data of optimized ORC turbines spanning wide

ranges of size (i.e., SP), expansion ratio (i.e., VR) and working fluids.

As for the radial turbine SP-VR map, it has been possible to calculate the size parameter and volumetric flow ratio for a high size turbine of known efficiency. Available data refer to the maximum turbine efficiency reached by the four radial inflow turbines equipping the 48 MWe (gross) Stillwater geothermal power plant, recently built in Nevada (USA) [46], whose design point efficiency approaches 90%. These 12 MW radial turbines were designed by one of the leading turbine manufacturer in the world and can be considered among the biggest radial turbines operating in ORC systems. Their working point falls on the right edge of the map in Fig. 5.6 and at an average volumetric expansion ratio slightly lower than 6.0. At these conditions the map predicts a turbine efficiency in the range 89.0-89.5%, which closely agrees with the experimental data presented in [46].

Conclusions

The aim of this work was to obtain general efficiency maps to predict the performance of organic fluid turbines in a wide range of design specifications (mass flow rate and enthalpy drop) and working fluids.

The fundamental principles of similarity traditionally employed in the turbine design practice are reviewed to identify the design variables that are able (i) to reduce the dependency of the efficiency on the fluid nature and (ii) to take into account the scale and compressibility effects. In agreement with the similarity principles, it was shown that:

1. The strict flow similarity cannot be preserved in the turbine design when the working fluid is changed.

Nevertheless, it was rigorously demonstrated that:

2. the volumetric flow ratio (VR) and the size parameter (SP) can be used as similarity parameters in substitution of the machine Mach number to account for the fluid compressibility (VR) and for technological features (e.g., surface roughness, trailing and leading edge thicknesses, radial clearance, etc.) which cannot scale with the main geometry of the turbine (SP).

The rationale of SP-VR performance maps originally introduced more than thirty years ago by Macchi and Perdichizzi is explained and the validity of this representation is confirmed. In particular, results show that:

3. The SP-VR maps allow to extend the efficiency data of a turbine operating with a specific fluid to a turbine of the same type operating with a different fluid, when the deviation of the compressibility factor from the unit value is negligible, or when the two turbines work at thermodynamic states featuring similar values of the compressibility factor.

Experimental data derived from real manufacturer design charts of radial inflow turbines operating with air have been used to build the corresponding SP-VR map. It is believed that:

4. This map supplies reliable predictions of ORC turbine efficiency starting from turbines designed for operation with traditional fluids (air, steam) whenever the ORC system specifications do not suggest a new turbine design, keeping the turbine technology and designs that are available for traditional fluids.

Mean line models for the preliminary design of radial inflow turbines and axial flow turbine stages have been developed to investigate the effects on turbine performance of

- design specifications (i.e., mass flow rate and enthalpy drop), and
- design parameters (i.e., specific speed (n_s) and velocity ratio (ν_s) for radial turbines, and loading coefficient (ψ) and flow coefficient (ϕ) for axial turbines, respectively).

In particular, the analysis of $n_s - \nu_s$ charts obtained for radial turbines working with R245fa has highlighted that:

5. the optimum specific speed (n_s) lies within a narrow range centered on 0.42 regardless of the expansion ratio. This value is approximately 25% lower than that suggested for common fluids (air, flue gases), but consistent with the optimum values suggested by the most recent

studies on radial turbines in ORC systems. The optimum velocity ratio (ν_s) approaches 0.70, for turbines working at low expansion ratios, whereas it decreases to 0.60 at the high expansion ratios common for ORC turbines.

As per the $\psi - \phi$ charts for the axial turbines it has been demonstrated that

6. The optimum loading coefficient ψ slightly increases as the volumetric flow ratio increases (i.e., from 1 to 1.2 when VR changes from 1.7 to 9), whereas the optimum flow coefficient remain unchanged ($\phi = 0.4$).

However, the discussion on $n_s - \nu_s$ and $\psi - \phi$ charts for the same fluid (R245fa) and different VR and SP showed that

7. Both VR and SP have a not negligible effect on the turbine efficiency. These parameters play a crucial role in the definition of ORC turbine performance and cannot be disregarded even in the preliminary design phase. This appears even more clearly in the SP-VR maps collecting the turbine efficiency of designs featuring optimum design parameters for a wide range of design specifications. The SP-VR map for radial inflow turbines handling R245fa shows that the optimum volumetric expansion ratio (VR) is around 3.7-4.0. At higher expansion ratios the efficiency penalty is moderate and it is mainly due to the onset of supersonic flow conditions at nozzle outlet and the increase of the leaving kinetic energy loss at rotor exit. The efficiency decay is approximately equal to 3%-points when the volumetric expansion ratio increases from 4 to 12. The turbine size strongly affects the efficiency: a decrease of the size parameter from 0.25 to 0.02 m results in an efficiency drop of approximately 3.5%-points.

As per the SP-VR maps for the axial turbines, eight fluids belonging to different classes (i.e., hydrocarbons, hydrofluorocarbons and hydrofluoroolefines) were considered to investigate the effect of molecular properties on the efficiency and the advantages of SP-VR maps in this respect.

This investigation shows that the turbine efficiency falls in the range 85 to 89%. Moreover, the same general trend is shared by turbines designed to operate with these eight fluids: efficiency increases as VR decreases and SP increases. For instance, considering R1234yf, an increase of SP from 0.067 to 0.173 m (at constant VR) improves the efficiency from 86% to 88%, whereas a VR increase from 1.6 to 8.9 (at constant SP) produces an efficiency decay from 88% to 86.8%. Effects of SP and VR variations on the main geometrical features have been shown as well: an increase of SP mainly produces a linear increase of the mean diameter and blade height, whereas an increase of VR leads to an increase in flaring angles and blade axial chords to better accommodate the volumetric flow rate variation.

A detailed comparison of the SP-VR maps has highlighted that

8. Working fluids having lower critical temperature at equal values of the size parameter - volume flow ratio result in higher turbine efficiency;

9. Efficiency differences are lower between fluids belonging to the same class and having similar critical temperatures. These differences become slighter for high SP and low VR where negligible differences exist among different fluids.

These results suggested to consider the critical temperature as a third efficiency predictor in addition to the size parameter and volumetric flow ratio. By applying a statistical stepwise regression technique to the entire efficiency data set,

10. An analytical correlation between turbine efficiency and size parameter, volumetric flow ratio, and critical temperature is obtained. This

correlation permits to easily calculate the turbine efficiency for any working fluid having critical temperature in the range 350 - 500 K without the need of to the meanline design procedure. Accordingly, in the absence of experimental data it represents a tool to estimate the maximum turbine efficiency.

This correlation can be easily included in the thermodynamic optimization procedures of the whole ORC system to improve the thermodynamic cycle, since SP and VR depend only on cycle parameters (and the critical temperature is a fluid property). So, the limitations due to a separate design of turbine and system can be overcome and misleading predictions about power plant net production can be avoided.

On the other hand, only a patient collection of experimental data for a step-by-step creation of an extensive database of measured efficiency data could effectively improve the estimates of the suggested model. Moreover, the preliminary designs obtained here could be studied with CFD analyses to obtain additional indications about the validity of performance predictions.

Bibliography

[1] S. Quoilin, S. Declaye, F. Bertrand Tchanche, and V. Lemort. Thermo-economic optimization of waste heat recovery organic Rankine cycles. *Applied Thermal Engineering 31, 2885-2893*, 2011.

[2] U. Drescher and D. Brüggemann. Fluid selection for the Organic Rankine Cycle (ORC) in biomass power and heat plants. *Applied Thermal Engineering 27, 223-228*, 2007.

[3] S. Quoilin, M. Orosz, H. Hemond, and V. Lemort. Performance and design optimization of a low-cost solar organic Rankine cycle. *Solar Energy 85, 955-966*, 2011.

[4] A. Toffolo, A. Lazzaretto, G. Manente, and M. Paci. A multi-criteria approach for the optimal selection of working fluid and design parameters in Organic Rankine Cycle systems. *Applied Energy 121: 219-232*, 2014.

[5] B. Saleh, G. Koglbauer, M. Wendland, and J. Fischer. Working fluids for low-temperature organic Rankine cycles. *Applied Thermal Engineering 31, 1210-1221*, 2007.

[6] E. Macchi and M. Astolfi. *Organic Rankine Cycle (ORC) Power Systems: Technologies and Applications.* Woodhead Publishing, 2016.

[7] M. Pini, G. Persico, E. Casati, and V. Dossena. Preliminary design of

a centrifugal turbine for organic Rankine cycle applications. *Journal of Engineering for Gas Turbines and Power 135*, 2013.

[8] D. Maraver, J. Rojo, V. Lemort, and S. Quolin. Systematic optimization of subcritical and transcritical organic Rankine cycles (ORCs) constrained by technical parameters in multiple applications. *Applied Energy 117: 11-29*, 2014.

[9] H. Yu, X. Feng, and Y. Wang. A new pinch based method for simultaneous selection of working fluid and operating conditions in an ORC (Organic Rankine Cycle) recovering waste heat. *Energy 90: 36-46*, 2015.

[10] J. Vivian, G. Manente, and A. Lazzaretto. A general framework to select working fluid and configuration of ORCs for low-to-medium temperature heat sources. *Applied Energy 156: 727-746*, 2015.

[11] E. Sauret and A. S. Rowlands. Candidate radial-inflow turbines and high-density working fluids for geothermal power systems. *Energy 36, 4460-4467*, 2011.

[12] P. Colonna and S. Rebay. Numerical simulation of dense gas flows on unstructered grids with an implicit high resolution upwind Euler solver. *International Journal of Numerical Methods in Fluids 46: 735-765*, 2004.

[13] C. A. M. Ventura, P. A. Jacobs, A. S. Rowlands, P. P. Repar, and E. Sauret. Preliminary design and performance estimation of radial inflow turbines: an automated approach. *Journal of fluid engineering, 134*, 2012.

[14] D. Fiaschi, G. Manfrida, and F. Maraschiello. Thermo-fluid dynamics preliminary design of turbo-expanders for ORC cycles. *Applied Energy 97: 601-608*, 2012.

[15] D. Fiaschi, G. Manfrida, and F. Maraschiello. Design and performance prediction of radial ORC turboexpanders. *Applied Energy 138: 517-532*, 2015.

[16] K. Rahbar, S. Mahmoud, R. K. Al-Dadah, and N. Moazami. Parametric analysis and optimization of a small-scale radial turbine for Organic Rankine Cycle. *Energy 83: 696-711*, 2015.

[17] D. Fiaschi, G. Innocenti, G. Manfrida, and F. Maraschiello. Design of micro radial turboexpanders for orc power cycles: From 0d to 3d. *Applied Thermal Energineering 99: 402-410*, 2016.

[18] E. Sauret and Y. Gu. Three-dimensional off-design numerical analysis of an organic rankine cycle radial-inflow turbine. *Applied Energy 135: 202-211*, 2014.

[19] H. Moustapha, M. F. Zelesky, N. C. Baines, and D. Japikse. *Axial and radial turbines*. Longman Scientific and Technical, Harlow, England, 2003.

[20] E. Martelli, F. Capra, and S. Consonni. Numerical optimization of Combined Heat and Power Organic Rankine Cycles - Part A: Design optimization. *Energy 90: 310-328*, 2015.

[21] A. Meroni, J. Andreasen, L. Pierobon, and F. Haglind. Optimization of Cycle and Expander Design of an Organic Rankine Cycle Unit Using Multi-Component Working Fluids. *ASME Turbo Expo 2016, Paper No. GT2016-58065*, 2016.

[22] S. F. Smith. A simple correlation of turbine efficiency. *Journal of Aeronautical Society 69: 467-470*, 1965.

[23] O. E. Balje. *Turbomachines: A Guide to Design, Selection and Theory*. Wiley, New York, 1981.

[24] E. Macchi and A. Perdichizzi. Efficiency prediction for axial flow turbines operating with nonconventional fluids. *Trans. ASME Journal of Engineering for Power 103: 718-724*, 1981.

[25] A. Perdichizzi and G. Lozza. Design criteria and efficiency prediction for radial inflow turbines. *Proceedings of the Gas Turbine Conference and Exhibition, Anaheim, CA (USA)*, 1987.

[26] C. M. Invernizzi. *Closed Power Cycles: Thermodynamic Fundamentals and Applications*. Springer-Verlag, London, 2013.

[27] A. Whitfield and N. C. Baines. *Design of radial turbomachines*. Longman Scientific and Technical, Harlow, England, 1990.

[28] S. A. Korpela. *Principles of Turbomachinery*. John Wiley, New York, 2011.

[29] S. L. Dixon. *Fluid mechanics and Thermodynamics of Turbomachinery*. Butterworth-Heinemann, London, 2010.

[30] C. Rodgers and R. Gleiser. Performance of a high-efficiency radial/axial turbine. *ASME Journal of Turbomachinery, 109: 151-154*, 1987.

[31] H. Rohlik. Analytical determination of radial inflow turbine design geometry for maximum efficiency. *Techical report TN D-4384, NASA, Lewis Research Center*, 1975.

[32] S. Sandrolini and G. Naldi. *Macchine*. Pitagora editore, Bologna (in Italian), 1996.

[33] J. H. Horlock. *Axial Flow Turbines*. Butterworth Publishers Ltd, London, 1966.

[34] A. Catania. *Complementi di macchine*. Levrotto e Bella, Torino (in Italian), 1979.

[35] O. E. Balje. Axial turbine performance evaluation. Part B. Optimization with and without constraints. *Trans ASME 74: 349-360*, 1968.

[36] J. M. Smith, H. C. Van Ness, and M. M. Abbott. *Introduction to chemical engineering thermodynamics*. McGraw-Hill, 2004.

[37] P. A. Thompson. A fundamental derivative in gasdynamics. *The Physics of Fluids 14: 1843-1849*, 1971.

[38] E. Buckingham. On physically similar systems; illustrations of the use of dimensional equations. *Physical Review Journals Archive 4, 345*, 1914.

[39] G. T. Csanady. *Theory of Turbomachinery*. McGraw-Hill, Waterloo, 1964.

[40] G. F. Wislicenus. *Fluid mechanics of turbomachinery*. Dover publications, New York, 1965.

[41] C. V. Davis. *Handbook of applied hydraulics*. Mc Graw Hill, New York and London, 1942.

[42] K. Rutschi. Zur wirkungsgradaufwertung von stromungsmachinen. *Schweiz. Bauzth. 76: 603-606*, 1958.

[43] B. Eckert. Uberblick forschungsergebnisse des f.k.f.s. an axial durchstromten verdichtern. *Report 171 of the Lilienthal Society: 34-49*, 1943.

[44] R. Capata and E. Sciubba. Experimental Fitting of the Re-Scaled Balje Maps for Low Reynolds Radial Turbomachinery. *Energies 8: 7986-8000*, 2015.

[45] R. H. Aungier. *Turbine Aerodynamics: Axial-Flow and Radial-Flow turbines Design and Analysis*. ASME, New York, 2006.

[46] G. Manente. Analysis and development of innovative binary cycle power plants for geothermal and combined geo-solar thermal resources. *Ph.D. thesis. Italy; University of Padova*, 2011.

[47] E. W. Lemmon, M. L. Huber, and M. O. McLinden. NIST standard reference database 23: reference fluid thermodynamic and transport properties-REFPROP, version 9.0. *National Institute of Standards and Technology, Standard Reference Data Program, Gaithersburg*, 2007.

[48] D. Japikse and N. C. Baines. *Introduction to Turbomachinery*. Concepts ETI and Oxford University Press, Norwich, Vermont, USA, 1994.

[49] J. H. Horlock. Review of losses and efficiencies in axial-flow turbines. *International Journal of Mechanical Science 2: 48-75*, 1960.

[50] O. E. Balje. A contribution to the problem of designing radial turbomachines. *Trans ASME 74: 451-472*, 1952.

[51] C. Rodgers. Mainline performance prediction for radial inflow turbines. *VKI lecture series 1987-07*, 1987.

[52] L. J. Kastner and F. B. Bhinder. A method for predicting the performance of a centripetal gas turbine fitted with a nozzleless volute casing. *Trans. ASME 75-GT-65, International Gas Turbine Conference and Products Show, Houston, Texas, USA, March 2-6*, 1975.

[53] C. Rogo. Development of a high tip speed radial turbine system for a small turboalternator. *SAE technical paper No. 710552*, 1971.

[54] D. Japikse. Advanced diffusion levels in turbochargers compressors and component matching. *Institution of Mechanical Engineer, London, UK, April 26-28*, 1982.

[55] R. S. Benson. An analysis of the losses in a radial gas turbine. *Institution of Mechanical Engineer, 180 3J: 41-53*, 1965.

[56] R. P. Benedict, N. A. Carlucci, and S. D. Swetz. Flow losses in abrupt enlargements and contractions. *Journal of Engineering for power, 88 3J: 73-81*, 1966.

[57] S. M. Futral and C. A. Wasserbauer. Off-design performance prediction with experimental verification for a radial-inflow turbine. *NASA Technical Note TN D-2621*, 1965.

[58] F. J. Wiesner. A review of slip factors for centrifugal impellers. *Journal of engineering for power, 89: 558-572*, 1967.

[59] J. D. Stanitz. Some theoretical aerodynamic investigations of impellers in radial and mixed flow centrifugal compressor. *Trans. ASME, 74: 473-497*, 1952.

[60] W. Jensen. The design and performance analysis of radial-inflow turbines. *NREC Report, 1067-1*, 1964.

[61] C. A. Wasserbauer and A. J. Glassman. FORTRAN program for predicting the off-design performance of radial inflow turbines. *NASA Technical Note TN-8063*, 1964.

[62] R. H. Aungier. *Centrifugal compressors: a strategy for aerodynamic design and analysis*. ASME press, New York, 2000.

[63] Y. P. Krylov and Y. A. Spunde. About the influence of the clearance between the working blades and housing of a radial turbine on its exponent. *USAF foreign technology division translation, FTD-MT-67-15*, 1963.

[64] S. M. Futral and D. E. Holeski. Experimental results of varying the

blade-shroud clearance in a 6.02 radial-inflow turbine. *NASA Technical Note TN D-5513*, 1965.

[65] I. Watanabe, I. Ariga, and T. Mashimo. Effect of dimensional parameters of impellers on performance characteristics of a radial inflow turbine. *Journal of engineering for power, 93: 81-102*, 1971.

[66] W. A. Spraker. Contour clearance losses in radial inflow turbines for turbochargers. *ASME Paper No 87-ICE-52*, 1987.

[67] J. W. Daily and R. E. Nece. Chamber dimensions effects on induced flow and frictional resistance of enclosed rotating disks. *Journal of Basic engineering 82: 217-232*, 1960.

[68] D. G. Ainley and G. C. R. Mathieson. A method for performance estimation for axial-flow turbines. *ARC Technical Report , R. and M. No.2974, Great Britain*, 1957.

[69] J. Dunham and P.M. Came. Improvements to the Ainley-Mathieson method of turbine performance prediction. *Trans. ASME Journal of Engineering for Power 92: 252-256*, 1970.

[70] S. C. Kacker and U. Okapuu. A mean line prediction method for axial flow turbine efficiency. *Trans. ASME Journal of Engineering for Power 104: 111-119*, 1982.

[71] S. H. Moustapha, S. C. Kacker, and B. Tremblay. An improved incidence losses prediction method for turbine airfoils. *Trans. ASME Journal of Turbomachinery 115: 400-408*, 1990.

[72] H. R. M. Craig and H. J. A. Cox. Performance estimation of axial flow turbines. *Proceedings of the Institution of Mechanical Engineers 185, No.32: 407-423*, 1971.

[73] W. Traupel. *Termische Turbomaschinen Zweiter Band Geländerte Betriebsbedingungen, Regelung, Mechanische Probleme, Temperaturprobleme*. Springer-Verlag Berlin heidelberg, New York, 1977.

[74] J. D. Denton. Loss mechanisms in turbomachinery. *Trans. ASME 93-GT-435, International Gas Turbine and Aeroengine Congress and Exposition Cincinnati, Ohio May 24-27*, 1993.

[75] J. Dunham. A review of cascade data on secondary losses in turbines. *Journal of Mechanical engineering science 12*, 1970.

[76] B. Lakshminarayana. Methods of predicting the tip clearance effects in axial flow turbomachinery. *Journal of Basic engineering 92: 467-480*, 1970.

[77] M. I. Yaras and S. A. Sjolander. Prediction of tip-leakage losses in axial turbines. *Trans. ASME 90-GT-154, Gas Turbine and Aeroengine Congress and Exposition - June 11-14, Brussels, Belgium*, 1990.

[78] O. Zweifel. The spacing of turbomachine blading, especially with large angular deflection. *Brown Boveri Rev 32, 12*, 1945.

[79] A. Meroni, J. G. Andreasen, G. Persico, and F. Haglind. Optimization of organic Rankine cycle power systems considering multistage axial turbine design. *Applied Energy 209: 339-354*, 2018.

[80] D. Vimercati, G. Gori, A. Spinelli, and A. Guardone. Non-ideal effects on the typical trailing edge shock pattern of orc turbine blades. *IV International Seminar on ORC Power Systems, ORC2017, Milan, Italy*, 2017.

[81] N. Mazzi, S. Rech, and A. Lazzaretto. Off-design dynamic model of a real Organic Rankine Cycle system fuelled by exhaust gases from industrial processes. *Energy 90: 537-551*, 2015.

[82] J. S. Brown, F. Polonara, G. Di Nicola, L. Fedele, S. Bobbo, and C. Zilio. Vapor Pressure of Hydrofluoroolefins: Critical Review of Experimental Data and Models. *International Refrigeration and air Conditioning Conference, Pardue University, USA*, 2012.

[83] M. Pini, C. De Siervi, M. Burigana, S. Bahamonde, A. Rubino, S. Vitale, and P. Colonna. Fluid-dynamic design and characterization of a mini-ORC turbine for laboratory experiments. *Energy Procedia 129: 1141-1148*, 2017.

Ringraziamenti

Desidero ringraziare il mio supervisore Prof. Andrea Lazzaretto per avermi dato la possibilità di intraprendere questo percorso fornendomi preziose indicazioni e suggerimenti.

Grazie al Dr. Giovanni Manente, co-supervisore, che mi ha pazientemente affiancato nel corso di questi tre anni e con cui ho condiviso dubbi e soluzioni.

Desidero inoltre ringraziare il Prof. Massimo Masi per la generosa disponibilità fornita nella fase finale del lavoro.

Un grazie anche a tutti i miei colleghi di dottorato e compagni d'ufficio.

Infine ringrazio la mia famiglia che ha sempre creduto in me e mi ha costantemente su(o)pportato durante la stesura di questa tesi.